Towards the Improvement of Hyperspectral Imaging Data: Limitations of the Raster Model and the Development of a Novel Point Cloud Data Format

Deep Inamdar

Department of Geography

McGill University, Montréal

August 2022

A thesis submitted to McGill University in partial fulfillment of the requirements of the degree of Doctor of Philosophy

© Deep Inamdar 2022

Abstract

The abundance of spectral-spatial information captured in airborne and spaceborne hyperspectral imaging (HSI) data allows end users to characterize the materials within each pixel based on their light-matter interactions. Such information provides insight to important problems such as climate change, food security and national defense. End users of HSI data are often provided with georeferenced raster end products that consist of uniformly distributed square pixels. When using raster end products, end users implicitly assume image pixels are: 1) directly comparable, 2) square and 3) uniformly distributed in space. These assumptions do not hold in HSI. This thesis investigates how raster end products misrepresent HSI data.

Hyperspectral imagers are affected by errors that appear in various spectral bands and spatial pixels. To confidently compare the spectrum from different pixels, it is critical to know the location of imaging errors. The first analytical chapter of this thesis develops an algorithm to localize imaging errors both spectrally and spatially by analyzing HSI data in (i.e., before geometric correction and rasterization). In 8 HSI datasets, the developed algorithm was used to determine the effectiveness of various processing methodologies and the consistency of the spectra collected across the sensor field of view. This chapter highlights imperfections in HSI data, showcasing the importance of analyzing data in its raw sensor geometry.

The second analytical chapter studies the consequences of assuming that pixels are square. By deriving and analyzing the sensor point spread function, this chapter emphasizes that only ~ 55.5% of the signal to any given spectrum originates from the spatial boundaries defined by the raw pixel resolution. Modifying the algorithm developed in the first analytical chapter, the overlap in the point spread function of neighbouring pixels was shown to introduce sensor generated spatial correlations. Using a simulated HSI scene, sensor generated spatial correlations were found to remove 31.1-38.9% of the spectral variability. A deconvolution algorithm was developed to restore the lost variability. After deconvolution, the spectral variability from the simulated imagery was within 6.8% of the original value. When tested on real HSI data, the algorithms sharpened the imagery while characterizing the spatial correlation structure of the data. This chapter highlights that the non-square nature of pixels mask and distort the natural

spatial dynamics of the imaged scene, showcasing that the raster data model mispresents HSI data.

The final analytical chapter quantifies the consequences of assuming that pixels are uniformly distributed. In raster end products, pixels appear to be uniformly distributed due to the use of nearest neighbour spatial resampling. This process compromises spatial data integrity as pixels from the geometrically corrected HSI data are shifted, duplicated and eliminated to produce a raster end product. By quantifying resampling errors, the uniform pixel distribution assumption could be studied. In four different HSI datasets, conventional raster end products were characterized by pixel duplication (up to 75%), pixel loss (up to 75%) and pixel shifting (up to 1.95 pixels). A novel point cloud data format was developed, fusing digital elevation data with HSI data while preserving the raw sensor geometry. This data format optimally preserved the spatial-spectral integrity of HSI data (zero resampling errors) while being up to 13 times smaller in file size than raster end products. In various data applications (classification, spectra geolocation and target detection), the hyperspectral point cloud data format outperformed conventional raster end products.

Overall, this thesis project re-evaluates the use of raster end products, proposing an alternative format that pushes the boundaries of HSI data acquisition, processing, analysis and application.

Key Words: Remote Sensing, Hyperspectral Imaging, Error Detection, Image Enhancement, Point Spread Function, Hyperspectral Point Cloud, Spatial Resampling, Hyperspectral Processing

Résumé

Des images hyperspectrales conteine une abondance d'information spectrale et spatiale qui permet l'étude des matériaux présents dans chaque pixel par leurs interactions lumière-matière. Ces informations l'aident des problèmes tels que le changement climatique, la sécurité alimentaire et la défense nationale. Les utilisateurs des données d'imagerie hyperspectrales reçoivent des produits finaux géoréférencés et rastérisés qui comprisent des pixels carrés et uniformément répartis. Lorsqu'ils utilisent des produits finaux rastérisés, les utilisateurs présument que les pixels des imagens sont: 1) directement comparables, 2) carrés et 3) uniformément répartis dans l'espace. Ces hypothèses sont érronés pour des images hyperspectrales. Cette thèse quantifie les erreurs dans les produits finaux rastérisés des images hyperspectrales.

Les imageurs hyperspectraux sont affectés par des erreurs qui apparaissent dans diverses bandes spectrales et pixels spatiaux. Le premier chapitre développe un algorithme pour localiser les erreurs spectrales et spatiales dans imagerie en analysant les images hyperspectrales dans leur géométrie brute de capteur. Dans 8 données d'imagerie hyperspectrale, l'algorithme a déterminé l'efficacité de diverses méthodologies et la cohérence des spectres recueillis dans le champ de vision du capteur. Ce chapitre met en évidence les imperfections des données HSI, montrant l'importance d'analyser le géométrie brute de capteur.

Le deuxième chapitre étudie les conséquences de présumer que des pixels sont carrés. En dérivant et en analysant la fonction d'étalement du point, on a découvert que ~ 55,5 % du signal d'un spectre donné provient des limites spatiales définies par la résolution brute des pixels. En modifiant l'algorithme développé, on a montré que le chevauchement de la fonction d'étalement du point des pixels adjacents introduit des corrélations spatiales générées par le capteur. En utilisant une scène hyperspectrale simulée, les corrélations spatiales générées par le capteur ont éliminé 31,1-38,9 la variabilité spectrale. Un algorithme de déconvolution a été développé montrant la variabilité spectrale de l'imagerie simulée se situait à 6,8 % de la valeur originale. Lorsqu'ils ont été testés sur des images hyperspectrales réelles, les algorithmes ont rendu l'imagerie plus nette et caractérisent la structure de corrélation spatiale des données. Alors, la nature non carrée des pixels masque et déforme la dynamique spatiale naturelle de la scène

imagée, montrant ainsi que le modèle de données rastérisés représente faussement les images hyperspectrales.

Le dernier chapitre quantifie les conséquences de présumer que des pixels uniformément répartis. Dans les produits finaux rastérisés, les pixels semblent être uniformément distribués après l'utilisation du rééchantillonnage spatial du plus proche voisin. Ce processus compromet l'intégrité des données spatiales. Dans quatre imageries hyperspectrale, les produits finaux rastérisés étaient caractérisés par la duplication de pixels (jusqu'à 75 %), la perte de pixels (jusqu'à 75 %) et le décalage de pixels (jusqu'à 1,95 pixel). Un nouveau format de données de nuage de points a été développé, préservant la géométrie brute du capteur. Ce format de données a préservé de manière optimale l'intégrité spatiale et spectrale des images hyperspectrales (zéro erreur de rééchantillonnage) tout en étant jusqu'à 13 fois plus que les produits finaux rastérisés. Dans diverses applications (classification, géolocalisation de spectres et détection de cibles), le format de données de nuages de points hyperspectraux a surpassé les produits finaux rastérisés conventionnels.

En tout, ce projet de thèse réévalue l'utilisation des produits finaux rastérisés, en proposant un format alternatif qui repousse les limites de l'acquisition, du traitement, de l'analyse et de l'application d'imagerie hyperspectrale.

Contributions to Original Knowledge

This thesis project makes several contributions to original knowledge within the field of hyperspectral remote sensing:

- Investigates the limitations of georeferenced raster end products in hyperspectral imaging (HSI) efforts
 - a. Developed a simple tool to identify non-linear imaging errors that are masked in georeferenced HSI raster end products.
 - b. Quantifies the relative spatial contribution to the spectrum from each pixel in HSI data, highlighting that a large portion of the signal (>44%) originates from materials outside the square spatial boundaries defined by the spatial resolution.
 - c. Showcases negative implications of using the pixel boundaries in HSI data to define the spatial characteristics of each measured spectra during flight planning, data cross-validation and data fusion.
 - d. Quantifies pixel loss, pixel duplication and pixel shifting errors that are introduced while generating georeferenced HSI raster end products.
 - e. Showcases the negative implications of pixel loss, pixel duplication and pixel shifting errors in practical remote sensing tasks such as classification, spectra geolocation and target detection.
- Overcomes limitations in the raster data model through the development of the Directly Georeferenced Hyperspectral Point Cloud (DHPC), a novel point cloud data paradigm for HSI efforts.
 - a. DHPC preserves the spectral and spatial integrity of HSI data (zero pixel loss, duplication and shifting errors) while including surface elevation.
 - b. DHPC improves performance in various practical remote sensing tasks (e.g., classification, spectra geolocation and target detection) when compared to conventional raster end products.
 - c. DHPC is more compact in data storage requirements than the raster data formats. This makes HSI data easier to distribute and analyze.
 - d. DHPC data representation bridges the gap between ground and hyperspectral imaging data collected at various spatial scales by providing a clear physical

- interpretation of the collected spectral measurements. This will lead to reduced errors due to differences in spatial scale between ground and HSI data during application.
- e. DHPC is provided as a comma delimited text file as a list of multivariate observations (including elevation, reflectance values, position and other desired variables such as off-nadir look angle) that researchers in various fields are comfortable manipulating. This makes HSI data more approachable to a wider array of scientists that are unfamiliar with raster data structures.
- 3. Lowers the barrier to entry to HSI by developing various algorithms (e.g., data quality assessment, spatial autocorrelation analysis, image sharpening, data simulation, data fusion, flight planning) that can be readily implemented by end users of all expertise levels.

Table of Contents

Abstract	2
Résumé	4
Contributions to Original Knowledge	6
Table of Contents	8
List of Figures	12
List of Tables	24
List of Abbreviations	26
Acknowledgements	28
Preface	29
Thesis Structure and Style	29
Contribution of Authors	
1. Introduction	31
Connecting Statement (Chapter 1 to Chapter 2)	35
2. Literature Review	36
2.1. Sensor Design	38
2.2. Sensor Characterization	
2.2.1. Radiometric Response	
2.2.2. Spectral Response	
2.2.3. Spatial Response	
2.3. Data Acquisition	
2.4. Data Processing.	
2.4.1. Radiometric Correction, Spectral Smile Correction and Spatial Keystone Correction2.4.2. Deconvolution	
2.4.2. Deconvolution	
2.4.4. Geometric Correction	
2.4.5. Rasterization	
2.5. Data End Products	
2.5.1. The Raster Data Model	
2.5.2. The Vector Data Model	
2.5.3. Effective Integration of the Vector Data Model in Hyperspectral Imaging	64

2.6.	Concluding Remarks	66
Con	necting Statement (Chapter 2 to Chapter 3)	69
	The Correlation Coefficient as a Simple Tool for the Localization of	5 0
	ors in Spectroscopic Imaging Data	
	ract	
3.1.	Introduction	
3.2.	Materials and Methods	74
_	.1. In-Situ Ground Hyperspectral Data	
3.2		75
3.2	.3. Characterization of the Correlation Coefficient with Averaged and Interpolated in-Situ Radiance perspectral Data	77
	erspectral Data	
3.3.		
	.1. In-Situ Ground Hyperspectral Data	
3.3		
Hy	perspectral Data	86
	.3. Application of the Correlation Coefficient to Airborne Hyperspectral Imagery (Error Detection)	
3.4.	Discussion	. 104
3.5.	Conclusions	. 107
3.6.	References	. 107
3.7.	Author Contributions	. 111
3.8.	Acknowledgements	
4. Airb	necting Statement (Chapter 3 to Chapter 4)	in .113
Abstr	ract	
4.1.	Introduction	
4.2.	Materials and Methods	
	.1. Airborne HSI Data	
4.2		
4.2		
4.2 4.2		
4.2		
4.2		
4.3.	Results	
4.3		
4.3	<u>.</u>	
4.3	C 11	
4.3		
4.4.	Discussion	
4.5.	Conclusions	
4.6.	References	
4.7.	Author Contributions	
1 Q	A cknowledgments	15/

Conn	necting Statement (Chapter 4 to Chapter 5)	155
	The Directly-Georeferenced Hyperspectral Point Cloud (DHPC): erving the Integrity of Hyperspectral Imaging Data	156
	act	
5.1.	Introduction	
5.2.	Materials and Methods	
5.2.1 5.2.2	$\boldsymbol{\varepsilon}$	
5.2.3		
	Results	
5.3.1		
5.3.2	,, , , , , , , , , , , , , , , , , , ,	
5.4.	Discussion	
5.5.	References	
5.6.	Author Contribution	
5.7.	Acknowledgements	
5.8.		
3.8.	Supplementary Material	203
C	on the Charles of (Charles 5 to Charles ()	204
Conn	necting Statement (Chapter 5 to Chapter 6)	204
<i>(</i> T		205
	Discussion and Conclusion	
6.1.	Discussion of Research	
6.2.	Impact of Research	
6.3.	Limitations and Future Directions of Research	
6.4.	Conclusion	218
7. A	Appendix	219
7.1.	Spatial Response Resampling (SR ²): Accounting for the Spatial Point Spread Fur	ection in
	spectral Image Simulation	219
	tract	
	phical Abstract	
-	l. Background	
7.1.2		
7.1.3		
7.1.4		
7.1.5		
7.1.6 7.1.7		
7.1.8		
7.2.	Implementation of the Directly-Georeferenced Hyperspectral Point Cloud (DHPC	
	tract	/
	phical Abstract	
7.2.1		
7.2.2		265
7.2.3		
7.2.4		
7.2.5	*	272 277

8.	Ref	ference List	279
		Supplementary Material	
	7.2.8.	Acknowledgements	278
	7.2.7.	Author Contribution	278

List of Figures

FIGURE	2.1. EXAMPLE SPECTRAL RESPONSE FUNCTIONS FOR THREE ADJACENT BANDS FROM THE CASI-1500. THE
SI	PECTRAL RESPONSE FUNCTIONS OF THE BANDS DISPLAYED IN THE FIGURE ARE DEFINED BY FOURTH-ORDER
В	UTTERWORTH FILTER FUNCTIONS CENTRED AT 597.757 NM, 600.150 NM AND 602.543 NM. THE SPECTRAL
	ESOLUTION IS DEFINED BY THE FULL WIDTH AT HALF-MAXIMUM AND IS APPROXIMATELY EQUAL TO 2.4 NM (SEE
	LACK DOUBLE-SIDED ARROW IN THE FIGURE). HYPERSPECTRAL IMAGING SYSTEMS COLLECT CONTIGUOUS
	PECTRAL INFORMATION, WHICH CAN BE SEEN IN THE OVERLAP BETWEEN ADJACENT SPECTRAL RESPONSE
	UNCTIONS
1.0	THE HONG.
FIGURE	2.2. REPRESENTATION OF SPECTRAL SMILE AND KEYSTONE ARTIFACTS IN PUSHBROOM HYPERSPECTRAL
IN	MAGING DATA. IN THE IDEAL SCENARIO, THE SPECTRUM FROM EACH PIXEL COLLECTS DATA ON THE SAME
W	AVELENGTH ARRAY. FURTHERMORE, EACH BAND FROM A SINGLE HYPERSPECTRAL IMAGE PIXEL CORRESPONDS
TO	O THE SAME AREA ON THE GROUND. IN REALITY, EACH HYPERSPECTRAL PIXEL COLLECTS SPECTRAL DATA ON A
SI	LIGHTLY DIFFERENT WAVELENGTH ARRAY (SPECTRAL SMILE). ADDITIONALLY, EACH BAND FROM ANY GIVEN
Н	YPERSPECTRAL IMAGE PIXEL CORRESPONDS TO A SLIGHTLY DIFFERENT AREA ON THE GROUND (KEYSTONE) 45
FIGURE	2.3. EXAMPLE POINT SPREAD FUNCTION DERIVED FOR IMAGERY COLLECTED BY THE COMPACT AIRBORNE
	PECTROGRAPHIC IMAGER (CASI-1500). THE RELATIVE SPATIAL CONTRIBUTION TO A SINGLE PIXEL IS A FUNCTION
	F ACROSS TRACK AND ALONG TRACK DISPLACEMENT FROM THE PIXEL CENTER. FIGURE REPRODUCED WITHOUT
	ODIFICATIONS FROM INAMDAR ET AL. (2020) UNDER THE TERMS AND CONDITIONS OF THE CREATIVE COMMONS
	TTRIBUTION (CC BY) LICENSE (HTTP://CREATIVECOMMONS.ORG/LICENSES/BY/4.0/)
А	TRIBOTION (CC BT) EICENSE (ITTIT ://CREATIVECONIMONS.ORG/EICENSES/BT/4.0/).
FIGURE	2.4. EXAMPLE SPATIAL RESPONSE FUNCTION IN THE ACROSS TRACK DIRECTION FOR THREE ADJACENT PIXELS
FI	ROM CASI-1500 IMAGERY. SPATIAL RESOLUTION CAN BE DEFINED BY THE FULL WIDTH AT HALF-MAXIMUM (SEE
B	LACK DOUBLE-SIDED ARROW IN THE FIGURE). HYPERSPECTRAL IMAGING SYSTEMS COLLECT CONTIGUOUS
SI	PATIAL INFORMATION, WHICH CAN BE SEEN IN THE OVERLAP BETWEEN ADJACENT SPATIAL RESPONSE
FU	UNCTIONS
FIGURE	2.5. THE APPROXIMATE SPATIAL RESOLUTION AND GEOGRAPHIC EXTENT OF HYPERSPECTRAL IMAGING
S	YSTEMS ON VARIOUS PLATFORMS
FIGURE	2.6. TRANSMISSION OF ELECTROMAGNETIC RADIATION IN THE ATMOSPHERE FROM 200 NM TO 13000 NM
	ALCULATED USING MODTRAN FOR A SUMMERTIME MID-LATITUDE HAZY ATMOSPHERE (5 KM VISIBILITY). THE
	HADED LIGHT-BLUE REGION GIVES THE TRANSMISSIVITY (IN UNITS OF %) OF ELECTROMAGNETIC RADIATION IN
	HE ATMOSPHERE AS A FUNCTION OF WAVELENGTH. THE COLORED BARS DISPLAY THE WIDTH OF LANDSAT'S
	PECTRAL BANDS FROM THE FIRST GENERATION MULTISPECTRAL SCANNER SYSTEM (MSS) TO LANDSAT 9'S
	PERATIONAL LAND IMAGER 2 (OLI-2). ALL SPECTRAL BANDS ARE DESIGNED TO EXPLOIT AVAILABLE
	TMOSPHERIC WINDOWS (FIGURE COPIED FROM BARSI AND ROCCHIO (2020) FOLLOWING THE NASA MEDIA USAGE
G	UIDELINES)
FIGURE	2.7. SCHEMATIC SKETCH OF THE MAJOR SOLAR RADIATION COMPONENTS FROM THE SIGNAL MEASURED BY A
Н	YPERSPECTRAL (HS) IMAGER. THE ATMOSPHERIC COMPENSATION ATTEMPTS TO RECOVER THE REFLECTANCE (P)
0	F THE MATERIAL THAT IS RESPONSIBLE FOR THE REFLECTED RADIANCE55
FIGURE	2.8. SCHEMATIC OF THE GEOMETRIC CORRECTION. WITH A KNOWN SENSOR POSITION (P) AND LOOK DIRECTION
(0	$\Phi_{\rm L}$), THE POSITION OF EACH PIXEL IN THE IMAGE SPACE CAN BE LOCATED IN A REAL-WORLD COORDINATE
SI	PACE. THE PIXEL IS LOCATED AT THE INTERSECTION (A) OF THE INPUT DIGITAL SURFACE MODEL (SHOWN IN
	REEN) AND A STRAIGHT LINE PROJECTED AT THE PIXEL-DEPENDENT LOOK DIRECTION FROM THE SENSOR

	POSITION. THE LOOK DIRECTION IS THE ANGLE AT WHICH INCOMING ELECTROMAGNETIC RADIATION IS
	OBSERVED BY ANY GIVEN PIXEL OF THE HYPERSPECTRAL IMAGER (MÜLLER ET AL., 2002). THE LOOK DIRECTION IS
	CALCULATED FROM THE SENSOR'S ATTITUDE, FOCAL GEOMETRY AND BORESIGHT MISALIGNMENT DURING DATA
	ACQUISITION (BRUNN ET AL., 2003; MÜLLER ET AL., 2002). FIGURE REPRODUCED WITHOUT MODIFICATIONS FROM
	INAMDAR ET AL. (2021) UNDER THE TERMS AND CONDITIONS OF THE CREATIVE COMMONS ATTRIBUTION (CC BY)
	LICENSE (HTTP://CREATIVECOMMONS.ORG/LICENSES/BY/4.0/)
EIGI	IDE 1.1. AN EMPERIMENTAL CETTUREOR ACQUIRING BY CITTLE CROUDIN HARPROPECTRAL MEACUREMENTS OF AN
riGt	JRE 3.1. A) EXPERIMENTAL SETUP FOR ACQUIRING IN-SITU GROUND HYPERSPECTRAL MEASUREMENTS OF AN
	ASPHALT TARGET USING THE HR-1024I SPECTROMETER. B) THE HEMISPHERICAL SKY PHOTO WAS ACQUIRED
	SIMULTANEOUSLY WITH THE GROUND SPECTROMETER MEASUREMENTS AS A MEANS OF ESTIMATING THE
	POTENTIAL INFLUENCE OF CLOUD AND VISIBLE AEROSOL (HAZE) DURING THE TIME OF DATA ACQUISITION. ALL
	DATA WERE COLLECTED UNDER STABLE CONDITIONS
FIGU	JRE 3.2. STUDY SITE AT THE MACDONALD–CARTIER INTERNATIONAL AIRPORT IN OTTAWA, ONTARIO, CANADA. THE
	FLIGHT LINE FOLLOWED A 306.5° TRUE NORTH PATH AS SHOWN BY THE BLUE ARROW. GROUND CALIBRATION
	MEASUREMENTS WERE TAKEN ON THE ASPHALT SURFACE LOCATED BY THE RED X
FIGU	URE 3.3. SCHEMATIC VIEW OF THE BASIC ALGORITHM FOR THE CHARACTERIZATION OF THE CC79
FICI	JRE 3.4. SCHEMATIC VIEW OF THE BASIC ALGORITHM FOR THE CHARACTERIZATION OF THE CC IN THE PRESENCE OF
1100	SIGNAL NOISE
EIGI	THE 1.5 NON GEOCORDECTED GARANGERY OF THE DATA ACQUIRITION RITE THE DIVIE I BE DIDICATED THE DOL
rige	JRE 3.5. NON-GEOCORRECTED CASI IMAGERY OF THE DATA ACQUISITION SITE. THE BLUE LINE INDICATES THE ROL
	SELECTED FOR THE ANALYSIS. THE ROI CONTAINED A SINGLE PIXEL FROM EACH COLUMN ACROSS THE ASPHALT
	ROAD. GROUND CALIBRATION MEASUREMENTS WERE TAKEN ON THE ASPHALT SURFACE LOCATED BY THE RED X,
	IN ACCORDANCE WITH FIGURE 3.2
FIGU	URE 3.6. SCHEMATIC VIEW OF THE BASIC ALGORITHM FOR THE APPLICATION OF THE CC IN THE SPATIAL
	LOCALIZATION OF ERRORS IN HSI DATA
FIGU	URE 3.7. SCHEMATIC VIEW OF THE BASIC ALGORITHM FOR THE APPLICATION OF THE CC IN THE SPECTRAL
	LOCALIZATION OF ERRORS IN HSI DATA
FIGI	JRE 3.8. SCHEMATIC VIEW OF THE BASIC ALGORITHM FOR THE APPLICATION OF THE CC IN THE LOCALIZATION OF
1100	FINER ERRORS IN HSI DATA
FICI	IDE 2.6. AVED A CED AND MODMALIZED COOLING OBECTRUM OF A CRITALT DEFORE AND A FTED INTERPOLATION. THE
riGt	JRE 3.9. AVERAGED AND NORMALIZED GROUND SPECTRUM OF ASPHALT BEFORE AND AFTER INTERPOLATION. THE
	DIFFERENCES BETWEEN THE TWO CURVES CAN BE SEEN IN THE SUBPLOT, WHICH ZOOMS IN ON THE 1185–1255 NM
	SPECTRAL WINDOW. THE INTERPOLATED CURVE, $R\lambda$, WAS USED FOR THE METHODOLOGIES DESCRIBED IN SECTION
	3.2.3. THE MEAN SQUARED ERROR BETWEEN OVERLAPPING DATA POINTS BEFORE AND AFTER INTERPOLATION
	WAS NEGLIGIBLE ($<10^{-30}$). THE AKIMA INTERPOLATION METHOD GENERATED A QUALITATIVELY SMOOTH $R\lambda$ 86
FIGU	URE 3.10. THE CC BETWEEN $R\lambda$ AND EACH OF THE TRANSFORMED DATASETS, $Rt\lambda$. A) THE CC ASYMPTOTICALLY
	REDUCED FROM ONE WHEN THE SNR DECREASED THROUGH THE INTRODUCTION OF AWGN. B) THE CC WAS
	INVARIANT TO ADDITIVE TRANSFORMATIONS. C) MULTIPLICATIVE TRANSFORMATIONS HAD NO IMPACT ON THE
	CC. D) THE INTRODUCTION OF A SPECTRAL SHIFT RESULTED IN A SMALL BUT CLEAR DECREASE IN THE CC. E) THE
	MULTIPLICATIVE TRANSFORMATION OF A SINGLE FEATURE WAS DETECTED IN THE CC BY A GRADUAL
	REDUCTION
FIGI	JRE 3.11. THE CC BETWEEN $RAWGN(\lambda)$ AND EACH OF THE TRANSFORMED DATASETS, Rt $AWGN(\lambda)$. ALL SIGNALS WERE

 $\textbf{CHARACTERIZED BY AN SNR VALUE OF 100:1. THE TRENDS FROM \textbf{FIGURE 3.10} PERSISTED, DESPITE BEING MASKED}$

	BY THE NOISE TO SOME DEGREE. A) THE CC WAS INVARIANT TO THE ADDITIVE TRANSFORMATION. B) MULTIPLICATIVE TRANSFORMATIONS HAD NO IMPACT ON THE CC. C) THE INTRODUCTION OF A SPECTRAL SHIFT RESULTED IN A SMALL, BUT CLEAR DECREASE IN THE CC. D) THE MULTIPLICATIVE TRANSFORMATION OF A SINGLE FEATURE WAS DETECTED IN THE CC BY A GRADUAL REDUCTION
FIGUI	RE 3.12. THE STANDARD DEVIATION OF THE CCS AT VARIOUS NOISE LEVELS. THERE WAS AN ASYMPTOTIC INCREASE IN THE STANDARD DEVIATION OF THE CCS WHEN THE SNR DECREASED THROUGH THE INTRODUCTION OF AWGN
	RE 3.13. THE CCS CALCULATED ACROSS THE FIELD-OF-VIEW WITH RESPECT TO THE ENTIRE SPECTRUM FROM THE CENTER PIXEL. A) THE CC OF THE CASI IMAGERY (23 JUNE 2016); B) SASI IMAGERY (23 JUNE 2016); C) CASI IMAGERY (24 JUNE 2016); D) SASI IMAGERY (24 JUNE 2016). A,C) THE CASI IMAGERY WAS CHARACTERIZED BY SYSTEMATIC REDUCTIONS NEAR THE EDGES OF THE FOV. THESE REVEALED POTENTIAL ERRORS CONSISTENT WITH THE SPECTRAL SMILE EFFECT AND OTHER CROSS-TRACK ILLUMINATION EFFECTS. THIS REDUCTION WAS MOST SUBSTANTIAL FOR THE CASI IMAGES GENERATED BY THE OLD PROCESSING METHODOLOGY. COMPARED TO THE IMAGERY FROM THE 24TH, THE CCS WERE MORE UNIFORM ACROSS THE FOV FOR THE CASI DATA FROM THE 23RD. B,D) THE SASI IMAGERY WAS CONSISTENT ACROSS ALL DATES AND PROCESSING METHODOLOGIES. THERE WAS A NOTABLE REDUCTION IN THE CCS ACROSS THE FOV FROM PIXELS 548–564. THIS REVEALED THE SPATIAL LOCATION OF AN ERROR
FIGUI	RE 3.14. HISTOGRAM-EQUALIZED CASI IMAGE (24 JUNE WITH THE ORIGINAL PROCESSING) AT 393.068 NM. THE ASPHALT ROAD ALONG THE SOUTH SIDE OF THE IMAGE WAS BRIGHTEST ALONG THE EDGE PIXELS. THE ERRORS IN THE DATA ARE HIGHLIGHTED BY THE RED ARROWS94
	RE 3.15. HISTOGRAM-EQUALIZED CASI IMAGERY (24 JUNE WITH THE REFINED PROCESSING) AT 393.068 NM. THE ASPHALT ROAD ALONG THE SOUTH SIDE OF THE IMAGE WAS BRIGHTEST ALONG THE EDGE PIXELS. THESE ERRORS IN THE DATA ARE HIGHLIGHTED BY THE RED ARROWS AND WERE LESS NOTICEABLE IN THE IMAGERY THAT WAS GENERATED FROM THE REFINED PROCESSING
FIGUI	ACROSS PIXELS 548–564 IS IDENTIFIED BY THE RED ARROW90
	RE 3.17. THE CCS CALCULATED ACROSS THE FIELD-OF-VIEW WITH RESPECT TO THE SPECTRUM COMPLEMENTARY TO THE WINDOWS IN TABLE 3.3. A) CASI IMAGERY (23 JUNE 2016); B) SASI IMAGERY (23 JUNE 2016); C) CASI IMAGERY (24 JUNE 2016); D) SASI IMAGERY (24 JUNE 2016). A,C) THE CCS OF THE CASI IMAGERY INCREASED GREATLY, ESPECIALLY ALONG THE EDGES, INDICATING THAT THE ERROR WAS PRIMARILY CONTAINED WITHIN THE SPECTRAL REGIONS IDENTIFIED IN TABLE 3.3. THE CASI DATA FROM THE 23RD WERE RELATIVELY CONSISTENT BETWEEN BOTH PROCESSING METHODOLOGIES. ALTHOUGH THIS TREND GENERALLY HELD FOR THE DATA FROM THE 24TH, C) SHOWED A NOTABLE OFFSET. D,B) THE LARGE REDUCTION IN THE CCS FROM THE SASI IMAGERY AT PIXELS 548–564 WAS NOT PRESENT AFTER REMOVING THE PROBLEMATIC BAND THAT WAS FOUND BETWEEN 993 AND 1008 NM.
	RE 3.18. THE CCS CALCULATED ACROSS THE FIELD-OF-VIEW OF THE CASI IMAGERY WITH RESPECT TO THE SPECTRUM FROM THE CENTER PIXEL. THE WAVELENGTH REGIONS USED TO CALCULATE THE CCS ARE IDENTIFIED IN EACH GRAPH AND CORRESPOND TO THE VALUES IN TABLE 3.4. PLOTS (A,C,E,G,I) CORRESPOND TO THE CASI DATA THAT WERE PROCESSED WITH THE ORIGINAL METHODOLOGY. PLOTS (B,D,F,H,J) CORRESPOND TO THE CASI DATA THAT WERE PROCESSED WITH THE REFINED METHODOLOGY. A,B) THE CCS FOR THE 680–712 NM REGION WERE HIGHLY VARIABLE WITH A LOW FREQUENCY SINUSOIDAL STRUCTURE. C,D) THE CCS FOR THE 710–745 NM REGION WERE RELATIVELY CONSTANT ACROSS THE FOV. A DISTINCT REDUCTION WAS DETECTED IN THE CC OF A SINGLE BIYEL NEAR THE RIGHT EDGE FOR THE IMAGERY PROCESSED WITH THE ORIGINAL METHODOLOGY. BUT

	NOT THE REFINED PROCESSING. E,F) THERE WAS A REDUCTION OF APPROXIMATELY 0.021 IN THE CC FOR THE /50-
	775 NM REGION NEAR THE EDGES OF THE FOV. THIS EFFECT IS LIKELY CAUSED BY THE SMILE EFFECT OR OTHER
	CROSS-TRACK ILLUMINATION EFFECTS. G,H) FOR THE DATA FROM THE 804–846 NM WINDOW OF THE IMAGERY
	PROCESSED WITH THE ORIGINAL METHODOLOGY, THERE WERE CHARACTERISTIC REDUCTIONS IN THE CC
	GREATER THAN 0.05 DETECTED. THESE REDUCTIONS REVEALED POTENTIAL IMAGING ERRORS FOR THE SPECTRAL
	WINDOW IN THE FOLLOWING SPATIAL RANGES: 256–276, 551–576, 912–936 AND 1209-1235. THESE REDUCTIONS WERE
	NOT PRESENT IN THE CCS FOR THE IMAGE DERIVED WITH THE REFINED PROCESSING. I,J) IN THE 883–992 NM
	REGION, THE CCS WERE RELATIVELY CONSTANT ACROSS THE FOV
FIGU	URE 3.19. HISTOGRAM-EQUALIZED CASI IMAGERY (24 JUNE WITH THE ORIGINAL PROCESSING) AT 706.4 NM. THE
	IMAGE IS ZOOMED IN TO DISPLAY COLUMNS 57–513 FROM LEFT TO RIGHT. THERE ARE "STRIPING" ARTEFACTS
	ACROSS THE FOV. THIS RIPPLE IS CLEARLY VISIBLE NEAR THE CENTER OF THE FIGURE, AS INDICATED BY THE RED
	ARROW
FIGU	JRE 3.20. HISTOGRAM-EQUALIZED CASI (24 JUNE WITH ORIGINAL PROCESSING) IMAGERY AT 744.653 NM. THE IMAGE
	IS ZOOMED IN TO DISPLAY COLUMNS 1248–1482 FROM LEFT TO RIGHT. THE RED AND ORANGE ARROWS POINT TO
	THE ERRORS IN PIXELS 1454 AND 1456 IN THE CROSS-TRACK. RESPECTIVELY. THESE ERRORS WERE VISUALIZED AS
	A BRIGHT AND DARK VERTICAL STRIPE
FIGU	JRE 3.21. HISTOGRAM-EQUALIZED CASI IMAGERY (24 JUNE WITH ORIGINAL PROCESSING) AT 835.491. THE RED LINES
	SHOW THE LOCATIONS OF DISTINCT "STRIPING" ARTEFACTS
FIGU	URE 3.22. HISTOGRAM-EQUALIZED CASI IMAGERY (24 JUNE WITH ORIGINAL PROCESSING) AT 931.099 NM. THE
	IMAGERY IS STABLE, WITH NO OBVIOUS ERRORS
FIGU	URE 4.1. UNMANNED AERIAL VEHICLE PHOTOGRAPH OF THE MER BLEUE PEATLAND IN OTTAWA, ONTARIO, CANADA.
	THERE ARE EVIDENT MICRO-SPATIAL PATTERNS IN VEGETATION THAT CORRESPOND TO THE HUMMOCK-HOLLOW
	MICROTOPOGRAPHY. A HUMMOCK MICROTOPOGRAPHY IS A DRIER ELEVATED MOUND WITH A DENSE COVER OF
	VASCULAR PLANTS WHILE A HOLLOW MICROTOPOGRAPHY IS A LOWER-LAYING DEPRESSION THAT IS WETTER
	AND DOMINATED BY MOSSES SUCH AS SPHAGNUM SPP. ADJACENT HUMMOCKS AND HOLLOWS CAN DIFFER IN
	ABSOLUTE ELEVATION BY AS MUCH AS 0.30 M OVER A HORIZONTAL DISTANCE OF 1–2 M
FIGU	JRE 4.2. THE RELATIVE SPATIAL CONTRIBUTION TO A SINGLE COMPACT AIRBORNE SPECTROGRAPHIC IMAGER 1500
	(CASI) IMAGE PIXEL AS A FUNCTION OF ACROSS TRACK (PLOT A) AND ALONG TRACK (PLOT B) DISPLACEMENT
	FROM THE CENTER OF THE PIXEL. THE OPTICAL, DETECTOR, MOTION AND NET POINT SPREAD FUNCTION (PSF) ARE
	DISPLAYED SEPARATELY. THE WIDTH OF THE DETECTOR POINT SPREAD FUNCTION REPRESENTS THE RAW
	SPATIAL RESOLUTION IN THE ACROSS TRACK DIRECTION. THE WIDTH OF THE MOTION POINT SPREAD FUNCTION
	REPRESENTS THE RAW SPATIAL PIXEL RESOLUTION IN THE ALONG TRACK DIRECTION. A SUBSTANTIAL PORTION
	OF THE NET PSF LIES OUTSIDE THE TRADITIONAL PIXEL BOUNDARIES DEFINED BY THE RAW RESOLUTION OF 0.55
	M IN THE ACROSS TRACK DIRECTION. AS SUCH, THE SPECTRUM FROM EACH PIXEL HAS SIZEABLE CONTRIBUTIONS
	FROM THE MATERIALS WITHIN THE SPATIAL BOUNDARIES OF NEIGHBOURING PIXELS IN THE ACROSS-TRACK. A
	SUBSTANTIAL PORTION OF THE NET PSF LIES OUTSIDE THE TRADITIONAL PIXEL BOUNDARIES DEFINED BY THE
	RAW RESOLUTION OF 1.99 M IN THE ALONG TRACK DIRECTION AS WELL. THESE CONTRIBUTIONS ARE NOT AS
	$SIGNIFICANT\ AS\ THEY\ ARE\ IN\ THE\ ACROSS-TRACK,\ HOWEVER,\ THERE\ ARE\ STILL\ NOTABLE\ CONTRIBUTIONS\ FROM$
	MATERIALS WITHIN THE SPATIAL BOUNDARIES OF NEIGHBOURING ALONG TRACK PIXELS124
FIGU	JRE 4.3. THE RELATIVE SPATIAL CONTRIBUTION TO A SINGLE COMPACT AIRBORNE SPECTROGRAPHIC IMAGER 1500
	(CASI) IMAGE PIXEL AS A FUNCTION OF ACROSS TRACK AND ALONG TRACK DISPLACEMENT FROM THE CENTER OF

THE PIXEL. THE GRID IN THE X–Y PLANE CORRESPONDS WITH THE ACTUAL PIXEL SIZES (0.55~M IN THE ACROSS TRACK DIRECTION AND 1.99~M IN THE ALONG TRACK DIRECTION). AS SUCH, EACH SQUARE WITHIN THE GRID

FROM MATERIALS WITHIN THE SPATIAL BOUNDARY OF THE CENTER PIXEL. IT IS IMPORTANT TO NOTE THAT
THERE IS A SUBSTANTIAL CONTRIBUTION FROM MATERIALS WITHIN THE SPATIAL BOUNDARIES OF
NEIGHBOURING PIXELS
FIGURE 4.4. THE VEGETATION REGION OF INTEREST SELECTED FROM THE MER BLEUE PEATLAND. THE REGION OF
INTEREST IS CHARACTERIZED BY A HUMMOCK-HOLLOW MICROTOPOGRAPHY THAT CORRESPONDS TO SMALL
SCALE PATTERNS (2–4 M) IN SURFACE VEGETATION AND SURFACE REFLECTANCE. HUMMOCKS ARE ELEVATED
MOUNDS OF DENSE VASCULAR COVER WHILE HOLLOWS ARE THE LOWER-LYING AREAS COMPOSED PRIMARILY
OF SPHAGNUM SPP. MOSSES. THE ORTHOPHOTO (0.2 M SPATIAL RESOLUTION) WAS COLLECTED FOR THE NATIONAL
CAPITAL COMMISSION OF CANADA (SOURCE: OTTAWA ORTHOPHOTOS, 2011)
FIGURE 4.5. THE SPATIAL CONTRIBUTION TO THE SPECTRUM OF THE CENTER COMPACT AIRBORNE SPECTROGRAPHIC
IMAGER 1500 (CASI) PIXEL FROM MATERIALS WITHIN THE BOUNDARIES OF NEIGHBOURING PIXELS. THE RED
SQUARE REPRESENTS THE SPATIAL BOUNDARIES OF THE CENTER PIXEL, AS DETERMINED BY THE RAW PIXEL
RESOLUTION. THE BLACK SQUARES REPRESENT THE SPATIAL BOUNDARIES OF NEIGHBOURING PIXELS. ONLY 55.
OF THE SPECTRAL SIGNAL ORIGINATES FROM MATERIALS WITHIN THE SPATIAL BOUNDARIES OF THE CENTER
PIXEL. THE REMAINING 44.5% OF THE SIGNAL COMES FROM THE MATERIALS WITHIN THE SPATIAL BOUNDARIES (
THE NEIGHBOURING PIXELS. THE UNDERLYING SCENE IN THE FIGURE IS A PHOTOGRAPH OF THE MER BLEUE
PEATLAND COLLECTED FROM AN UNMANNED AERIAL VEHICLE1
FIGURE 4.6. SIMULATED HYPERSPECTRAL IMAGING DATA REPRESENTATIVE OF THE MER BLEUE PEATLAND. THE IMAG
ARE DISPLAYED IN TRUE COLOUR (RED = 639.5 NM \pm 1.2, GREEN = 551.0 NM \pm 1.2, BLUE = 460.1 NM \pm 1.2). IN THE
DISPLAY, ALL THREE BANDS ARE LINEARLY STRETCHED BETWEEN 0% AND 12%. A) THE IDEAL SIMULATED IMAG
THAT WAS DERIVED WITH A UNIFORM POINT SPREAD FUNCTION. B) THE NON-IDEAL SIMULATED IMAGE THAT
WAS DERIVED WITH THE COMPACT AIRBORNE SPECTROGRAPHIC IMAGER 1500 (CASI) POINT SPREAD FUNCTION.
THE CORRECTED NON-IDEAL SIMULATED IMAGE THAT WAS DERIVED BY APPLYING THE DEVELOPED
DECONVOLUTION ALGORITHM TO THE NON-IDEAL SIMULATED IMAGE. ALL IMAGES WERE SIMULATED AT THE
SAME SPATIAL RESOLUTION AS THE REAL-WORLD CASI IMAGERY (ACROSS TRACK = 0.55 M, ALONG TRACK = 1.99
M). THE SIMULATED DATASETS WERE USED TO CHARACTERIZE THE IMPLICATIONS OF SENSOR-GENERATED
SPATIAL CORRELATIONS WHILE TESTING THE DEVELOPED ALGORITHMS
FIGURE 4.7. THE MEAN (PLOT A) AND STANDARD DEVIATION (PLOT B) FOR EACH SPECTRAL BAND OF THE IDEAL
(UNIFORM POINT SPREAD FUNCTION) AND NON-IDEAL (COMPACT AIRBORNE SPECTROGRAPHIC IMAGER 1500
POINT SPREAD FUNCTION) SIMULATED IMAGES. THERE WERE NO OBSERVABLE DIFFERENCES IN THE MEAN
SPECTRUM FROM EACH IMAGE. THE ATTENUATION IN STANDARD DEVIATION SUGGESTS THAT SENSOR BLURRIN
ELIMINATED SOME OF THE NATURAL VARIABILITY OBSERVED IN THE IDEAL IMAGE. THIS IS PROBLEMATIC GIVE
THE IMPORTANCE OF SECOND-ORDER STATISTICS IN THE ANALYSIS OF HIGH DIMENSIONAL DATA
FIGURE 4.8. THE MEAN CORRELATION COEFFICIENT AS A FUNCTION OF PIXEL DISPLACEMENT IN THE ACROSS TRACK
(PLOT A) AND ALONG TRACK (PLOT B) DIRECTIONS OF THE IDEAL (UNIFORM POINT SPREAD FUNCTION), NON-
IDEAL (COMPACT AIRBORNE SPECTROGRAPHIC IMAGER 1500 POINT SPREAD FUNCTION) AND CORRECTED NON-
IDEAL SIMULATED IMAGES. THE BARS AROUND EACH MEAN GIVE THE 1–SIGMA WINDOW. THE MEAN AND
STANDARD DEVIATION QUANTIFIED THE STRENGTH AND VARIABILITY OF THE SPATIAL CORRELATIONS PRESENT
WITHIN EACH IMAGE. THE CORRECTED NON-IDEAL IMAGE WAS GENERATED BY APPLYING THE DEVELOPED
DECONVOLUTION ALGORITHM. IN THE IDEAL IMAGE, THERE WAS NO SPATIAL CORRELATION STRUCTURE. THE
COMPACT AIRBORNE SPECTROGRAPHIC IMAGER 1500 POINT SPREAD FUNCTION USED TO SIMULATE THE NON-
IDEAL IMAGE, AND THE ASSOCIATED IMAGE BLURRING, INTRODUCED A SPATIAL CORRELATION STRUCTURE. TH

CORRESPONDS TO THE TRADITIONAL SPATIAL BOUNDARY OF A SINGLE PIXEL. MOST OF THE SIGNAL ORIGINATES

SPATIAL CORRELATION STRUCTURE OF THE IDEAL IMAGE WAS RECOVERED FROM THE NON-IDEAL IMAGE USI THE DEVELOPED DECONVOLUTION ALGORITHM	
FIGURE 4.9. THE STANDARD DEVIATION IN EACH SPECTRAL BAND OF THE IDEAL (UNIFORM POINT SPREAD FUNCTION NON-IDEAL (COMPACT AIRBORNE SPECTROGRAPHIC IMAGER 1500 POINT SPREAD FUNCTION) AND CORRECTED NON-IDEAL IMAGE. THE CORRECTED NON-IDEAL IMAGE WAS GENERATED BY APPLYING THE DEVELOPED DECONVOLUTION ALGORITHM. THE ATTENUATION IN THE STANDARD DEVIATION OF THE NON-IDEAL IMAGE SUGGESTS THAT SENSOR BLURRING ELIMINATED SOME OF THE NATURAL VARIABILITY OBSERVED IN THE IDEAL IMAGE. THE NATURAL VARIABILITY IN EACH SPECTRAL BAND OF THE IDEAL IMAGE WAS RESTORED FROM THE NON-IDEAL IMAGE BY APPLYING THE DECONVOLUTION ALGORITHM.	A L
FIGURE 4.10. THE EUCLIDEAN DISTANCE (IN UNITS OF REFLECTANCE) BETWEEN THE IDEAL IMAGERY AND BOTH THE	
NON–IDEAL (PLOT ${f A}$) AND CORRECTED NON–IDEAL (PLOT ${f B}$) IMAGES. THE GRAYSCALE DISPLAY IS LINEARLY	
STRETCHED BETWEEN 10% AND 20%. AFTER THE APPLICATION OF THE DECONVOLUTION ALGORITHM, THE	
EUCLIDEAN DISTANCE BETWEEN THE IDEAL AND NON-IDEAL IMAGERY DECREASED BY AN AVERAGE OF 1.91%	. 136
FIGURE 4.11. HYPERSPECTRAL IMAGING DATA OVER THE MER BLEUE PEATLAND BEFORE AND AFTER THE APPLICATION OF THE MER BLEUE PEATLAND BEFORE AND AFTER THE APPLICATION OF THE MER BLEUE PEATLAND BEFORE AND AFTER THE APPLICATION OF THE MER BLEUE PEATLAND BEFORE AND AFTER THE APPLICATION OF THE MER BLEUE PEATLAND BEFORE AND AFTER THE APPLICATION OF THE MER BLEUE PEATLAND BEFORE AND AFTER THE APPLICATION OF THE MER BLEUE PEATLAND BEFORE AND AFTER THE APPLICATION OF THE MER BLEUE PEATLAND BEFORE AND AFTER THE APPLICATION OF THE MER BLEUE PEATLAND BEFORE AND AFTER THE APPLICATION OF THE MER BLEUE PEATLAND BEFORE AND AFTER THE APPLICATION OF THE MER BLEUE PEATLAND BEFORE AND AFTER THE APPLICATION OF THE MER BLEUE PEATLAND BEFORE AND AFTER THE APPLICATION OF THE MER BLEUE PEATLAND BEFORE AND AFTER THE APPLICATION OF THE MER BLEUE PEATLAND BEFORE AND AFTER THE APPLICATION OF THE MER BLEUE PEATLAND BEFORE AND AFTER THE APPLICATION OF THE MER BLEUE PEATLAND BEFORE AND AFTER THE APPLICATION OF THE MER BLEUE PEATLAND BEFORE AND AFTER THE APPLICATION OF THE APPLIC	ON
OF THE DECONVOLUTION ALGORITHM. THE IMAGES ARE DISPLAYED IN TRUE COLOUR (RED = 639.5 NM \pm 1.2 GR	EEN
= 551.0 NM \pm 1.2, BLUE = 460.1 NM \pm 1.2). IN THE DISPLAY, ALL THREE BANDS ARE LINEARLY STRETCHED BETWEEN STREET CHECK BANDS ARE LINEARLY BANDS	ΞN
0% AND 12%. PANELS (A) AND (C) DISPLAY THE ORIGINAL IMAGERY. PANELS (B) AND (D) REPRESENT THE SAME	
TWO SCENES AFTER THE DECONVOLUTION ALGORITHM WAS APPLIED. BOTH IMAGES WERE QUALITATIVELY	
SHARPENED BY THE DECONVOLUTION ALGORITHM.	. 137
FIGURE 4.12. HYPERSPECTRAL IMAGING DATA OVER THE MACDONALD–CARTIER INTERNATIONAL AIRPORT (OTTAWA	A ,
ONTARIO, CANADA) BEFORE AND AFTER THE APPLICATION OF THE DEVELOPED DECONVOLUTION ALGORITHM	
THE IMAGES ARE DISPLAYED IN TRUE COLOUR (RED = 639.5 NM \pm 1.2, GREEN = 551.0 NM \pm 1.196, BLUE = 460.1 NM	±
1.2). IN THE DISPLAY, ALL THREE BANDS ARE LINEARLY STRETCHED BETWEEN 0% AND 40%. PANELS (A) AND (C)
DISPLAY THE ORIGINAL IMAGERY. PANELS (B) AND (D) REPRESENT THE SAME TWO SCENES AFTER THE	
DECONVOLUTION ALGORITHM WAS APPLIED. BOTH IMAGES WERE QUALITATIVELY SHARPENED BY THE	
DECONVOLUTION ALGORITHM.	. 138
FIGURE 4.13. A,B) THE 7 ADJACENT ACROSS TRACK PIXELS TO THE EDGE OF THE CALIBRATION TARP IN THE MER BLE	UE
IMAGERY BEFORE (PLOT A) AND AFTER (PLOT B) THE DECONVOLUTION ALGORITHM WAS APPLIED. PIXEL 4 WA	S
THE CLOSEST TO THE STUDIED EDGE. THE PIXEL NUMBER REPRESENTS THE ORDER OF EACH ADJACENT PIXEL	ίN
THE ACROSS TRACK DIRECTION. PIXELS 1–3 REPRESENTED SPECTRA FROM THE CALIBRATION TARP WHILE PIX	ELS
5–7 REPRESENTED SPECTRA FROM VEGETATION. C,D) THE 7 ADJACENT ACROSS TRACK PIXELS TO THE EDGE OF	
THE CONCRETE-ASPHALT TRANSITION AT THE CALIBRATION SITE WITHIN THE AIRPORT IMAGERY BEFORE (PLOSE)	TC
C) AND AFTER (PLOT \mathbf{D}) THE DECONVOLUTION ALGORITHM WAS APPLIED. PIXEL 4 WAS THE CLOSEST TO THE	
STUDIED EDGE. PIXELS 1–3 REPRESENTED SPECTRA FROM THE CONCRETE WHILE PIXELS 5–7 REPRESENTED	
SPECTRA FROM ASPHALT. IN BOTH THE MER BLEUE AND AIRPORT IMAGERY, THE SPECTRA FROM PIXELS 3 AND) 5
WERE CLOSER TO THE SPECTRA OF THEIR RESPECTIVE MATERIALS AFTER THE APPLICATION OF THE	
DECONVOLUTION ALGORITHM. IN PARTICULAR, SPECTRA FROM PIXEL 5 DROPPED IN MAGNITUDE, ALIGNING W	'ITH
THAT OF PIXELS 6 AND 7 IN BOTH SETS OF IMAGERY. THIS SUGGESTS THAT THE ALGORITHM MITIGATED	
INFLUENCES FROM NEIGHBOURING PIXEL MATERIALS.	. 139
FIGURE 4.14. A) THE MAXIMUM CHANGE IN REFLECTANCE PER PIXEL ACROSS THE EDGE OF THE CALIBRATION TARP	ίΝ
THE MER BLEUE IMAGERY. B) THE MAXIMUM CHANGE IN REFLECTANCE PER PIXEL ACROSS THE EDGE ALONG $^{\circ}$	ГНЕ
BORDER OF THE CONCRETE-ASPHALT TRANSITION AT THE CALIBRATION SITE WITHIN THE AIRPORT IMAGERY.	
THE LARGER THE NUMBER, THE SHARPER THE CHANGE FROM THE TWO MATERIALS THAT DEFINED THE EDGE.	THE

REAL-WORLD COMPACT AIRBORNE SPECTROGRAPHIC IMAGER 1500 (CASI) DATA. THE	HE CORRECTED IMAGERY WAS
SHARPER THAN THE ORIGINAL IMAGERY. THE IMAGERY WAS SHARPENED BY THE D	DEVELOPED DECONVOLUTION
ALGORITHM	140
FIGURE 4.15. THE MEAN CORRELATION COEFFICIENT AS A FUNCTION OF PIXEL DISPLACEM	MENT IN THE ACROSS TRACK
(PLOT ${f A}$) AND ALONG TRACK (PLOT ${f B}$) DIRECTION OF THE VEGETATION REGION OF I	NTEREST FROM THE MER
BLEUE CASI IMAGERY. THE BARS AROUND EACH MEAN GIVE THE 1-SIGMA WINDOW	. THE MEAN AND STANDARD
DEVIATION QUANTIFIED THE STRENGTH AND VARIABILITY OF THE SPATIAL CORRE	LATIONS PRESENT WITHIN
EACH IMAGE. THE CORRECTED IMAGE WAS GENERATED BY APPLYING THE DEVELO	PED DECONVOLUTION
ALGORITHM TO THE REAL-WORLD MER BLEUE COMPACT AIRBORNE SPECTROGRAP	PHIC IMAGER 1500 (CASI) DATA.
IN GENERAL, THE DECONVOLUTION ALGORITHM DECREASED THE OBSERVED SPATI	AL CORRELATIONS WHILE
INCREASING SPATIAL VARIABILITY. AFTER APPLYING THE DEVELOPED DECONVOLU	UTION ALGORITHM, THE
MICRO-SPATIAL PATTERNS OF VEGETATION COULD BE OBSERVED MORE CLEARLY	IN THE ACROSS TRACK
DIRECTION. THE MICRO-SPATIAL PATTERNS OF VEGETATION COULD NOT BE OBSER	VED IN THE ALONG TRACK. 141
FIGURE 4.16. THE MEAN (PLOT A) AND STANDARD DEVIATION (PLOT B) OF THE VEGETATION	ON REGION OF INTEREST FROM
THE MER BLEUE IMAGERY. THE CORRECTED IMAGE WAS GENERATED BY APPLYING	THE DEVELOPED
DECONVOLUTION ALGORITHM TO THE REAL-WORLD MER BLEUE COMPACT AIRBOR	RNE SPECTROGRAPHIC IMAGER
1500 (CASI) DATA. THE STANDARD DEVIATION VALUED MEASURED THE VARIABILIT	Y IN EACH SPECTRAL BAND.
ALTHOUGH THERE WAS NO DIFFERENCE IN THE MEAN, THE STANDARD DEVIATION	INCREASED AFTER APPLYING
THE DECONVOLUTION ALGORITHM. THIS INCREASE LIKELY OCCURRED AS THE DEC	ONVOLUTION REINTRODUCED
SOME OF THE LOST NATURAL VARIATIONS IN EACH SPECTRAL BAND	142
FIGURE 5.1. PIXEL LOSS AND PIXEL DUPLICATION DURING NEAREST NEIGHBOR SPATIAL R	ESAMPLING. CONSIDER
SPATIALLY RESAMPLING A HYPERSPECTRAL IMAGING DATASET (GIVEN BY THE CO.	LORED CIRCLES) ACQUIRED
ALONG AN APPROXIMATE TRUE NORTH HEADING WHERE THE PIXEL SPACING IN TH	E CROSS TRACK IS HALF THAT
OF THE ALONG TRACK. TO GENERATE A RASTERIZED DATA PRODUCT (GIVEN BY TH	E GREY RASTER GRID AND THE
SMALL BLACK DOTS WHICH DESIGNATE THE CENTER OF EACH CELL), THE DATA MU	JST BE RESAMPLED ON A
NORTH-ORIENTED GRID. PANELS (A) AND (B) SHOW TWO RESAMPLING GRIDS THAT (
NEAREST NEIGHBOR RESAMPLING	
FIGURE 5.2. FLOW CHART OF THE HYPERSPECTRAL IMAGING (HSI) PROCESSING WORKFIOW	V FOR BOTH CONVENTIONAL
RASTERIZED HYPERSPECTRAL IMAGING END PRODUCTS AND THE DIRECTLY-GEORE	EFERENCED HYPERSPECTRAL
POINT CLOUD (DHPC)	166
FIGURE 5.3. HYPERSPECTRAL IMAGING DATA (R = 639.6 NM, G = 550.3 NM, B = 459.0 NM) FRO	DM THE μCASI-1920 OVER THE
MER BLEUE PEATLAND. PANELS (A, B) ARE RASTERIZED HYPERSPECTRAL IMAGING	DATASETS RESAMPLED TO 1.5
imes 1.5 CM (A) AND 3 $ imes$ 3 CM (B). PANEL (C) REPRESENTS THE DIRECTLY-GEOREFERENCE	ED HYPERSPECTRAL POINT
CLOUD (DHPC) VIEWED FROM ABOVE. PANEL (D) DISPLAYS A VIDEO STILL OF THE D	HPC IN A 12 × 12 M REGION
AROUND THE IMAGE ZOOM CENTER. IN ALL PANELS, EACH DISPLAYED BAND IS LIN	EARLY STRETCHED BETWEEN 0
AND 12%. THE FULL VIDEO CAN BE SEEN IN SUPPLEMENTARY VIDEO S1. THE WHITE	STRIPES IN THE DHPC
[CLEARLY VISIBLE IN THE IMAGE ZOOM OF PANEL (C)] REPRESENT AREAS ON THE G	ROUND THAT WERE NOT
SAMPLED BY THE HYPERSPECTRAL IMAGER DURING DATA ACQUISITION. THESE GA	PS ARE NOT PRESENT IN THE
RASTER IMAGES (A, B) AS THEY ARE INTERPOLATED OVER WITH DUPLICATED PIXEL	S FROM THE EDGES OF THE
STRIPES DURING THE NEAREST NEIGHBOR RESAMPLING	
FIGURE 5.4. HYPERSPECTRAL IMAGING DATA (R = 640.8 NM, G = 549.9 NM, B = 459.0 NM) FOR	R THE CASI-1500 OVER THE MER
BLEUE PEATLAND. PANELS (A, B) ARE RASTERIZED HYPERSPECTRAL IMAGING DATA	

CORRECTED IMAGE WAS GENERATED BY APPLYING THE DEVELOPED DECONVOLUTION ALGORITHM TO THE

- FIGURE 5.6. HYPERSPECTRAL IMAGING DATA (R = 640.8 NM, G = 549.9 NM, B = 459.0 NM) FOR THE CASI-1500 OVER THE PARC NATIONAL DU MONT- MÉGANTIC. PANELS (A, B) ARE RASTERIZED HYPERSPECTRAL IMAGING DATASETS RESAMPLED TO 110 × 110 CM (A) AND 260 × 260 CM (B) GRIDS. PANEL (C) REPRESENTS THE DIRECTLY-GEOREFERENCED HYPERSPECTRAL POINT CLOUD (DHPC) VIEWED FROM ABOVE. PANEL (D) DISPLAYS A VIDEO STILL OF THE DHPC. THE FULL VIDEO CAN BE SEEN IN SUPPLEMENTARY VIDEO S4. IN ALL PANELS, EACH DISPLAYED BAND IS LINEARLY STRETCHED BETWEEN 0 AND 12%. THE WHITE STRIPES IN THE DHPC REPRESENT AREAS ON THE GROUND THAT WERE NOT SAMPLED BY THE HYPERSPECTRAL IMAGER DURING DATA ACQUISITION. THE WHITE STRIPES IN THE DHPC [CLEARLY VISIBLE IN THE IMAGE ZOOM OF PANEL (C)] REPRESENT AREAS ON THE GROUND THAT WERE NOT SAMPLED BY THE HYPERSPECTRAL IMAGER DURING DATA ACQUISITION. THESE GAPS ARE NOT PRESENT IN THE RASTER IMAGES (A, B) AS THEY ARE INTERPOLATED OVER WITH DUPLICATED PIXELS FROM THE EDGES OF THE STRIPES DURING THE NEAREST NEIGHBOR RESAMPLING..... 180
- FIGURE 5.8. BIOMASS ESTIMATION ERRORS (DIFFERENCE BETWEEN MEAN OF PREDICTED AND ACTUAL BIOMASS) FOR
 THE DEVELOPED HUMMOCK HOLLOW CLASSIFICATION MODELS FOR THE μCASI-1920 HYPERSPECTRAL IMAGING
 DATA FROM THE MER BLEUE PEATLAND. THIS DATA INCLUDED THE DIRECTLY-GEOREFERENCED HYPERSPECTRAL
 POINT CLOUD (DHPC) IN ADDITION TO THE TWO RESAMPLED HYPERSPECTRAL IMAGES. EACH OF THE MODELS
 WERE DIFFERENTIATED BY THE TRAINING DATASET (GIVEN BY BAR COLOURS) AND TRAINING VARIABLES. THE

BARS ABOVE () CORRESPOND TO HOLLOW BIOMASS ESTIMATION ERRORS WHILE THE BARS BELOW CORRESPONT TO HUMMOCKS.	
FIGURE 5.9. THE MEAN AND SD OF THE NUMBER OF SPECTRA, NUMBER OF UNIQUE SPECTRA AND NUMBER OF UNIQUE SPECTRA PROPERLY LOCATED PER EACH 3 × 3 M VIRTUAL VEGETATION PLOT (N = 100) FROM THE MER BLEUE PEATLAND CASI-1500 DATA. THE CASI-1500 DATA INCLUDED THE DIRECTLY-GEOREFERENCED HYPERSPECTRAL POINT CLOUD (DHPC) IN ADDITION TO THE TWO RESAMPLED HYPERSPECTRAL IMAGES. THE ERROR BARS GIVE 1 1-SIGMA WINDOW AROUND EACH MEAN VALUE. PROPERLY LOCATED SPECTRA REFER TO THOSE WHICH WERE CONTAINED WITHIN EACH PLOT BEFORE AND AFTER RASTERIZATION (IN THE CASE OF THE RESAMPLED DATA PRODUCTS)	ГНЕ
FIGURE 5.10. TARGET DETECTION RESULTS FROM THE CASI-1500 HYPERSPECTRAL IMAGING DATA OVER THE MER BLE PEATLAND. ARTIficial targets (N = 1,000) Were randomly placed within the scene. The Casi-1500 data INCLUDED THE DIRECTLY-GEOREFERENCED HYPERSPECTRAL POINT CLOUD (DHPC) IN ADDITION TO THE TWO RESAMPLED HYPERSPECTRAL IMAGES. PANEL (A) DISPLAYS THE NUMBER OF TARGETS (OUT OF A MAXIMUM 1,0 IDENTIFIED IN THE TARGET DETECTION. PANEL (B) AND (C) GIVE THE FALSE DISCOVERY AND FALSE NEGATIVE RATES, RESPECTIVELY	000)
FIGURE 5.11. FALSE DISCOVERIES AND FALSE NEGATIVES CAUSED BY PIXEL LOSS AND PIXEL DUPLICATION IN A TARC DETECTION EXERCISE. CONSIDER SPATIALLY RESAMPLING A HYPERSPECTRAL IMAGING DATASET (GIVEN BY TO COLORED CIRCLES) ACQUIRED ALONG AN APPROXIMATE TRUE NORTH HEADING WHERE THE PIXEL SPACING IN THE CROSS TRACK IS HALF THAT OF THE ALONG TRACK. TO GENERATE A RASTERIZED DATA PRODUCT (GIVEN IN THE RASTER GRID AND THE SMALL BLACK DOTS WHICH DESIGNATE THE CENTER OF EACH CELL), THE DATA MUST BE RESAMPLED ON A NORTH-ORIENTED GRID. IN THIS SCENE THERE IS ONE TARGET OF INTEREST (PURPLE STARTHAT CAN BE DETECTED BY THE HYPERSPECTRAL DATA POINT REPRESENTED BY THE PURPLE CIRCLE. PANEL (ASHOWS THAT PIXEL DUPLICATION CAN CAUSE FALSE DISCOVERIES WHILE PANEL (B) SHOWS THAT PIXEL LOSS CAN CAUSE FALSE NEGATIVES	HE BY JST () A)
FIGURE 7.1. FLOWCHART OF THE SPATIAL RESPONSE RESAMPLING (SR ²) WORKFLOW. THE WORKFLOW DEGRADES FIN SPATIAL RESOLUTION HYPERSPECTRAL IMAGING (HSI) DATA TO THE SPATIAL CHARACTERISTICS OF A COARSEL RESOLUTION SENSOR.	R
FIGURE 7.2. THE HYPERSPECTRAL IMAGING DATA USED TO SHOW THE UTILITY OF THE DEVELOPED SPATIAL RESPONSI RESAMPLING (SR²) WORKFLOW. CASI-1500 AND μCASI-1920 DATA WERE COLLECTED OVER THE MER BLEUE PEATLAND (MBP), WHILE CASI-1500 AND SASI-640 DATA WERE COLLECTED OVER THE PUERTO JIMÉNEZ AIRPORT (PJA). A) HYPERSPECTRAL IMAGING DATA COLLECTED OVER THE MBP WITH THE CASI-1500 (R=640.8 NM, G=549.9 NM, B=459.0 NM, LINEARLY SCALED FROM 0 TO 12 %). THE RED BOX SHOWS THE LOCATION WHERE THE μCASI-150 (R=639.6 NM, G=550.3 NM, B=459.0 NM, LINEARLY SCALED FROM 0 TO 12 %). C) HYPERSPECTRAL IMAGING DATA COLLECTED OVER THE PJA WITH THE CASI-1500 (R=641.2 NM, G=550.3 NM, B=458.3 NM, LINEARLY SCALED FROM 0 TO 20 %). D) HYPERSPECTRAL IMAGING DATA COLLECTED OVER THE PJA WITH THE SASI-640 (R=1240.1 NM AND LINEARLY SCALED FROM 0 TO 50 %, G=1540.7 NM AND LINEARLY SCALED FROM 0 TO 50 %, B=1846.0 NM AND LINEARLY SCALED FROM 0 TO 30 %).	920
FIGURE 7.3. THE POINT SPREAD FUNCTION (PSF) FOR THE CASI-1500 DATA COLLECTED OVER THE MER BLEUE PEATLAN A) THE OPTICAL PSF (PSF _{OPT}), DETECTOR PSF (PSF _{DET}) AND NET PSF (PSF _{NET}) IN THE CROSS TRACK DIRECTION (UNSUMMED AND SUMMED PSFS ARE DESIGNATED BY THE S=1 AND S=2 TAGS, RESPECTIVELY). B) THE PSF _{OPT} , PSF _{DET} , MOTION PSF (PSF _{MOT}) AND PSF _{NET} IN THE ALONG TRACK DIRECTION. C) THE PSF _{NET} AS A FUNCTION OF	√D.

DISPLACEMENT FROM THE CENTER OF THE PIXEL IN THE EASTING AND NORTHING DIRECTIONS. THE GRID IN THE

FIGURE 7.4. EXAMPLE DATA CROSS-VALIDATION APPLICATION OF THE SPATIAL RESPONSE RESAMPLING (SR2) WORKFLOW. A) SPATIAL SUBSET OF THE MER BLEUE PEATLAND (MBP) CASI-1500 HYPERSPECTRAL IMAGING DATA (R=640.8 NM, G=549.9 NM, B=459.0 NM, LINEARLY SCALED FROM 0 TO 12 %). B) ORIGINAL μCASI-1920 HYPERSPECTRAL IMAGING DATA COLLECTED OVER THE MBP (R=639.6 NM, G=550.3 NM, B=459.0 NM, LINEARLY SCALED FROM 0 TO 12 %). C) SPATIALLY DEGRADED μCASI-1920 HYPERSPECTRAL IMAGING DATA (R=639.6 NM, G=550.3 NM, B=459.0 NM, LINEARLY SCALED FROM 0 TO 12 %) GENERATED USING CONVENTIONAL RESAMPLING METHODOLOGIES (PIXEL AGGREGATE METHOD). D) SPATIALLY DEGRADED μCASI-1920 HYPERSPECTRAL IMAGING DATA (R=639.6 NM, G=550.3 NM, B=459.0 NM, LINEARLY SCALED FROM 0 TO 12 %) GENERATED USING THE SR² WORKFLOW. E) THE MEAN OF EACH SPECTRAL BAND FROM THE TWO SPATIALLY DEGRADED µCASI-1920 IMAGES AND THE ORIGINAL CASI-1500 IMAGERY, SPATIALLY SUBSET TO COVER THE SAME EXTENT. F) THE STANDARD DEVIATION IN EACH SPECTRAL BAND FROM THE TWO SPATIALLY DEGRADED μCASI-1920 IMAGES AND THE CASI-1500 IMAGERY, SPATIALLY SUBSET TO COVER THE SAME EXTENT. G) RELATIVE DIFFERENCE IN THE CALCULATED MEAN REFLECTANCE SPECTRUM BETWEEN THE ORIGINAL CASI-1500 IMAGERY AND THE TWO SPATIALLY DEGRADED μCASI-1920 IMAGES. H) RELATIVE DIFFERENCE BETWEEN THE CALCULATED STANDARD DEVIATION IN REFLECTANCE OF THE ORIGINAL CASI-1500 IMAGERY AND THE TWO SPATIALLY DEGRADED μCASI-1920 IMAGES. THE SIMULATED DATA PRODUCT GENERATED USING THE SR2 WORKFLOW WAS THE MOST SPATIALLY CONSISTENT WITH THE CASI-1500 IMAGERY. THE MEAN IN THE REFLECTANCE WAS CONSISTENT BETWEEN THE TWO SIMULATED DATA PRODUCTS AND THE CASI-1500 DATA. THE STANDARD DEVIATION CALCULATED FOR THE SIMULATED IMAGERY DERIVED FROM THE SR2 WORKFLOW WAS THE CLOSEST TO THAT OF THE CASI-1500 IMAGERY, INDICATING THAT THE DATASETS ARE CHARACTERIZED BY SIMILAR LEVELS OF SENSOR BLURRING.. 239

FIGURE 7.6. HUMMOCK AND HOLLOW SPECTRA EXTRACTED FROM THE SPATIALLY DEGRADED μCASI-1920
HYPERSPECTRAL IMAGING DATA GENERATED USING THE SR² WORKFLOW WITH THE DATA ACQUISITION
PARAMETERS IN TABLE 7.2. A) ORIGINAL μCASI-1920 HYPERSPECTRAL IMAGING DATA (R=639.6 NM, G=550.3 NM,
B=459.0 NM, LINEARLY SCALED FROM 0 TO 12 %). THE ANALYZED EXAMPLE HUMMOCK AND HOLLOW WERE
IDENTIFIED IN THE IMAGE. IN GENERAL, THE HUMMOCKS APPEAR GREEN IN COLOR WHILE HOLLOWS APPEAR RED.
PANELS B AND C SHOW THE EXAMPLE HOLLOW AND HUMMOCK SPECTRA, RESPECTIVELY. PANEL D SHOWS THE
DIFFERENCE BETWEEN THE HOLLOW AND HUMMOCK SPECTRA AT DIFFERENT SPATIAL SCALES. PANEL E SHOWS
THE NORMALIZED DIFFERENCE BETWEEN THE HOLLOW AND HUMMOCK SPECTRA AT DIFFERENT SPATIAL SCALES
IN UNITS OF STANDARD DEVIATION (STD). THESE VALUES WERE OBTAINED BY DIVIDING THE DIFFERENCE
SPECTRUM IN PANEL D BY THE STANDARD DEVIATION IN EACH SPECTRAL BAND OF THE IMAGE FROM WHICH THE
SPECTRA WERE OBTAINED. THE ABSOLUTE VALUE OF THE NORMALIZED DIFFERENCE IS REPRESENTATIVE OF
SEPARABILITY BETWEEN THE EXAMPLE HUMMOCK AND HOLLOW AS A FUNCTION OF WAVELENGTH. AS THE
SPATIAL SCALE BECOMES COARSER, HUMMOCK AND HOLLOW REFLECTANCE SPECTRA BECOME MORE SIMILAR

DUE TO MIXING WITH NEIGHBOURING ENDMEMBERS. FOR INSTANCE, AT FINE SPATIAL RESOLUTIONS, TH	E
SPHAGNUM FROM THE HOLLOW SPECTRA CAN BE OBSERVED BY THE SHIFTED GREEN PEAK AND THE HIG	H NIR
REFLECTANCE. AT SCALE 3-6, THESE CHARACTERISTICS WERE LOST, AND THE SPECTRA WERE MORE CON	SISTENT
WITH THE EXAMPLE HUMMOCK	246

FIGURE 7.7. EXAMPLE DATA FUSION APPLICATION OF THE SPATIAL RESPONSE RESAMPLING (SR2) WORKFLOW FOR GENERATING A FULL-RANGE IMAGE FROM SEPARATE VNIR AND SWIR HYPERSPECTRAL IMAGERY. THE TWO TESTED FULL-RANGE DATA PRODUCTS WERE THE SAME IN THE SHORTWAVE INFRARED (SWIR) AND ONLY DISTINGUISHABLE IN THE VISIBLE NEAR INFRARED (VNIR). THE CONVENTIONAL FULL-RANGE DATA PRODUCT WAS GENERATED USING A NEAREST NEIGHBOUR RESAMPLING TECHNIQUE, WHILE THE NOVEL DATA FUSION APPROACH USED THE SR2 TECHNIQUE DESCRIBED IN THIS STUDY. A-C) THE FOREST REGION OF INTEREST IN THE VNIR (R=641.2 NM, G=550.3 NM, B=458.3 NM, LINEARLY SCALED FROM 0 TO 20 %) AND THE SWIR (R=1240.1 NM AND LINEARLY SCALED FROM 0 TO 60 %, G=1540.7 NM AND LINEARLY SCALED FROM 0 TO 50 %, B=1846.0 NM AND LINEARLY SCALED FROM 0 TO 30 %) FOR BOTH FULL-RANGE DATA PRODUCTS. D-F) THE URBAN REGION OF INTEREST IN THE VNIR AND SWIR (RGB DISPLAY IDENTICAL TO THE FOREST REGION OF INTEREST) FOR BOTH FULL-RANGE PRODUCTS. G) THE MEAN REFLECTANCE SPECTRUM FROM THE CONVENTIONAL AND SR2 FULL-RANGE END PRODUCTS OVER THE FOREST REGION OF INTEREST. H) THE MEAN REFLECTANCE SPECTRUM FROM THE CONVENTIONAL AND SR2 FULL-RANGE END PRODUCTS OVER THE URBAN REGION OF INTEREST. SUBPLOTS I AND J DISPLAY THE STANDARD DEVIATION IN THE REFLECTANCE SPECTRUM SHOWN IN SUBPLOTS G AND H, RESPECTIVELY. THE OFFSET BETWEEN THE VNIR AND SWIR IN SUBPLOTS I AND J SHOWS THAT THE SR² WORKFLOW IS CRITICAL IN ENSURING THAT THE MERGED SASI-640 IMAGERY AND CASI-1500 IMAGERY ARE

FIGURE 7.8. EXAMPLE DATA FUSION APPLICATION OF THE SPATIAL RESPONSE RESAMPLING (SR2) WORKFLOW FOR GENERATING A FULL-RANGE IMAGE FROM SEPARATE VNIR AND SWIR HYPERSPECTRAL IMAGERY. THE TWO TESTED FULL-RANGE DATA PRODUCTS WERE THE SAME IN THE SHORTWAVE INFRARED (SWIR) AND ONLY DISTINGUISHABLE IN THE VISIBLE NEAR INFRARED (VNIR). THE CONVENTIONAL FULL-RANGE DATA PRODUCT WAS GENERATED USING A NEAREST NEIGHBOUR RESAMPLING TECHNIQUE, WHILE THE NOVEL DATA FUSION APPROACH USED THE SR2 TECHNIQUE DESCRIBED IN THIS STUDY. A) THE FOREST REGION OF INTEREST (ROI) IN THE SWIR (R=1240.1 NM AND LINEARLY SCALED FROM 0 TO 60 %, G=1540.7 NM AND LINEARLY SCALED FROM 0 TO 50 %, B=1846.0 NM AND LINEARLY SCALED FROM 0 TO 30 %). PANELS B AND C SHOW THE ABSOLUTE DIFFERENCE IN REFLECTANCE ACROSS THE TRANSITION BETWEEN THE VNIR AND SWIR FOR THE TWO STUDIED FULL-RANGE DATA PRODUCTS IN THE FOREST ROI. D) THE URBAN ROI IN THE SWIR (DISPLAYED IDENTICALLY TO PANEL A). PANELS E AND F SHOW THE ABSOLUTE DIFFERENCE IN REFLECTANCE ACROSS THE TRANSITION BETWEEN THE VNIR AND SWIR FOR THE TWO STUDIED FULL-RANGE DATA PRODUCTS IN THE URBAN ROI. G) VIOLIN PLOT (INCLUDES MEAN AND QUARTILES) OF THE ABSOLUTE DIFFERENCE IN REFLECTANCE ACROSS THE TRANSITION BETWEEN THE VNIR AND SWIR FOR THE TWO STUDIED FULL-RANGE DATA PRODUCTS IN THE FOREST ROI. H) VIOLIN PLOT (INCLUDES MEAN AND QUARTILES) OF THE ABSOLUTE DIFFERENCE IN REFLECTANCE ACROSS THE TRANSITION BETWEEN THE VNIR AND SWIR FOR THE TWO STUDIED FULL-RANGE DATA PRODUCTS IN THE URBAN ROI. I) SPECTRA FROM VARIOUS MATERIALS EXTRACTED FROM THE CONVENTIONAL DATA FUSION END PRODUCT WITHIN THE STUDIED ROIS. J) SPECTRA FROM VARIOUS MATERIALS EXTRACTED FROM THE SR² DATA FUSION END PRODUCT WITHIN THE STUDIED ROIS. THE OFFSET BETWEEN THE VNIR AND SWIR IN THE CONVENTIONAL FULL-RANGE DATA PRODUCT WOULD LEAVE THE SPECTRA UNUSABLE IN SPECTROSCOPY ANALYSES SUCH AS MATERIAL IDENTIFICATION AND CHARACTERIZATION. 252

FIGURE 7.10. SCHEMATIC OF THE GEOMETRIC CORRECTION. WITH A KNOWN SENSOR POSITION (P) AND LOOK DIRECTION
(ΘL) THE POSITION OF EACH PIXEL IN THE IMAGE SPACE CAN BE LOCATED IN A REAL-WORLD COORDINATE SPACE.
THE PIXEL IS LOCATED AT THE INTERSECTION (A) OF THE INPUT DIGITAL SURFACE MODEL (SHOWN IN GREEN)
AND A STRAIGHT LINE THAT IS PROJECTED AT THE PIXEL DEPENDENT LOOK DIRECTION FROM THE SENSOR
POSITION. THE LOOK DIRECTION IS THE ANGLE AT WHICH INCOMING ELECTROMAGNETIC RADIATION IS
OBSERVED BY ANY GIVEN PIXEL OF THE HYPERSPECTRAL IMAGER (MÜLLER ET AL., 2002). THE LOOK DIRECTION IS
CALCULATED FROM THE ATTITUDE, FOCAL GEOMETRY AND BORESIGHT MISALIGNMENT OF THE SENSOR DURING
DATA ACQUISITION (MÜLLER ET AL., 2002; WARREN ET AL., 2014)
FIGURE 7.11. THE DATA PRODUCTS USED TO GENERATE THE DHPC OVER THE MER BLEUE PEATLAND. A)
RADIOMETRICALLY AND ATMOSPHERICALLY CORRECTED HYPERSPECTRAL IMAGING DATA IN RAW SENSOR
GEOMETRY FROM THE μ CASI-1920 (R=639.6 NM, G=550.3 NM, B=459.0 NM, LINEARLY STRETCHED FROM A
REFLECTANCE VALUE OF 0% TO $12~\%$ FOR DISPLAY PURPOSES). B) ORIGINAL DIGITAL SURFACE ELEVATION MODEL.
C) BLURRED DIGITAL SURFACE MODEL (LINEARLY STRETCHED FROM A ELEVATION VALUE OF 68 M TO 69 M). D)
THE DIRECTLY-GEOREFERENCED HYPERSPECTRAL POINT CLOUD (DHPC) VIEWED FROM ABOVE (R=639.6 NM,
G=550.3 NM, B=459.0 NM, LINEARLY STRETCHED FROM A REFLECTANCE VALUE OF 0% TO 12 % FOR DISPLAY
PURPOSES). E) A VIDEO OF THE DHPC IN A 12 X 12 M REGION (R=639.6 NM, G=550.3 NM, B=459.0 NM, LINEARLY
STRETCHED FROM A REFLECTANCE VALUE OF 0% TO 12 % FOR DISPLAY PURPOSES). THE VIDEO
$(SUPPLEMENTARY_VIDEO_1.MP4)\ CAN\ BE\ FOUND\ IN\ THE\ SUPPLEMENTAL\ MATERIAL.\ THE\ FULL\ DHPC$
(HPC_288BAND_XYZ_FINAL.TXT) IS ALSO IN THE SUPPLEMENTARY MATERIAL
FIGURE 7.12. THE POINT SPREAD FUNCTION (PSF) FOR THE μCASI-1920. PANEL A DISPLAYS THE OPTICAL PSF (PSF _{OPT}),
DETECTOR PSF (PSF_{DET}) AND NET PSF (PSF_{NET}) IN THE CROSS TRACK DIRECTION. THE PSF_{NET} IS THE CONVOLUTION OF
THE PSF_{OPT} AND THE PSF_{DET} IN THE CROSS TRACK DIRECTION. PANEL B DISPLAYS THE PSF_{OPT} , PSF_{DET} , MOTION PSF_{DET}
$(PSF_{MOT}) \ AND \ PSF_{NET} \ IN \ THE \ ALONG \ TRACK \ DIRECTION. \ THE \ PSF_{NET} \ IS \ THE \ CONVOLUTION \ OF \ THE \ PSF_{MOT}, \ PSF_{OPT} \ AND$
THE PSF $_{\!\!\text{DET}}$ IN THE ALONG TRACK DIRECTION. PANEL C DISPLAYS THE NET PSF IN BOTH DIMENSIONS
SIMULTANEOUSLY

List of Tables

TABLE 2.1. KEY WORDS USED IN THIS LITERATURE REVIEW IN ADDITION TO ("REMOTE* SENS*" OR "HYPERSPECTRAL" OI "MULTISPECTRAL")
TABLE 3.1. THE FIVE MODIFICATIONS APPLIED TO $R\lambda$ TO GENERATE THE TRANSFORMED SIGNAL, $Rt(\lambda)$ 7
TABLE 3.2. THE APPROXIMATE SPECTRAL LOCATION OF KNOWN ATMOSPHERIC ABSORPTION FEATURES (PALLÉ ET AL., 2009). IT IS IMPORTANT TO NOTE THAT THE WAVELENGTH RANGES FOR SOME ATMOSPHERIC ABSORPTION FEATURES MAY VARY IN RESPONSE TO EXTERNAL FACTORS. FOR INSTANCE, THE RANGE OF THE WATER ABSORPTION FEATURES IS HIGHLY DEPENDENT ON WATER VAPOR AND AEROSOL OPTICAL THICKNESS (KING ET AL., 1992).
TABLE 3.3. SPATIAL AND SPECTRAL LOCALIZATION OF LARGE IMAGING ERRORS. SPATIAL ERRORS WERE DETECTED FROM THE DATA IN FIGURE 3.13 USING THE DEFINED THRESHOLD. POTENTIAL ERRORS WERE SPECTRALLY LOCATED THROUGH THE WINDOW-BASED METHODOLOGY DESCRIBED IN SECTION 3.2.4. ERRORS WERE DETECTED ALONG THE EDGES OF THE CASI IMAGERY IN THE BLUE END OF THE SPECTRA. A SINGLE BAND ERROR WAS DETECTED IN THE SASI IMAGERY FROM 993–1008 ACROSS PIXELS 548–564
TABLE 3.4. IDENTIFIED ATMOSPHERIC ABSORPTION FEATURES IN THE SPECTRAL RANGE COVERED BY THE CASI
TABLE 4.1. FLIGHT PARAMETERS FOR THE HYPERSPECTRAL DATA ACQUIRED OVER THE MER BLEUE PEATLAND AND THI MACDONALD-CARTIER INTERNATIONAL AIRPORT. 12
TABLE 5.1. PARAMETERS FOR THE HYPERSPECTRAL IMAGING DATA ACQUIRED OVER THE MER BLEUE PEATLAND (MBP), THE COWICHAN GARRY OAK PRESERVE (CGOP) AND THE PARC NATIONAL DU MONT- MÉGANTIC (MMG) WITH THE μCASI-1920 AND THE CASI-1500. NOMINAL ALTITUDES ARE REPORTED AS HEIGHT ABOVE GROUND LEVEL 16
TABLE 5.2. THE fiLE SIZE, PIXEL LOSS (PL), PIXEL DUPLICATION (PD), THEORETICAL PIXEL LOSS (PL _H), THEORETICAL PIXEL DUPLICATION (PD _H) AND HORIZONTAL ROOT MEAN SQUARE ERROR (RMSE _R) IN THE RADIAL DIRECTION FOR THE μCASI-1920 AND CASI-1500 DATA OVER THE MER BLEUE PEATLAND. THESE DATA INCLUDE THE RESAMPLED HYPERSPECTRAL IMAGING DATASETS AND THE DIRECTLY-GEOREFERENCED HYPERSPECTRAL POINT CLOUDS (DHPC)
TABLE 5.3. THE fiLE SIZE, PIXEL LOSS (PL), PIXEL DUPLICATION (PD), THEORETICAL PIXEL LOSS (PL _H), THEORETICAL PIXEL DUPLICATION (PD _H) AND HORIZONTAL ROOT MEAN SQUARE ERROR (RMSE _R) IN THE RADIAL DIRECTION FOR THE μCASI-1920 DATA FROM THE COWICHAN GARRY OAK PRESERVE AND THE CASI-1500 DATA FROM THE PARC NATIONAL DU MONT- MÉGANTIC. THESE DATA INCLUDE THE RESAMPLED HYPERSPECTRAL IMAGING DATASETS AND THE DIRECTLY-GEOREFERENCED HYPERSPECTRAL POINT CLOUDS (DHPC)
TABLE 5.4. ACCURACY RESULTS FOR THE HUMMOCK-HOLLOW CLASSIFICATION MODELS (μCASI-1920 HYPERSPECTRAL IMAGING (HSI) DATA FROM THE MER BLEUE PEATLAND). EACH OF THE MODELS WERE DIFFERENTIATED BY THE TRAINING DATASET AND TRAINING VARIABLES. THE TRAINING DATASETS INCLUDED THE DIRECTLY-GEOREFERENCED HYPERSPECTRAL POINT CLOUD (DHPC) IN ADDITION TO THE THREE RESAMPLED HYPERSPECTRAL IMAGES. THE SUPERSCRIPTS ^{S, E} CORRESPONDED TO THE INCLUSION OF THE SPECTRAL REFIECTANCE AND SURFACE ELEVATION, RESPECTIVELY
TABLE 7.1. PARAMETERS FOR THE HYPERSPECTRAL IMAGING DATA ACQUIRED OVER THE MER BLEUE PEATLAND (MBP) AND PHERTO HIMÉNEZ AIRPORT (PLA) WITH THE SASL-644 CASL-1500 AND HCASL-1920

TABLE 7.2. TESTED CASI-1500 DATA ACQUISITION PARAMETERS FOR DEGRADING THE μ CASI-1920 AT M	ULTIPLE SPATIAL
SCALES. THE DIFFERENT SPATIAL SCALES WERE ACQUIRED BY MODIFYING SENSOR ALTITUDE A	AND INTEGRATION
TIME. THE BOLDED ENTRIES INDICATE THE PARAMETERS THAT WERE VARIED BETWEEN SCALES	S. IT IS IMPORTANT
TO NOTE THAT IT IS NOT FEASIBLE TO MAINTAIN SUCH PRECISE ALTITUDES OVER LONG DURAT	IONS AT THE
AIRBORNE LEVEL WITH MANNED AIRCRAFTS.	243
TABLE 7.3. PARAMETERS FOR THE HYPERSPECTRAL IMAGING DATA ACQUIRED OVER THE MER BLEUE	DEATLAND (MRD)
`	,
WITH THE MCASI-1920	

List of Abbreviations

μCASI Micro Compact Airborne Spectrographic Imager

AWGN Additive White Gaussian Noise

AR Augmented Reality

AVIRIS Airborne Visible InfraRed Imaging Spectrometer

AVIRIS-NG Airborne Visible InfraRed Imaging Spectrometer - Next Generation

CASI Compact Airborne Spectrographic Imager

CC Correlation Coefficient

CGOP Cowichan Garry Oak Preserve

DHPC Directly-Georeferenced Hyperspectral Point Cloud

DN Digital Number

DSM Digital Surface Model

EO Earth Observation

FWHM Full Width at Half Maximum

FOV Field-of-View

GNSS Global Navigation Satellite System

GPS Global Positioning System

HSI Hyperspectral imaging

IMU Inertial Measurement UnitINS Inertial Navigation System

LiDAR Light Detection and Ranging

MBP Mer Bleue Peatland

MMG Mont- Mégantic

NTRIP Networked Transport of Radio Technical Commission for Maritime

Services via Internet Protocol

PD Pixel Duplication

PL Pixel Loss

PSF Point Spread Function

RTCM3-iMAX Radio Technical Commission for Maritime Individualized Master

Auxiliary

RTK Real-Time Kinematic

SASI Shortwave Airborne Spectrographic Imager

SfM-MVS Structure-from-Motion Multiview Stereo

SNR Signal-to-Noise Ratio

SWIR Shortwave Infrared

UAS Unmanned Aerial System

UAV Unmanned Aerial Vehicle

VNIR Visible and Near Infrared

VR Virtual Reality

WISE WaterSat Imaging Spectrometer Experiment

Acknowledgements

I believe that solitary achievements do not exist in science. I have been incredibly lucky to have so much support in my academic journey. Dr. Margaret Kalacska, thank you for always encouraging me to chase down my ideas, even if they were not conventional or even likely to work out. You have an amazing ability to bring out creativity in everyone around you and I will miss discussing fun and exciting new ideas. Dr. George Leblanc, thank you for taking the chance on me for my first research job and guiding me for almost 8 years now. I appreciated your support in both personal and academic matters. I really would not be where I am today if it were not for the opportunities and advice you have given me. Dr. Pablo Arroyo-Mora, thank you for always pushing me to dream big. You bring a great deal of passion into your work and life; I hope I can do the same moving forward. Ray Soffer, your patience and kindness in guidance is something that I hope to emulate someday. A lot of the ideas and work from this thesis were inspired by conversations we have had over the years. Dr. Nigel Roulet, thank you for all the advice and feedback you have given me not only as a graduate student, but as a teaching assistant. I enjoyed all of our discussions and always left with new ideas and perspectives. Dr. Ronald Resmini, thank you for the critical feedback on my thesis work. You always brought up thought provoking questions and suggestions that helped improve my work. Oliver Lucanus, thank you for always keeping field work fun (and for taking all those awesome pictures). Dr. Carolyn Eyles, I am grateful for all the doors you have opened for me. As an undergrade that was very uncertain about his future, you helped me find something to be passionate about.

I am extremely lucky to have support from my amazing family and friends. To my parents, Sandeep and Jilloo, thank you for everything you have done to get me to this point. I know you sacrificed a lot so that I would not have to struggle in life. Hailey, thank you for being my biggest supporter in life. To the many friends that I have made at McGill, I will cherish the moments we spent together. I hope to make more memories soon! To the friends I made at McMaster, you all got me through my undergrad, and I would not be here without your support. I would also like to thank my high school friends for keeping me laughing and giving me a little perspective when things were tough. Lindsey thanks for being the best in all things- you push me towards great things.

I would like to thank my various funding sources, without which this research would not be possible. Firstly, the Canadian Airborne Biodiversity Observatory funded by the Natural Sciences and Engineering Research Council Canada (NSERC) Discovery Frontiers program provided a unique environment to learn and conduct cutting-edge research. I must also thank NSERC for the Master and Doctoral level, Alexander Graham Bell Canada Graduate Scholarship and Alexander Graham Bell Canada Graduate Scholarships. I must also thank the Fonds de recherche du Québec for the Bourse de Doctorat en Recherche Scholarship. I would also like to thank Mr. Roger Warren for his support through the Rathlyn Fellowship. I would also like to convey my sincerest thanks to McGill GPS for granting me the Lorne Trottier Science Accelerator Fellowship and Dr. and Mrs. Milton Leong Fellowships.

I would also like to thank Dr. Crystal Schaaf, Dr. Viacheslav Adamchuk and Dr. Bernhard Lehner for the insightful feedback they provided during the thesis examination process.

Preface

This dissertation was part of the Canadian Airborne Biodiversity Observatory (CABO) project funded by the Natural Sciences and Engineering Research Council of Canada (NSERC) Discovery Grant. The overarching mission of CABO is to study and understand major drivers of changes in plant biodiversity across Canada using spectranomics. My Research developed novel tools for the acquisition, processing, analysis, quality assessment and application of hyperspectral imaging data that are actively being implemented across the CABO project.

Thesis Structure and Style

This thesis is written in the Manuscript-Based (Article-Based) style in accordance with the guidelines set out by McGill University. Formatting of the references follows the Author-Date formatting style used in the Journal *Remote Sensing of Environment*. The first chapter of the thesis gives a general introduction outlining overall goal and primary objectives of the project. The second chapter provides the background literature required to address the thesis objectives. The next three chapters present three published manuscripts that specifically address the project's three objectives. The sixth chapter provides a discussion of the presented manuscripts, highlighting their importance and identifying future research avenues. Two additional published

methods manuscripts are appended to the thesis in chapter 7. These papers give a detailed description of two versatile methods developed in this thesis, providing all the required information for implementation (e.g., code, high-level explanations, documentation). As per McGill Guidelines, chapter 8 contains list of all the references cited throughout the non-manuscript sections of the thesis.

Contribution of Authors

All 5 of the first-author manuscripts in this thesis (Chapters 3, 4, 5, 7.1, 7.2) have an appended Author Contributions section that clearly identifies the work done by each collaborator. All other content in this thesis was produced by Deep Inamdar and edited with feedback from Dr. Margaret Kalacska and Dr. George Leblanc.

1. Introduction

In hyperspectral remote sensing, contiguous narrow-band spectral information is collected for each spatial pixel of an image over an area of interest. In the visible to the shortwave infrared portion of the electromagnetic spectrum (~400- 3000 nm), this spectral information quantifies the reflectance of the materials within each spatial pixel and the interactions that have occurred with light as it passes through the atmosphere. The reflective properties of materials are representative of their chemical and physical properties (Eismann, 2012). After compensating for atmospheric effects (Berk et al., 1999), the reflectance of pixel materials derived from hyperspectral imaging (HSI) data can be used to characterize materials over large areas at fine spatial resolutions. HSI has been successfully applied in a variety of fields such as ecology (Arroyo-Mora et al., 2018a; Asner et al., 2017; Kalacska et al., 2018; Lassalle et al., 2021; Turner et al., 2003), forensics (Kalacska and Bell, 2006; Kalacska et al., 2009; Leblanc et al., 2014; Silván-Cárdenas et al., 2021), agriculture (Aneece and Thenkabail, 2018; Dale et al., 2013; Migdall et al., 2012; Wang et al., 2019; Yao et al., 2011; Zhong et al., 2020), defense (Khodor et al., 2021; Xu and Wang, 2007; Yuen and Richardson, 2010), forestry (Asner et al., 2017; Koch, 2010; Peng et al., 2003; Smith et al., 2003; Zhang et al., 2020) and geology (Booysen et al., 2022; Cloutis, 1996; Murphy et al., 2012; van der Meer et al., 2012), amongst others.

For example, HSI at the spaceborne level has been used to accurately predict the type and growth stage of the five leading world crops (corn, soybean, winter wheat, rice and cotton) using Google Earth Engine (Aneece and Thenkabail, 2018). HSI has been used at the airborne level to map forest functional diversity and canopy functional traits across the Peruvian Andes-to-Amazon biodiversity hotspot (Asner et al., 2017), in addition to leaf metal content over industrial brownfields (Lassalle et al., 2021). On a smaller scale, RPAS-HSI has been used in geological efforts for the detection of rare earth metals (Booysen et al., 2022). In controlled laboratory environments, HSI has been valuable in agricultural efforts for the early detection of tomato spotted wilt virus using novel deep learning analytical approaches (Wang et al., 2019). Given these brief examples, the widespread applicability of HSI provides valuable economic, environmental and social insight into some of the most challenging problems that the Earth and its inhabitants face (e.g., climate change, food security and national defense).

During data application, HSI end users are typically provided with raster products for analysis. Raster end products have been a standard for HSI data for over 40 years (Goetz, 2009; Vane et al. 1984,; Wilkinson, 1996), likely since virtually all spectral imaging systems view analyzed scenes as fields of informative continuous variables (e.g., spectral reflectance) that are discretized into pixel arrays (Couclelis, 1992). In georeferenced raster end products, a reflectance spectrum is given for each uniformly distributed square pixel that spans the imaged scene. When using raster end products, end users implicitly assume all image pixels are: 1) directly comparable, 2) square and 3) uniformly distributed across the image scene. These assumptions are not true (Fisher, 1997; Schläpfer et al., 2007; Shlien, 1979), and thus the raster model misrepresents HSI data. In the HSI literature, the consequences of the stated assumptions have not been well studied, which is alarming given the prevalence of the raster model in data analytics. When HSI was established, landscape-level and larger studies could only be conducted using the raster data model due to hardware and software limitations (Kennedy and Meyers, 1977; Wade et al., 2003). However, it is critical to recognize that the raster model is a heritage of the old computing era (Lim, 2008); more complex data formats may be permissible given current technologies. The overall goal of this thesis is to investigate how raster end products misrepresent HSI data, presenting an alternative data representation that pushes the boundaries of HSI data analytics and application. This thesis is composed of three specific objectives:

(1) Localize imaging errors both spectrally and spatially by analyzing HSI data in its raw sensor geometry

Hyperspectral imagers are affected by errors (e.g., dead pixels, spectral smile artifacts) that appear in various spectral bands and spatial pixels (Schläpfer et al., 2007). To confidently compare the spectrum from different pixels, it is critical to know the location of imaging errors. The first analytical chapter of this thesis aims to develop an algorithm to localize data artifacts both spectrally and spatially by analyzing the imagery in its raw sensor geometry (i.e., before geometric correction and rasterization). Overall, this chapter strives to highlight imperfections in HSI data that need to be considered when comparing the spectra from different pixels. It also aims to showcase the importance of considering the raw sensor geometry in data analytics.

(2) Investigate the implications of assuming that pixels are square

The spatial response to the spectrum from any HSI pixel is not uniform across its square spatial boundaries as it may appear in georeferenced raster end products. The spatial response for each HSI pixel can be described by the spatial point spread function (PSF). Theoretically, the overlap in the PSF of neighbouring pixels results in spatial correlations that are unrelated to the observed scene. The second analytical chapter aims to quantify the consequences of assuming that pixels are square, exploiting the methods developed in the first analytical chapter to characterize and mitigate sensor-generated spatial correlations. As with the first analytical chapter, this work highlights the importance of preserving the raw sensor geometry and considering the sensor point spread function in HSI data analytics.

(3) Quantify the implications of assuming pixels are uniformly distributed across imaged scenes and develop an alternative HSI data representation to overcome the limitations of the raster data model

HSI data pixels are not uniformly distributed across the imaged scene due to various factors such as sensor design, rugged terrains and sensor movement. To generate raster end products, pixels are spatially resampled, theoretically introducing pixel duplication, pixel loss and pixel shifting. Such errors compromise spectral-spatial data integrity. The third analytical chapter aims to quantify the magnitude of these errors and their practical implications in HSI data applications. Integrating the knowledge from the first two analytical chapters, the third analytical chapter strives to develop a novel point cloud data format, fusing digital elevation data with HSI data while preserving the raw sensor geometry.

Raster end products have remained the standard for HSI for over 40 years. This thesis reevaluates their use, proposing an alternative data format that improves data applications. Overall, this research aims to push the boundaries of hyperspectral remote sensing data acquisition, processing, analysis and application.

The following thesis chapter (2) reviews HSI sensor design, sensor characterization, data acquisition and data processing, describing how georeferenced rater end products are generated. The literature review highlights how raster end products misrepresent HSI data, acknowledging alternative vector-based end products that may be able to improve on existing HSI techniques.

The proceeding three chapters (3-5) contain three published manuscripts that directly address the aforementioned project objectives. Chapter 6 discusses the thesis findings, emphasizing all significant contributions and describing future research avenues. In chapter 7, two appended methodological manuscripts are presented (one published, one submitted for publication). These manuscripts give a detailed description of the important methodologies developed in chapters 4-5, providing all of the resources (MATAB function and examples) for their implementation.

Connecting Statement (Chapter 1 to Chapter 2)

The first chapter introduced the thesis structure and project objectives. Chapter 2 introduces the main theoretical context and technical background required for the thesis objectives. Since each of the presented manuscripts from this thesis contains their own introduction and literature review, this chapter will concentrate on general concepts in hyperspectral imaging (data acquisition, processing, analysis), highlighting the need for the research conducted in this thesis.

2. Literature Review

In hyperspectral remote sensing, contiguous narrow-band spectral information is measured for each spatial pixel of an image collected over objects or scenes on the Earth's surface (Bioucas-Dias et al., 2013). This spectral information quantifies the spectral radiance (energy emitted by a surface into a unit solid angle per unit by a projected area over a unit wavelength interval, e.g., μ W·cm⁻²·sr⁻¹·nm⁻¹) emitted or reflected by the materials that contribute to each pixel. Radiance can be used to extract the reflectance and emittance of the studied materials, which are representative of their chemical and physical properties (Eismann, 2012). The term "hyperspectral imaging" (HSI) is currently synonymous with imaging spectroscopy and was first coined by Goetz et al. (1985) when discussing early results from data collected by the Airborne Imaging Spectrometer (AIS). Since then, HSI technology has improved substantially, leading to successful applications in various fields such as ecology, agriculture, geology and forensics, amongst many others, as discussed below.

In ecology, the rich spectral information in hyperspectral imagery provides insight into plant chemical and structural characteristics (Curran, 1989; Gates et al., 1965) that are critical in studying species richness (e.g., Carlson et al., 2007), invasive species (e.g., Lawrence et al., 2006) and plant stress (e.g., Pu et al., 2008). For example, Carlson et al. (2007) used HSI data to map woody vascular plant species richness in lowland tropical forest ecosystems in Hawai'i. Lawrence et al. (2006) used imagery collected from the Probe-1 sensor to map two invasive species (leafy spurge and spotted knapweed) in Madison County, Montana using random forest classification models (>84% overall accuracy). Pu et al. (2008) used CASI airborne HSI data to detect mortality and vegetation stress caused by a spreading hard wood forest disease in China Camp State Park, a forested peninsula on the east side of Marin County, California.

In agricultural applications, HSI data can be used to retrieve various crop attributes such as productivity (e.g., Mariotto et al., 2013), type (e.g., Mariotto et al., 2013), biomass (e.g., Marshall and Thenkabail, 2015) and nutrient content (e.g., Liu et al., 2021b). Specifically, Mariotto et al. (2013) used Hyperion and field spectrometer data from irrigated croplands of the Syr Darya river basin in Uzbekistan, which contained cotton, maize, wheat, rice and alfalfa. The study used a crop productivity model capable of predicting yield for all the studied crops (R²>0.93). The Hyperion data in thus study could also discriminate between crop types (>90%)

overall accuracy). Marshall and Thenkabail (2015) developed accurate crop biomass models for rice (R²=0.91), cotton (R²=0.97) and wheat crops (R²=0.94) using Hyperion data collected over the Central Valley in California. Liu et al. (2021b) quantified the nutrient status and predicted yield in potato crops across various growth stages and growing seasons.

In geological efforts, HSI data has been exploited for lithological mapping (e.g., Harris et al., 2005), hydrocarbon exploration (e.g., Hörig et al. 2001) and mapping hydrothermal alteration zones (e.g., van Ruitenbeek et al., 2012). For instance, Harris et al. (2005) used airborne PROBE HSI data from Baffin Island in Canada to produce a lithological map comparable to existing geological maps of the area. Hörig et al. (2001) used HyMap airborne HSI data to detect hydrocarbon-bearing substances in a controlled field site. In particular, the SWIR portion of the electromagnetic spectrum detected the presence of hydrocarbons via the 1730 nm and 2310 nm absorption features, while the VNIR portion of the spectrum was capable of distinguishing between different hydrocarbon-bearing materials. In van Ruitenbeek et al. (2012), HyMap HSI data collected over a well-exposed volcanic sequence in Western Australia was used to study the distribution of white mica, which allowed for the characterization of the hydrothermal system and reconstruction of the paleo fluid pathways. Finally, in forensics, HSI data can be used to detect buried single graves (e.g., Leblanc et al., 2014) and mass graves (e.g., Kalacska et al., 2009) by analyzing the reflectance properties of the overlying soil and vegetation over time.

Regardless of the application, HSI end users are conventionally provided with georeferenced raster data products, usually in units of spectral reflectance. In such end products, a reflectance spectrum is given for each uniformly distributed square pixel that spans the imaged scene. As mentioned in the thesis introduction, when using raster end products, end users implicitly assume that all pixels are directly comparable, square and uniformly distributed across the image scene. These assumptions are untrue for real HSI data (Fisher, 1997; Schläpfer et al., 2007; Shlien, 1979). The raster data model misrepresents HSI data on a fundamental level, which can theoretically lead to problems in downstream applications. To understand the physical significance of each spectral measurement and how the raster data model misrepresents HSI data, information is required with respect to sensor design, sensor characteristics, data acquisition plan and data processing.

The overall goal of this literature review was to provide the main theoretical context and technical background required for the thesis objectives, which re-evaluate the use of the raster data model in HSI efforts. This literature review covers five topics: (1) sensor design, (2) sensor characterization, (3) data acquisition, (4) data processing and (5) data end products. Although topic (1) describes various sensor architectures, topics (2-5) focus on considerations relevant to pushbroom HSI due to its popularity in remote sensing efforts. Overall, this literature review identifies limitations in HSI data processing and representation, presenting potential solutions that could push the boundaries of data analysis and application.

The literature review was conducted of English language peer-reviewed articles, theses, books and conference papers relating to the five identified topics (sensor design, sensor characterization, data acquisition, data processing and data end products) with no time constraints. The scope of the literature review is also limited to the reflective portion of the electromagnetic spectrum that covers the visible near-infrared (VNIR) ranging from ~ 400 nm to 1400 nm and the shortwave infrared (SWIR) ranging from ~ 1400 nm to 3000 nm. The literature was found by keyword search using the logic ("Remote* sens*" OR "hyperspectral" OR "spectrographic imag*" OR "multispectral") paired with the keywords given in **Table 2.1** (at the end of the document) using Scopus and google scholar. Relevant literature was selected for further investigation based on their abstract if it provided important information on any of the five topics covered in this review. The bibliographies of selected references were also consulted to extract other relevant sources. A small selection of other references has also been included regarding topics not directly related to HSI but important to the review topics. A total of 404 references were selected using the described search process, 174 of which were included in this review.

2.1. Sensor Design

Hyperspectral imagers detect spectrally and spatially dispersed incoming electromagnetic radiation from the sensor's field of view. In the VNIR to SWIR, hyperspectral imagers typically use electro-optical detection mechanisms. Electro-optical detectors are semi-conductors that quantify incoming electromagnetic radiation. When subjected to electromagnetic radiation, electro-optical detectors absorb photonic energy, exciting electrons from the valence band to the conduction band of the semi-conductor (National Research Council, 2010). When sufficiently

cooled, virtually all electrons in electro-optical detectors are located in the valence band, and no electrical current is carried. In these cooled conditions, incident electromagnetic energy can excite electrons from the valence band to the conduction band, generating a measurable current that is ideally proportional to the intensity of the incident radiation (National Research Council, 2010).

Different detectors are sensitive to electromagnetic radiation at specific wavelengths. In the VNIR, silicon-based detectors can be designed to show characterizable sensitivity. For example, the ITRES Compact Airborne Spectrographic Imager (CASI) uses a silicon-based detector that covers the spectral range from approximately 0.4 µm to 1.0 µm (Babey and Anger, 1989; Babey and Anger, 1993). Indium Gallium Arsenide (InGaAs) and Mercury Cadmium Telluride (MeCdTe) detectors are prominently used in the SWIR region of the electromagnetic spectrum (Dhar et al. 2013). MeCdTe-based detectors are particularly interesting as they can be tuned to cover a wide spectral range anywhere from 0.4 µm to 20 µm (Long et al., 2019; Wang et al., 2017). For instance, the Airborne Visible-Infrared Imaging Spectrometer - Next Generation (AVIRIS-NG) uses an MCT-based detector that covers the spectral range from approximately 0.4 µm to 2.5 µm (Chapman et al., 2019).

To capture electromagnetic energy across multiple spatial pixels and contiguous spectral bands, hyperspectral imagers use multiple detectors arranged in either a 1-D or 2-D array. All sensors spectrally and spatially disperse incoming electromagnetic radiation onto their detectors, which record the signal during a user-specified integration time. Due to the design of the spectral dispersion and spatial redirection mechanisms, the digital number (DN) output by each detector corresponds to electromagnetic radiation within a narrow band spectral range that is reflected from a specific area on the Earth's surface. Spectral dispersion is typically carried out using filters, gratings or prisms (Jia et al., 2020). Spatial redirection of incoming electromagnetic radiation is typically carried out with elements such as fiber optic cables, lenses and mirrors (Markham et al., 2018).

Four main hyperspectral sensor types are commonly implemented for remote sensing efforts: whiskbroom, pushbroom, snapshot and sequential spectral scanning. These sensor types are differentiated by how they disperse electromagnetic radiation spatially and spectrally across their detectors. Whiskbroom sensors spectrally disperse incoming electromagnetic radiation from a

solid angle on the ground across a linear detector array, typically with diffraction gratings or prisms. Using a mirror, spectral measurements can be taken one pixel at a time across the sensor field of view (Mouroulis et al., 2000). As the platform moves forward, this process can be repeated to generate images from multiple solid angle measurements. The whiskbroom sensor type was a popular choice in the design of early airborne hyperspectral imagers (e.g., Airborne Visible-Infrared Imaging Spectrometer (AVIRIS) (Green et al., 1998), HyMap (Cocks et al., 1998)). In pushbroom sensors, detector arrays (2-D array of detectors) are designed so that the incident radiation is spectrally dispersed across one dimension of the array and spatially dispersed across the other. These sensors collect a single line of hyperspectral image pixels at a time. An image is formed by stacking multiple lines that cover a given scene (Mouroulis et al., 2000). The pushbroom sensor design is the most commonly implemented in current HSI efforts (e.g., CASI (Babey and Anger, 1989), AVIRS-NG (Chapman et al., 2019), Environmental Mapping and Analysis Program (EnMap) (Guanter et al., 2015)). Although less common, snapshot sensor designs have been implemented in Earth Observation efforts (e.g., Aasen et al. 2015; Cao et al. 2018). Snapshot sensors operate by spectrally and spatially dispersing electromagnetic radiation onto a detector array in a strategic manner, such that spatial-spectral information is dispersed across multiple 2-D detector subarrays that can be recombined to generate a full hyperspectral image from a single integration period (Hagen and Kudenov, 2013). Since pixels are dispersed across two spatial dimensions, no motion is required to generate an image. Stationary vantage points (laboratory setups, outdoor tripod setups) are advantageous for mitigating motion blur effects. At the airborne level, snapshot imagers have primarily been used in remotely piloted aircraft system (RPAS) HSI efforts as the platform can maintain constant position and viewing angles with a gimbal (Aasen et al., 2018). Snapshot imagers are also advantageous as the full frame images can be used in structure from motion algorithms that use multiple full frame hyperspectral images to reconstruct 3D geometry (Aasen et al., 2015). For instance, Aasen et al. (2015) used Cubert UHD 185-Firefly snapshot images to derive 3D hyperspectral information for vegetation monitoring. Similar to snapshot sensors, spectral scanning imagers are capable of collecting full frame images. Unlike in snapshot sensors, sequential spectral scanning sensors are designed so that the incident radiation is spatially dispersed in 2D across the detector array. A hyperspectral data cube is formed by collecting spectral data one band at a time over multiple integration periods through the use of a filter

wheel, acousto-optic tunable filter, liquid crystal tunable filter or Fabry-Perot interferometer (Aasen et al., 2018; Liu et al., 2021a). Examples of spectral scanning imagers include the Rikola FPI and IMEC SM5X5.

In each of the described designs, electromagnetic radiation is dispersed across a finite number of detectors. There is often a trade-off between the spectral and spatial resolution of hyperspectral systems. This dynamic is further complicated as the number of sensor elements has a direct effect on system calibration; the more detector elements a sensor has, the more difficult it is to calibrate the system. With these considerations, whiskbroom sensors can collect higher fidelity spectral information compared to the other sensor designs at the cost of spatial coherency. Due to the use of a scanning mirror in the whiskbroom design, the sensor field of view can be large (e.g., up to 70 degrees for HyMap (Cocks et al., 1998)). Although advantageous for data acquisitions, the mechanical scanning mechanism increases the sensor's weight and volume, which can lead to practical disadvantages. For instance, the added weight and volume could be problematic for RPAS HSI efforts (Aasen et al., 2018). Furthermore, the scanning mechanism imposes limitations on the integration time for whiskbroom sensors as each spectral pixel in the cross track direction (direction perpendicular to the scan direction) needs to be collected independently. The relatively short integration time (<1 ms) of whiskbroom sensors can result in low signal-to-noise ratios (<150 @600 nm) compared to other sensor designs (Jia et al., 2020). Due to the lack of a mechanical scanning mechanism, snapshot imagers can collect data with high signal-to-noise ratios (> 150 @ 600 nm) (Hagen and Kudenov, 2013). Snapshot imagers are also advantageous because there is greater spatial coherency between the image x and y directions. However, the spectral and spatial resolution is typically limited since the finite number of detectors are split between two spatial and one spectral dimension simultaneously (Hagen and Kudenov, 2013). Generally speaking, spectral scanning sensors can collect the highest resolution spatial data as electromagnetic radiation is exclusively dispersed in 2 spatial dimensions across the detector array. Since HSI data is collected one band at a time, dwell times per image can be quite large compared to snapshot and whiskbroom sensors. If the imaging platform is not stable over the duration of a single hyperspectral image acquisition, spatial offsets can be observed between bands, resulting in low spectral fidelity. Pushbroom sensors offer an intermediate between the whiskbroom, snapshot and spectral scanning imagers, providing high spatial and spectral resolution pixels that are accurately aligned and cover relatively large

spectral-spatial regions. As with the snapshot designs, pushbroom sensors have no mechanical scanning mechanism and thus can have larger integration times (>1 ms) and signal-to-noise ratios (>2000 @ 600 nm). For instance, the change from the whiskbroom to pushbroom design from AVIRS to AVIRS-NG greatly contributed to the increase in signal-to-noise ratio from \sim 150 to \sim 2000 @ 600 nm (Curran and Dungan, 1989; Jia et al., 2020). Although the concepts discussed in the remainder of this literature review apply to all sensor architectures, this work focuses on pushbroom HSI due to its popularity in remote sensing efforts.

2.2. Sensor Characterization

2.2.1. Radiometric Response

The radiometric response of a sensor describes the relationship between the radiance of electromagnetic radiation that reaches each detector element and the DN that they record when the photoelectric effect induces a current (Pathakoti et al., 2018; Vane et al., 1987). The radiometric response of a sensor is often assumed to be linear. This can be confirmed by varying the radiance of a controlled electromagnetic radiation source and measuring the response of each detector (Davis et al., 2002; Schaepman et al., 1998). In the literature, the radiometric response of each detector is not typically characterized for a wide range of radiance levels as linearity is assumed (Cocks et al., 1998; Vane et al., 1987). The radiometric response of a sensor is typically defined by radiometric sensitivity coefficients that are calculated in a well-controlled laboratory environment by linearly regressing the radiance of incident electromagnetic radiation against the DN recorded by the excited detector element (Vane et al., 1987).

Although HSI data products derived from lab-based radiometric calibrations can yield high accuracy spectral information, radiometric sensitivity coefficients can change over time due to stresses that occur as the sensor is transported, installed and operated (Folkman et al., 2001; Secker et al. 2001). In such cases, vicarious calibration has been successful in calculating accurate radiometric sensitivity coefficients from operational imagery using known spectral references (e.g., Secker et al., 2001; Teillet et al., 2001). For instance, Secker et al. (2001) used ground-based reflectance data simultaneously collected during HSI data acquisition to derive new radiometric sensitivity coefficients that resulted in more accurate reflectance spectra.

Although it is widely accepted that the radiometric response is linear, there are noted exceptions in the literature. For instance, Soffer et al. (2021) found that the WaterSat Imaging

Spectrometer Experiment (WISE) instrument was characterized by a non-linear radiometric response for low signal targets (e.g., water, shadows). Correspondingly, a two-part radiometric refinement (linear for mid to high radiance levels, non-linear for low signal levels) was designed and implemented to retrieve radiance values consistent with the 6S radiative transfer model. Although such a correction may not be necessary for all sensors, it is critical to assess the validity of assuming that the radiometric response is linear. If non-linearities exist, radiometric sensitivity coefficients may not be sufficient to characterize the radiometric response.

While measuring DNs, it is also important to note that the signal is quantized. This quantization is captured in the radiometric response. In most cases, the quantization is so detailed (>12 bit) that the measurements vary in a relatively continuous manner (Davis et al., 2002; Green et al., 1998; Schaepman et al., 1998).

2.2.2. Spectral Response

The spectral response defines the relative spectral contribution to the signal from each detector as a function of wavelength (Schowengerdt, 2006c) (see Figure 2.1). The spectral response of an imager can be measured with a monochromator, a device that transmits mechanically selectable narrow-band electromagnetic radiation. To derive the spectral response of each detector, hyperspectral images are taken while varying the monochromator. Each detector is then mapped against its responsivity to electromagnetic radiation as a function of wavelength (Skauli, 2012). The spectral resolution of a sensor is defined by the full width at half-maximum of the spectral response function (see Figure 2.1). Due to the design of pushbroom hyperspectral imagers and their spectral dispersion mechanisms, the center wavelength of most spatial pixels varies across the field of view. This distortion is known as the spectral smile effect (Yokoya et al., 2010) and is typically corrected while processing the data (see Figure 2.2). Spectral smile is typically less than 0.1 pixels across the sensor field of view. Generally speaking, hyperspectral imagers collect contiguous spectral information as there is overlap in the spectral response of neighbouring spectral bands (see Figure 2.1) (Roger and Arnold, 1996).

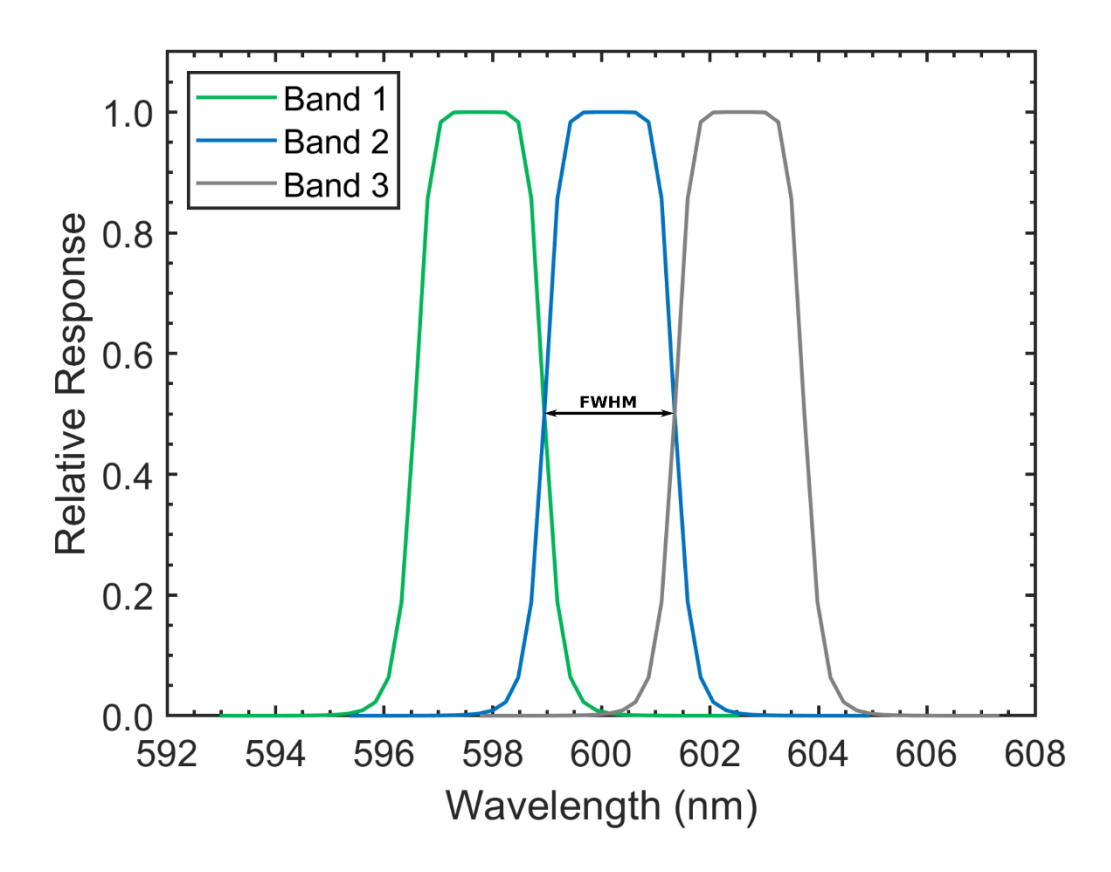


Figure 2.1. Example spectral response functions for three adjacent bands from the CASI-1500. The spectral response functions of the bands displayed in the figure are defined by fourth-order Butterworth filter functions centred at 597.757 nm, 600.150 nm and 602.543 nm. The spectral resolution is defined by the full width at half-maximum and is approximately equal to 2.4 nm (see black double-sided arrow in the figure). Hyperspectral imaging systems collect contiguous spectral information, which can be seen in the overlap between adjacent spectral response functions.

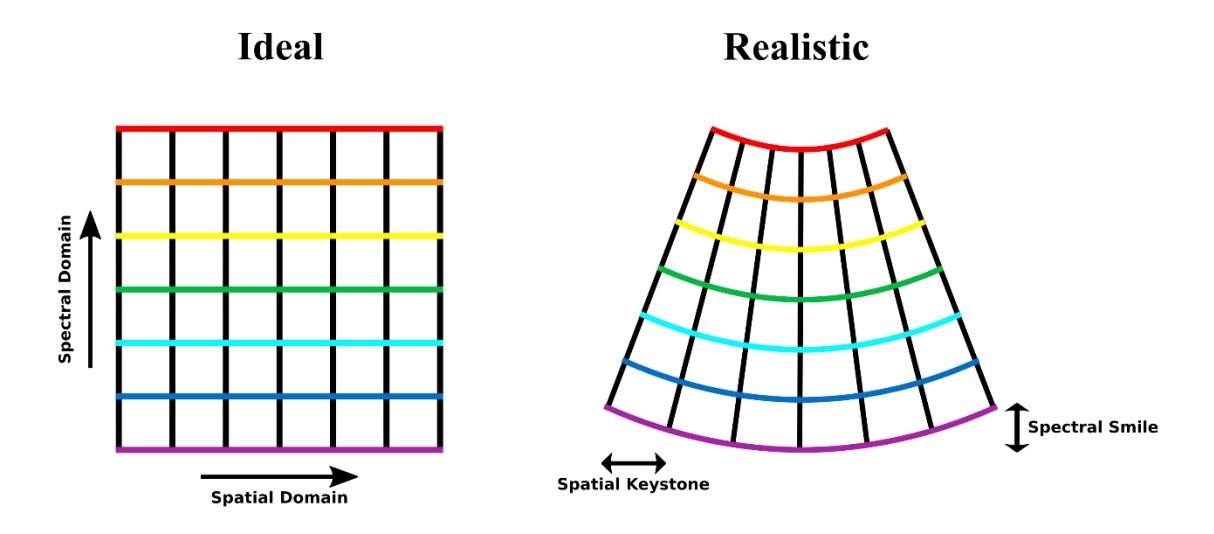


Figure 2.2. Representation of spectral smile and keystone artifacts in pushbroom hyperspectral imaging data. In the ideal scenario, the spectrum from each pixel collects data on the same wavelength array. Furthermore, each band from a single hyperspectral image pixel corresponds to the same area on the ground. In reality, each hyperspectral pixel collects spectral data on a slightly different wavelength array (spectral smile). Additionally, each band from any given hyperspectral image pixel corresponds to a slightly different area on the ground (keystone).

2.2.3. Spatial Response

The spatial response defines the spatial contribution to the spectrum from a single pixel. The spatial response is typically characterized by the net point spread function (PSF_{net}) or its normalized Fourier transform, the modulation transfer function (MTF). Formally, the PSF_{net} gives the relative response of an imaging system to a point source as a function of distance from the pixel center (Schowengerdt, 2006b). An example PSF is shown in **Figure 2.3**.

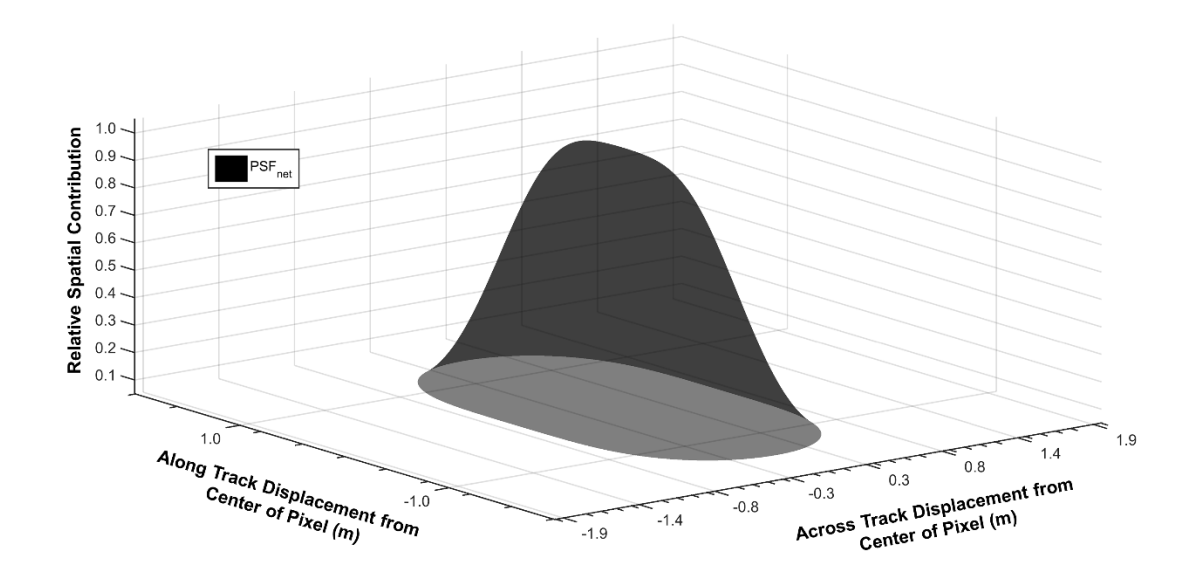


Figure 2.3. Example point spread function derived for imagery collected by the Compact Airborne Spectrographic Imager (CASI-1500). The relative spatial contribution to a single pixel is a function of across track and along track displacement from the pixel center. Figure reproduced without modifications from Inamdar et al. (2020) under the terms and conditions of the Creative Commons Attribution (CC BY) license (http://creativecommons.org/licenses/by/4.0/).

Traditionally, the spatial response of a sensor is measured in a controlled laboratory environment. In the laboratory characterization, the sensor is used to image a well-characterized point source target. By capturing multiple images while varying the location of the point source, it is possible to obtain the spatial response of each detector in two dimensions (Jemec et al., 2017). This characterization does not account for the dynamics of motion that occurs during the integration time in real data acquisitions. These dynamics can be simulated by convolving the spatial response by a rectangular pulse function with a width equal to the distance traveled during a single integration time. The net spatial response function can also be measured from operational imagery over man-made objects that represent point sources (e.g., mirrors and geometric patterns) or targets of opportunity (e.g., bridges and coastlines) (see Holt et al. (2021) Schowengerdt et al. (1974) and Rauchmiller and Schowengerdt (1988) for more details). Due to sensor optics, detectors and motion during data acquisition, the spatial contribution to each pixel is non-uniform (often Gaussian in shape), extending past the traditionally square spatial boundaries designated by the pixel resolution. It is critical to note that pixels are not square as they appear in conventional raster end products (Fisher, 1997; Smith, 1995). The spatial response of each spatial pixel is primarily dependent on the altitude, speed, integration time, size of the

detectors and the optics (Inamdar et al., 2020; Schowengerdt, 2006b). Similar to spectral resolution, the spatial resolution of a sensor can be defined by the full width at half-maximum of the spatial response function. Alternatively, spatial resolution can be defined by the ground instantaneous field of view, which is the geometric projection of a single detector width onto the Earth's surface (Schowengerdt, 2006a). Generally speaking, hyperspectral imagers collect contiguous spatial information as there is overlap in the spatial response of neighbouring spectral pixels (see **Figure 2.4**).

Due to the design of pushbroom hyperspectral imagers, there is spatial misregistration between the spectral bands of each spatial pixel. This distortion is known as the keystone effect and is the spatial analog of the spectral smile effect (see **Figure 2.2**) (Yokoya et al., 2010). As with the spectral smile effect, it is typically corrected while processing the data. Keystone is typically less than 0.1 pixels across the sensor field of view.

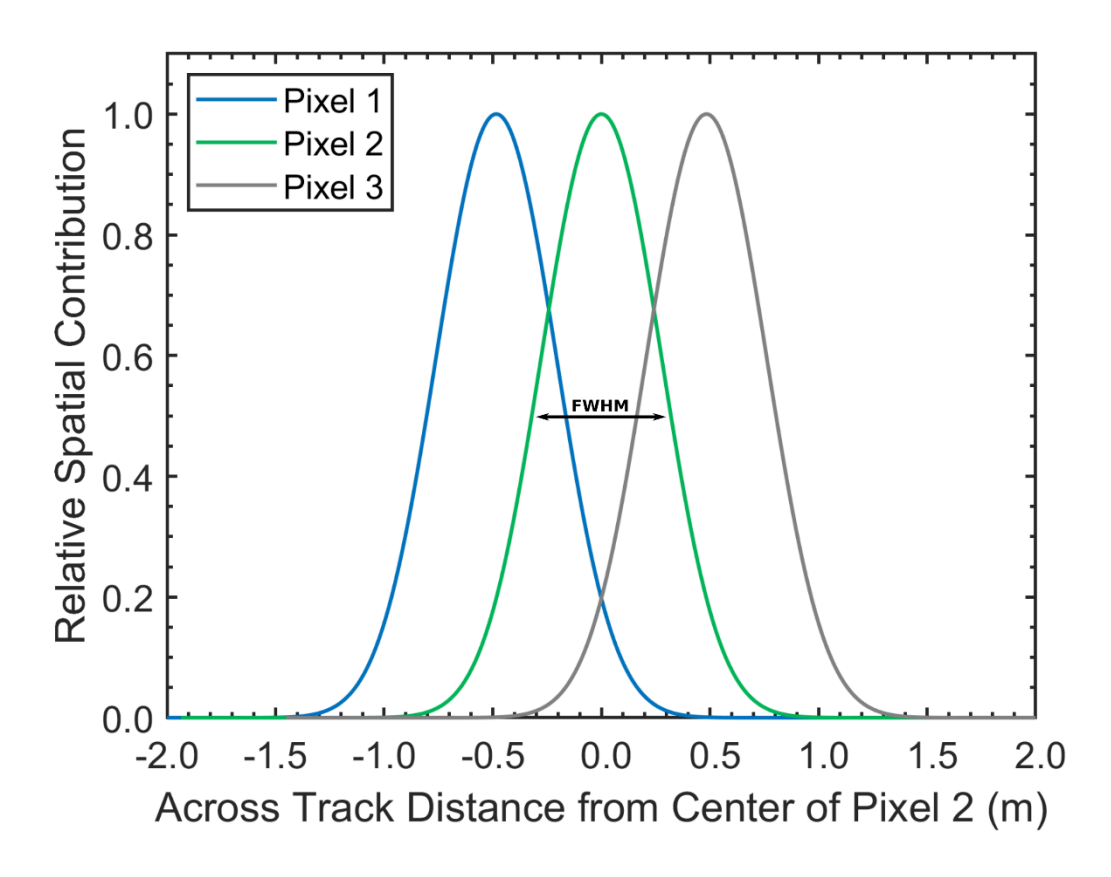


Figure 2.4. Example spatial response function in the across track direction for three adjacent pixels from CASI-1500 imagery. Spatial resolution can be defined by the full width at half-maximum (see black double-sided arrow in the figure). Hyperspectral imaging systems collect contiguous spatial information, which can be seen in the overlap between adjacent spatial response functions.

2.3. Data Acquisition

Mission planning is fundamental to collecting high-quality HSI data (Cline et al., 1987; Zhao et al., 2019). Data acquisition missions must be conducted under stable illumination conditions so that the atmospheric compensation can accurately mitigate atmospheric absorption and scattering effects. Soffer et al. (2019) point out that the rate of change in the solar zenith angle and shadow coverage are minimized at solar noon. As such, acquisitions near solar noon are ideal in many situations, especially since incoming solar radiation and thus signal levels are maximized (Vreys et al., 2016b). It is critical to ensure motion is controlled (e.g., stable speed, attitude, heading and altitude) during data acquisition, considering factors such as wind and pilot experience in manned aircrafts (Pepe et al., 2018) and gimbal effectiveness (if one is used) and

flight motion accuracy and precision (effectiveness of flight controller and inertial navigation system) in RPASs (Arroyo-Mora et al., 2019).

The spatial resolution and the pixel spacing of an image are affected by sensor speed, altitude, view angle, integration time and frame rate (Schowengerdt, 2006b). Ideally, missions should be planned to generate pixels with a similar spatial resolution in the cross track and along track directions. For pushbroom sensors, this can be technically difficult since the resolution in the along track is determined by the integration time and platform speed (Schowengerdt, 2006b; Zhao et al., 2019), both of which have impacts on other aspects of the data (e.g., signal to noise ratio, platform stability, etc.), especially for low altitude platforms such as RPASs (Arroyo-Mora et al., 2019). Given the discrepancy in the cross track and along track resolutions, the spectrum from any given pixel rarely corresponds to a square area on the ground (Inamdar et al., 2020).

Sensor speed and altitude are practically limited by the carrying platform of the sensor (Aasen et al., 2018). HSI data is typically collected using RPAS (fine spatial resolution allowed by low altitude and speed), manned aerial aircrafts (intermediate spatial resolution due to altitude and speed) or spaceborne platforms (coarse spatial resolution due to high altitude and speed) (see **Figure 2.5**).

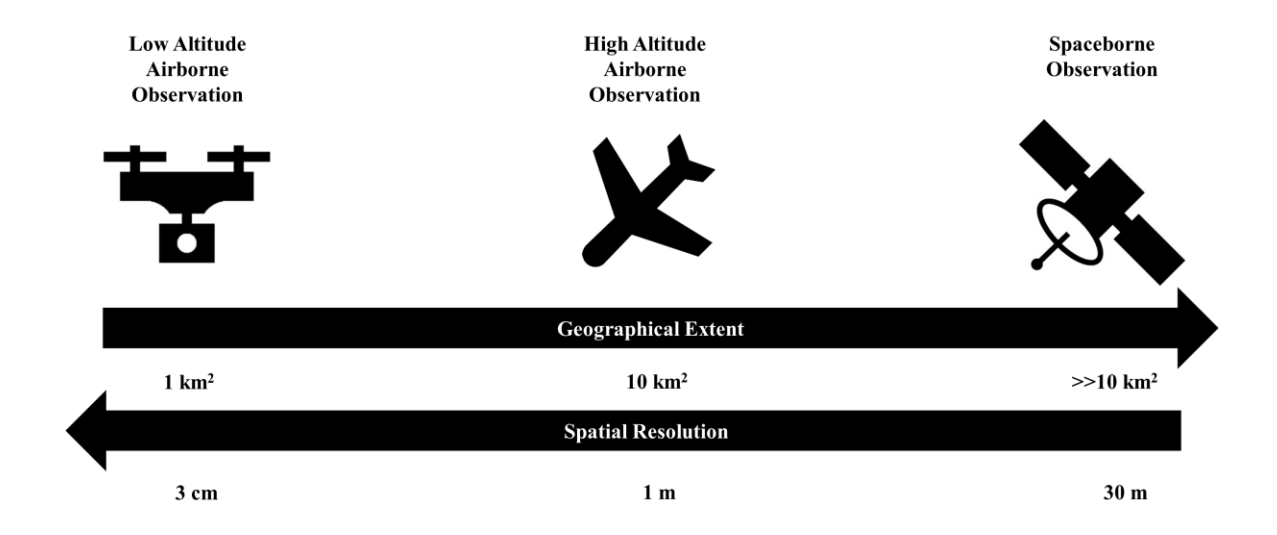


Figure 2.5. The approximate spatial resolution and geographic extent of hyperspectral imaging systems on various platforms.

The integration time must be considered simultaneously with the signal-to-noise ratio; a suitable integration time maximizes the signal over a scene without saturating any detectors during data acquisition (Clark and Rilee, 2010). It is important to recognize that there is a tradeoff between pixel resolution and area coverage (Aasen et al., 2018). As such, there may be logistic restrictions to the spatial resolution given area coverage requirements for specific projects. If the required spatial resolution is unknown, it is ideal to collect finer spatial resolution data since spatial detector measurements can be summed to boost signal-noise ratios in postprocessing (Cornish, 2014). Furthermore, the data can be resampled to simulate the imaged scene at a coarser resolution. The spectral resolution of a sensor has similar constraints concerning the signal-to-noise ratio. However, since spectral detector measurements can be summed to boost signal-to-noise ratio (Cornish, 2014; Kalacska et al., 2016), it is ideal to collect data at the highest spectral resolution possible. Additional considerations must also be made with respect to the implementation of pixel summing. When summing in the spatial domain, the spatial response is modified. Typically, this results in sharper spatial responses, in the sense that the signal from the summed pixel has less contributions from the materials outside of its traditional rectangular pixel boundaries defined by the spatial resolution in the cross track and along track directions. Summing in the spectral domain also increases the sharpness, as the signal from the summed pixels has less contributions from outside of their covered spectral region (Schowengerdt, 2006c). Overall, the spatial resolution of an HSI system is typically limited by the aircraft. RPASs typically offer the highest spatial resolution if there are no monetary restrictions, followed by manned aircrafts and satellite platforms. However, it is important to recognize that restrictions, such as weather and airspace logistics, may impede the implementation of specific platforms (Arroyo-Mora et al., 2019; Vreys et al., 2016b).

2.4. Data Processing

2.4.1. Radiometric Correction, Spectral Smile Correction and Spatial Keystone Correction

To generate an HSI dataset where every spatial pixel is associated with the spectral radiance of materials within the pixel instantaneous field of view, it is critical to apply the radiometric correction, spectral smile correction and spatial keystone correction.

The radiometric correction adjusts the raw DN collected by each detector of an imaging system, converting the measurement to radiance. The first stage in the radiometric correction is

to remove additive signals from the instrument itself. The most prominent additive signal originates from dark current. During data acquisition, the temperature difference between the environment and the cooled detector elements allows electrons to pass through the conduction band of the semi-conductor and induce a current (Manea and Calin, 2015; National Research Council, 2010). Dark current is relatively constant during data acquisition (Chapman et al., 2019). To measure this additive contribution to the recorded DNs when hyperspectral data is acquired, multiple frames are collected while the aperture is still closed and the detector array only records signal from the instrument itself. The signal recorded in these dark frames (measured dark current) is removed from the signal acquired while the aperture is open (de Miguel et al., 2014). After removing additive contributions from the instrument, the radiometric sensitivity coefficients are applied, and the raw DN from each detector is converted into units of spectral radiance (Warren et al., 2014). As mentioned in section 2.2.1, although a linear sensor response is typically assumed, it is critical to recognize that non-linearities exist and can affect imaging systems. For instance, the non-linear refinement implemented by Soffer et al. (2021) for the WISE hyperspectral imager was critical to obtaining at sensor-radiance values for dark targets (water, shadows, asphalt, black tarp) that were consistent with 6S simulations. Without this refinement, many dark targets were characterized by negative radiance values, which have no real physical significance. This research emphasizes that the linear radiometric response assumption must be verified when applying conventionally derived radiometric sensitivity coefficients.

To compare the spectra from various spatial pixels, it is critical to correct for the spectral smile. In this process, the spectrum from each spatial pixel across the field of view is spectrally resampled to a common wavelength array (usually that of the central pixel location). The spectral smile correction is possible as the center wavelength of the spectral bands for each spatial pixel is determined during sensor characterization (Yokoya et al., 2010).

A similar correction can be applied in the spatial domain with spatial resampling techniques. In particular, the data can be spatially resampled on a uniform grid, where each pixel is separated by the same distance. Once again, this correction is possible due to the known location of each spatial pixel across the spectral domain, as determined during sensor characterization (Yokoya et al., 2010).

Given enough details about any HSI sensor and its calibration, end users could theoretically implement the radiometric, spectral smile and spatial keystone correction in their programming language of choice. However, these steps are practically carried out using software developed by the sensor manufacturer as the details required to implement such processing are not always provided.

2.4.2. Deconvolution

Overlap in the spatial-spectral response between adjacent spatial pixels and spectral bands causes sensor-generated correlations in the imagery (see Figure 2.1 and Figure 2.4) (Inamdar et al., 2020). These correlations are commonly observed as sensor blurring. Sensor blurring can impede HSI data applications that depend on the contrast of fine spatial-spectral details in the imaged scene. The impacts of sensor-induced blurring effects have been characterized at the satellite level for multispectral data. In Huang et al. (2002), sensor blurring was found to reduce the natural variability in scenes observed by satellite spectrographic imagers. This reduction in variability is associated with information loss (Lee and Landgrebe, 1993) and has been found to negatively affect various remote sensing tasks such as classification (Huang et al., 2002), subpixel feature detection (Radoux et al., 2016) and spectral unmixing (Wang et al., 2018). In Huang et al. (2002), the land cover classification of a simulated MODIS image that accounted for the sensor PSF decreased in accuracy by 5.4% compared to a control simulated image that ignored the PSF, treating pixels as squares. Although some reports acknowledge the implications of sensor-induced blurring at the airborne level, many studies do not attempt to characterize or mitigate their impact (e.g., Bergen et al., 2005; Heiskanen, 2006; Simms et al., 2014; Tarrant et al., 2010; Torres-Rua et al., 2016). Schläpfer et al. (2007) found sensor-induced blurring modified fine resolution HSI data (5 m) to a greater degree than the lower resolution data (28.3 m). These results suggest that sensor blurring may be more prominent for airborne sensors due to their high spatial resolution. The impacts of sensor-induced blurring for fine resolution HSI data should be further evaluated.

Spectral-spatial blurring can be reduced with deconvolution methodologies (e.g., (Fang et al., 2017; Henrot et al., 2013; Jackett et al., 2011)), which minimize the contributions of materials outside the spatial boundaries of the pixel and electromagnetic radiation beyond the spectral region defined by each band. Generally speaking, deconvolution algorithms act to sharpen the imagery. It is critical to recognize that deconvolution is an ill-posed problem; due to the

information loss associated with sensor blurring, a unique solution is often unobtainable even in the absence of noise (Chaudhuri et al., 2014). Furthermore, deconvolution techniques can introduce artifacts and struggle with restoring high-frequency features. Henrot et al. (2013) show that some deconvolution algorithms can introduce ringing artifacts that generate negative values from non-negative images. Since negative values have no physical significance in HSI data, this would be problematic in data applications. It is important to consider the trade-off between sharpness and information content, as per the requirements of the research question. As such, deconvolution is not always performed in practice, unlike the other processing steps (e.g., radiometric correction, atmospheric compensation, geometric correction) which are fundamental to exploiting the spectral and spatial information in HSI data.

2.4.3. Atmospheric Compensation

HSI data is collected in atmospheric windows that allow for the transmissivity of electromagnetic radiation (see **Figure 2.6**). Even in these atmospheric windows, as solar electromagnetic radiation travels along the Sun-surface-sensor ray path, it interacts with the molecules and particles in the atmosphere through scattering and absorption mechanisms (Gao et al., 2009). This is problematic for hyperspectral remote sensing in the VNIR-SWIR as atmospheric influences mask the surface information encoded in the radiance spectra.

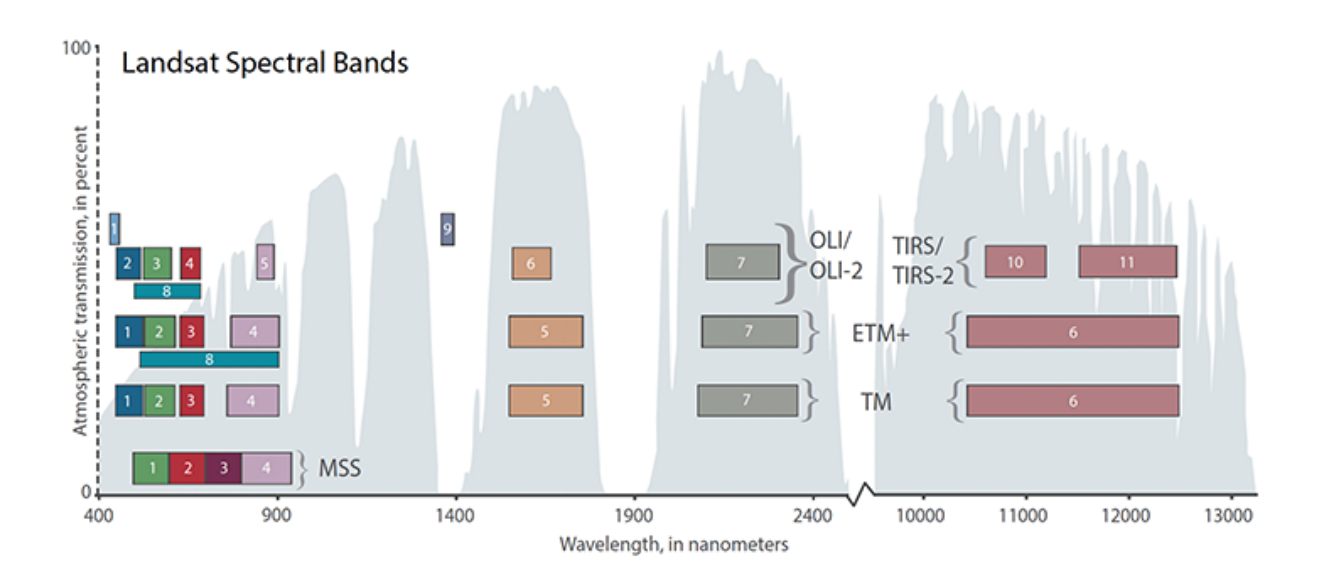


Figure 2.6. Transmission of electromagnetic radiation in the atmosphere from 200 nm to 13000 nm calculated using MODTRAN for a summertime mid-latitude hazy atmosphere (5 km visibility). The shaded light-blue region gives the transmissivity (in units of %) of electromagnetic radiation in the atmosphere as a function of wavelength. The colored bars display the width of Landsat's spectral bands from the first generation Multispectral Scanner System (MSS) to Landsat 9's Operational Land Imager 2 (OLI-2). All spectral bands are designed to exploit available atmospheric windows (figure copied from Barsi and Rocchio (2020) following the NASA Media usage guidelines).

To extract surface information based on the reflectance properties of the surface materials within each pixel, these atmospheric influences must be compensated for (Asmat et al., 2011; Gao et al. 2009; Ibrahim et al. 2018). In the reflective portion of the electromagnetic spectrum, major atmospheric absorptions occur at approximately 0.94, 1.14, 1.38 and 1.88 μm from water, 0.76 μm from oxygen and 2.08 μm from carbon dioxide (Gao et al., 2009). In addition, path radiance from backscattered particles in the atmosphere has additive effects that are not representative of the materials within the sensor's field of view. Radiation is also observed from nearby surfaces outside the sensor's field of view after adjacent electromagnetic radiation is reflected and scattered into the optics (see **Figure 2.7**) (Richter et al., 2006). Considering the accumulative effects of these factors, it is clear that only a portion of the measured signal originates from the material of interest (Richter and Schläpfer, 2020). The primary objective of the atmospheric correction is to minimize atmospheric absorption and scattering effects, observed path radiance and contributions from surface reflected and scattered radiation outside the field of view. In atmospheric compensation processing, at-sensor radiance is converted into units of reflectance, which are independent of the atmosphere.

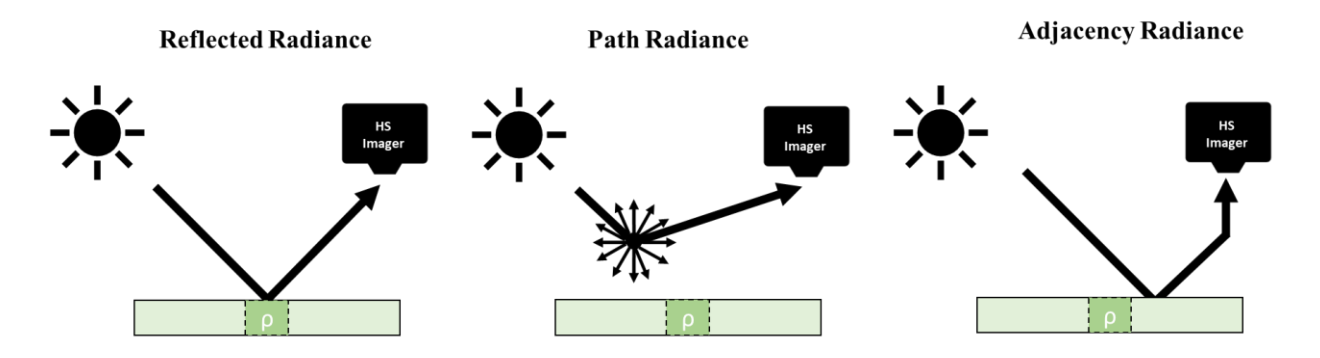


Figure 2.7. Schematic sketch of the major solar radiation components from the signal measured by a hyperspectral (HS) imager. The atmospheric compensation attempts to recover the reflectance (ρ) of the material that is responsible for the reflected radiance.

There are three main approaches to atmospheric compensation: 1) scene-based empirical approach; 2) radiative transfer model approach; and 3) hybrid approach (Gao et al., 2009; Jia et al. 2020). Scene-based empirical approaches use the spectral information within a given hyperspectral dataset to remove atmospheric effects. Many of these methods simply scale the data by a strategically selected spectrum to obtain a measure of relative reflectance. For instance, the Internal Average Reflectance (IAR) approach (Kruse, 1988) scales HSI data by the average spectrum to estimate the relative reflectance across the scene. The flat field approach developed by Roberts et al. (1986) is another empirical method that scales the imagery by the average spectra of spectrally neutral materials in the scene (i.e. materials whose reflective properties do not vary substantially with wavelength). In some empirical methods, additional ground truth reflectance data is utilized. For instance, the empirical line approach linearly fits *in situ* reflectance measurements of spectrally invariant surfaces in the scene to their corresponding sensor readings (Conel et al., 1987). This linear fit is then applied to all pixels for which no ground control data was acquired. To date, empirical approaches are still common in HSI efforts (e.g., Quick Atmospheric Correction (QUAC) (Bernstein et al., 2012)).

The radiative transfer model approach uses physically derived expressions for radiative transfer in the atmosphere to approximate the at-sensor radiance of a perfect reflector, accounting for atmospheric absorption, path radiance and the adjacent radiance (Gao et al., 2009). This information makes it possible to measure apparent reflectance, which is scaled from 0 to 1 and indicates the relative amount of electromagnetic radiation reflected by the surface. The radiative transfer model, and its constituent equations, depend on various environmental variables that can

either be directly input from ground-based measurements or retrieved from the HSI data. The most important atmospheric variables include aerosol type (typically based on geographical location), atmospheric water vapour column and visibility (Richter and Schläpfer, 2020). ATREM (Gao et al., 1993), ATCOR (Richter and Schläpfer, 2020), FLAASH (Cooley et al., 2002) and HATCH (Zheng et al., 2003) are examples of commonly used atmospheric compensation software that use radiative transfer codes such as LOWTRAN (Kneizys, 1988), MODTRAN (Berk et al., 1999) and 6S (Vermote et al., 2006).

Scene-based empirical approaches are typically less accurate than the radiative transfer methods but much faster. For example, the spectra used to calculate relative reflectance can introduce unnatural absorption features as no materials are truly spectrally neutral (i.e., all materials have some absorption features) (Clark and King, 1998). Scene-based approaches that use *in situ* reflectance measurements may be inaccurate if atmospheric conditions vary spatially and temporally (Gao et al., 2006). On the other hand, radiative transfer approaches can struggle with complex and varying atmospheric conditions due to their sensitivity to uncertainty in the atmospheric gas and aerosol state (Thompson et al., 2016). As such, scene-based empirical approaches can play a complementary role in difficult atmospheric corrections (Arroyo-Mora et al., 2021).

In hybrid approaches to atmospheric compensation, scene-based empirical methods are synergized with radiative transfer approaches (Gao et al., 2006; Jia et al., 2020). In these efforts, radiative transfer modeling can derive a reasonable estimate of reflectance, which is fine-tuned by scene-based empirical methods with ground truth hyperspectral point measurements. For instance, Thompson et al. (2016) developed an atmospheric compensation methodology that fine-tunes a radiative transfer model-based solution by incorporating in-situ reflectance measurements via Bayesian inference. Opposite to this approach, other hybrid methods apply empirical methods first, fine-tuning the results with radiative transfer approaches. For example, Richter and Schläpfer (2020) developed an in-flight radiometric calibration module in ATCOR-4 that fine-tunes the sensor observed radiance using in-situ reflectance measurements. With the fine-tuned radiance values, their radiative transfer model approach to atmospheric compensation can result in more accurate reflectance spectra (Soffer et al., 2019).

2.4.4. Geometric Correction

The purpose of the geometric correction is to locate the position of each image pixel on the Earth's surface. This task requires accurate attitude and position data of the imager at a sampling rate higher than the sensor's frame rate (reciprocal of frame time). The geometric correction must also use interior orientation parameters that define the image space of the sensor (i.e., imager focal length, principal point location and radial lens distortion) (Barbieux et al., 2016; Warren et al., 2014).

The sensor's motion can be characterized at the required frequency for geometric correction (frequency > sensor frame rate) by a sensor-mounted inertial navigation system (INS). Typically, the INS of a sensor records global navigation satellite system (GNSS) data (positional), attitude data and acceleration data (Warren et al., 2014). To obtain highly accurate positional data, a differential correction is typically applied. This differential correction requires highly accurate base station GNSS data with a small baseline (ideally 5-10 km for L1 antennas and 60-100 km for multi-band antennas) (Aasen et al., 2018; Emlid, 2022; Famiglietti et al., 2021). The closer the base station to the hyperspectral data acquisition site, the more accurate the differential correction (Farrell, 2008). Generally speaking, base station data is not typically collected at the frequency required by the geometric correction (frequency > sensor frame rate). This is problematic as the GNSS data from the INS is usually downsampled to the base station sampling frequency after differential correction. To accurately upsample the data to the required frequency, the high-frequency attitude and acceleration data are fused with the differentially corrected positional data through a Kalman filtering process (Da, 1997). The positional data is then shifted by the spatial offset from the center of the INS to the sensor's optical center. In addition, the roll, pitch and yaw are adjusted by the attitude offset from the INS to the sensor (Lenz et al., 2014).

The INS-sensor offset, along with the interior orientation parameters, is typically calculated through a bundle adjustment. In the bundle adjustment, the position offset, attitude offset, focal length and principal point location are calculated by analyzing a grid of collected hyperspectral images over multiple ground control points with highly accurate positional data (Barbieux et al., 2016; Triggs et al., 2000). These images are planned to have a substantial amount of overlap so that the desired parameters can be calculated based on the relative position of each ground control point in each of the images (Barbieux et al., 2016; Triggs et al., 2000).

On a fundamental level, the geometric correction is a geometry problem that projects the collected data from the image space onto an elevation model in a physical space. Specifically, each pixel is located at the intersection of the surface elevation model and a straight line projected from the sensor position at the pixel-dependent look direction (see Figure 2.8). The look direction is calculated by accounting for the sensor attitude (roll, pitch yaw), focal geometry and boresight misalignment (Warren et al., 2014). The accuracy of the geometric correction is dependent on the accuracy of the bundle adjustment and the INS data (Brunn et al., 2003; Müller et al., 2002). For relatively flat terrain at high altitudes, a flat surface model can be used (de Miguel et al., 2014). For low altitude data acquisition, variations in the surface elevation become increasingly important (Arroyo-Mora et al., 2019). The same can be said for areas of extreme elevational variations (e.g., mountains). In these cases, a digital surface elevation model must be acquired, typically from either LiDAR (Liu, 2008) radar altimetry (Leslie, 2018), synthetic aperture radar altimetry (Raney, 1998) or interferometric synthetic aperture radar altimetry (Gao et al., 2017). For low altitude acquisitions, a structure from motion workflow can be applied to generate a dense point cloud, and subsequently a digital surface elevation model, from regular RGB images (Westoby et al., 2012). LiDAR data can also be acquired using RPAS for digital surface model generation at low altitudes (Kalacska et al., 2021).

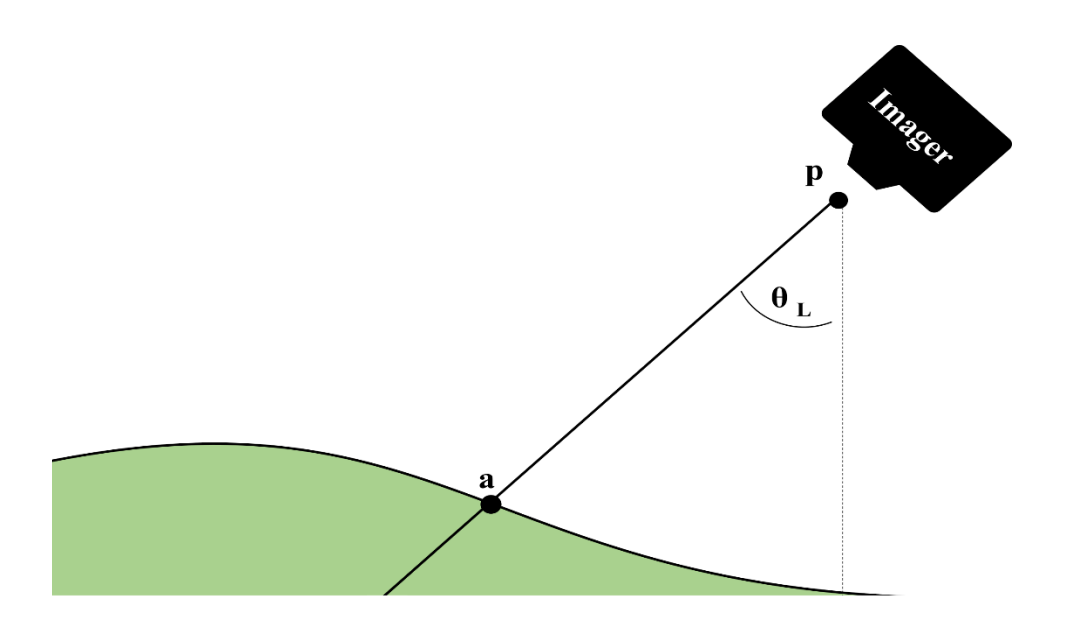


Figure 2.8. Schematic of the geometric correction. With a known sensor position (p) and look direction (θ_L), the position of each pixel in the image space can be located in a real-world coordinate space. The pixel is located at the intersection (a) of the input digital surface model (shown in green) and a straight line projected at the pixel-dependent look direction from the sensor position. The look direction is the angle at which incoming electromagnetic radiation is observed by any given pixel of the hyperspectral imager (Müller et al., 2002). The look direction is calculated from the sensor's attitude, focal geometry and boresight misalignment during data acquisition (Brunn et al., 2003; Müller et al., 2002). Figure reproduced without modifications from Inamdar et al. (2021) under the terms and conditions of the Creative Commons Attribution (CC BY) license (http://creativecommons.org/licenses/by/4.0/).

2.4.5. Rasterization

Hyperspectral pixels are not uniformly spaced over the imaged scene after the geometric correction due to factors such as lens distortion, sensor movement and rugged terrains (Galbraith et al. 2003; Vreys et al. 2016a). To correct this non-uniformity, the geometrically corrected data are typically spatially resampled on a north-oriented linear grid (Shlien, 1979). Each grid cell is typically separated by an equal distance in the easting and northing directions, leading to a rasterized end product with square pixels (Richards and Jia, 1999; Shlien, 1979; Warren et al., 2014). A nearest neighbour approach is conventionally used when spatially resampling HSI data (Roy, 2000; Williams et al., 2017). In this technique, the spectrum for each cell in a pre-specified linear grid is determined by the nearest spectrum from the original imagery that is being resampled (Shlien, 1979). This resampling is conventionally applied as it does not modify the value recorded in any measured spectrum and thus preserves spectral data integrity (Schläpfer et al., 2007). If not properly implemented, the nearest neighbour method can compromise the

spatial integrity of the collected data. Nearest neighbour resampling can lead to a blocky appearance due to pixel duplication if oversampling occurs (Arif and Akbar, 2005). On the other hand, if the data is undersampled during nearest neighbour resampling, pixels can be lost altogether, eliminating valid spectral information (Arif and Akbar, 2005). Even if properly implemented, nearest neighbour resampling results in pixel shifting as the true position of each pixel is moved up to 0.5 pixels in the image x and y directions to fit the pre-specified resampling grid (Roy, 2000; Shlien, 1979).

In the pushbroom sensor design, the spatial characteristics of collected HSI data are different between the cross track and along track directions. This creates some difficulties when deciding on the spatial resampling grid resolution for HSI efforts; the data will either be oversampled or undersampled depending on the resampling resolution selected, leading to pixel loss and pixel duplication. Even though pixel loss and duplication are present in virtually all HSI datasets generated with the nearest neighbor resampling technique, these errors have only been noted in a limited number of remote sensing studies (Kimerling, 2002; Kollasch, 2005; Williams et al., 2017). Of these works, only Williams et al. (2017) focused on HSI data (Williams et al., 2017). Unfortunately, the implications of pixel duplication and pixel loss on HSI data applications have not been rigorously characterized. Pixel shifting from spatial resampling has been shown to negatively affect various applications such as multi-temporal datasets compositing and alignment (Tan et al., 2006), change detection (Roy, 2000) and classification (Alcantara et al., 2012). Tan et al. (2006) used simulated MODIS data to show that the sensor observation in any grid cell is only partially derived from materials within the location of the cell; due to pixel shifting, the average spatial overlap between observations and their corresponding pixel was less than 30%. In this work, pixel shifting was found to introduce bias when compositing multi-temporal datasets. Roy (2000) had similar findings, showing that pixel shifting from nearest neighbour resampling contributed to systematic bias estimates of location and area when compositing data for the purposes of change detection. Alcantara et al. (2012) mapped abandoned agriculture using multi-temporal MODIS data, attributing high classification errors to pixel shifting that caused changes in spectral information reported for a given MODIS pixel over time.

To preserve the information content of a hyperspectral image, the data should not be rasterized. Rasterization can potentially introduce pixel duplication and loss while shifting the

known location of pixels to fit a north-south oriented square grid. With best practices, it may be possible to rasterize the data according to a rectangular pixel regime oriented along the flight line heading. However, even this approach is limited in its application as the spatial origin of each pixel will be lost to some degree.

2.5. Data End Products

2.5.1. The Raster Data Model

Raster end products have been a standard for HSI data for over 40 years (Goetz, 2009; Vane et al., 1984; Wilkinson, 1996) as virtually all spectral imaging systems view analyzed scenes as fields of informative continuous variables (e.g., spectral reflectance) that are discretized into pixel arrays (Couclelis, 1992). The concept of rasterization predates the inception of HSI by more than 20 years. In 1957, Russel Kirsch at the National Bureau of standards created a drum scanner to digitize analogue photographs into a raster array that was stored on Standards Eastern Automatic Computer. The digitized image was interesting as the computer could be used to program pattern recognition routines to analyze the imagery (e.g., counting the percentage of the image that was black). Visualization of stored images were mediated through an oscilloscope screen, where the raster data was represented as a collection of plotted points (Kirsch et al., 1957). In 1971, Michael Noll improved on the display of rasterized images, developing a television-like scanned-display system with raster computer graphics (Noll, 1971). Since the seminal work of Kirsch and Noll, the raster data model has become fundamental to displaying multivariate data stored digital devices. As shown by the work of Kirsch et al. (1957), the raster data model was important for data analytics (via pattern recognition).

From an analytics perspective, the raster data model is desirable for many reasons. By viewing spatial phenomena in such a discretized fashion, data are stored as matrices that can be mathematically manipulated and analyzed with minimal computational requirements (Maguire, 1992). For instance, map algebra can be used to perform point operations (e.g., arithmetic and Boolean) and spatial operations (e.g., spatial interpolation and filtering) in a computationally efficient manner (Tomlin, 1990). Another major advantage of the raster data model is that its structure provides continuous coverage in the spatial extent at a resolution that is always explicitly defined by the size of the raster cells (Goodchild, 2011). In the context of HSI, this means that reflectance measurements can be related to spatial areas that continuously span large spatial extents (Bioucas-Dias et al., 2013; Maguire 1992). When HSI was established, landscape-

level and larger studies could only be conducted using the raster data model due to hardware and software limitations (Wade et al., 2003). Despite its obvious advantages in displaying multivariate data, the raster model is a heritage of the old computing era that may not be ideal for data analytics (Lim, 2008); more complex data formats may be permissible given current technologies. Thus, it is critical to re-evaluate the disadvantages of raster end products in HSI efforts.

By discretizing continuous spatial phenomena, the raster data model is a simplification of reality. Although this is advantageous in some respects, it does lead to various disadvantages. Firstly, both natural and non-natural features in the landscape cannot always be accurately represented by squares, especially at coarse resolutions (Fisher, 1997). For instance, even a simple line (e.g., from the edge of a building) is difficult to reconstruct with a string of pixels, especially when the direction of the line is not in one of the image x or y dimensions. In such situations, a simple line takes on a jagged stair-step configuration (Maffini, 1987). Secondly, coordinate transformations for raster end products are a non-trivial task and can introduce gridding artefacts that compromise data integrity (Tan et al., 2006). Finally, raster end products have large computer data storage requirements as raster sizes grow quadratically, not linearly (Bugya and Farkas, 2018). This can be problematic for programming languages that load data onto the computer memory during analysis (e.g., MATLAB).

2.5.2. The Vector Data Model

The vector data model is a popular alternative to the raster data model for representing spatial phenomena (Couclelis, 1992; Maffini, 1987; Wilkinson, 1996). In the vector data model, spatial phenomena are represented with coded points, lines and polygons (Maffini, 1987). Although the vector data model is typically concerned with representing spatial phenomena as objects with well-defined boundaries (Couclelis, 1992), it can also be used to represent continuous fields (Goodchild, 2011). Generally speaking, the vector model is more complex than the raster model. This added complexity presents both advantages and disadvantages over conventional rasters. As the vector data model does not store information in matrices, data processing is not nearly as computationally efficient (Wade et al., 2003). For instance, Wade et al. (2003) compared raster and vector methods for calculating landscape metrics used in the environmental assessments for approximately 1000 watersheds in Maryland and Washington, D.C. Given technological limitations at the time, raster approaches were up to 80 times faster than vector approaches but

less accurate. Without conforming to a uniform grid, measured quantities in vector data representations can be georeferenced more accurately (Kennedy and Meyers, 1977). Furthermore, the flexibility of the vector model allows complex spatial phenomena to be mapped more accurately (Jakubowski et al., 2013; Maffini, 1987; Wade et al., 2003). Another major advantage of the vector data model is that it allows for topological processing that manages spatial relationships between data points to minimize errors and extract information (Cox and Gifford, 1997).

The use of vector data products in the HSI literature has concentrated on point cloud representations where each spectral measurement captured by a sensor is coded as a point in space (e.g. Brell et al., 2019; Oliveira et al., 2019; Vauhkonen et al., 2013). Generally speaking, hyperspectral point clouds are less popular than their raster counterparts. In comparison to the 17432 peer-reviewed articles retrieved when searching ("hyperspectral image") on Scopus, only 15 results are obtained when searching ("hyperspectral point cloud"). Although these searches are not comprehensive, they show the difference in popularity between the use of the vector and raster data models in HSI. Brell et al. (2019) grouped hyperspectral point cloud generation methodologies into three main categories: (1) physical measurements with active hyperspectral LiDAR systems that collect simultaneous hyperspectral and surface elevation data (e.g. Hakala et al., 2012; Vauhkonen et al., 2013), (2) photogrammetric ranging from multiple full-frame hyperspectral images (e.g. Aasen et al., 2015; Oliveira et al., 2019) and (3) data fusion integrating conventional HSI data (from pushbroom, whiskbroom or snapshot sensors) and surface elevation data (typically from LiDAR or photogrammetric sources) (e.g. Brell et al., 2016; Brell et al., 2019; Buckley et al., 2013). Given current technological limitations, it is not feasible to collect high-quality spectral and elevation data with active hyperspectral LiDAR systems, especially at the fine spectral-spatial resolutions and high signal-to-noise ratios required for HSI applications (Brell et al., 2019). For instance, difficulties in radiometric calibration and beam alignment introduce significant challenges in field applications of active hyperspectral LiDAR systems (Calders et al., 2020; Disney et al., 2018). In photogrammetric ranging point cloud generation techniques, the necessity of multiple images with significant overlap requires substantial data storage. These data storage requirements can pose computational and operational difficulties, especially over large areas at fine spatial resolutions. Photogrammetric ranging techniques can also struggle in preserving spectral data integrity depending on how the spectral

information from each elevation point is selected (Aasen et al., 2015). Generally, it is the most logistically feasible to fuse separate surface elevation and HSI datasets to generate hyperspectral point clouds. Even in such approaches, it can be challenging to spectrally and spatially align the utilized datasets due to different sampling strategies, interaction with surface objects and fundamental differences in spectral-spatial point spread functions, illumination sources and viewing angles (Brell et al., 2016; Brell et al., 2017; Brell et al., 2019). Overall, many of the existing hyperspectral point cloud generation methods can be difficult to implement, computationally expensive and result in large file sizes. Furthermore, they can compromise the spatial-spectral integrity of the original HSI data set.

2.5.3. Effective Integration of the Vector Data Model in Hyperspectral Imaging

On a fundamental level, a hyperspectral point cloud is generated when the northing, easting and elevation of each pixel are calculated during the geometric correction. This vector information is rarely analyzed by end users, who are provided with the elevation removed, resampled HSI products in raster format. Overall, the widescale use of georeferenced raster end products are problematic as the rasterization process compromises data integrity. Section 2.4.5 discusses how rasterization via nearest neighbour resampling negatively affects HSI applications. However, issues in rasterization are not specific to the use of the nearest neighbour resampling technique. There is an abundance of studies in the geographic information systems literature that substantiate the loss of information content in all rasterization processes, regardless of resampling technique (e.g., Carver and Brunsdon, 1994; Congalton, 1997; Liao et al., 2012). For instance, Congalton (1997) studied the consequences of rasterizing simple geometric shapes by quantifying the change in area due to resampling. In this work, substantial errors were observed, even despite the simplicity of the shapes. In real-world applications where complexity is high (e.g., coastlines as discussed by Carver and Brunsdon (1994)), this information loss may be more significant and require fine spatial resolution. Overall, information loss due to rasterization is inherent; the individual squares that compose the raster data model oversimplify the complex observations made by each HSI pixel.

An interesting parallel can be drawn between the HSI and LiDAR literature concerning the highlighted issues in the use of the raster model. On a fundamental level, LiDAR data is collected as a vector-based point cloud. Through the use of point cloud specific analytical

techniques and software (e.g., cloudcompare (CloudCompare, 2022) and LAStools (Hug et al., 2004)), LiDAR data has been effectively used in a variety of remote sensing applications. For instance, Li et al. (2012) developed an algorithm to segment individual trees from a lidar airborne point cloud collected over a mixed conifer forest in the Sierra Nevada Mountains. Tree segmentation is important to forestry as it is critical to deriving structural attributes such as tree height, crown diameter and canopy-based height. In urban areas, Zhang et al. (2013) developed an object base classification algorithm to segment ground, buildings, powerlines, vehicles and vegetation with overall accuracy greater than 92.34 % across three different scenes (town center of Shenyang City in China, town of Enschede in the Netherlands and a residential area of Melbourne in Australia). Despite the effectiveness of point cloud specific analytical techniques, LiDAR point clouds are often spatially resampled by end users to derive raster-based end products (e.g., digital surface model, digital terrain model, canopy height model, digital elevation model) that are analyzed in place of the original point cloud due to fast processing speeds and the accessibility of image processing software in general (Zhang et al., 2015). The use of raster end products is problematic in LiDAR studies as interpolating the original point cloud data can introduce data artefacts that ultimately affect data applications (Smith et al., 2004; Suárez et al., 2005; Tiede et al., 2005). For instance, Jakubowski et al. (2013) compared vector- and rasterbased segmentation approaches for delineating individual trees using LiDAR data. The vectorbased approach used a point cloud segmentation algorithm, while the raster approach applied object-based image analysis to a derived canopy height model. The analysis showed that the vector-based segmentation approach produced fewer, more complex and larger tree polygons that more closely resembled real forest structures. This work was followed up by Zhang et al. (2015), who approximated crown size using the original LiDAR point cloud more accurately than studies that used raster LiDAR end products (Gill et al., 2000; Popescu and Wynne, 2004). Due to the acknowledged issues with the rasterized LiDAR end products, the point cloud data representation is favored in the literature. For instance, there are 4547 raster based studies in the LiDAR literature found on Scopus by searching ("lidar" AND ("digital elevation model" OR "digital surface model" OR "digital terrain model" OR "canopy height model")) in comparison to the 7231 vector-based articles found by searching ("lidar" AND "point cloud" ANDNOT "digital elevation model" ANDNOT "digital surface model" ANDNOT "digital terrain model" ANDNOT "raster" ANDNOT "canopy height model"). Overall, the LiDAR literature presents a

compelling case to avoid rasterization of vector-based point cloud data due to the errors introduced during spatial resampling that impede data applications.

Although the negative impacts of rasterization are broadly acknowledged in the spectrographic imaging community, there is very limited literature considering the use of vector end products as a solution to rasterization errors. Acknowledging the problems associated with rasterization, Kristóf and Pataki (2009) proposed a vector-based data product for MODIS multispectral data that used swath reflectance (MOD02) and geolocation (MOD03) products to calculate the footprint of each observation and to represent and process them as rectangular polygons. Importantly, this work avoided the rasterization process altogether and showed a precedent for improved data applications using vector end products. Kristóf (2015) expanded on this work, showcasing its practical importance for time series applications. A survey of the remote sensing literature shows that the developed data format has not been implemented past these studies. Although Duveiller et al. (2011) and Gomez-Chova et al. (2011) acknowledged the potential of the vector data representation, the approach was not widely adopted

2.6. Concluding Remarks

Over the last four decades, HSI technologies and data processing approaches (e.g., radiometric correction, atmospheric compensation, geometric correction) have advanced significantly (Jia et al., 2020). In these efforts, pushbroom sensors have become extremely prominent, making it possible to produce fine spatial and spectral resolution HSI data end products that cover large geographic extents with high signal-to-noise ratios. Data acquisitions must be carefully planned based on the limitations of the sensor and the desired characteristics of the resultant imagery. In mission planning, atmospheric conditions are of utmost concern as they substantially impact the uniformity and signal-to-noise ratio of the collected data. When processing hyperspectral data, the radiometric and spectral properties of the sensor need to be addressed so that the data can be related to real physical units such as wavelength and radiance. Although data processing can compensate for many undesirable characteristics of hyperspectral sensors (e.g., variation in the radiometric calibration, spectral smile, spatial keystone), it does not completely remove their presence from the imagery. As such, error detection methodologies (e.g., (Berk et al., 1999; Dadon et al., 2010; Guanter et al., 2006; Han et al., 2002) may be beneficial, especially when comparing spectra derived from different spatial pixels across the

field of view. Atmospheric compensation is fundamental to converting environmentally dependent radiance into reflectance. Before HSI data can be spatially analyzed, each hyperspectral pixel must be located via the geometric correction. After the geometric correction, HSI data is fundamentally representative of a point cloud data product as each spectrum is non-uniformly distributed in space. To account for this non-uniformity, rasterization is typically performed, generating a georeferenced raster end product.

Raster datasets have been the standard since HSI technologies were first developed as many of the earlier aerial and satellite-based spectral imaging systems digitally sampled all collected data, producing images with a raster structure based on pixels (Goetz, 2009; Vane et al., 1984; Wilkinson, 1996). When applying georeferenced raster data products, end users implicitly assume all image pixels are: 1) directly comparable, 2) square and 3) uniformly distributed across the image scene. These assumptions do not hold for real HSI data. Although there are reports that acknowledge the negative impacts of such assumptions, the raster data model is still standard in HSI remote sensing. Thus, it is critical to investigate these assumptions and their implications for data applications. It is also fundamental to reconsider the use of raster end products in favour of vector alternatives that do not make such implicit assumptions.

As defined in chapter 1, this thesis aims to investigate how raster end products misrepresent HSI data, presenting an alternative data representation that pushes the boundaries of HSI data analytics and application. Each of the three defined objectives relates to implicit assumptions that end users make when using raster HSI datasets. The first analytical chapter develops an error localization methodology that can be used to identify errors in HSI data and assess the comparability of pixels across the sensor field of view. The second analytical chapter investigates the consequences of assuming that pixels are square, exploring the significance of PSFs and their link to spatial and spectral variability in HSI data. This work is supported by Appendix 7.1, which showcases the importance of considering PSFs in flight planning, data fusion and data cross-validation. The final analytical chapter investigates the consequences of assuming that pixels are uniformly distributed in space, developing an alternative point cloud HSI data representation to overcome the limitations of the raster data model. This work is supported by Appendix 7.2, which provides the tools to generate the point cloud data model.

Table 2.1. Key words used in this literature review in addition to ("Remote* sens*" OR "hyperspectral" OR "multispectral")

Key Words	
atmospheric correction	point spread function
atmospheric compensation	pushbroom
calibration	radiometric correction
cross-validation	rasterization
data acquisition	snapshot
data models	spatial keystone
deconvolution	spectral response
direct georeferencing	spectral scanning
error detection	spectral smile
flight planning	validation
geometric correction	whiskbroom
gridding	spectral response
modular transfer function	
point cloud	

Connecting Statement (Chapter 2 to Chapter 3)

The second chapter provided the background literature required to complete the objectives of this thesis. Chapter 3 addressed objective 1, developing novel algorithms to localize errors in hyperspectral imaging data. The chapter uses the correlation coefficient as a similarity metric when identifying errors. The correlation coefficient is an ideal metric as it is widely utilized and understood in most scientific fields, making the developed algorithms more approachable for end users. Overall, the developed error localization algorithm was able to determine the effectiveness of various processing methodologies and the consistency of the spectral information collected across the sensor field of view. The chapter highlights imperfections in HSI data, showcasing the importance of analyzing data in its raw sensor geometry.

3. The Correlation Coefficient as a Simple Tool for the Localization of Errors in Spectroscopic Imaging Data

Deep Inamdar ^{1,2}, George Leblanc ^{1,2*}, Raymond J. Soffer ¹ and Margaret Kalacska ²

This chapter is published in *Remote Sensing*, 10, 231 under the terms and conditions of the Creative Commons Attribution (CC BY) license (http://creativecommons.org/licenses/by/4.0/).

Minor modifications have been made with respect to formating style.

DOI: https://doi.org/10.3390/rs10020231

Abstract

The correlation coefficient (CC) was substantiated as a simple, yet robust statistical tool in the quality assessment of hyperspectral imaging (HSI) data. The sensitivity of the metric was also characterized with respect to artificially-induced errors. The CC was found to be sensitive to spectral shifts and single feature modifications in hyperspectral ground data despite the high, artificially-induced, signal-to-noise ratio (SNR) of 100:1. The study evaluated eight airborne hyperspectral images that varied in acquisition spectrometer, acquisition date and processing methodology. For each image, we identified a uniform ground target region of interest (ROI) that was comprised of a single asphalt road pixel from each column within the sensor field-of-view (FOV). A CC was calculated between the spectra from each of the pixels in the ROI and the data from the center pixel. Potential errors were located by reductions in the CCs below a designated

¹ Flight Research Laboratory, National Research Council of Canada, Ottawa, ON K1A 0R6, Canada; deep.inamdar@mail.mcgill.ca (D.I.); Raymond.Soffer@nrc-cnrc.gc.ca (R.J.S.)

² Applied Remote Sensing Laboratory, Department of Geography, McGill University, Montréal, QC H3A 0B9, Canada; margaret.kalacska@mcgill.ca

^{*} Correspondence: George.Leblanc@nrc-cnrc.gc.ca; Tel.: +1-613-998-3525; Fax: +1-613-952-1704

threshold, which was derived from the results of the sensitivity tests. The spectral range associated with each error was established using a windowing technique where the CCs were recalculated after removing the spectral data within various windows. Errors were isolated in the spectral window that removed the previously-identified reductions in the CCs. Finer errors were detected by calculating the CCs across the ROI in the spectral range surrounding various atmospheric absorption features. Despite only observing deviations in the CCs from the 3rd–6th decimal places, non-trivial errors were detected in the imagery. An error was detected within a single band of the shortwave infrared imagery. Errors were also observed throughout the visible-near-infrared imagery, especially in the blue end. With this methodology, it was possible to immediately gauge the spectral consistency of the HSI data across the FOV. Consequently, the effectiveness of various processing methodologies and the spectral consistency of the imaging spectrometers themselves could be studied. Overall, the research highlights the utility of the CC as a simple, low monetary cost, analytical tool for the localization of errors in spectroscopic imaging data.

Keywords: imaging spectroscopy, hyperspectral, correlation coefficient, error detection, data quality assessment

3.1. Introduction

In imaging spectroscopy, contiguous narrow-band spectrographic information is collected for each spatial pixel in an imaging system. The technology is presently synonymous with hyperspectral imaging (HSI) and is commonly implemented within the discipline of remote sensing to characterize the physical and chemical properties of observed materials. This is performed via spectroscopic and spatial analysis methodologies (Green et al., 1998). Imaging spectroscopy technologies have shown their utility in numerous remote sensing applications in geology (Cloutis, 1996; Murphy et al., 2012; van der Meer et al., 2012), defense (Xu and Wang, 2007; Yuen and Richardson, 2010), agriculture (Dale et al., 2013; Migdall et al., 2012; Yao et al., 2011), forestry (Koch, 2010; Peng et al., 2003; Smith et al., 2003), oceanography (Chang et al., 2004; Kruse et al., 1997; Ryan et al., 2014), forensics (Kalacska and Bell, 2006; Kalacska et al., 2009; Leblanc et al., 2014) and ecology (Chambers et al., 2007; Ryan et al., 2014; Turner et al., 2003), among others. In theory, spectrographic imaging data are spectrally and spatially piece-wise smooth; neighboring locations and wavelengths are well-correlated due to the high

spatial-spectral resolution allowed by the narrow band criterion (Bioucas-Dias et al., 2013; Camps-Valls et al., 2011).

With such an abundance of information, the processing and analysis of HSI data are not trivial. Relevant spectral signatures are often difficult to identify, especially given the presence of signal noise, which further impedes information extraction (Plaza et al., 2011). Spatial and spectral correlations can be exploited to aid in the analysis of imaging spectroscopy data with a correlation metric. The Pearson product-moment correlation coefficient (CC) is one of the simplest statistical tools that has been widely implemented to measure levels of correlation (Lee Rodgers and Nicewander, 1988).

The CC is a measure of linear association between two variables. It is formally given (Lee Rodgers and Nicewander, 1988) by Equation (1):

$$CC = \frac{\sum (x - \bar{x})(y - \bar{y})}{\sqrt{\sum (x - \bar{x})^2 \sum (y - \bar{y})^2}}$$
(1)

where x, y, \bar{x}, \bar{y} represent the two variables of interest and their means, respectively. In mathematical terms, the CC represents the sum of the centered and normalized cross-product of x and y (Lee Rodgers and Nicewander, 1988). Each variable is centered by removing its mean. The denominator normalizes the numerator by the variance of the studied variables. Using the Cauchy–Swartz inequality, it can be shown (Lee Rodgers and Nicewander, 1988) that the numerator is always less than or equal to the denominator. Therefore, the value of the CC is bounded between -1 and 1. The boundary values represent a perfect linear correlation between x and y. A value of zero corresponds to no linear correlation between the variables. Values greater than zero indicate a positive correlation between the variables of interest; the opposite is true for values less than zero. The CC is a useful descriptive measure of correlation since its value does not depend on the scales of measurement for the studied variables (Lee Rodgers and Nicewander, 1988). It is important to note that the calculation of the CC is not limited by any statistical assumptions; however, its value as an input to other statistical metrics may need to conform to certain restraints (e.g., normally-distributed data).

To date, the CC has been widely implemented to investigate spectrographic imaging data (Clarisse et al., 2010; Du and Yang, 2008; ElMasry et al., 2007; Huang and He, 2005;

Koponen et al., 2002; Lu and Peng, 2006; Peng et al., 2003; Qiao et al., 2007; Richter et al., 2011; Tanabe and Saeki, 1975; Thiemann and Kaufmann, 2002; Toivanen et al., 2005). In these efforts, the literature has concentrated on applying the statistical tool to establish bands that linearly associate with quantifiable physical and chemical properties. Exploiting the linear relation, this method of band selection has been used to create and improve predictive models that associate hyperspectral data with useful parameters (Clarisse et al., 2010; Du and Yang, 2008; ElMasry et al., 2007; Huang and He, 2005; Koponen et al. 2002; Lu and Peng 2006; Peng et al. 2003; Qiao et al. 2007; Thiemann and Kaufmann 2002). For example, Peng et al. (2003) applied the CC to establish bands that strongly correlate with forest leaf area index, improving predictive models at the landscape level. To a lesser extent, the CC has been applied for the purposes of data reduction and correction (Du and Fowler, 2007; Huang and He, 2005; Richter et al., 2011; Toivanen et al., 2005). In 2011, Richter et al. (2011) outlined a corrective method for HSI data that relied, in part, on the CC. The correction accounted for the effects of the spectral smile, a spectral non-uniformity in the across track direction that is caused by the optical design of the spectrometer and results in per pixel changes in wavelength registration across the fieldof-view (FOV) (Richter et al., 2011). In the study, the CC was used to measure uniformity levels across the FOV, indirectly assessing the effects of the spectral smile defect. A corrective solution was selected by maximizing this metric. From this application, the CC was shown to be a useful tool in the assessment of HSI data. Following this example, the CC can be used for the detection and quantification of other errors. This was exemplified by Tanabe and Saeki (Tanabe and Saeki, 1975), who rigorously quantified the sensitivity of the CC to spectral shifts in infrared spectra. Such research was fundamental to the application of the CC for error detection in infrared spectroscopy. Unfortunately, the findings were somewhat limited in their application to hyperspectral remote sensing as the study was conducted in an ideal environment with a laboratory-grade spectrometer. Earth observation (EO) remotely-sensed measurements are most often collected with airborne spectrometers under less than the ideal conditions. Before the CC can be confidently applied to hyperspectral EO data, the sensitivity of the tool needs to be characterized with respect to various potential errors and noise levels.

The purpose of this study was to use the CC to develop an easy to implement methodology to detect issues with HSI data. The methodology was intended explicitly for the detection of errors, not for the identification of their origin. Although other error detection methodologies exist

(e.g., Dadon et al., 2010; Guanter et al., 2006; Han et al., 2002; Tan and Acharya, 1999), they can be expensive to implement and rely on a higher level of mathematical understanding. To develop a novel method, the CC was first characterized with respect to artificially-induced errors in ground data. Afterwards, this information was applied to locate the spatial location and spectral bands associated with errors in real HSI data. The overall objective of this study was to substantiate the CC metric as a low monetary cost, robust and simple statistical tool in the quality assessment of EO HSI data through the detection of errors.

3.2. Materials and Methods

3.2.1. In-Situ Ground Hyperspectral Data

In-situ hyperspectral radiance measurements were collected on 23 June 2016, from 16:54:19–17:00:36 GMT with a Spectra Vista Corporation (Poughkeepsie, NY, USA) HR-1024i ground spectrometer at the Flight Research Laboratory of the National Research Council of Canada (NRC) under stable illumination conditions (**Figure 3.1**). The HR-1024i is a solid-state device that collects radiance data in a circular FOV. The device collects spectral data over 1024 spectral bands, which are non-uniformly distributed between 350 and 2500 nm using three independent detectors: a single 512-chanel silicon photodiode array and two 256-channel indium gallium arsenide arrays. The three detectors are characterized by nominal spectral resolutions of \leq 3.5 nm (340 nm–1014 nm), \leq 9.5 nm (971 nm–1911 nm) and \leq 6.5 nm (1897 nm–2523 nm), respectively. In this study, spectral measurements were acquired with a 4° FOV fore-optics from a height of 1 m at 10 different locations on an asphalt target. Each measurement covered a single 38.3 cm² segment of asphalt that was contained within the area imaged by the airborne HSI systems (ITRES Research Limited, Calgary, AB, CA) described in Section 3.2.2. The in-situ datasets were used to provide ground truth measurements for the characterization of the CC.

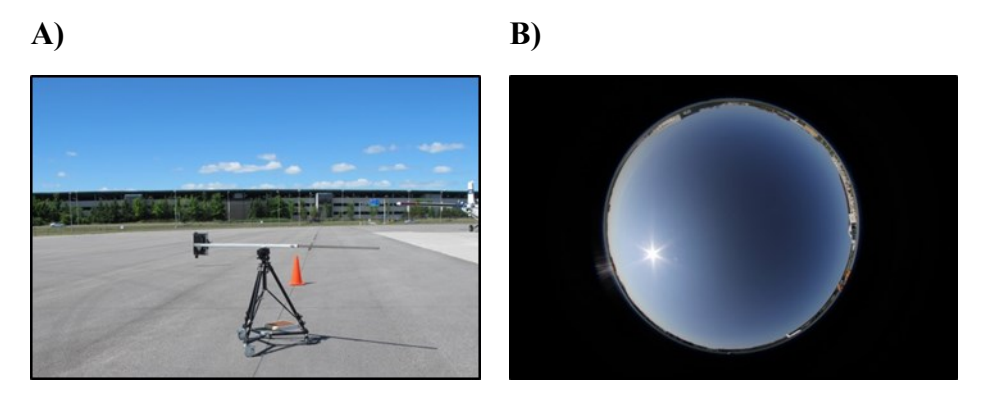


Figure 3.1. A) Experimental setup for acquiring in-situ ground hyperspectral measurements of an asphalt target using the HR-1024i spectrometer. B) The hemispherical sky photo was acquired simultaneously with the ground spectrometer measurements as a means of estimating the potential influence of cloud and visible aerosol (haze) during the time of data acquisition. All data were collected under stable conditions.

A wavelength (λ)-dependent, interpolated and normalized mean in-situ radiance spectrum for asphalt, $R(\lambda)$, was derived from the collected ground measurements for use in Section 3.2.3. In particular, ten asphalt radiance spectra were averaged, normalized by the maximum and then resampled at 0.1 nm intervals using the Akima interpolation method (Akima, 1969) to produce the "true" spectral signature of asphalt to be used in the characterization phase of the CC tool. The Akima interpolation method was selected due to its robust ability to provide a smooth interpolation that closely matched the original input signal (Akima, 1969). The spectrum was interpolated to place $R(\lambda)$ on a uniform wavelength array and increase the density of spectral information while preserving the overall shape and content of the original signal.

3.2.2. Airborne Hyperspectral Image Acquisition and Processing

Airborne HSI data were acquired on 23 June 2016 at 14:53:13 GMT and 24 June 2016 at 13:24:16 GMT over the Macdonald–Cartier International Airport (containing the Flight Research Laboratory calibration site) in Ottawa, Ontario, Canada (**Figure 3.2**). Asphalt is an ideal target for real airborne acquisition as it is effectively ubiquitous in urban settings and can be found on the roadway systems surrounding the studied area. Furthermore, the surface reflectance of the material has a low amplitude (nearly flat), smoothly varying spectral response and is thus useful for in-field pseudo-calibration and validation (Puttonen et al., 2009).



Figure 3.2. Study site at the Macdonald–Cartier International Airport in Ottawa, Ontario, Canada. The flight line followed a 306.5° True North path as shown by the blue arrow. Ground calibration measurements were taken on the asphalt surface located by the red X.

Airborne imaging spectrometry data were acquired aboard the NRC's Twin Otter fixed-wing aircraft with two complimentary HSI systems. The imagers each recorded an adjacent and partially-overlapping portion of the reflective electromagnetic spectrum between 366 nm and 2530 nm. Both imagers were manufactured by ITRES Research Limited. The first sensor system, the Compact Airborne Spectrographic Imager 1500 (CASI), acquired 288 bands (wavelength samples) within the 366–1053 nm range. The CASI is a variable frame rate, grating-based, pushbroom imager with a 39.7° FOV across 1500 spatial pixels. The device has a 0.49-mrad instantaneous FOV with a variable f-number aperture, configurable between 3.5 and 18.0. The second imaging system was the Shortwave Airborne Spectrographic Imager (SASI). The SASI is a prism-based pushbroom imager that acquires data from 160 spectral bands within the 885–2530 nm range with 640 spatial pixels across a 39.8° FOV. The device has an instantaneous

FOV of 1.14 mrad and an aperture with a constant f-number of 1.8. Imagery is acquired at a fixed frame rate of 60 hertz with a programmable integration time of \leq 16.6 ms. On both data acquisition days, imagery was obtained from a nominal height of 1115 m AGL with an approximate heading of 306.5° True North (**Figure 3.2**).

Prior to CC analysis, the HSI data underwent three pre-processing steps. The first step was a correction in the calibration to take into consideration the effects of small, but measurable pressure and temperature-induced shifts in the spatial-spectral sensor alignment. The second step was a spectroradiometric calibration that, following removal of estimated signal offset contributions (electronic offset, dark current, frame shift smear (CASI only), internal scattered light (CASI only) and 2nd order (CASI only)), converted the resulting radiance-induced digital pixel signal into units of spectral radiance (uW·cm⁻²·sr⁻¹·nm⁻¹). The final step was implemented to remove the laboratory-measured spectral smile by resampling the data from each spatial pixel to a uniform wavelength array. Although most of the spectral smile effects are removed by this pre-processing, extremely small residual effects may remain. Geocorrection of the data was not performed in order to preserve the original spectral response per pixel.

The described pre-processing methodologies utilized NIST traceable calibration data provided by the sensor manufacturer. Using the initial calibration data, various artefacts were identified in the resulting calibrated imagery. Independent of this study, the processing methodology was updated to refine the steps described above, resulting in new calibration programs and calibration data files. This refined processing removed many of the identified artefacts in the data. The CC analysis was performed on the raw imagery after being processed with both the initial and refined calibration files and methodologies. Overall, the study examined 8 datasets: the four raw hyperspectral images collected by the CASI and SASI over the two acquisition dates processed with both the original and refined processing methodologies.

3.2.3. Characterization of the Correlation Coefficient with Averaged and Interpolated in-Situ Radiance Hyperspectral Data

Before the CC was applied to the airborne imagery, the sensitivity of the statistical tool needed to be characterized with respect to the natural variances within asphalt spectra. This was accomplished by calculating the CC between each of 10 raw in-situ hyperspectral radiance measurements and their averaged spectral response.

The sensitivity of the CC to common signal issues in HSI data was also characterized by artificially inducing errors in $R(\lambda)$, the spectral response derived in Section 3.2.1. Five artificial errors were introduced independently by modifying $R(\lambda)$ in accordance with **Table 3.1** to generate a variety of transformed signals, $R_t(\lambda)$. The following modifications were applied: introduction of additive white Gaussian noise (AWGN), additive transformation, multiplicative transformation, introduction of spectral shift and multiplicative transformation of a single feature. The transformation models in **Table 3.1** were developed to mediate the desired modifications. Parameters were carefully selected to mimic realistic potential errors. The AWGN modification was applied to generate a transformed spectral response with a specified signal-tonoise ratio, SNR. SNR designates the ratio between the energy of the original signal and the generated noise. For example, to obtain an SNR of 100:1, 4.31% AWGN was added to the signal. β , γ and Δ represent the additive factor, multiplicative factor and spectral shift (in nm), respectively, used to carry out each modification. Although there was no reason for the additive and multiplicative modifications to influence the CC, these tests were included to help provide a clear understanding of the approach. The multiplicative transformation of a single spectral feature was mediated through a normal distribution scaled by α and vertically shifted with a minimum value of 1. σ and μ corresponded to the standard deviation and mean values, respectively, of the distribution. A normal distribution was used for the multiplicative factor to ensure the feature remained continuous along the edges of the spectral feature. μ was selected to capture the atmospheric absorption feature centered at 935 nm. The σ of 12 nm was chosen to ensure that the shoulders of the feature between 899 nm and 971 nm were within 3σ of μ . α was varied from 1–50 to control the degree to which the absorption feature was modified.

Table 3.1. The five modifications applied to $R(\lambda)$ to generate the transformed signal, $R_t(\lambda)$.

Modification	Transformation Model	Data Parameters	
Introduction of Additive White Gaussian Noise	$R_t(\lambda) = R(\lambda) + AWGN$	$SNR = \frac{\sum R(\lambda) ^2}{\sum AWGN ^2},$ $\{SNR SNR\epsilon\mathbb{Z}, 1 \le n \le 1000\}$	
Additive Transformation	$R_t(\lambda) = R(\lambda) + \beta$	$\beta = \frac{n}{100} , \{n n\epsilon \mathbb{Z}, 0 \le n \le 100\}$	
Multiplicative Transformation	$R_t(\lambda) = \gamma R(\lambda)$	$\gamma = \frac{n}{100},$ $\{n n\epsilon\mathbb{Z}, 50 \le n \le 150\}$	
Introduction of Spectral Shift	$R_t(\lambda) = R(\lambda - \Delta)$	$\Delta = \frac{n}{10}$, $\{n n\epsilon\mathbb{Z}$, $0 \le n \le 100\}$	
`Multiplicative Transformation of a Single feature	$R_t(\lambda) = \left(\alpha \frac{e^{-(\lambda-\mu)^2/2\sigma^2}}{\sigma\sqrt{2\pi}} + 1\right) R(\lambda)$	$\sigma = 12, \mu = 935,$ $\{\alpha \alpha \in \mathbb{Z}, 1 \le \alpha \le 50\}$	

The tested ranges of values for SNR, β , γ and Δ were selected to introduce nominal to substantial errors. The CC was calculated between $R(\lambda)$ and each of the transformed datasets, $R_t(\lambda)$, in accordance with **Figure 3.3**.

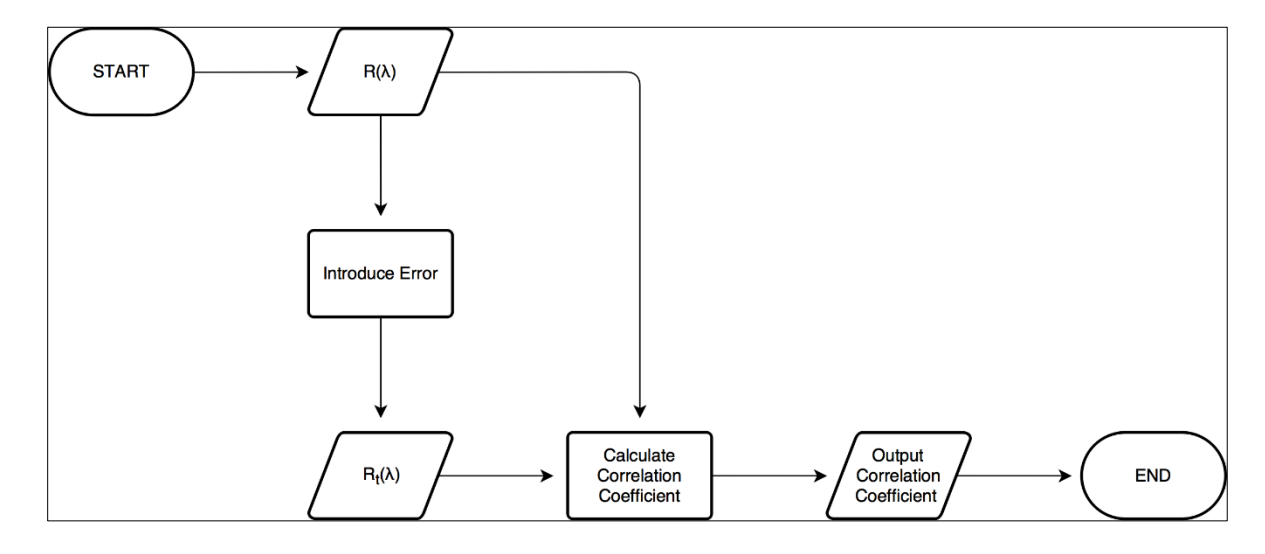


Figure 3.3. Schematic view of the basic algorithm for the characterization of the CC.

To test the persistence of the acquired trends with the presence of signal noise, the CC calculations for the last four modifications were repeated with AWGN. In particular, 4.31% AWGN was introduced to $R(\lambda)$ to acquire a new radiance signal, $R_{AWGN}(\lambda)$, with an SNR of 100:1, a reasonable value for airborne HSI data. A new transformed signal, $R_{t\,AWGN}(\lambda)$, was acquired by applying transformation models from the last four rows of **Table 3.1** to $R(\lambda)$ after introducing AWGN to generate a signal with an SNR of 100:1. The CC was calculated between $R_{AWGN}(\lambda)$ and each $R_{t\,AWGN}(\lambda)$ in accordance with **Figure 3.4**.

As a final test of consistency, the standard deviation of the CC was assessed in the presence of noise. In particular, the AWGN transformation in **Table 3.1** was applied to $R(\lambda)$ 1000 times. A CC was calculated between $R(\lambda)$ and each of its transformations. The standard deviation of the CCs from each distinct SNR was calculated.

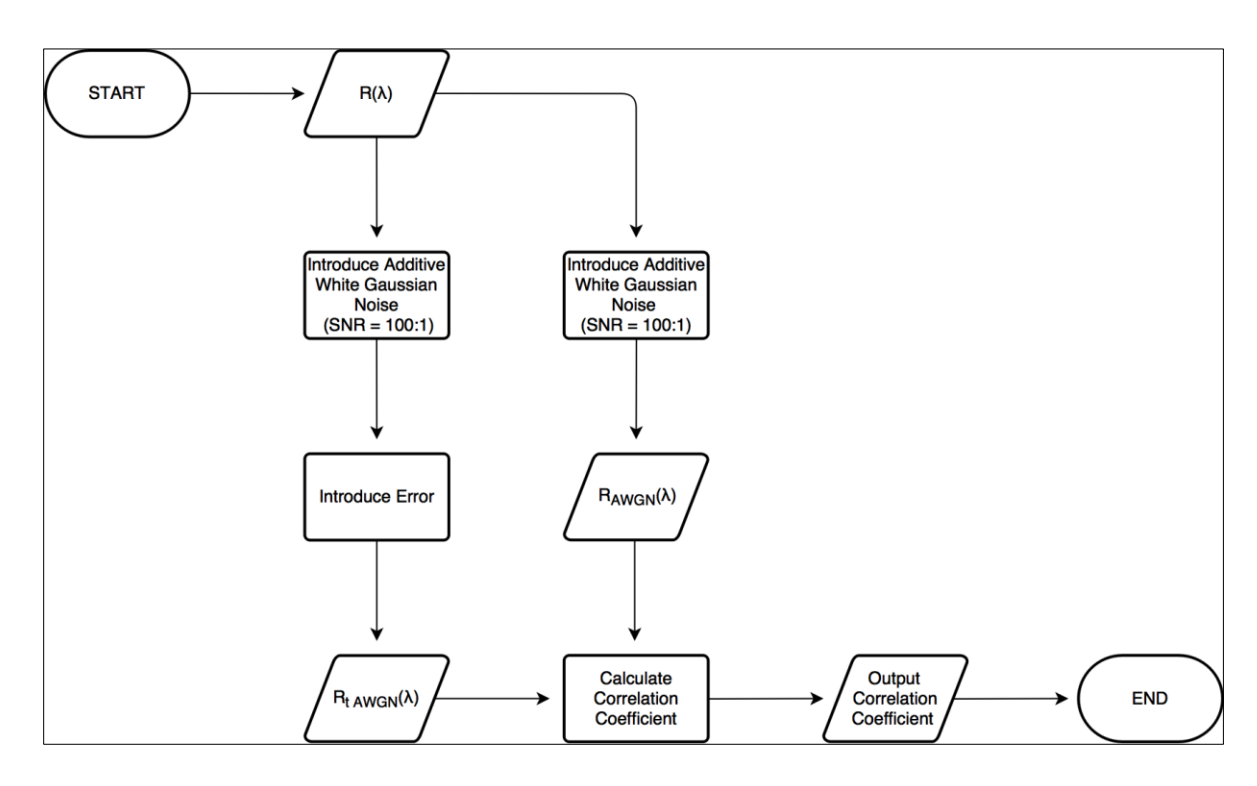


Figure 3.4. Schematic view of the basic algorithm for the characterization of the CC in the presence of signal noise.

3.2.4. Application of the Correlation Coefficient to Airborne Hyperspectral Imagery (Error Detection)

Before applying the CC, a region of interest (ROI) (blue line in **Figure 3.5**) was identified across the FOV, along the taxiway located directly south of the calibration site. The ROI was comprised of a single asphalt road pixel from each column within the sensor FOV. Every attempt

was made to acquire spectra from asphalt pixels that were uncontaminated by non-asphalt substances such as paint, vegetation and other non-asphalt hydrocarbons. "Wobbles" in the imagery in **Figure 3.5** are caused by the movement of the aircraft and can be readily accounted for through various geocorrective methodologies. In this work, it was fundamental to preserve the original sensor geometry in the analysis, so no geocorrection process was applied.



Figure 3.5. Non-geocorrected CASI imagery of the data acquisition site. The blue line indicates the ROI selected for the analysis. The ROI contained a single pixel from each column across the asphalt road. Ground calibration measurements were taken on the asphalt surface located by the red X, in accordance with **Figure 3.2**.

The spectrum from the center asphalt pixel in the ROI was designated as the reference for the application of the CC since it was the center of the instruments' FOV. The center pixel was evaluated to ensure that it was a reasonable reference that contained no obvious errors. A CC was calculated between the spectrum from each pixel in the ROI and the designated central pixel reference in accordance with **Figure 3.6**.

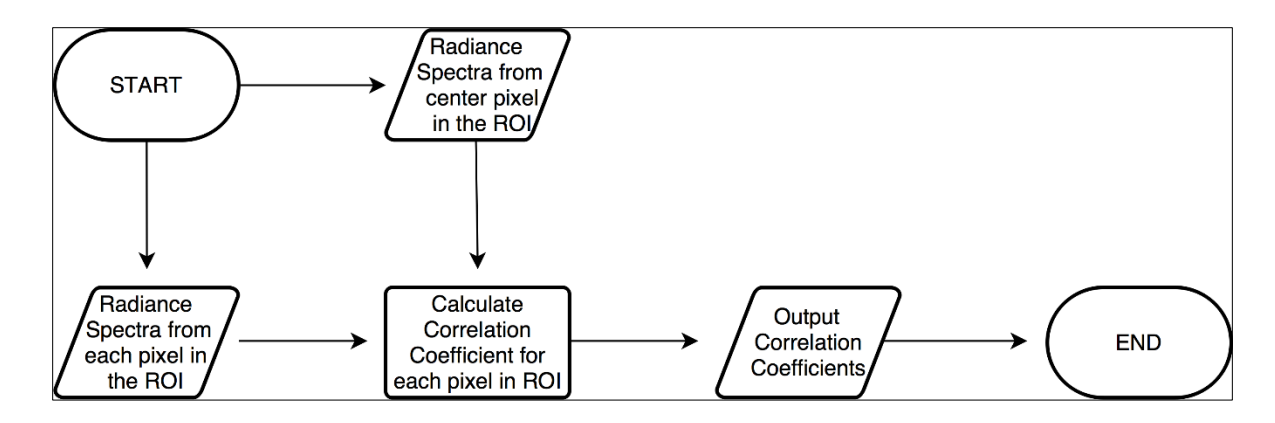


Figure 3.6. Schematic view of the basic algorithm for the application of the CC in the spatial localization of errors in HSI data.

Theoretically, the CCs should be exactly 1 across the FOV. Although this is not the case in real data, the CC between well-behaved target spectra will vary around a mean value that is still quite close to 1. The spatial pixels associated with substantial reductions in the CCs were recorded as potential locations for errors in the HSI data. Substantial reductions were characterized by CCs that fell below a designated threshold that was derived from the sensitivity testing.

To calculate the threshold, a stable spatial region was manually identified by consistent CCs that varied around a constant mean. Using the mean CC of this region, the SNR of a stable spectrum was approximated using the noise sensitivity data derived in Section 3.2.3. With the approximate SNR, the data from the final test in Section 3.2.3 were used to estimate the expected standard deviation of the CCs derived from stable spectra. Using the estimated standard deviation and the mean value of the CCs in the stable region, potential errors were detected by reductions more than 3σ below the mean. A 3σ threshold was selected to ensure that at least 99.7% of the stable data were not flagged as a potential error. Consequently, CCs below the threshold were likely associated with errors in the HSI data.

To spectrally isolate the potential errors in the recorded spatial locations, the CCs across the ROI were recalculated after removing the data in pre-defined spectral windows. The schematic in **Figure 3.7** was carried out for various spectral windows. The spectral windows were designed to vary in size and spectral location. The window sizes were selected to ensure that windows contained anywhere from 1 to half of the total spectral bands. For any given size, the window was spectrally located beginning at the lower boundary of the spectral range. Each window was

shifted by 5 nm until its edge surpassed the upper boundary of the dataset. For each window size and location, the average CC was calculated across the spatial regions associated with the detected potential errors. By maximizing the average CC over these regions, it was possible to identify the spectral window that was associated with a majority of the studied potential error.

To verify the spectral window and specify the nature of the potential errors, the imagery was visualized for a single band within the identified spectral ranges. In this visualization, image intensities were histogram equalized to enhance contrast by making the histogram of the resulting image equalized to a constant value. To verify that the reductions in the CCs were associated with these errors, the CCs were calculated across the FOV with respect to the center pixel after the removal of the identified spectral region.

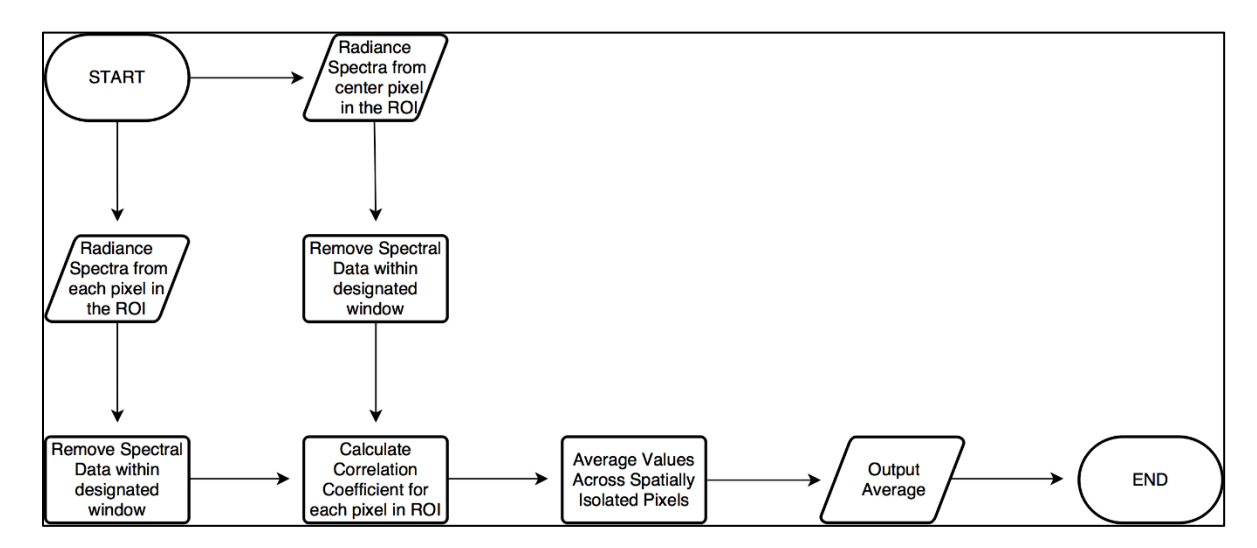


Figure 3.7. Schematic view of the basic algorithm for the application of the CC in the spectral localization of errors in HSI data.

Atmospheric absorption features were used to locate finer errors in the imagery that might not be easily visible in the CCs when calculated with the entire spectrum. These features were manually identified in the spectrum of the center asphalt pixel using the theoretical locations in **Table 3.2** for guidance.

Table 3.2. The approximate spectral location of known atmospheric absorption features (Pallé et al., 2009). It is important to note that the wavelength ranges for some atmospheric absorption features may vary in response to external factors. For instance, the range of the water absorption features is highly dependent on water vapor and aerosol optical thickness (King et al., 1992).

Source	Start Wavelength (nm)	End Wavelength (nm)
O ₂	686	695
H_2O	713	734
O_2	757	770
H_2O	806	840
H_2O	888	997
H_2O	1087	1176
O_2	1223	1285
H_2O	1300	1521
CO_2	1591	1620
H_2O	1759	1982
CO_2	1991	2038
CO_2	2037	2079
CH ₄	2139	2400

Atmospheric absorption features are distinctive and constant under stable conditions (Bogumil et al., 2003). As such, the CC was thought to be able to detect inconsistencies in these regions since error-induced changes located within these features are more easily identifiable. As depicted in **Figure 3.8**, a CC was calculated between the spectrum from each pixel in the ROI and the designated central reference pixel using only the hyperspectral data that corresponded to each of the approximate wavelength regions identified in **Table 3.2**.

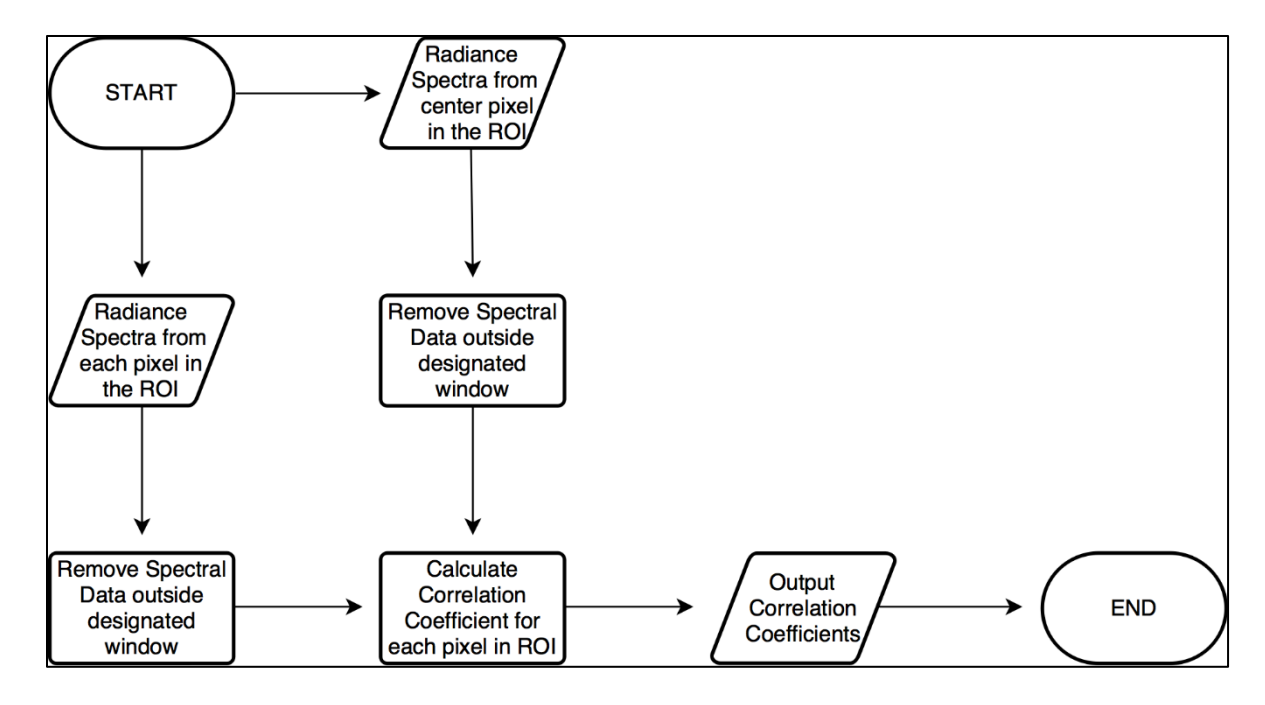


Figure 3.8. Schematic view of the basic algorithm for the application of the CC in the localization of finer errors in HSI data.

For each spectral range, the imagery was visualized for a single band within the specified window to study the nature of any detected errors. Once again, image intensities were histogram equalized to enhance contrast and clearly display potential errors. The methodologies presented in this section were repeated for each of the 8 processed images described in Section 3.2.2.

3.3. Results

3.3.1. In-Situ Ground Hyperspectral Data

The data points in the normalized and averaged in-situ radiance signature were preserved after the Akima interpolation process was applied to generate $R(\lambda)$ (**Figure 3.9**).

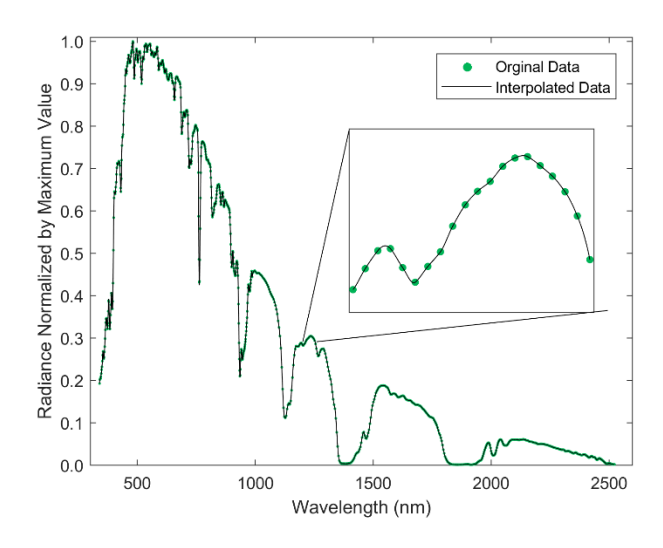


Figure 3.9. Averaged and normalized ground spectrum of asphalt before and after interpolation. The differences between the two curves can be seen in the subplot, which zooms in on the 1185–1255 nm spectral window. The interpolated curve, $R(\lambda)$, was used for the methodologies described in Section 3.2.3. The mean squared error between overlapping data points before and after interpolation was negligible ($<10^{-30}$). The Akima interpolation method generated a qualitatively smooth $R(\lambda)$.

3.3.2. Characterization of the Correlation Coefficient with Averaged and Interpolated in-Situ Radiance Hyperspectral Data

The CC between the mean in-situ asphalt radiance and any given individual sample used to comprise the mean signal was very close to one, ranging from 0.99987–0.99998, with a standard deviation of 0.000023.

The CCs between $R(\lambda)$ and each of the transformed datasets outlined in **Table 3.1** are recorded in **Figure 3.10**.

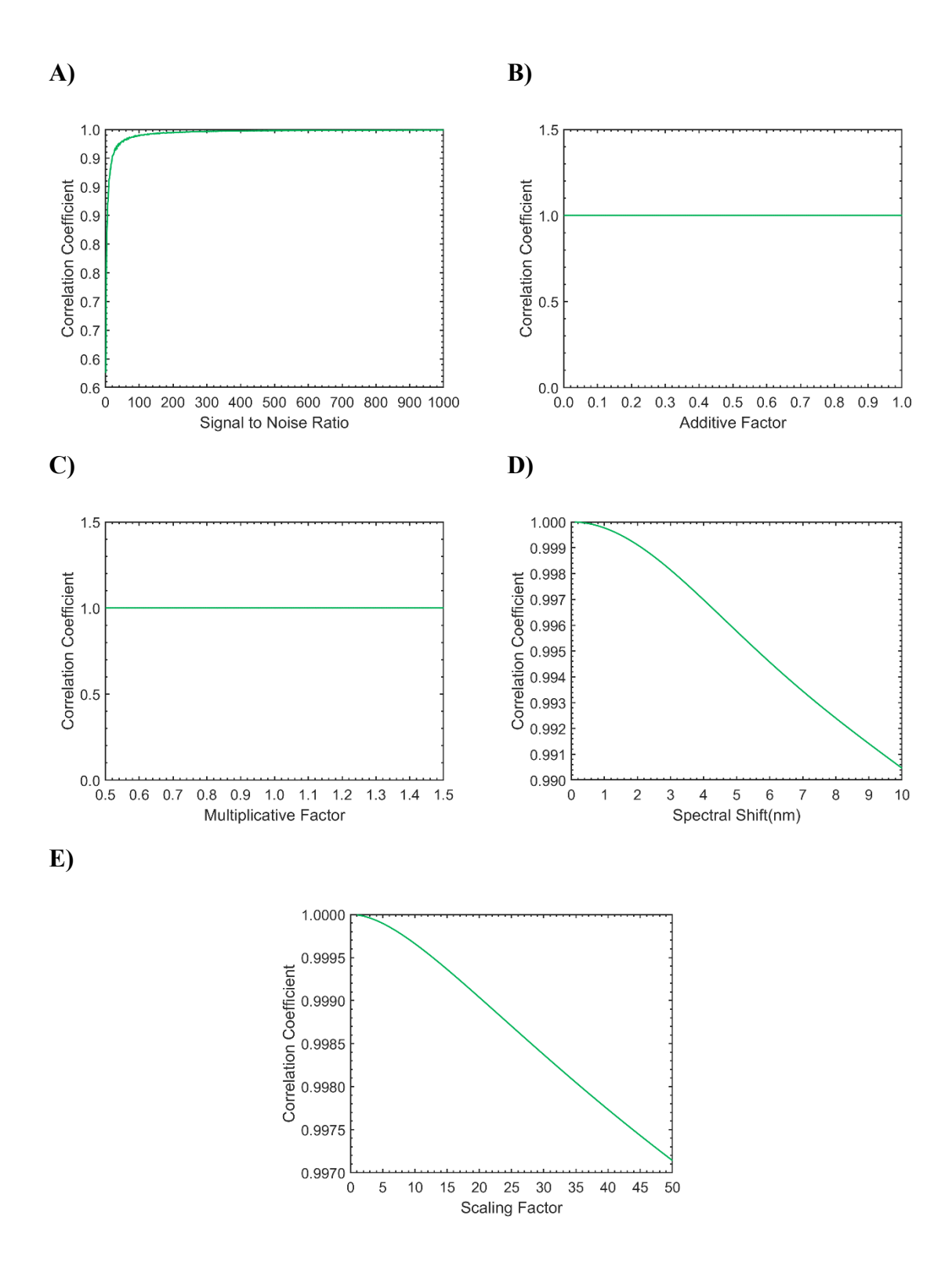


Figure 3.10. The CC between $R(\lambda)$ and each of the transformed datasets, $R_t(\lambda)$. A) The CC asymptotically reduced from one when the SNR decreased through the introduction of AWGN. B) The CC was invariant to additive transformations. C) Multiplicative transformations had no impact on the CC. D) The introduction of a spectral shift resulted in a small but clear decrease

in the CC. **E)** The multiplicative transformation of a single feature was detected in the CC by a gradual reduction.

The CC decreased with the addition of AWGN (**Figure 3.10A**). At SNR values below 9:1, the CC was under 0.9. As the SNR increased, the CC raised in an asymptotic fashion. After reaching an SNR of 1000:1, the CC equilibrated at approximately one. The CC remained constant at one for all linear transformations (**Figure 3.10B,C**). As the spectral shift increased from 0–10 nm, the CC decayed from a value of 1–0.991 (**Figure 3.10D**). A similar result was found after the atmospheric absorption feature at 935 nm was modified. In this case, the CC reduced from one to a value of 0.9970 as the scaling factor increased (**Figure 3.10E**).

As can be seen in **Figure 3.11**, the general trends outlined in **Figure 3.10B,E** persisted even after the application of AWGN at an SNR of 100:1.

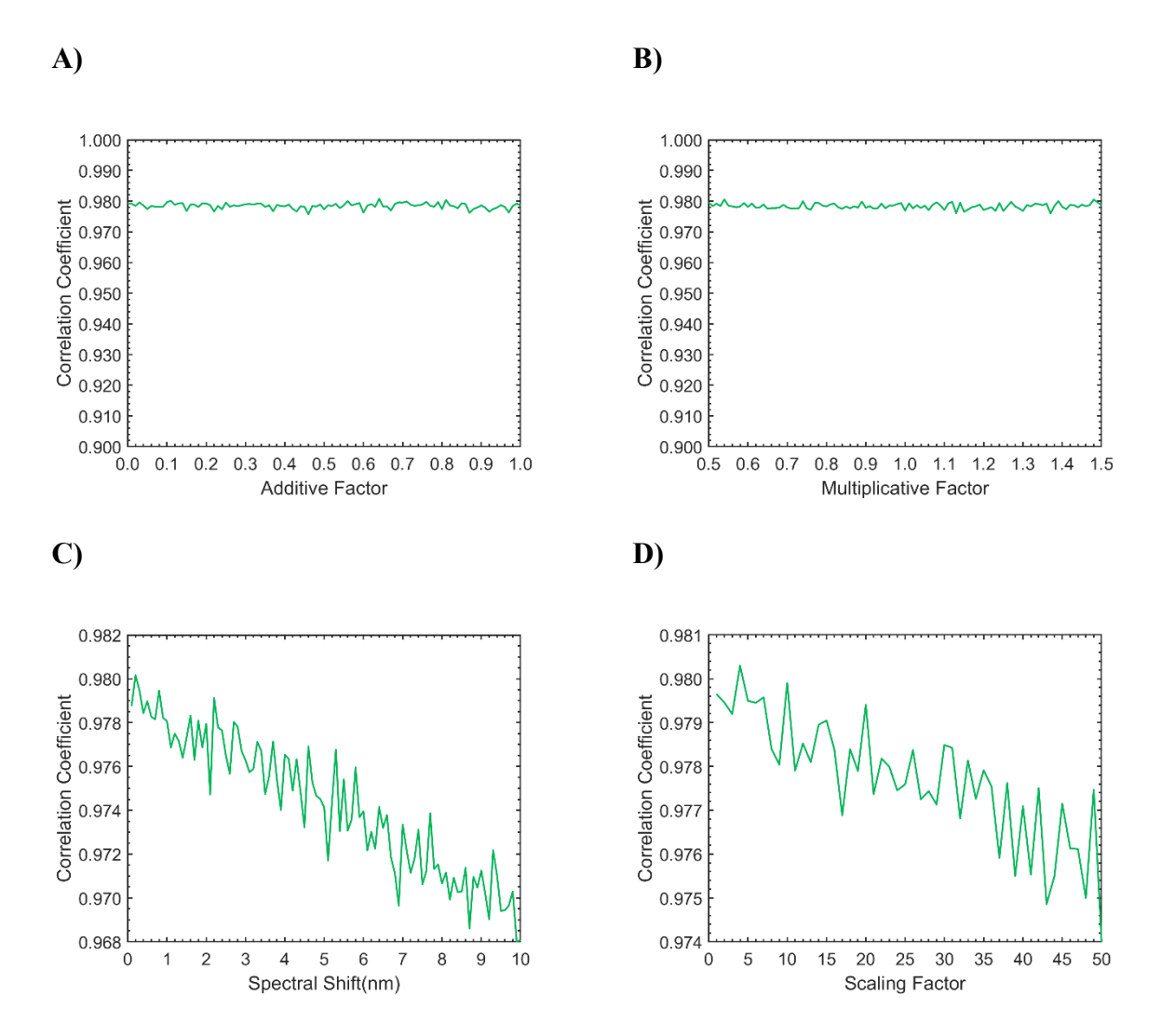


Figure 3.11. The CC between $R_{AWGN}(\lambda)$ and each of the transformed datasets, $R_{t\ AWGN}(\lambda)$. All signals were characterized by an SNR value of 100:1. The trends from Figure 3.10 persisted, despite being masked by the noise to some degree. A) The CC was invariant to the additive transformation. B) Multiplicative transformations had no impact on the CC. C) The introduction of a spectral shift resulted in a small, but clear decrease in the CC. D) The multiplicative transformation of a single feature was detected in the CC by a gradual reduction.

The CC remained invariant to linear transformations (**Figure 3.11A,B**). However, the average value of the CC reduced to approximately 0.98. Although the detailed relationships in **Figure 3.11C,D** were masked by the variation induced by the introduced noise, the first-order trends are clearly present and identifiable. The CC reduced from 0.980–0.968 after a 10 nm spectral shift in **Figure 3.11C**. As the scaling factor increased from 0–50, the CC decreased from 0.9815–0.975. At an SNR of 100:1, the average standard deviation in the CC for each modification was approximately 0.001. As seen in **Figure 3.12**, this value matched the results

derived from the final CC test, which calculated the standard deviation in the calculated CC at various noise levels.

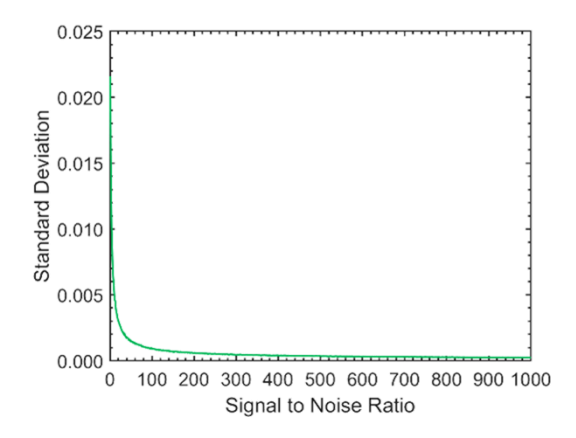


Figure 3.12. The standard deviation of the CCs at various noise levels. There was an asymptotic increase in the standard deviation of the CCs when the SNR decreased through the introduction of AWGN.

At a SNR of 100, the standard deviation is approximately 0.001. The standard deviation in the CC asymptotically increased from zero to approximately 0.22 when the SNR decreased through the introduction of AWGN.

3.3.3. Application of the Correlation Coefficient to Airborne Hyperspectral Imagery (Error Detection)

For each hyperspectral image, the calculated CCs recorded in **Figure 3.13** adhered very closely to one across the FOV when calculated with respect to the spectrum from the center pixel. The CCs for the CASI imagery were consistently lower than that of the SASI by an average value of 0.0021 (**Figure 3.13**). In addition, the average standard deviation in the CCs of the CASI data was over 18-times larger than that of the SASI.

For the CASI imagery, the CCs systematically reduced in value by more than one standard deviation near the edges of the FOV. This reduction was largest for the CASI data derived from the original processing methodology. When compared to the imagery collected on the 23rd, the CASI data from the 24th were characterized by more substantial reductions in the CCs near the edges of the FOV, especially along the left side. The CCs for the SASI imagery were almost identical, regardless of the processing methodology or the acquisition date. The CCs for the SASI imagery were consistently lower than the mean across the FOV from Pixels 548–564. As seen in **Figure 3.13B,D**, this reduction appeared to be parabolic in nature, reaching a minimum

value of approximately 0.995 and 0.997 in the SASI imagery from the 23rd and 24th, respectively.

The spatial locations associated with distinct reductions in the CCs were identified using the threshold defined in Section 3.2.4. These locations were used to spectrally isolate the potential errors to the windows identified in **Table 3.3** using the windowed-based methodology described in Section 3.2.4.

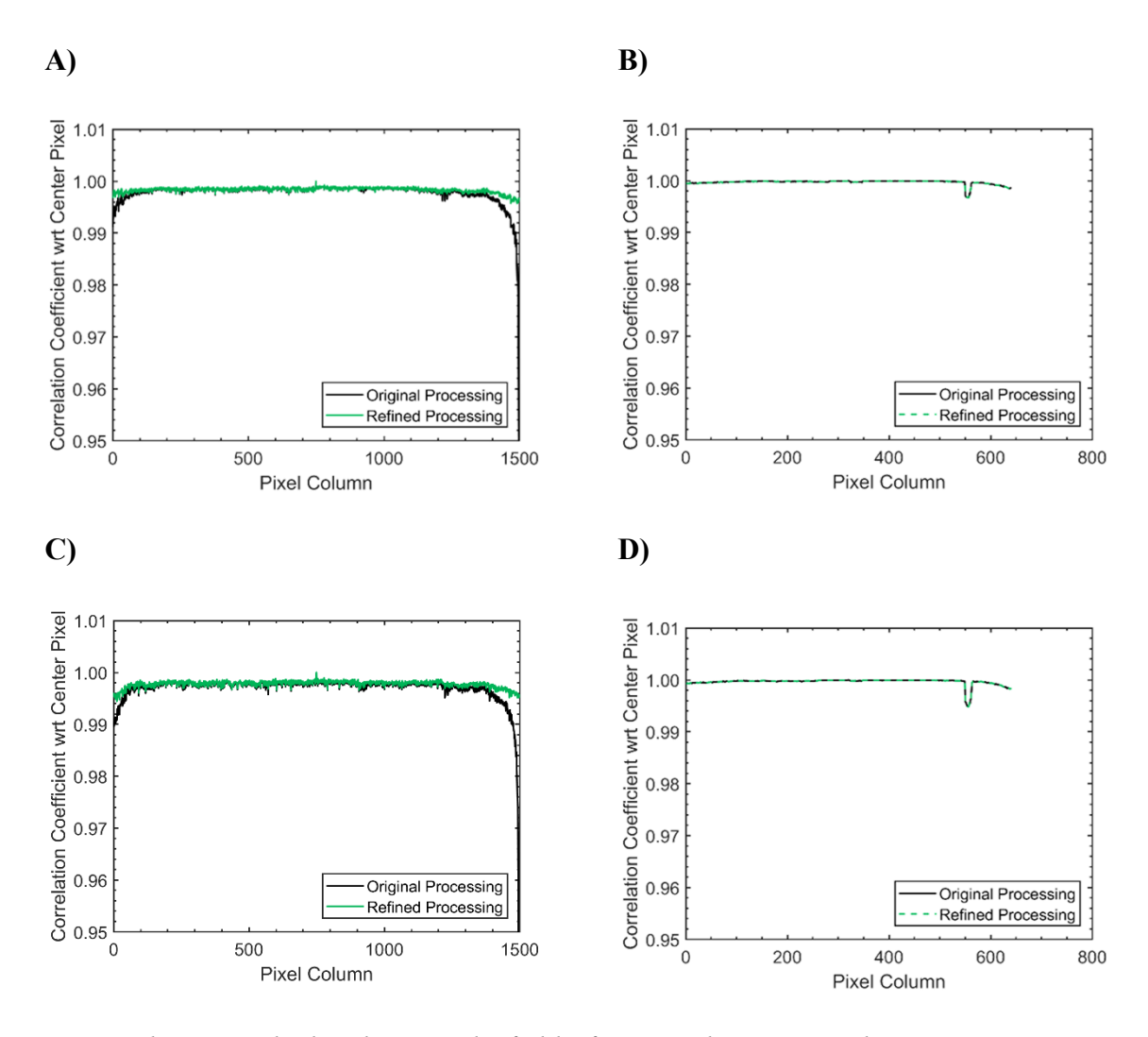


Figure 3.13. The CCs calculated across the field-of-view with respect to the entire spectrum from the center pixel. A) The CC of the CASI imagery (23 June 2016); B) SASI imagery (23 June 2016); C) CASI imagery (24 June 2016); D) SASI imagery (24 June 2016). A,C) The CASI imagery was characterized by systematic reductions near the edges of the FOV. These revealed potential errors consistent with the spectral smile effect and other cross-track illumination effects. This reduction was most substantial for the CASI images generated by the old processing methodology. Compared to the imagery from the 24th, the CCs were more uniform across the FOV for the CASI data from the 23rd. B,D) The SASI imagery was consistent across all dates and processing methodologies. There was a notable reduction in the CCs across the FOV from Pixels 548–564. This revealed the spatial location of an error.

Table 3.3. Spatial and spectral localization of large imaging errors. Spatial errors were detected from the data in **Figure 3.13** using the defined threshold. Potential errors were spectrally located through the window-based methodology described in Section 3.2.4. Errors were detected along the edges of the CASI imagery in the blue end of the spectra. A single band error was detected in the SASI imagery from 993–1008 across Pixels 548–564.

Imager	Date	Processing	Problematic Pixels	Spectrally-Isolated Range (nm)
CASI	23 June 2016	Original	1-70 and 1285-1498	366–453
CASI	23 June 2016	Refined	1403-1498	396-483
CASI	24 June 2016	Original	1-149 and 1258-1498	366–453
CASI	24 June 2016	Refined	1-141 and 1252-1498	396–483
SASI	23 June 2016	Original	548–564	993–1008
SASI	23 June 2016	Refined	548–564	993–1008
SASI	24 June 2016	Original	548–564	993–1008
SASI	24 June 2016	Refined	548–564	993–1008

Errors in the imagery were clearly detected though the visualization of the spectral windows in **Table 3.3**. An example of the error in the CASI imagery is displayed in **Figure 3.14**. In the imagery, the asphalt road is clearly brightest along the edge pixels.

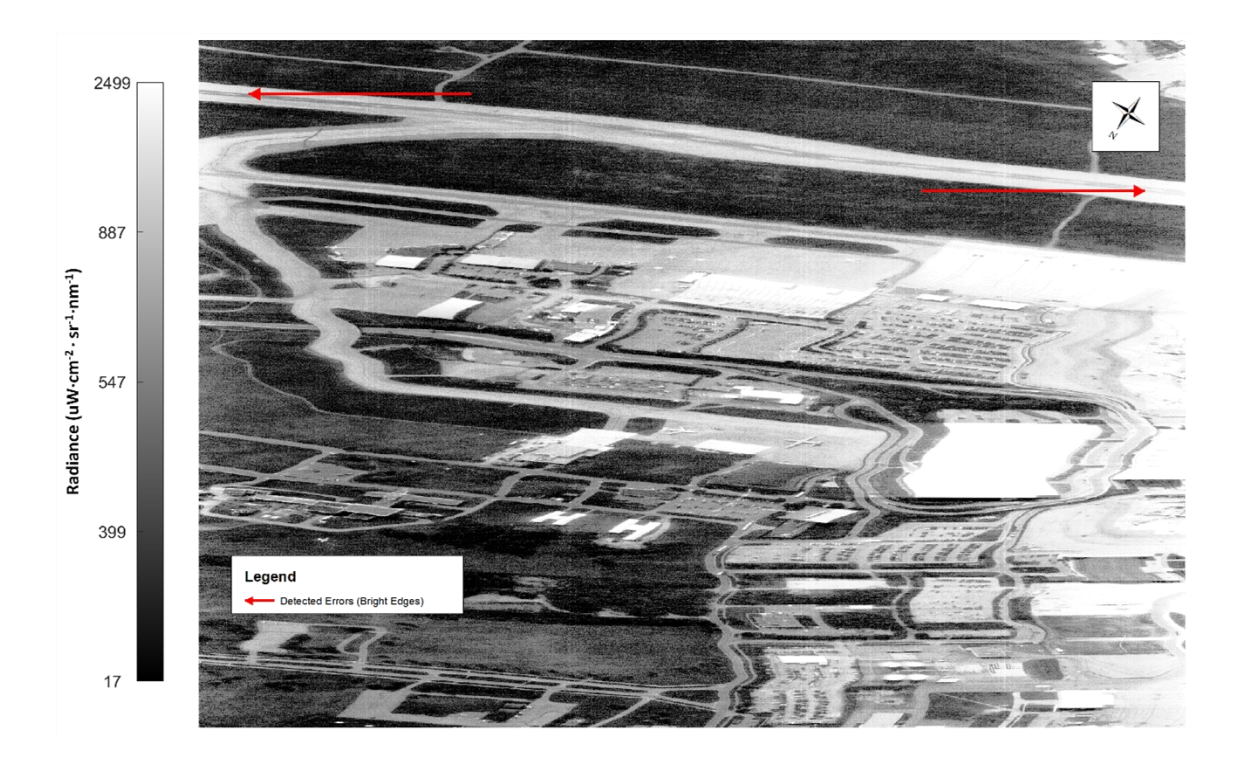


Figure 3.14. Histogram-equalized CASI image (24 June with the original processing) at 393.068 nm. The asphalt road along the south side of the image was brightest along the edge pixels. The errors in the data are highlighted by the red arrows.

This general trend held for all CASI imagery and was less prominent with the refined processing methodology (**Figure 3.15**). The asphalt road is still brightest along the edge pixels, but to a lesser degree than in **Figure 3.14**.

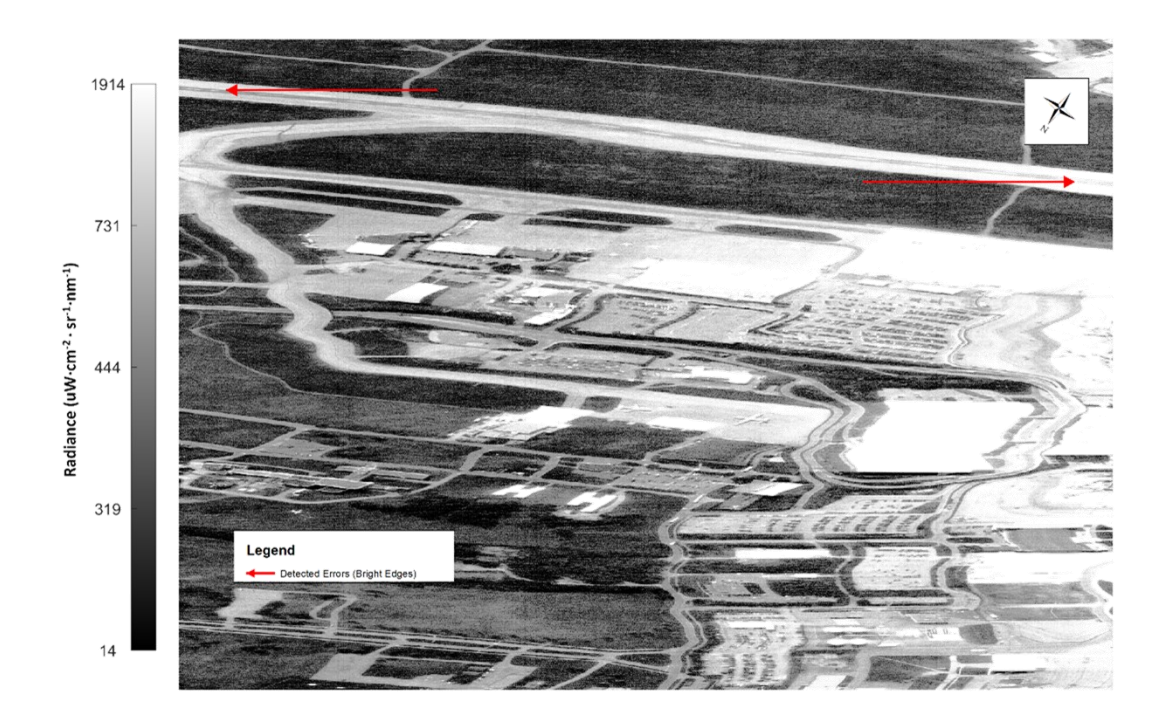


Figure 3.15. Histogram-equalized CASI imagery (24 June with the refined processing) at 393.068 nm. The asphalt road along the south side of the image was brightest along the edge pixels. These errors in the data are highlighted by the red arrows and were less noticeable in the imagery that was generated from the refined processing.

The error within all SASI imagery was located at the same spatial pixels and spectral range. The error could be displayed by visualizing the only band in the 993–1008 spectral range (**Figure 3.16**).



Figure 3.16. Histogram-equalized SASI imagery (24 June with the refined processing) at 1003 nm. An error across Pixels 548–564 is identified by the red arrow.

After removing data in the spectral windows in accordance with **Table 3.3**, there was a substantial increase in the values of CCs across the FOV in all images (**Figure 3.17**), especially at spatial locations associated with the previously identified imaging errors. Comparing **Figure 3.13B,D** and **Figure 3.17B,D**, the large reduction in the SASI imagery from Pixels 548–564 was completely removed. Furthermore, the CCs along the FOV of the CASI images remained relatively constant, even at the edge pixels. Overall, there was more consistency between the images derived by the different processing methodologies and acquisition dates.

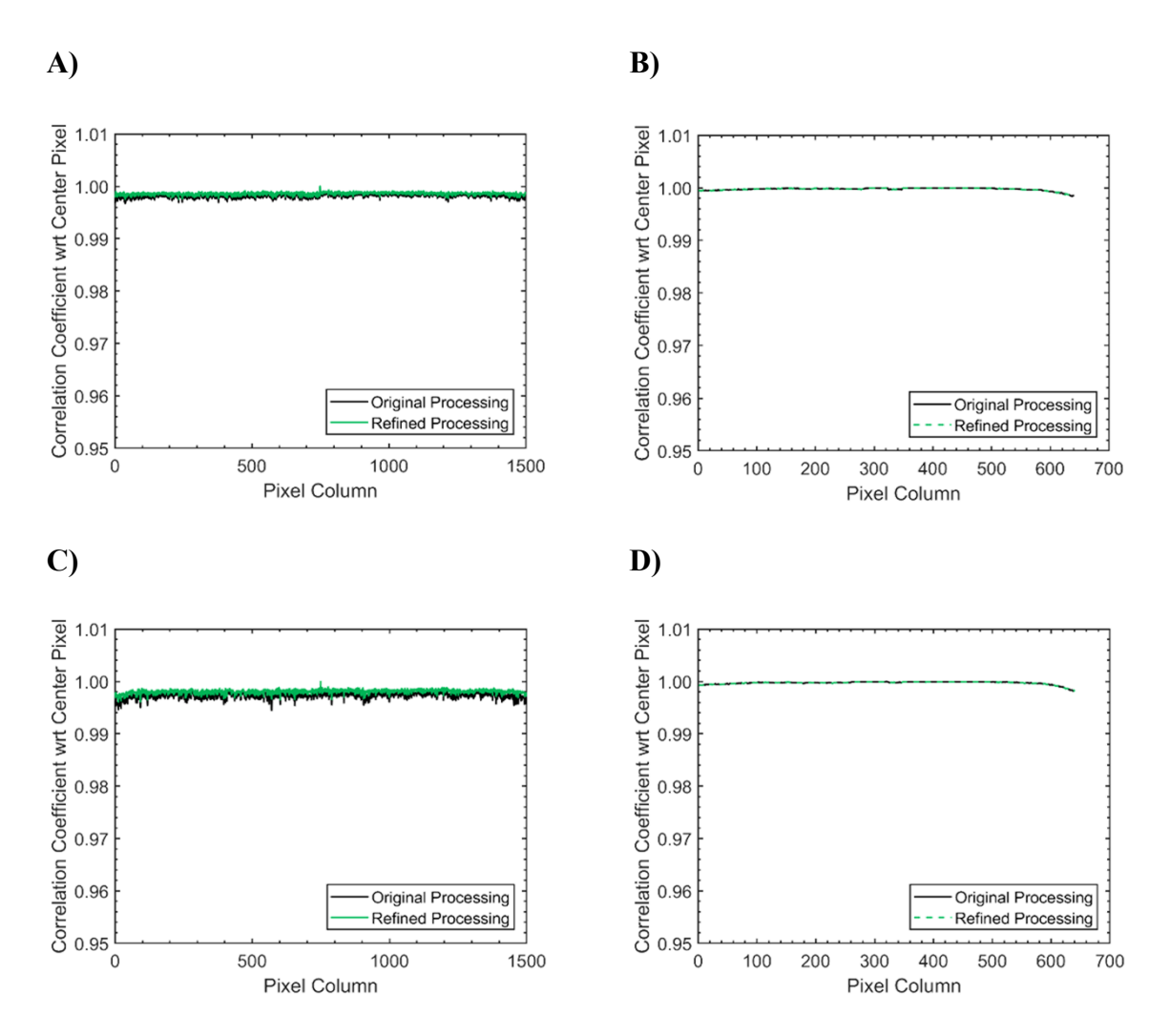


Figure 3.17. The CCs calculated across the field-of-view with respect to the spectrum complementary to the windows in Table 3.3. A) CASI imagery (23 June 2016); B) SASI imagery (23 June 2016); C) CASI imagery (24 June 2016); D) SASI imagery (24 June 2016). A,C) The CCs of the CASI imagery increased greatly, especially along the edges, indicating that the error was primarily contained within the spectral regions identified in Table 3.3. The CASI data from the 23rd were relatively consistent between both processing methodologies. Although this trend generally held for the data from the 24th, C) showed a notable offset. D,B) The large reduction in the CCs from the SASI imagery at Pixels 548–564 was not present after removing the problematic band that was found between 993 and 1008 nm.

Comparing **Figure 3.13A,C** to **Figure 3.17A,C**, there was more consistency in the CCs of the CASI imagery from the 23rd between the original and refined processing. Although this trend holds for the CASI data from the 24th, there was still a notable average offset of 0.0007 between the two curves. Significance testing yielded p-values less than 10^{-5} for all observed relationships.

To further the analysis and spectrally locate smaller residual errors in the CASI data from the 24th, five atmospheric absorption features were identified in the spectral range from 365–1050 nm (**Table 3.4**).

Table 3.4. Identified atmospheric absorption features in the spectral range covered by the CASI.

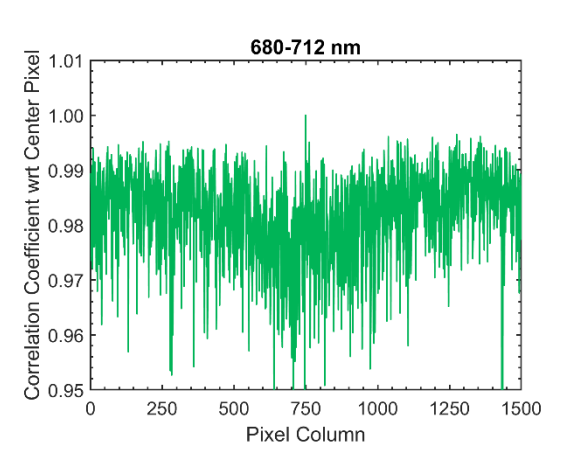
Feature Number	Source	Start Wavelength (nm)	End Wavelength (nm)
1	O_2	680	712
2	H ₂ O	710	745
3	O_2	750	776
4	H ₂ O	804	846
5	H ₂ O	883	992

The CCs across the FOV of the CASI images from the 24th were calculated with respect to the center pixel over the spectral regions identified in **Table 3.4** and are shown in **Figure 3.18**. The CCs in the 680–712 nm region were highly variable, ranging from 0.95–1 with a subtle low frequency sinusoidal structure (**Figure 3.18A,B**). Visual inspection of the associated imagery in **Figure 3.19** indicated that, throughout much of the FOV, there were discrete pixels and groups of pixels that appeared to be non-uniform across the entire FOV, noticeably varying in brightness even amongst neighboring pixels. These pixels lead to "striping" artefacts across the entire FOV in the image data. These trends were apparent in both CASI images. The low frequency sinusoidal structure could not be clearly visualized in the imagery. The sinusoidal structure was not a numerical computational effect.

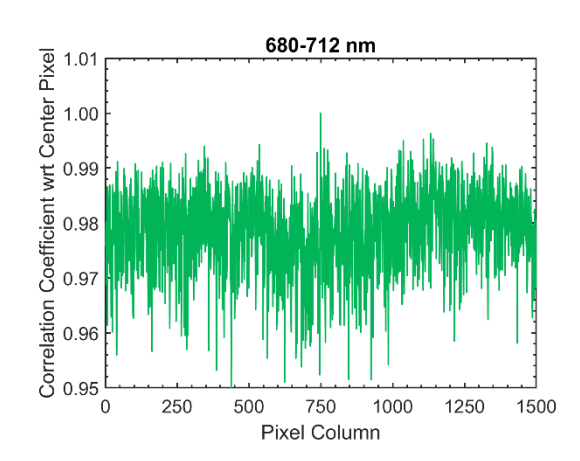
Original Processing

Refined Processing

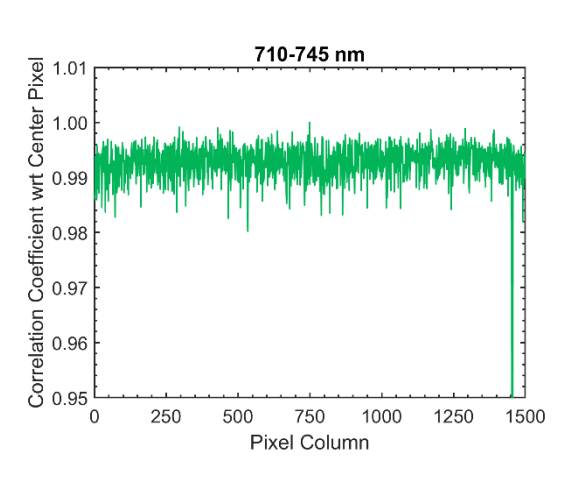




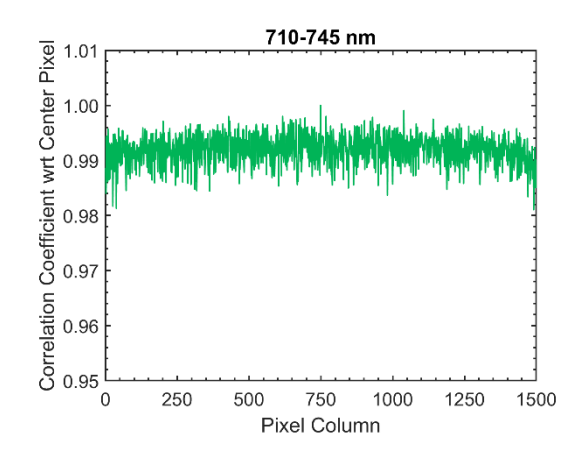
B)



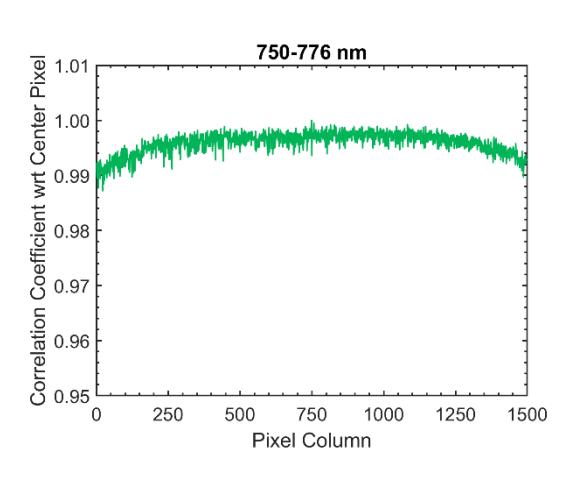
C)



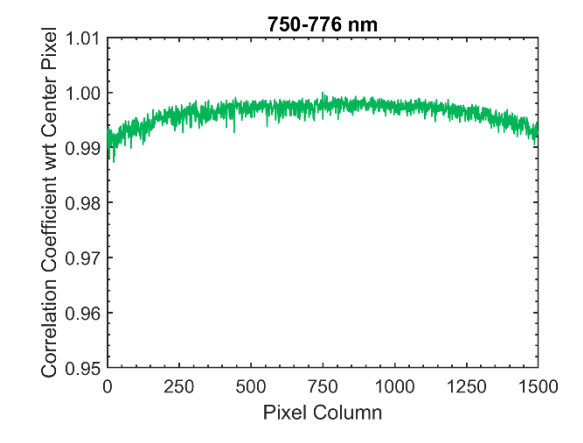
D)



E)



F)



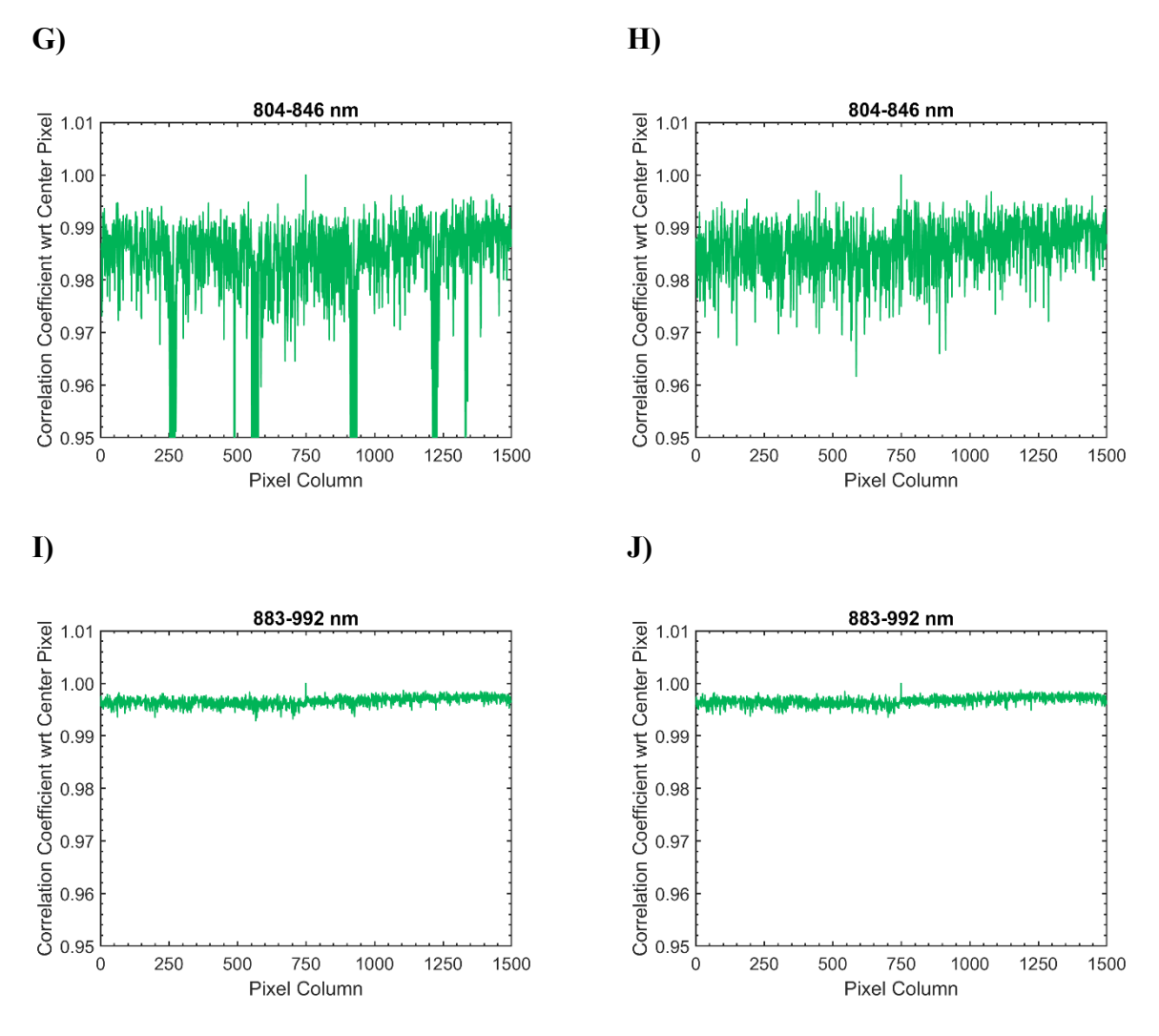


Figure 3.18. The CCs calculated across the field-of-view of the CASI imagery with respect to the spectrum from the center pixel. The wavelength regions used to calculate the CCs are identified in each graph and correspond to the values in **Table 3.4**. Plots (A, C, E, G, I) correspond to the CASI data that were processed with the original methodology. Plots (B,D,F,H,J) correspond to the CASI data that were processed with the refined methodology. A,B) The CCs for the 680–712 nm region were highly variable with a low frequency sinusoidal structure. **C,D**) The CCs for the 710–745 nm region were relatively constant across the FOV. A distinct reduction was detected in the CC of a single pixel near the right edge for the imagery processed with the original methodology, but not the refined processing. **E,F)** There was a reduction of approximately 0.021 in the CC for the 750–775 nm region near the edges of the FOV. This effect is likely caused by the smile effect or other cross-track illumination effects. **G,H)** For the data from the 804–846 nm window of the imagery processed with the original methodology, there were characteristic reductions in the CC greater than 0.05 detected. These reductions revealed potential imaging errors for the spectral window in the following spatial ranges: 256–276, 551–576, 912–936 and 1209-1235. These reductions were not present in the CCs for the image derived with the refined processing. I,J) In the 883–992 nm region, the CCs were relatively constant across the FOV.

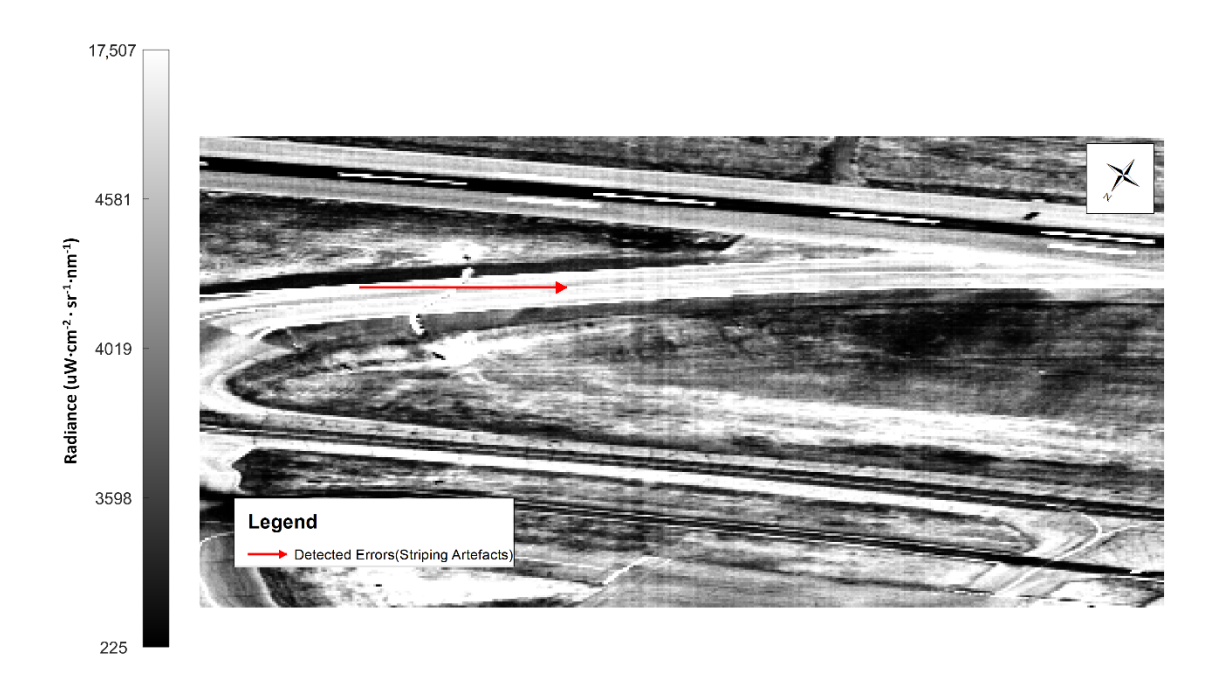


Figure 3.19. Histogram-equalized CASI imagery (24 June with the original processing) at 706.4 nm. The image is zoomed in to display Columns 57–513 from left to right. There are "striping" artefacts across the FOV. This ripple is clearly visible near the center of the figure, as indicated by the red arrow.

Although **Figure 3.18C** remained relatively consistent across the asphalt road, there was a sudden reduction near the end of the FOV at Pixels 1454 and 1456. After independently displaying all bands in the specified spectral window in greyscale, errors were spatially located in Columns 1454 and 1456; these errors were visualized as a bright and dark vertical stripe, respectively, across the imagery (**Figure 3.20**). The vertical stripes were not present in the CASI imagery with the refined processing or **Figure 3.18D**.



Figure 3.20. Histogram-equalized CASI (24 June with original processing) imagery at 744.653 nm. The image is zoomed in to display Columns 1248–1482 from left to right. The red and orange arrows point to the errors in Pixels 1454 and 1456 in the cross-track, respectively. These errors were visualized as a bright and dark vertical stripe.

There was a reduction of approximately 0.021 in the CC near the edges of the FOV in **Figure 3.18E,F**. The effects associated with these reductions could not be visualized within the imagery. **Figure 3.18G** was characterized by sporadic reductions in the CC of greater than 0.05. These reductions revealed potential imaging errors for the spectral window in the following spatial ranges: 256–276, 551–576, 912–936 and 1209–1235. After independently displaying all of the bands in the specified spectral window in greyscale, it was possible to detect groups of non-uniform pixels that noticeably varied in brightness. These groups created distinct "striping" artifacts that can be seen at several spatially-isolated points across the CASI imagery from the 24th with the original processing (**Figure 3.21**). This effect was not present in the CASI imagery with the refined processing or **Figure 3.18H**.

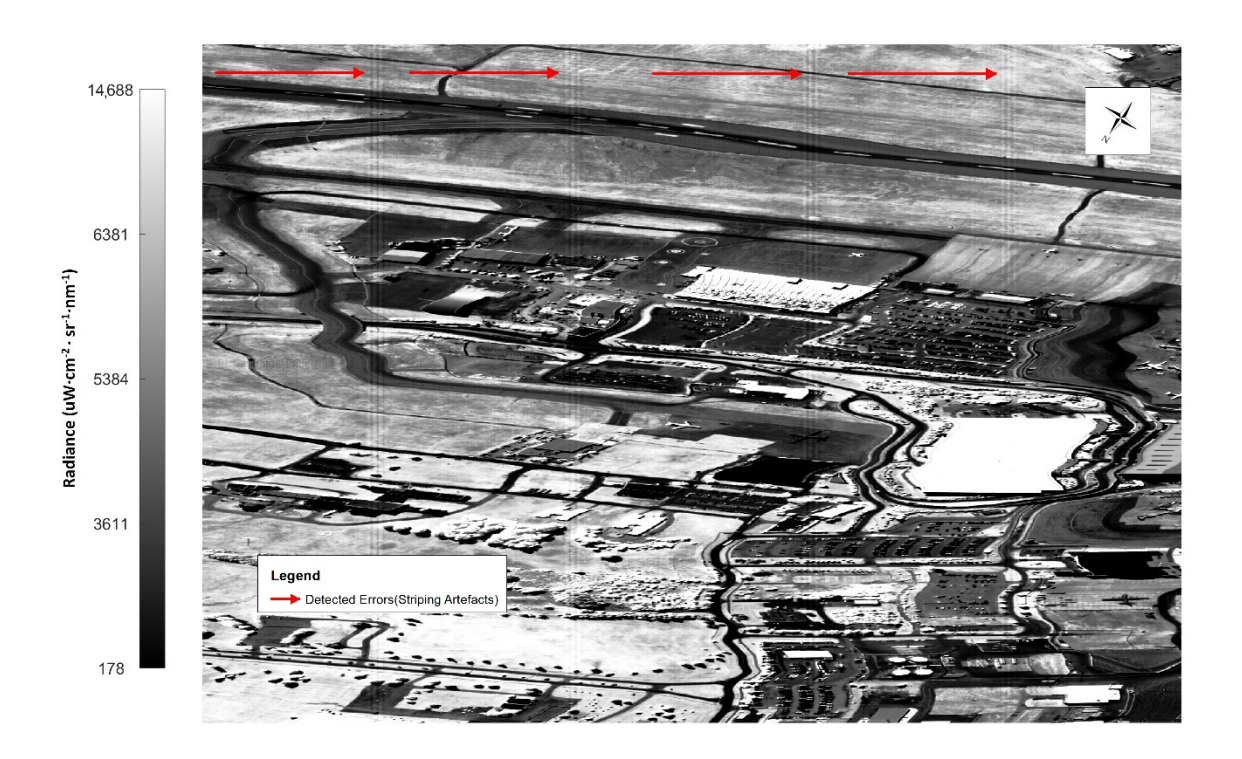


Figure 3.21. Histogram-equalized CASI imagery (24 June with original processing) at 835.491. The red lines show the locations of distinct "striping" artefacts.

The CCs in **Figure 3.18I,J** remained relatively constant with very little variation. The associated imagery was visualized in greyscale with one of the bands from the identified spectral range (**Figure 3.22**). No large errors could be seen in any of the analyzed CASI imagery within this spectral range.

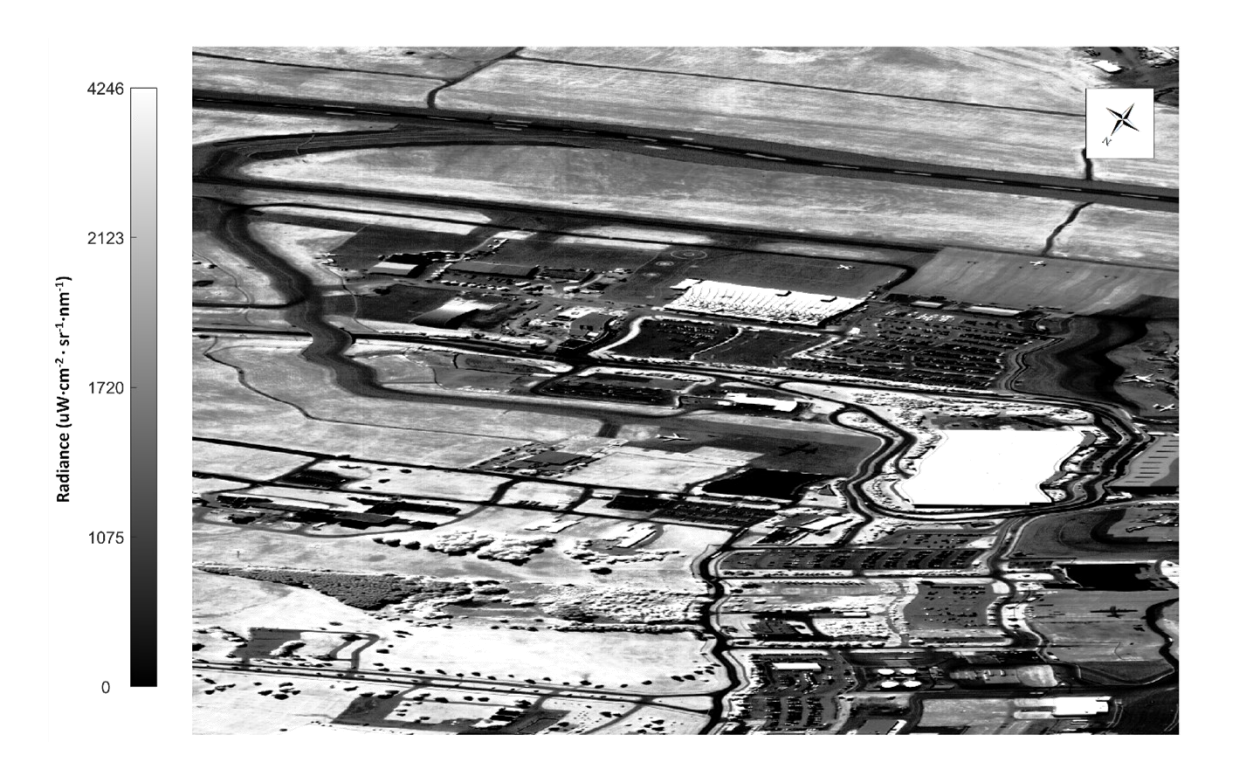


Figure 3.22. Histogram-equalized CASI imagery (24 June with original processing) at 931.099 nm. The imagery is stable, with no obvious errors.

3.4. Discussion

By characterizing the sensitivity of the CC before its application to real airborne HSI data, it was possible to verify the detective capabilities of the metric in the localization of errors in hyperspectral data. The findings generally agreed with all basic intuition and theoretical expectation of the CC. Linear transformations, in agreement with theory, had no impacts on the value of the CC. By calculating the CC between two similar spectra, the value could be used to gauge the consistency independent of the effects associated with linear transformations. Because of this property, the CC was shown to be extremely insensitive to the natural variances between different asphalt spectra. This was important for the detection of errors in HSI data as it implied that the differences in the calculated CCs were not primarily due to the variations between asphalt samples. All modifications, aside from the linear transformations, resulted in a consistent reduction in the CC. Consequently, the CC could detect spectral shifts and modified spectral features. Although the CC was sensitive to signal noise, all general trends held irrespective of the AWGN in hyperspectral data with an SNR of 100:1, which is a reasonably high noise level for airborne HSI data. This trend was fundamental to the application of the CC as it meant that the metric was sufficiently resistant to noise for the purposes of error detection; so long as errors are

not being completely masked by noise, the CC can detect their presence. Implementing this knowledge, the CC was applied to real airborne HSI data.

Through the application of the CC, the quality of remotely-sensed hyperspectral data could be assessed through error detection in a quantitative manner. This was evident in the analysis of the eight hyperspectral images that were studied. By calculating the CCs across the FOV with the entire spectra, it was possible to immediately gauge the spectral consistency of the HSI data collected by the CASI and SASI, across the FOV. It is important to note that the method was explicitly designed for the detection of errors, not for the identification of their origin.

In the CASI imagery, the methodology was able to spatially detect errors along the edges of **Figure 3.13A,C** by systematic reductions in the CCs near the boundaries of the FOV. The spectral locations of these effects were found in the blue end of the spectrum, in accordance with **Table 3.3**. Visualization of the imagery in **Figure 3.14** and **Figure 3.15** revealed an error that is consistent with the effects of the spectral smile or other cross-track illumination effects (San and Süzen, 2011). With a greater decline in the CCs near the edges of the FOV, this error was more prominent in the CASI data collected with the original processing methodology. As such, it is possible to deduce that the refined processing was able to better correct for the effects observed at the edges. The CASI imagery from the 24th was characterized by slightly lower and more variable CCs then the data from the 23rd, especially near the edges of the FOV. With this information, there is some innate variability in the data acquisition of the CASI that could be quantified from the CCs.

The CCs of the SASI imagery were virtually identical regardless of the processing methodology and acquisition date. This suggested that the SASI was very stable in its data acquisition. Furthermore, it was clear that the refined processing methodology did not have a large impact on the data. Using the developed algorithms, an error was detected in the SASI imagery at a single spectral band by a reduction in the CCs from Pixels 548–564. This showcased the developed CC-based methodology as a strong tool in the localization of errors in imaging spectrometers.

After removing the data within the spectral windows identified in **Table 3.3**, there was a greater degree of consistency amongst all of the CASI and SASI images. That being said, not all datasets perfectly aligned; there was a slight offset between the CASI images collected from the

24th. To investigate the discrepancy in the CASI images from the 24th, finer errors were detected in the regions that surrounded the five atmospheric absorption features in **Table 3.4**. All but one of the spectral regions was characterized by non-uniform CCs across the FOV (Figure **3.18**). The irregular structure in **Figure 3.18A,B** was caused by non-uniform pixels, which noticeably varied in brightness. This error created "striping" artefacts across the image data. These artefacts have been observed in the literature and are likely due to radiometric calibration errors (Bachmann et al., 2014). Although the origin of the low frequency sinusoidal structure could not be established, it is clear that the trend is not a numerical computational effect. As such, there is likely a subtle wide spatial scale feature. The origin of the subtle feature in the CCs is still being investigated. The sporadic reduction in the CCs of Figure 3.18C detected errors at Pixel Columns 1454 and 1456, which were visualized as a bright and dark vertical stripe, respectively, across the imagery (Figure 3.20). Since this reduction was not present in Figure **3.18D**, the refined processing methodology was able to correct for this error. Based on the structure of the CCs near the edges of the FOV in Figure 3.18E,F, there were potential residual smile effects or other cross-track illumination effects that could not be clearly visualized in the imagery. The sporadic reductions in the CC of Figure 3.18G revealed groups of non-uniform pixels that created distinct "striping" artefacts that can be seen at several points across the CASI imagery from the 24th with the original processing (Figure 3.21). These errors were not present in Figure 3.18H or its associated imagery. As such, the refined processing methodology was able to correct for this error. The relatively constant CCs across the FOV in Figure 3.18I,J corresponded with stable imagery within the designated spectral window, as displayed in **Figure 3.22**. This information is fundamental as it showcases that the CC method can detect stable imagery, when it is present. The offset between the CASI imagery collected on the 24th in Figure 3.17 was likely due to the additional errors that were not corrected in the original processing methodology.

Although significance testing yielded p-values less than 10^{-5} for all observed relationships, it is important to note that these values did not necessarily imply practical significance. This was due to an issue inherent to the p-value itself; with such a large sample size and small variance, significance testing flagged even the most subtle of changes as significantly different (Lin et al., 2013). Fortunately, this was not an issue within the study as all of the flagged potential errors could be visualized and verified in the imagery itself. A similar statement can be made for the

differences observed in the CCs between the distinct processing methodologies and acquisition devices.

Overall, errors were detected in the CASI and SASI imagery though the application of the CC. Although more sophisticated error detection methodologies exist (e.g., Dadon et al., 2010; Han et al., 2002; Tan and Acharya, 1999), they can be monetarily expensive to implement and rely on a higher level of mathematical understanding. Without a fundamental understanding of a method, its implementation can lead to inaccurate interpretations. The presented method is intuitive; the CC is a rather simple statistical tool and its application is straight forward. The detection can be conducted on radiance spectra prior to atmospheric correction, quickly after acquisition. After removing the wavelength region associated with large errors, the described methodologies could be repeated to isolate smaller errors. Although the application was developed for hyperspectral technologies, it can be easily generalized for data collected by other imaging spectrometers. This versatility showcases the CC as a strong and simple statistical tool for the analysis of spectrographic imaging data through the detection of errors.

3.5. Conclusions

This work substantiated the versatility of the CC with respect to the localization of errors in spectrographic imaging data. The sensitivity of the CC was characterized with respect to subtle spectral changes in the averaged in-situ level radiance data. Errors were spectrally and spatially detected in real airborne acquired HSI data. As per the original intent of the study, the methodology was successfully developed for the detection of errors, not for the identification of their origin. The method was able to gauge the effectiveness of various processing methodologies and the imaging systems themselves. Overall, the CC is clearly a strong, simple, low monetary cost, analytical tool for studying hyperspectral remotely-sensed data quality through error detection.

3.6. References

Akima, H. (1969). A method of smooth curve fitting. *Institute for telecommunication Sciences Boulder Co, USA*

Bachmann, M., Müller, R., Schneider, M., Walzel, T., Habermeyer, M., Storch, T., Kaufmann, H., Segl, K., & Rogass, C. (2014). Data Quality Assurance for hyperspectral L1 and L2 products-Cal/Val/Mon Procedures within the EnMAP Ground Segment. In: *Proceedings of the Land Product Validation and Evolution Workshop (pp. 1-35)*

- Bioucas-Dias, J.M., Plaza, A., Camps-Valls, G., Scheunders, P., Nasrabadi, N., & Chanussot, J. (2013). Hyperspectral remote sensing data analysis and future challenges. *IEEE Geoscience and Remote Sensing Magazine*, 1, 6-36
- Bogumil, K., Orphal, J., Homann, T., Voigt, S., Spietz, P., Fleischmann, O., Vogel, A., Hartmann, M., Kromminga, H., & Bovensmann, H. (2003). Measurements of molecular absorption spectra with the SCIAMACHY pre-flight model: instrument characterization and reference data for atmospheric remote-sensing in the 230–2380 nm region. *Journal of Photochemistry and Photobiology A: Chemistry*, 157, 167-184
- Camps-Valls, G., Tuia, D., Gómez-Chova, L., Jiménez, S., & Malo, J. (2011). Remote sensing image processing. *Synthesis Lectures on Image, Video, and Multimedia Processing, 5*, 1-192
- Chambers, J.Q., Asner, G.P., Morton, D.C., Anderson, L.O., Saatchi, S.S., Espirito-Santo, F.D., Palace, M., & Souza, C., Jr. (2007). Regional ecosystem structure and function: ecological insights from remote sensing of tropical forests. *Trends Ecol Evol*, 22, 414-423
- Chang, G., Mahoney, K., Briggs-Whitmire, A., Kohler, D., Mobley, C., Lewis, M., Moline, M., Boss, E., Kim, M., & Philpot, W. (2004). The new age of hyperspectral oceanography. *Oceanography*, *17*,16-23
- Clarisse, L., Prata, F., Lacour, J.-L., Hurtmans, D., Clerbaux, C., & Coheur, P.-F. (2010). A correlation method for volcanic ash detection using hyperspectral infrared measurements. *Geophysical Research Letters*, *37*, L19806
- Cloutis, E.A. (1996). Review article hyperspectral geological remote sensing: evaluation of analytical techniques. *International Journal of Remote Sensing*, 17, 2215-2242
- Dadon, A., Ben-Dor, E., & Karnieli, A. (2010). Use of derivative calculations and minimum noise fraction transform for detecting and correcting the spectral curvature effect (smile) in Hyperion images. *IEEE Transactions on Geoscience and Remote Sensing*, 48, 2603-2612
- Dale, L.M., Thewis, A., Boudry, C., Rotar, I., Dardenne, P., Baeten, V., & Pierna, J.A.F. (2013). Hyperspectral imaging applications in agriculture and agro-food product quality and safety control: a review. *Applied Spectroscopy Reviews*, 48, 142-159
- Du, Q., & Fowler, J.E. (2007). Hyperspectral image compression using JPEG2000 and principal component analysis. *IEEE Geoscience and Remote Sensing Letters*, 4, 201-205
- Du, Q., & Yang, H. (2008). Similarity-based unsupervised band selection for hyperspectral image analysis. *IEEE Geoscience and Remote Sensing Letters*, *5*, 564-568
- ElMasry, G., Wang, N., ElSayed, A., & Ngadi, M. (2007). Hyperspectral imaging for nondestructive determination of some quality attributes for strawberry. *Journal of Food Engineering*, 81, 98-107
- Green, R.O., Eastwood, M.L., Sarture, C.M., Chrien, T.G., Aronsson, M., Chippendale, B.J., Faust, J.A., Pavri, B.E., Chovit, C.J., & Solis, M. (1998). Imaging spectroscopy and the airborne visible/infrared imaging spectrometer (AVIRIS). *Remote Sensing of Environment*, 65, 227-248
- Guanter, L., Richter, R., & Moreno, J. (2006). Spectral calibration of hyperspectral imagery using atmospheric absorption features. *Applied Optics*, 45, 2360-2370

- Han, T., Goodenough, D., Dyk, A., & Love, J. (2002). Detection and correction of abnormal pixels in Hyperion images. In: *Proceedings of the IEEE International Geoscience and Remote Sensing Symposium (IGARSS'02)*, 3 (pp. 1327-1330): IEEE
- Huang, R., & He, M. (2005). Band Selection Based on Feature Weighting for Classification of Hyperspectral Data. *IEEE Geoscience and Remote Sensing Letters*, 2, 156-159
- Kalacska, M., & Bell, L. (2006). Remote sensing as a tool for the detection of clandestine mass graves. *Canadian Society of Forensic Science Journal*, 39, 1-13
- Kalacska, M., Bell, L.S., Sanchez-Azofeifa, G.A., & Caelli, T. (2009). The application of remote sensing for detecting mass graves: an experimental animal case study from Costa Rica. *Journal of Forensic Sciences*, *54*, 159-166
- King, M.D., Kaufman, Y.J., Menzel, W.P., & Tanre, D. (1992). Remote sensing of cloud, aerosol, and water vapor properties from the Moderate Resolution Imaging Spectrometer (MODIS). *IEEE Transactions on Geoscience and Remote Sensing*, 30, 2-27
- Koch, B. (2010). Status and future of laser scanning, synthetic aperture radar and hyperspectral remote sensing data for forest biomass assessment. *ISPRS Journal of Photogrammetry and Remote Sensing*, 65, 581-590
- Koponen, S., Pulliainen, J., Kallio, K., & Hallikainen, M. (2002). Lake water quality classification with airborne hyperspectral spectrometer and simulated MERIS data. *Remote Sensing of Environment*, 79, 51-59
- Kruse, F.A., Richardson, L.L., & Ambrosia, V.G. (1997). Techniques developed for geologic analysis of hyperspectral data applied to near-shore hyperspectral ocean data. In: *The Fourth International Conference on Remote Sensing for Marine and Coastal Environments* (p. 19)
- Leblanc, G., Kalacska, M., & Soffer, R. (2014). Detection of single graves by airborne hyperspectral imaging. *Forensic Science International*, 245, 17-23
- Lee Rodgers, J., & Nicewander, W.A. (1988). Thirteen Ways to Look at the Correlation Coefficient. *The American Statistician*, 42, 59-66
- Lin, M., Lucas Jr, H.C., & Shmueli, G. (2013). Research commentary—too big to fail: large samples and the p-value problem. *Information Systems Research*, 24, 906-917
- Lu, R., & Peng, Y. (2006). Hyperspectral Scattering for assessing peach fruit firmness. *Biosystems Engineering*, 93, 161-171
- Migdall, S., Klug, P., Denis, A., & Bach, H. (2012). The additional value of hyperspectral data for smart farming. In: *Proceedings of IGARSS 2012* (pp. 7329-7332): IEEE
- Murphy, R.J., Monteiro, S.T., & Schneider, S. (2012). Evaluating classification techniques for mapping vertical geology using field-based hyperspectral sensors. *IEEE Transactions on Geoscience and Remote Sensing*, 50, 3066-3080
- Pallé, E., Osorio, M.R.Z., Montanes-Rodriguez, P., Barrena, R., & Martín, E.L. (2009). The transmission spectrum of Earth through lunar eclipse observations. *arXiv*
- Peng, G., Ruiliang, P., Biging, G.S., & Larrieu, M.R. (2003). Estimation of forest leaf area index using vegetation indices derived from hyperion hyperspectral data. *IEEE Transactions on Geoscience and Remote Sensing*, 41, 1355-1362

- Plaza, A., Plaza, J., Paz, A., & Sanchez, S. (2011). Parallel hyperspectral image and signal processing [Applications Corner]. *IEEE Signal Processing Magazine*, 28, 119-126
- Puttonen, E., Suomalainen, J., Hakala, T., & Peltoniemi, J. (2009). Measurement of reflectance properties of asphalt surfaces and their usability as reference targets for aerial photos. *IEEE Transactions on Geoscience and Remote Sensing*, 47, 2330-2339
- Qiao, J., Wang, N., Ngadi, M.O., Gunenc, A., Monroy, M., Gariepy, C., & Prasher, S.O. (2007). Prediction of drip-loss, pH, and color for pork using a hyperspectral imaging technique. *Meat Science*, 76, 1-8
- Richter, R., Schläpfer, D., & Muller, A. (2011). Operational Atmospheric correction for imaging spectrometers accounting for the smile effect. *IEEE Transactions on Geoscience and Remote Sensing*, 49, 1772-1780
- Ryan, J.P., Davis, C.O., Tufillaro, N.B., Kudela, R.M., & Gao, B.-C. (2014). Application of the hyperspectral imager for the coastal ocean to phytoplankton ecology studies in Monterey Bay, CA, USA. *Remote Sensing*, 6, 1007-1025
- San, B.T., & Süzen, M.L. (2011). Evaluation of cross-track illumination in EO-1 Hyperion imagery for lithological mapping. *International Journal of Remote Sensing*, 32, 7873-7889
- Smith, M.-L., Martin, M.E., Plourde, L., & Ollinger, S.V. (2003). Analysis of hyperspectral data for estimation of temperate forest canopy nitrogen concentration: comparison between an airborne (AVIRIS) and a spaceborne (Hyperion) sensor. *IEEE Transactions on Geoscience and Remote Sensing*, 41, 1332-1337
- Tan, Y.-P., & Acharya, T. (1999). A robust sequential approach for the detection of defective pixels in an image sensor. In: 1999 IEEE International Conference on Acoustics, Speech, and Signal Processing. Proceedings. ICASSP99 (pp. 2239-2242): IEEE
- Tanabe, K., & Saeki, S. (1975). Computer retrieval of infrared spectra by a correlation coefficient method. *Analytical Chemistry*, 47, 118-122
- Thiemann, S., & Kaufmann, H. (2002). Lake water quality monitoring using hyperspectral airborne data—a semiempirical multisensor and multitemporal approach for the Mecklenburg Lake District, Germany. *Remote Sensing of Environment*, 81, 228-237
- Toivanen, P., Kubasova, O., & Mielikainen, J. (2005). Correlation-based band-ordering heuristic for lossless compression of hyperspectral sounder data. *IEEE Geoscience and Remote Sensing Letters*, 2, 50-54
- Turner, W., Spector, S., Gardiner, N., Fladeland, M., Sterling, E., & Steininger, M. (2003). Remote sensing for biodiversity science and conservation. *Trends in Ecology & Evolution*, 18, 306-314
- Van der Meer, F.D., van der Werff, H.M.A., van Ruitenbeek, F.J.A., Hecker, C.A., Bakker, W.H., Noomen, M.F., van der Meijde, M., Carranza, E.J.M., Smeth, J.B.d., & Woldai, T. (2012). Multi- and hyperspectral geologic remote sensing: A review. *International Journal of Applied Earth Observation and Geoinformation*, 14, 112-128
- Xu, H., & Wang, X.-j. (2007). Applications of multispectral/hyperspectral imaging technologies in military. *Infrared and Laser Engineering*, 36, 13

Yao, H., Tang, L., Tian, L., Brown, R., Bhatnagar, D., & Cleveland, T. (2011). Using hyperspectral data in precision farming applications. *Hyperspectral Remote Sensing of Cegetation*, 591-607

Yuen, P.W., & Richardson, M. (2010). An introduction to hyperspectral imaging and its application for security, surveillance and target acquisition. *The Imaging Science Journal*, 58, 241-253

3.7. Author Contributions

G.L. conceived of the study. G.L. and D.I. developed the algorithms. R.J.S., D.I. and G.L. collected the data. D.I. processed the data. D.I. and G.L. analyzed the data with input from R.J.S. and M.K. D.I. wrote the manuscript with input from G.L., M.K. and R.J.S. G.L., M.K. and R.J.S. edited the manuscript.

3.8. Acknowledgements

This work was funded by the Flight Research Laboratory of the National Research Council of Canada, the National Sciences and Engineering Research Council of Canada and the Rathlyn Fellowship. The authors would like to thank Gabriela Ifmov, Thomas Naprestek, Daniel Macdonald and Shahrukh Alavi for supporting data acquisition; and Anthony Brown, Derek Gowanlock and Paul Kissman for piloting the Twin Otter. The authors also thank the two anonymous reviewers, whose comments helped to improve this manuscript. The authors would like to express their appreciation to Defence Research and Development Canada Valcartier for the loan of the CASI instrument.

Connecting Statement (Chapter 3 to Chapter 4)

In chapter 3, the developed error localization algorithm was able to determine the effectiveness of various processing methodologies and the consistency of the spectral information collected across the sensor field of view. The chapter highlights imperfections in HSI data, allowing non-expert end users to interactively identify and understand common errors (e.g., dead pixels, striping, spectral smile). In chapter 3, errors were only detectable as the imagery was analyzed in its raw sensor geometry. This same analysis could not be applied to georeferenced raster end products. Although it is possible to identify errors in georeferenced raster end products, the loss of sensor geometry makes it difficult to interpret them. This study showcases the importance of analyzing data in its raw sensor geometry before rasterization, inspiring the analyses in chapters 4 and 5 that re-evaluate the use of the raster data model in hyperspectral imaging efforts.

Chapter 4 studies the consequences of assuming that pixels are square. By deriving and analyzing the sensor point spread function, a function that maps the spatial response of a pixel, this chapter emphasizes that only ~ 55 % of the signal to any given spectrum originates from the spatial boundaries defined by the raw pixel resolution. Modifying the algorithm developed in chapter 3, it was possible to show that the overlap in the spatial response of neighbouring pixels resulted in sensor generated spatial correlations. Chapter 4 highlights that the non-square nature of pixels acts to mask and distort the natural spatial dynamics of the imaged scene, showcasing that the raster data model mispresents HSI data.

4. Characterizing and Mitigating Sensor Generated Spatial Correlations in Airborne Hyperspectral Imaging Data

Deep Inamdar ¹, Margaret Kalacska ^{1,*}, George Leblanc ^{2,1} and J. Pablo Arroyo-Mora ²

This chapter is published in *Remote Sensing*, 12, 641 under the terms and conditions of the Creative Commons Attribution (CC BY) license (http://creativecommons.org/licenses/by/4.0/).

Minor modifications have been made with respect to formating style.

DOI: https://doi.org/10.3390/rs12040641

Abstract

In hyperspectral imaging (HSI), the spatial contribution to each pixel is non–uniform and extends past the traditionally square spatial boundaries designated by the pixel resolution, resulting in sensor–generated blurring effects. The spatial contribution to each pixel can be characterized by the net point spread function, which is overlooked in many airborne HSI applications. The objective of this study was to characterize and mitigate sensor blurring effects in airborne HSI data with simple tools, emphasizing the importance of point spread functions. Two algorithms were developed to 1) quantify spatial correlations and 2) use a theoretically derived point spread function to perform deconvolution. Both algorithms were used to characterize and mitigate sensor blurring effects on a simulated scene with known spectral and spatial variability. The first algorithm showed that sensor blurring modified the spatial

¹ Applied Remote Sensing Laboratory, Department of Geography, McGill University, Montréal, QC H3A 0B9, Canada; deep.inamdar@mail.mcgill.ca (D.I.)

² Flight Research Laboratory, National Research Council of Canada, Ottawa, ON K1A 0R6, Canada; George.Leblanc@nrc-cnrc.gc.ca (G.L.); juanpablo.arroyomora@nrc-cnrc.gc.ca (J.P.A.-M.)

^{*} Correspondence: Margaret.kalacska@mcgill.ca; Tel.: +1-514-398-4347; Fax: +1-514-398-7437

correlation structure in the simulated scene, removing 54.0%–75.4% of the known spatial variability. Sensor blurring effects were also shown to remove 31.1%–38.9% of the known spectral variability. The second algorithm mitigated sensor–generated spatial correlations. After deconvolution, the spatial variability of the image was within 23.3% of the known value. Similarly, the deconvolved image was within 6.8% of the known spectral variability. When tested on real–world HSI data, the algorithms sharpened the imagery while characterizing the spatial correlation structure of the dataset, showing the implications of sensor blurring. This study substantiates the importance of point spread functions in the assessment and application of airborne HSI data, providing simple tools that are approachable for all end–users.

Keywords: hyperspectral imaging, point spread function, spatial correlations, image deconvolution

4.1. Introduction

Hyperspectral remote sensing has received considerable attention over the past three decades since the development of high-altitude airborne (Babey and Anger, 1989; Cocks et al., 1998; Green et al., 1998) and spaceborne platforms (Pearlman et al., 2003), leading to a paradigm shifting approach to Earth observation. In hyperspectral remote sensing, contiguous narrow—band spectral information is acquired for each spatial pixel of an image collected over the Earth's surface (Bioucas-Dias et al., 2013). The spectral information typically quantifies the absorbance and reflectance of the materials within each spatial pixel, as well as the interactions that have occurred with light as it passed through the atmospheric column. The reflectance and absorbance of materials are representative of their chemical and physical properties (Eismann, 2012). Assuming the atmospheric interactions (absorption and scattering) can be reasonably well modelled and removed from the signal of each pixel (Berk et al., 1999), the spectral information from hyperspectral remote sensing data can be used to identify and characterize materials over large spatial extents. Hyperspectral remote sensing is commonly known by its imaging modality term hyperspectral imaging (HSI) (Bioucas-Dias et al., 2013) and has prominent applications in fields such as geology (Cloutis, 1996; Murphy et al., 2012; van der Meer et al., 2012), agriculture (Dale et al., 2013; Migdall et al., 2012; Yao et al., 2011), forestry (Koch, 2010; Peng et al., 2003; Smith et al., 2003), oceanography (Chang et al., 2004; Kruse et al., 1997; Ryan et al., 2014),

forensics (Kalacska and Bell, 2006; Kalacska et al., 2009; Leblanc et al., 2014) and ecology (Arroyo-Mora et al., 2018a; Kalacska et al., 2018; Turner et al., 2003).

In HSI, many applications implicitly rely on the assumption that the spatial contribution to the spectrum from each pixel is uniform across the boundaries defined by the spatial resolution of the final geocorrected data product. This assumption does not hold for real imaging data (Huang et al., 2002). Due to technological limitations in spectrographic imagers in general, the spatial contribution to each pixel is non–uniform, extending past the traditionally square spatial boundaries designated by the pixel resolution. Consequently, the spectrum from each pixel has contributions from the materials within the spatial boundaries of neighbouring pixels. Practically, this phenomenon is observed as a sensor induced blurring effect within the imagery (Schowengerdt, 2006).

The sensor induced blurring effect of an imaging system can be described by the net point spread function (PSF_{net}), or alternatively by its normalized Fourier transform, the modulation transfer function. Formally, the PSF_{net} gives the relative response of an imaging system to a point source, characterizing the spatial contribution to the spectrum from a single pixel. The PSF_{net} is typically a two–dimensional function that depends on the position of the point source in the across track and along track directions within the sensor's field of view. In most spectrographic imagers, blurring effects are induced by sensor optics, detectors, motion and electronics (Schowengerdt, 2006; Zhang and Moore, 2015). The sensor blurring associated with each of these components can be modelled independently.

The optical blurring effect occurs as the imaging system spreads the energy from a single point over a very small area in the focal plane. If the optics of a sensor are only affected by optical diffraction, a 2–D, wavelength–dependent Airy function can be used to describe the point spread function associated with the optical blurring effect (PSF_{opt}). In practice, this is rarely the case as the optics are often affected by aberrations and mechanical assembly quality (Schowengerdt, 2006). As a result, a 2–D, wavelength–independent Gaussian function is commonly used as an approximation to the PSF_{opt} (Schowengerdt, 2006):

$$PSF_{opt}(x,y) = \frac{1}{\sigma_x \sqrt{2\pi}} e^{-\frac{x^2}{2\sigma_x^2}} \frac{1}{\sigma_y \sqrt{2\pi}} e^{-\frac{y^2}{2\sigma_y^2}},$$
 (1)

where x and y represent the disposition of the point source from the center of the pixel in the across track and along track directions while σ_x and σ_y represent the standard deviation, controlling the width of the function in the across track and along track directions, respectively.

The detector blurring is caused by the non–zero spatial area of each detector in the sensor. This blurring is typically characterized by a uniform rectangular pulse detector point spread function (PSF_{det}) with a width equal to the ground instantaneous field of view (GIFOV) (Schowengerdt, 2006; Zhang and Moore, 2015):

$$PSF_{det}(x,y) = \begin{cases} 1, & \text{if } |x|, |y| < \frac{GIFOV}{2} \\ \frac{1}{2}, & \text{if } |x|, |y| = \frac{GIFOV}{2} \\ 0, & \text{if } |x|, |y| > \frac{GIFOV}{2} \end{cases}$$
 (2)

The motion blurring is caused by the motion of the sensor while the shutter is open and the signal from each pixel is being integrated over time. For pushbroom sensors, the blurring is observed in the along track direction (assuming a constant heading) and can be described by a uniform rectangular pulse motion point spread function (PSF_{mot}) with a width equal to the speed of the sensor (v) multiplied by the integration time (IT) (Schowengerdt, 2006; Zhang and Moore, 2015):

$$PSF_{mot}(x,y) = \begin{cases} 1, & \text{if } |y| < \frac{IT \times v}{2} \\ \frac{1}{2}, & \text{if } |y| = \frac{IT \times v}{2} \\ 0, & \text{if } |y| > \frac{IT \times v}{2} \end{cases}$$
 (3)

For whiskbroom sensors, the PSF_{mot} can be modelled by a uniform rectangular pulse with a width equal to the scan velocity (s) multiplied by IT (Zhang and Moore, 2015):

$$PSF_{mot}(x,y) = \begin{cases} 1, & \text{if } |x| < \frac{IT \times s}{2} \\ \frac{1}{2}, & \text{if } |x| = \frac{IT \times s}{2} \\ 0, & \text{if } |x| > \frac{IT \times s}{2} \end{cases}$$
 (4)

An example of Equations (1-4) is given in Section 4.2.2.

Practically, the blurring effect of sensor motion and detectors are often characterized simultaneously as the scan point spread function (PSF_{scan}) (Schowengerdt, 2006):

$$PSF_{scan} = PSF_{det} * PSF_{mot}. (5)$$

The electronic blurring effect occurs in sensors that electronically filter the data to reduce noise. The electronic filtering operates in the time domain as spectral information is collected during each integration period. Due to the movement of the aircraft, this time dependency has an equivalent spatial dependency. As such, the data are blurred due to electronic filtering in accordance with this spatial dependency. The form of the electronic point spread function (*PSF*_{electronic}) is dependent on the nature of the filter itself (Schowengerdt, 2006).

The PSF_{net} can be written as the convolution of the four independent point spread functions that describe each of the sensor induced blurring effects (Schowengerdt, 2006; Zhang and Moore, 2015):

$$PSF_{net}(x,y) = PSF_{opt}(x,y) * PSF_{det}(x,y) * PSF_{mot}(x,y) ...$$
$$* PSF_{electronic}(x,y) .$$
(6)

The dynamics of the PSF_{net} in many of the popular imaging designs (i.e., pushbroom and whiskbroom) can be quite distinct between the across track and along track directions (Zhang and Moore, 2015). For instance, the raw pixel resolution of a pushbroom imaging system is typically defined by the full–width at half–maximum of the PSF_{mot} in the along track and the PSF_{det} in the across–track. As such, imaging systems are often characterized by different raw spatial resolutions in the across track and along track directions.

Traditionally, the PSF_{opt} of a sensor is measured in a controlled laboratory environment. In the laboratory characterization, the sensor is used to image a well–characterized point source target to obtain the PSF_{opt} in two dimensions (Schowengerdt, 2006). With the measured PSF_{opt} , the PSF_{net} of an imaging system during data acquisition can be approximated with equations (1–6). The PSF_{net} can also be measured from operational imagery over man–made objects that represent point sources (e.g., mirrors and geometric patterns) or targets–of–opportunity (e.g.,

bridges and coastlines) (Rauchmiller and Schowengerdt, 1988; Schowengerdt, 2006; Schowengerdt et al., 1974).

Generally, HSI system manufacturers have an understanding of the sensor induced blurring effects that their instruments induce and the point spread functions that describe them. However, in some cases, this information is not directly shared with end–users. This is problematic, given the effects of sensor blurring on HSI data.

Sensor blurring effects attenuate high–frequency components and modify the spatial frequency structure of HSI data (Chaudhuri et al., 2014). Given the relationship between frequency content and correlation, sensor induced blurring effects should theoretically introduce sensor–generated spatial correlations. Hu et al. (2012), showed that the spatial correlation structure of a clean monochromatic image was modified after introducing a sensor–generated blurring effect. Based on these results, sensor induced blurring should also systematically introduce spatial correlations in both satellite and airborne imagery.

The impacts of sensor induced blurring effects have been thoroughly analyzed for spaceborne multispectral sensors (e.g. (Markham, 1985; Markham, et al. 2018; Radoux et al., 2016)). Huang et al. (2002) determined that sensor–generated blurring effects reduce the natural variability of various scenes imaged by satellite spectrographic imagers. The nature of this effect was found to be dependent on the imaged area, with the most information being lost from heterogeneous scenes characterized by high levels of spatial variability. Sensor induced blurring effects have been found to impede basic remote sensing tasks such as classification (Huang et al., 2002), subpixel feature detection (Radoux et al., 2016) and spectral unmixing (Wang et al., 2018). Furthermore, in Aiazzi et al. (2019), the performances of onboard lossless compression of hyperspectral raw data are analyzed considering the blurring effects. In the literature, many studies acknowledge the potential for error due to sensor induced spatial blurring effects (e.g. (Bergen et al., 2005; Heiskanen, 2006; Simms et al., 2014; Tarrant et al., 2010; Torres-Rua et al., 2016)) but do not characterize the implications.

To a lesser degree, sensor induced blurring effects have also been analyzed at the airborne level for HSI platforms. For example, Schläpfer et al. (2007) rigorously analyzed the implications of sensor blurring by convolving real—world airborne HSI data collected by the Airborne Visible / Infrared Imaging Spectrometer (AVIRIS) sensor at high (5 m) and low (28.3)

m) spatial resolutions with numerous point spread functions that varied in full—width at half—maximum. Sensor induced blurring was found to modify the high spatial resolution imaging data to a greater degree than the low spatial resolution imaging data. Since the low spatial resolution imagery was on the same scale as data products collected by satellite sensors, these results suggest that sensor blurring may be more prominent for airborne sensors due to their high spatial resolution (Schläpfer et al., 2007). Although there are reports that acknowledge the implications of sensor induced blurring at the airborne level, many studies do not attempt to characterize or mitigate their impact.

Sensor induced blurring effects can be mitigated through means of image deconvolution. However, it is important to recognize that deconvolution is an ill–posed problem; due to the information loss associated with sensor blurring, a unique solution is often unobtainable even in the absence of noise (Chaudhuri et al., 2014). In remote sensing, many deconvolution algorithms have been developed to mitigate the effects of sensor induced blurring (Fang et al., 2017; Henrot et al., 2013; Jackett et al., 2011). Although these methods are effective, they can be difficult to implement due to the mathematical complexity of the algorithms and the computational expense. This combination of factors presents difficulties to end–users of HSI data who may lack the information or expertise to accurately apply these methods.

The PSF_{net} of most HSI systems are characterized to some degree by sensor manufacturers. Despite this, sensor point spread functions are often ignored by end–users in favour of parameters such as ground sampling distance, pixel resolution and geometric accuracy. Although such parameters are extremely important, they do not accurately describe the spatial contribution to the signal from each pixel or the sensor blurring caused by the overlap in the field of view between neighbouring pixels. This could be problematic for many remote sensing applications given the implications of sensor induced blurring effects.

The objective of this study was to characterize and mitigate sensor—generated blurring effects in airborne HSI data with simple and intuitive tools, emphasizing the importance of point spread functions. Two algorithms are presented. The first strategically applies a simple correlation metric, modifying the traditional spatial autocorrelation function, to observe and quantify spatial correlations. The second uses a theoretically derived PSF_{net} to mitigate sensor—generated spatial correlations in HSI data. The two algorithms were used to characterize and mitigate the

implications of sensor induced blurring on simulated HSI data, before and after introducing realistic sensor blurring. The algorithms were then applied to real-world HSI data.

4.2. Materials and Methods

4.2.1. Airborne HSI Data

Airborne HSI data were acquired on June 24th, 2016 aboard a Twin Otter fixed—wing aircraft with the Compact Airborne Spectrographic Imager 1500 (CASI) (ITRES, Calgary, Canada). The imagery was collected over two study areas: the Mer Bleue peatland (Latitude: 45.409270°, Longitude: –75.518675°) and the Macdonald–Cartier International Airport (Latitude: 45.325200°, Longitude: –75.664642°), near Ottawa, Ontario, Canada. The CASI acquires data over 288 spectral bands within a 366–1053 nm range. The CASI is a variable frame rate, grating–based, pushbroom imager with a 39.8° field of view across 1498 spatial pixels. The device has a 0.484 mrad instantaneous field of view at nadir with a variable f–number aperture that is configurable between 3.5 and 18.0 (Soffer et al., 2019). **Table 4.1** records the parameters (heading, speed, altitude, integration time, frame time, time and date) associated with the flight lines.

Table 4.1. Flight parameters for the hyperspectral data acquired over the Mer Bleue Peatland and the Macdonald–Cartier International Airport.

Parameter	Mer Bleue Peatland	Macdonald–Cartier International Airport
Time (hh.mm.ss GMT)	16.31.15	17.42.05
Date (dd-mm-yyyy)	24-06-2016	24-06-2016
Latitude of Flight Line Centre (DD)	45.399499	45.323259
Longitude of Flight Line Centre (DD)	-75.514790	-75.660129
Nominal Heading (°TN)	338.0	309.5
Nominal Altitude (m)	1142	1118
Nominal Speed (m/s)	41.5	41.6
Integration Time (ms)	48	48
Frame Time (ms)	48	48

The two studied sites are spectrally and spatially distinct. The Mer Bleue peatland is a ~8,500—year—old ombrotrophic bog (Lafleur et al., 2003) that is recognized as a Wetland of International Importance under the Ramsar Convention on Wetlands, a Provincially Significant Wetland, a Provincially Significant Life and Earth Science Area of Natural and Scientific Interest and a Committee for Earth Observation Satellites Land Product Validation supersite. In the peatland, there are evident micro—spatial patterns in vegetation that correspond to a hummock—hollow microtopography (**Figure 4.1**). A hummock microtopography is a drier elevated mound with a dense cover of vascular plants while a hollow microtopography is a lower—laying depression that is wetter and dominated by mosses such as *Sphagnum* spp. (Eppinga et al., 2008; Lafleur et al., 2005). Adjacent hummocks and hollows can differ in absolute elevation by as much as 0.30 m and are separated by an approximate horizontal distance of 1–2 m (Belyea and Baird, 2006; Malhotra et al., 2016; Wilson, 2012). Given that the overlying vegetation, and their associated reflective properties, covary with the patterns in microtopography (Arroyo-Mora et al., 2018a; Arroyo-Mora et al., 2018b; Kalacska et al., 2018), the Mer Bleue HSI data is likely characterized by a sinusoidal spatial correlation structure with a

period on the scale of 2–4 m. There are very few large high contrast targets in the Mer Bleue Peatland. Grey and black calibration tarps were laid out and captured in the imagery to provide high contrast edges. This Mer Bleue site provides a complex natural scene with which to test the algorithms.



Figure 4.1. Unmanned aerial vehicle photograph of the Mer Bleue Peatland in Ottawa, Ontario, Canada. There are evident micro–spatial patterns in vegetation that correspond to the hummock–hollow microtopography. A hummock microtopography is a drier elevated mound with a dense cover of vascular plants while a hollow microtopography is a lower–laying depression that is wetter and dominated by mosses such as Sphagnum spp. Adjacent hummocks and hollows can differ in absolute elevation by as much as 0.30 m over a horizontal distance of 1–2 m.

The Macdonald–Cartier airport and the surrounding area is primarily composed of man—made materials that have defined edges between spectrally homogenous matter such as asphalt and concrete (Puttonen et al., 2009; Soffer et al., 2019). The area surrounding the Macdonald–Cartier airport contains the Flight Research Laboratory's calibration site, which is composed of

asphalt and concrete that have been spectrally monitored over the past decade. This site provides a scene to test the algorithms that are nearly piece—wise smooth in the spatial domain.

The raw data acquired over the two sites underwent four processing steps. The first three steps were implemented with proprietary software developed by the sensor manufacturer. The first step modified the radiometric sensor calibration (traceable to the National Institute of Standards and Technology) to account for the effects of small, but measurable pressure and temperature—induced shifts in the spatial—spectral sensor alignment during data acquisition. The second step applied the modified sensor calibration, converting the raw digital numbers recorded by each spatial pixel and spectral band of the sensor into units of spectral radiance (uW·cm⁻²·sr⁻¹·nm⁻¹). The third step removed the laboratory—measured spectral smile by resampling the data from each spatial pixel to a uniform wavelength array. In the final processing stage, the imaging data were atmospherically corrected with ATCOR4 (ReSe, Wil, Switzerland), converting the measured radiance to units of surface reflectance (%) (Soffer et al., 2019). To preserve the original sensor geometry, the images were not geocorrected.

4.2.2. Deriving the Theoretical Point Spread Function for each CASI Pixel

The theoretical PSF_{net} was calculated separately in the across track and along track directions. The derivation relied on 2 assumptions: (1) the aircraft was flying at a constant altitude, speed and heading with 0 roll and pitch; (2) the aircraft flight line was perpendicular to the detector array. With the sensor properties and the flight parameters of the Mer Bleue imagery (Table 4.1), the GIFOV of the CASI was calculated to be 0.55 m in both the along track and the across track directions. The PSF_{opt} was derived from a Gaussian function with a full-width at half-maximum of 1.1 detector array pixels (value provided by sensor manufacturer) in both the across track and along track directions. The PSF_{net} in the across track direction was derived by convolving the PSF_{opt} with the PSF_{det} , which was a rectangular pulse function with a width equal to the GIFOV (**Figure 4.2A**). The PSF_{net} in the along track direction was calculated based on the same optical and detector point spread function as in the across track direction. The PSF_{mot} in the along track was approximated by a rectangular pulse function with a width equal to the along track pixel spacing or, equivalently, the nominal ground speed of the sensor (41.5 m/s) multiplied by the integration time (48 ms) for each line. No electronic filters were applied to the CASI data during data acquisition and thus the dynamics of the *PSF*_{electronic} were not considered. The PSF_{net} in the along track was calculated by convolving the detector, optical and motion point spread functions (**Figure 4.2B**). The total PSF_{net} was derived by multiplying the PSF_{net} in the across track and along track directions (**Figure 4.3**). Based on this derivation, the pixel resolution of the CASI imagery was approximately 0.55 m and 1.99 m in the across track and along track directions, respectively.

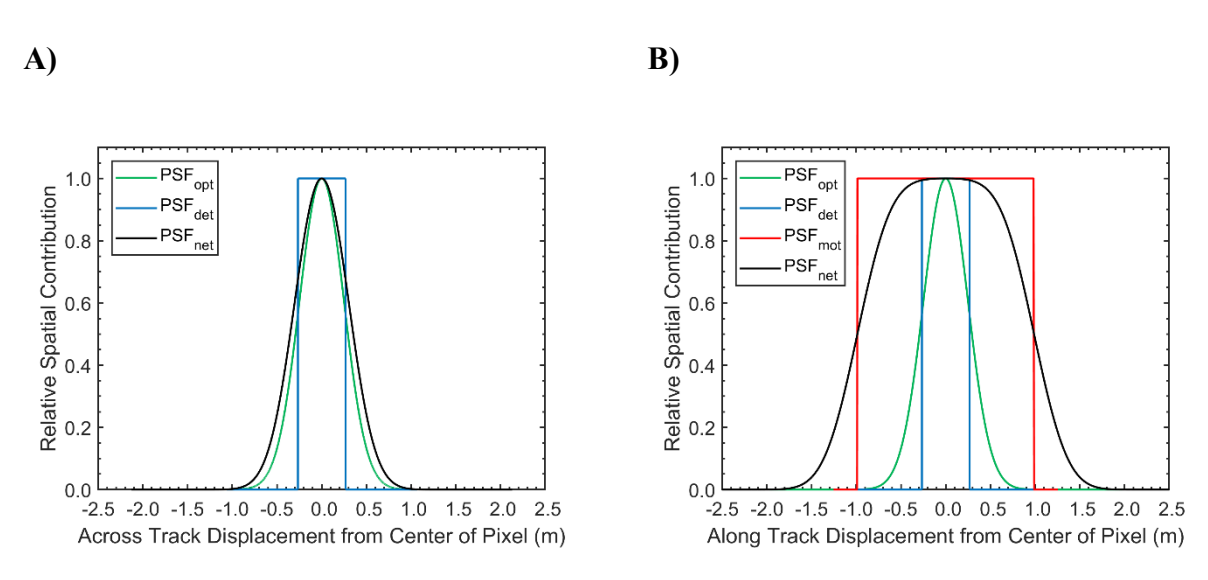


Figure 4.2. The relative spatial contribution to a single Compact Airborne Spectrographic Imager 1500 (CASI) image pixel as a function of across track (plot A) and along track (plot B) displacement from the center of the pixel. The optical, detector, motion and net point spread function (PSF) are displayed separately. The width of the detector point spread function represents the raw spatial resolution in the across track direction. The width of the motion point spread function represents the raw spatial pixel resolution in the along track direction. A substantial portion of the net PSF lies outside the traditional pixel boundaries defined by the raw resolution of 0.55 m in the across track direction. As such, the spectrum from each pixel has sizeable contributions from the materials within the spatial boundaries of neighbouring pixels in the across—track. A substantial portion of the net PSF lies outside the traditional pixel boundaries defined by the raw resolution of 1.99 m in the along track direction as well. These contributions are not as significant as they are in the across—track, however, there are still notable contributions from materials within the spatial boundaries of neighbouring along track pixels.

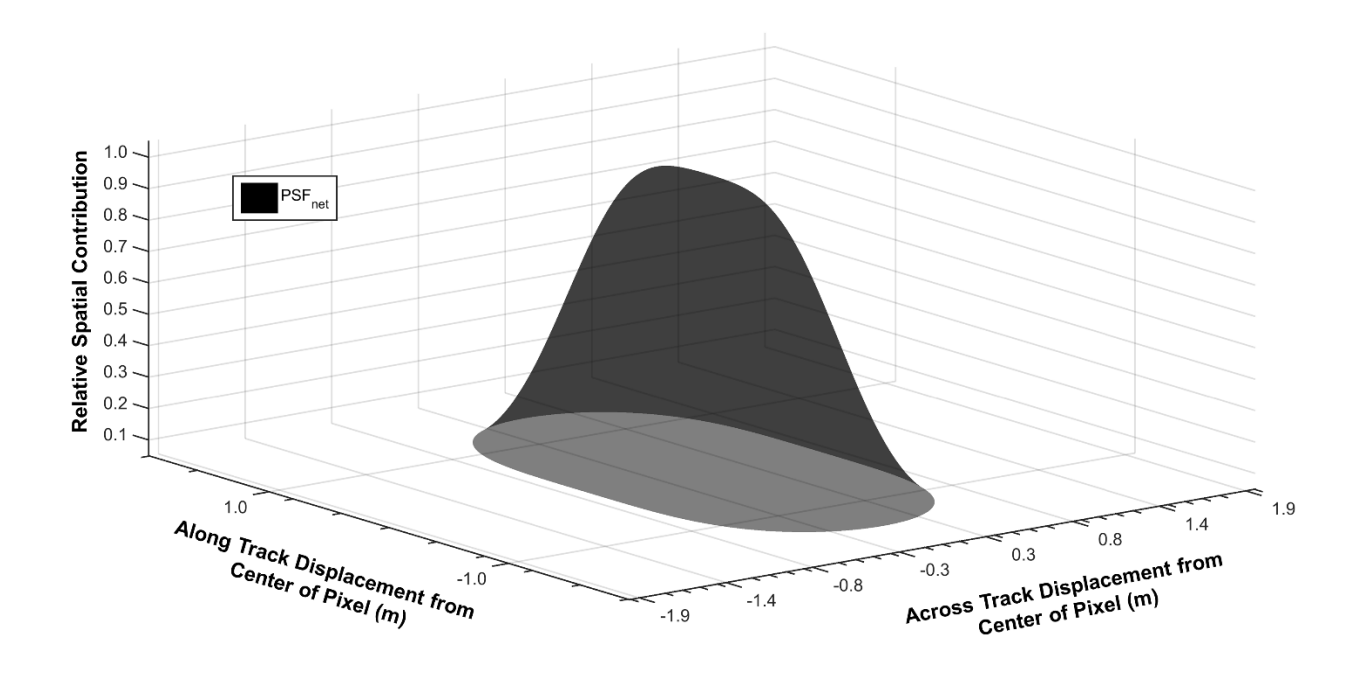


Figure 4.3. The relative spatial contribution to a single Compact Airborne Spectrographic Imager 1500 (CASI) image pixel as a function of across track and along track displacement from the center of the pixel. The grid in the x-y plane corresponds with the actual pixel sizes (0.55 m in the across track direction and 1.99 m in the along track direction). As such, each square within the grid corresponds to the traditional spatial boundary of a single pixel. Most of the signal originates from materials within the spatial boundary of the center pixel. It is important to note that there is a substantial contribution from materials within the spatial boundaries of neighbouring pixels.

4.2.3. Simulated HSI Data

To investigate the implication of sensor induced blurring, the study simulated two hyperspectral images at the same approximate spatial resolution of the Mer Bleue CASI dataset (0.55 m in the across track and 1.99 m in the along track). The two artificial images were only distinguished by the simulated sensor blurring. The first image (referred to as the ideal image) represented an ideal scenario where the PSF_{net} was uniform across the spatial boundaries of each pixel. The PSF_{net} of the second image (referred to as the non–ideal image) was modelled after the derived spatial response of the CASI.

Both datasets were derived from an image that was designed to represent a vegetation plot within the Mer Bleue Peatland at a spatial resolution 50 times finer than that of the real—world CASI data. The value for each spectral band and spatial pixel in the high spatial resolution imagery was randomly generated from a normal distribution. The mean and standard deviation of the normal distribution for each band were derived from the basic statistics of a 3660—pixel

vegetation region of interest (**Figure 4.4**) from the original Mer Bleu CASI imagery. All the pixels within the region of interest were examined to ensure that vegetation was not contaminated by any man—made structures or objects. The mean value of each spectral band from the vegetation region of interest in the Mer Bleue CASI imagery was used as the mean value of the normal distribution for each band. Due to the change in scale between the pixels within the high spatial resolution imagery and the real—world CASI imagery, the calculated standard deviation needed to be scaled up by a factor of 50 before it could be used as the standard deviation in the normal distribution.

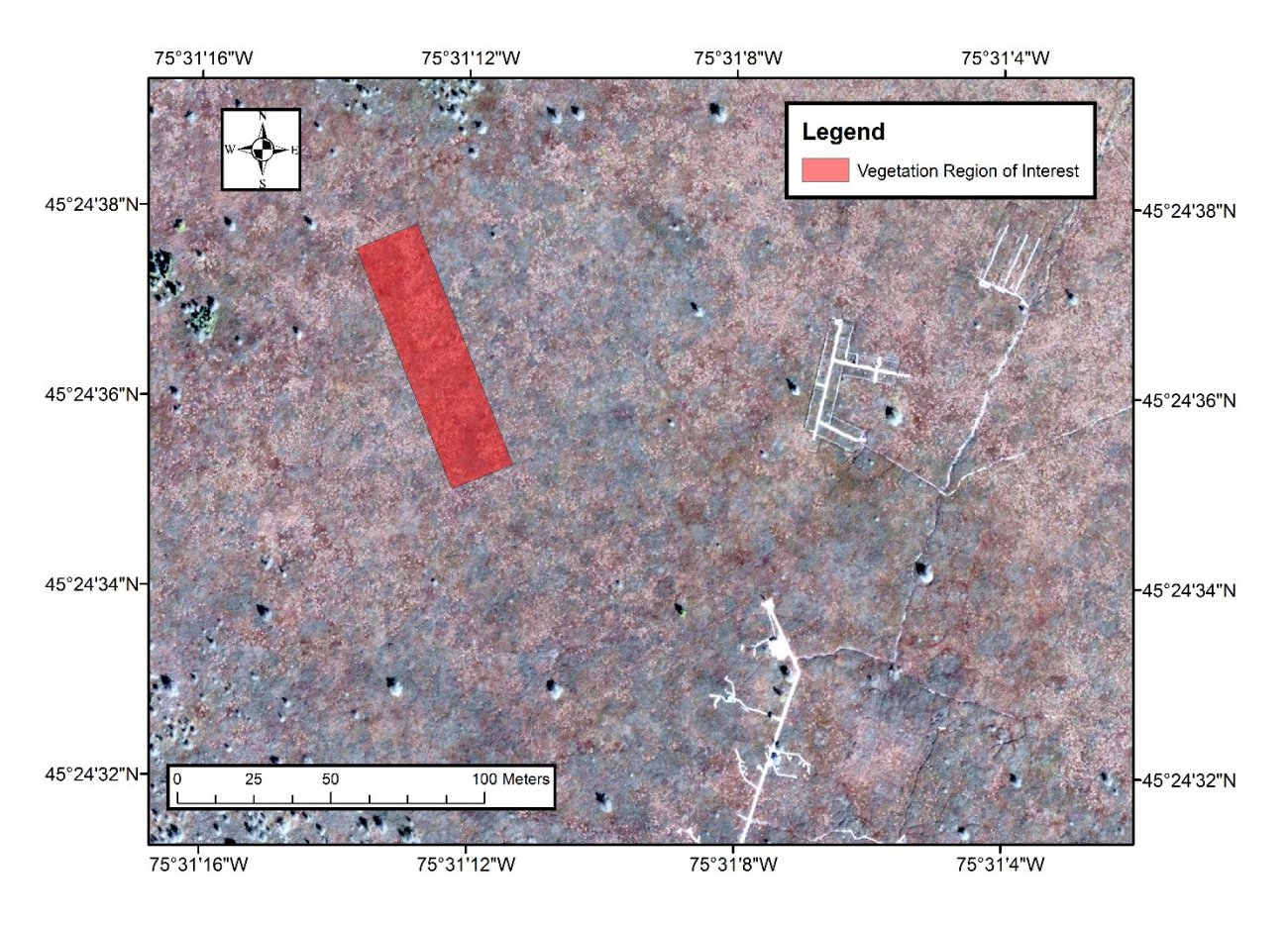


Figure 4.4. The vegetation region of interest selected from the Mer Bleue Peatland. The region of interest is characterized by a hummock–hollow microtopography that corresponds to small scale patterns (2–4 m) in surface vegetation and surface reflectance. Hummocks are elevated mounds of dense vascular cover while hollows are the lower–lying areas composed primarily of Sphagnum spp. mosses. The orthophoto (0.2 m spatial resolution) was collected for the National Capital Commission of Canada (Source: Ottawa Orthophotos, 2011).

To simulate the ideal and non-ideal images from the generated high spatial resolution imagery, the derived PSF_{net} function (Section 4.2.2) was convolved with the high spatial resolution imagery and spatially resampled to the native resolution of the CASI imagery using a nearest-neighbour resampling approach. The nearest neighbour resampling approach was equivalent to directly downsampling the convolved data by a factor of 50 to the native resolution of the CASI imagery. Given the described simulation process, 100% of the information content was known for both the ideal and non-ideal datasets and the environment that they represented. The mean and standard deviation for each spectral band within the two simulated images were calculated to assess the implication of sensor induced blurring effects on the global statistics of the simulated HSI data. When comparing the mean of the spectra from two different images, a ttest with unequal variances was applied separately for each spectral band. The mean spectra from the two compared images at a particular band were deemed significantly different if the p-value was less than 0.05. When comparing the standard deviation (and, in extension, variance) in the spectra from two different images, an F-test for equal variances was applied separately for each spectral band. The standard deviation in the spectra from the compared images at a particular band were deemed significantly different if the p-value was less than 0.05.

4.2.4. Visualizing and Quantifying Spatial Correlations

For an ideal sensor, the spatial correlations within HSI data are piece—wise smooth, meaning that neighbouring pixels are highly correlated (Bioucas-Dias et al., 2013). This correlation structure can be leveraged to quantify sensor—generated spatial correlations with a correlation metric. The Pearson product—moment correlation coefficient (*CC*) has been shown as a strong tool in the analysis of HSI data (Inamdar et al., 2018). The *CC* is a measure of linear association between two variables. It is formally given (Lee Rodgers and Nicewander, 1988) by the following equation:

$$CC = \frac{\sum (A_i - \bar{A})(B_i - \bar{B})}{\sqrt{\sum (A_i - \bar{A})^2 \sum (B_i - \bar{B})^2}},\tag{7}$$

where A_i , B_i , \bar{A} , \bar{B} represent the two variables of interest and their means, respectively.

The CC was implemented to characterize the spatial structure of correlations in the HSI data. In particular, the correlation coefficient was calculated between the spectra of adjacent pixels in both the across track and along track directions. This process was repeated for distant neighbors.

The calculated correlation coefficients were grouped by pixel displacement separately in the across track and along track. The mean and standard deviation of each group was calculated to quantify the strength and variability of the spatial correlations within each image as a function of pixel displacement. This algorithm fundamentally represents the horizontal and vertical cross–section of an autocorrelation function with characterized variability.

4.2.5. Mitigating Sensor Generated Spatial Correlations Using the PSF_{net}

A simple deconvolution algorithm was developed to mitigate sensor–generated blurring effects in HSI data. The approach utilizes the theoretically derived PSF_{net} to mitigate contributions from the materials within the spatial boundaries of neighbouring pixels. Let $S_{0,0}$ represent the reflectance spectrum of any given pixel in an ungeocorrected HSI dataset that is contaminated by sensor–generated blurring effects. Let $S_{i,j}$ represent the spectrum from the pixel displaced by i rows and j columns from the pixel of interest. Let $a_{i,j}$ represent the weighted contribution of $S_{i,j}$ to $S_{0,0}$, as calculated by integrating the PSF_{net} over the spatial boundaries of the pixel from which $S_{i,j}$ originated. By removing the relative contribution of all neighbouring pixels from $S_{0,0}$, it is possible to generate a new approximation, $\hat{S}_{0,0}$, in which sensor–generated blurring effects have been mitigated:

$$\hat{S}_{0,0} = \frac{S_{0,0} - \sum_{i \in Z | i \neq 0} \sum_{j \in Z | j \neq 0} a_{i,j} S_{i,j}}{a_{0,0}}.$$
(8)

The algorithm assumes sub–pixel materials are homogenous. Furthermore, neighbouring pixels are assumed to be unaffected by sensor blurring effects. Similar assumptions have been made in other deconvolution studies (e.g., (Huang et al., 2002; Townshend et al., 2000)). Although these assumptions may not be realistic for real–world spectral imagery, they are reasonable to simplify the system as the spatial variability within each pixel is often non–constant and unknown.

4.2.6. Algorithm Application to Simulated HSI Data

The developed algorithms were applied to the simulated datasets. In particular, the spatial correlation structure of the two simulated images were characterized by the *CC* based algorithm. The algorithm was assessed based on its ability to detect discrepancies in the spatial correlation structure. The deconvolution algorithm was implemented by applying Equation (8) to the

simulated dataset with a non-ideal PSF_{net} . The deconvolved dataset was referred to as the corrected non-ideal image. The deconvolution algorithm was assessed based on its ability to recover the global statistics of the ideal imagery from the non-ideal imagery. The deconvolution algorithm was also evaluated based on its ability to restore the spatial correlation structure observed in the ideal image by the CC based algorithm. The study used the same statistical tests as in Section 4.2.3 (t-test with unequal variances and f-test for equal variances) when comparing the mean and standard deviation of the spectra between the two images within the vegetation region of interest. To ensure that the observed trends in global statistics were actually linked to a decrease of difference between the ideal and non-ideal image after the application of the deconvolution algorithm, Euclidean distance was calculated on a pixel-by-pixel basis between the ideal imagery and both the non-ideal and corrected non-ideal images.

4.2.7. Algorithm Application to Real–World HSI Data

The developed algorithms were applied to the collected HSI data at the Mer Bleue peatland and the calibration site at the airport with a primary focus on the deconvolution algorithm. Image sharpness was assessed by calculating the slope of a horizonal profile across image structures with sharp edges that separated two materials with distinct spectral signatures. In the Mer Bleue image, the edge of the grey calibration tarp was analyzed. In the airport imagery, the edge along the border of a concrete—asphalt transition was used. The *CC* based algorithm was then applied to vegetation within the Mer Bleue image to assess the correlation structure of the images before and after the application of the deconvolution algorithm. The mean and standard deviation in each spectral band of the Mer Bleue imagery within the vegetation region of interest was calculated before and after the application of the deconvolution algorithm. The study used the same statistical tests as in Section 4.2.3 (t—test with unequal variances and f—test for equal variances) when comparing the mean and standard deviation of the spectra between the two images within the vegetation region of interest.

4.3. Results

4.3.1. Theoretical Point Spread Function for Each CASI Pixel

The total PSF_{net} was Gaussian in nature, with a maximum value at the origin, dropping off rapidly to approximately zero past a distance of 2 m (~1 pixel) in the along track and 1 m in the across track (~2 pixels) directions. **Figure 4.5** displays the relative contribution to the spectrum from a single pixel. Only 55.5% of the signal from each pixel originated from the materials

within its spatial boundaries. Neighbouring contributions in the across track were larger than in the along track.

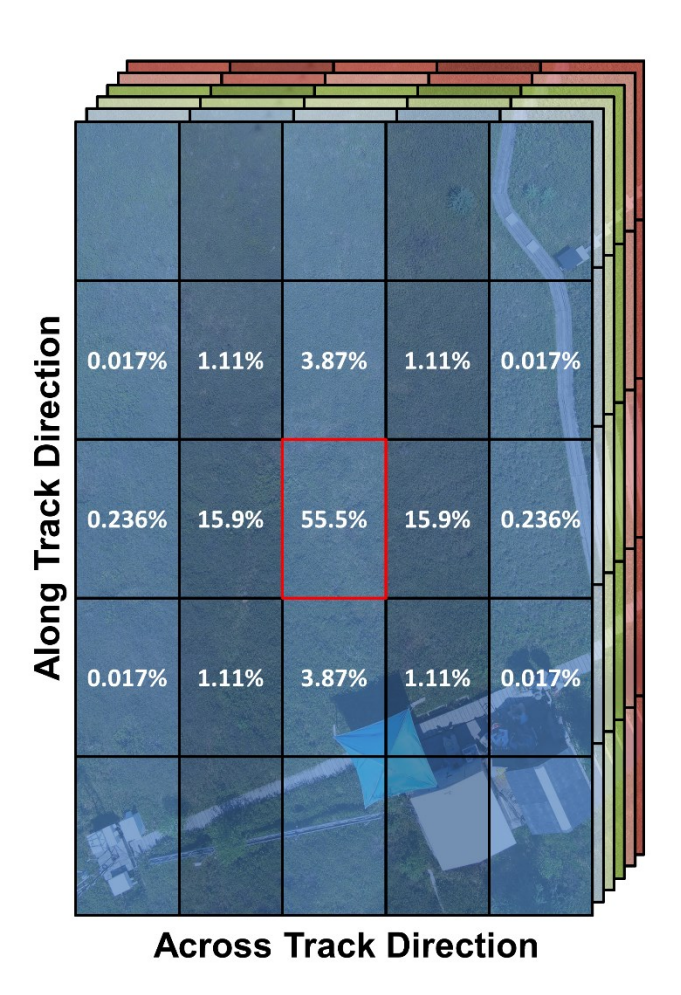


Figure 4.5. The spatial contribution to the spectrum of the center Compact Airborne Spectrographic Imager 1500 (CASI) pixel from materials within the boundaries of neighbouring pixels. The red square represents the spatial boundaries of the center pixel, as determined by the raw pixel resolution. The black squares represent the spatial boundaries of neighbouring pixels. Only 55.5% of the spectral signal originates from materials within the spatial boundaries of the center pixel. The remaining 44.5% of the signal comes from the materials within the spatial boundaries of the neighbouring pixels. The underlying scene in the figure is a photograph of the Mer Bleue Peatland collected from an unmanned aerial vehicle.

4.3.2. Simulated HSI Data

Panels A and B in **Figure 4.6** display the ideal and non-ideal simulated hyperspectral images, respectively. The mean and standard deviation of each spectral band from the ideal and non-ideal images are shown in **Figure 4.7**. The mean values for each spectral band between the two simulated datasets were not significantly different (two-sample t-test with unequal

variances applied separately for each spectral band; p-values > 0.792). In fact, the mean spectra were essentially identical, with an extremely small root-mean-square deviation (0.004%) relative to the range of the data (28.2%). The variances between the two simulated datasets for each spectral band were significantly different (F-test for equal variances applied separately for each spectral band; p-values < 1.29E-26). The standard deviation in each spectral band of the non-ideal simulated dataset were 31.1%–38.9% smaller when compared to the ideal imagery.

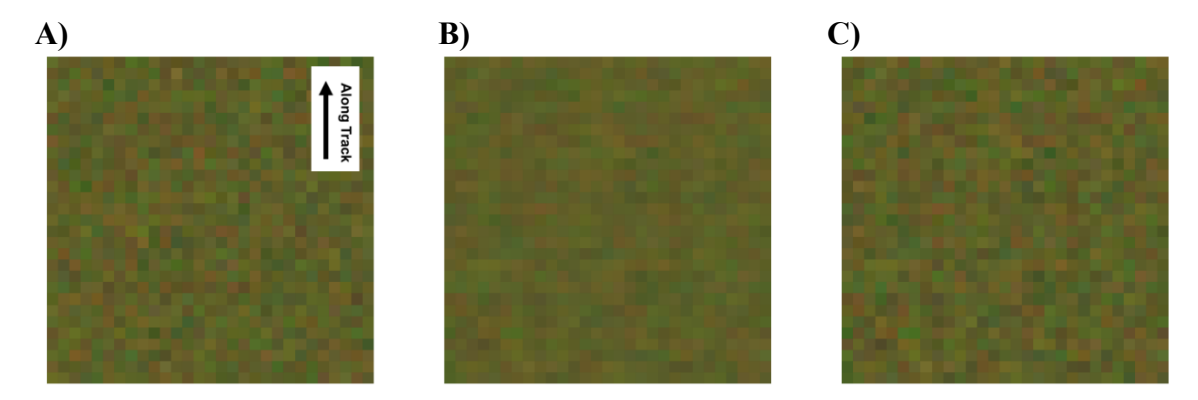


Figure 4.6. Simulated hyperspectral imaging data representative of the Mer Bleue Peatland. The images are displayed in true colour (Red = 639.5 nm \pm 1.2, Green = 551.0 nm \pm 1.2, Blue = 460.1 nm \pm 1.2). In the display, all three bands are linearly stretched between 0% and 12%. **A)** The ideal simulated image that was derived with a uniform point spread function. **B)** The non-ideal simulated image that was derived with the Compact Airborne Spectrographic Imager 1500 (CASI) point spread function. **C)** The corrected non-ideal simulated image that was derived by applying the developed deconvolution algorithm to the non-ideal simulated image. All images were simulated at the same spatial resolution as the real—world CASI imagery (across track = 0.55 m, along track = 1.99 m). The simulated datasets were used to characterize the implications of sensor—generated spatial correlations while testing the developed algorithms.

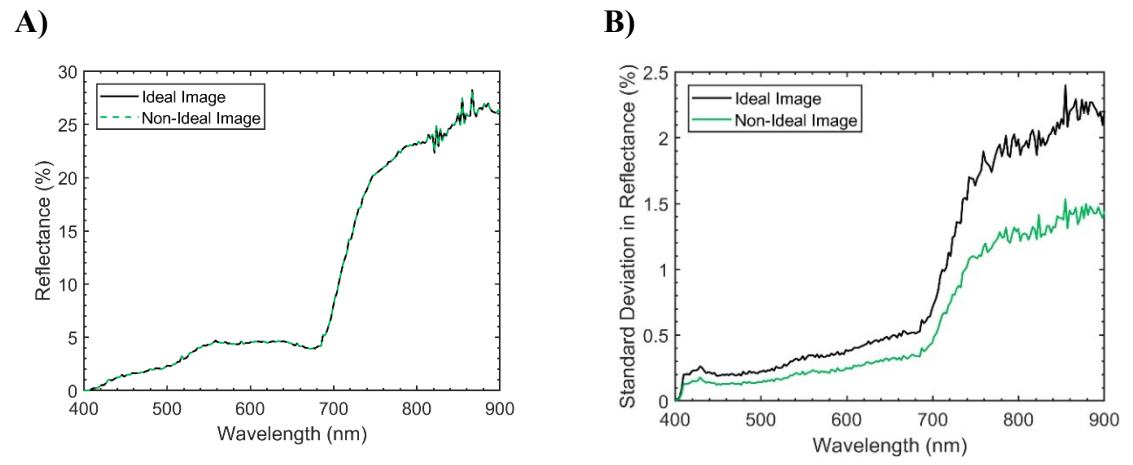


Figure 4.7. The mean (plot **A**) and standard deviation (plot **B**) for each spectral band of the ideal (uniform point spread function) and non-ideal (Compact Airborne Spectrographic Imager 1500 point spread function) simulated images. There were no observable differences in the mean spectrum from each image. The attenuation in standard deviation suggests that sensor blurring eliminated some of the natural variability observed in the ideal image. This is problematic given the importance of second-order statistics in the analysis of high dimensional data.

4.3.3. Algorithm Application to Simulated HSI Data

The results of the CC based method when applied to the ideal and non-ideal imagery are displayed in **Figure 4.8**. The figures also display the results of the CC based method when applied to the non-ideal imagery after using the developed deconvolution algorithm (referred to as the corrected non-ideal image). The corrected non-ideal image can be seen in panel C of **Figure 4.6**. In the ideal simulated imagery, the mean of each group was relatively constant at a value of \sim 0.982 for all pixel displacements in both the across track and along track directions. Similarly, the standard deviation around the mean was also constant at a value of \sim 0.002. For pixel displacements >1, the mean and standard deviation of each CC group in the non-ideal imagery was relatively constant at a value of 0.992 and 0.001, respectively. This trend held for both the across track and along track directions. For a pixel displacement value of 1, the mean CC was relatively large, at a value of 0.996 and 0.993 in the across track and along track directions, respectively. The corresponding standard deviations around these mean values were relatively small, at 0.0006 and 0.0008. The standard deviation in the calculated CCs for the non-ideal simulated dataset were 54.0%–75.4% smaller when compared to the ideal imagery.

The mean *CC* for each group in the corrected non–ideal image were similar in magnitude to the ideal image. For the corrected image in the along track direction, the mean and standard

deviation of each CC group was relatively constant at values of 0.981 and 0.002, respectively. This trend held for pixel displacements > 2 in the across–track. The mean CC for pixels displaced by 1 in the across track direction was relatively large (0.984). The opposite trend was observed for pixel displacements of 2 in the across–track, with a mean value of 0.978 and a standard deviation of 0.003. The standard deviation in the CCs of the corrected non–ideal image were within 23.3% of the values calculated for the ideal image.

The mean and standard deviation of each spectral band in the corrected non-ideal image were almost identical to those of the ideal image; there was no significant difference in the mean (two-sample t-test with unequal variances applied separately for each spectral band; p-values > 0.825) or variance (F-test for equal variances applied separately for each spectral band; p-values > 0.056). The mean spectra were essentially identical, with an extremely small root-mean—square deviation (0.004%) relative to the range of the data (28.2%). Similarly, the variability in each spectral band of the ideal and corrected non-ideal images were essentially identical, given the small root-mean-square deviation (0.03%) in the standard deviation relative to the range in the data (2.4%) (**Figure 4.9**). The standard deviations in each spectral band of the corrected non-ideal image were within 6.8% of the values calculated for the ideal image. The Euclidean distance (in units of reflectance) between the ideal imagery and both the non-ideal and corrected non-ideal images are displayed in **Figure 4.10A** and **Figure 4.10B**, respectively. After the application of the deconvolution algorithm, the Euclidean distance between the ideal and non-ideal imagery decreased by an average of 1.91%.

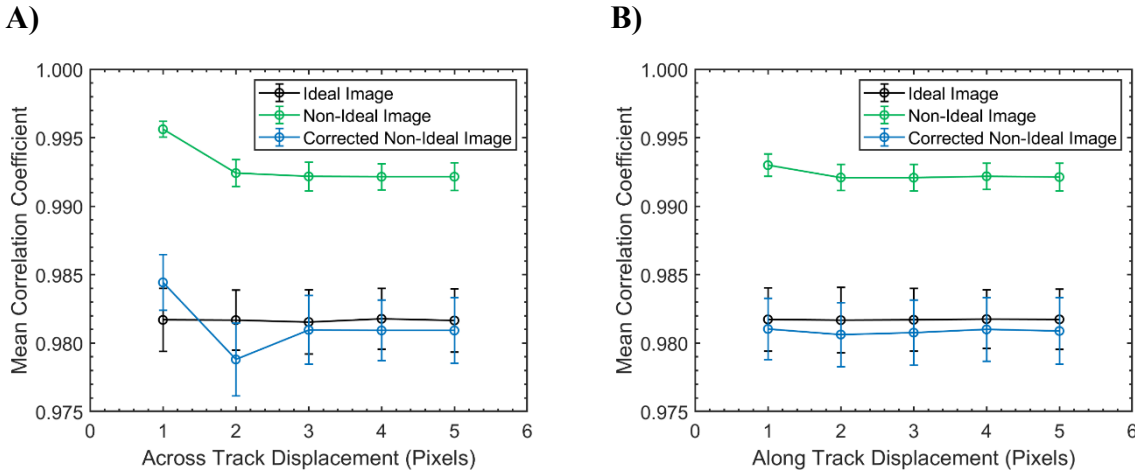


Figure 4.8. The mean correlation coefficient as a function of pixel displacement in the across track (plot A) and along track (plot B) directions of the ideal (uniform point spread function), non-ideal (Compact Airborne Spectrographic Imager 1500 point spread function) and corrected non-ideal simulated images. The bars around each mean give the 1-sigma window. The mean and standard deviation quantified the strength and variability of the spatial correlations present within each image. The corrected non-ideal image was generated by applying the developed deconvolution algorithm. In the ideal image, there was no spatial correlation structure. The Compact Airborne Spectrographic Imager 1500 point spread function used to simulate the non-ideal image, and the associated image blurring, introduced a spatial correlation structure. The spatial correlation structure of the ideal image was recovered from the non-ideal image using the developed deconvolution algorithm.

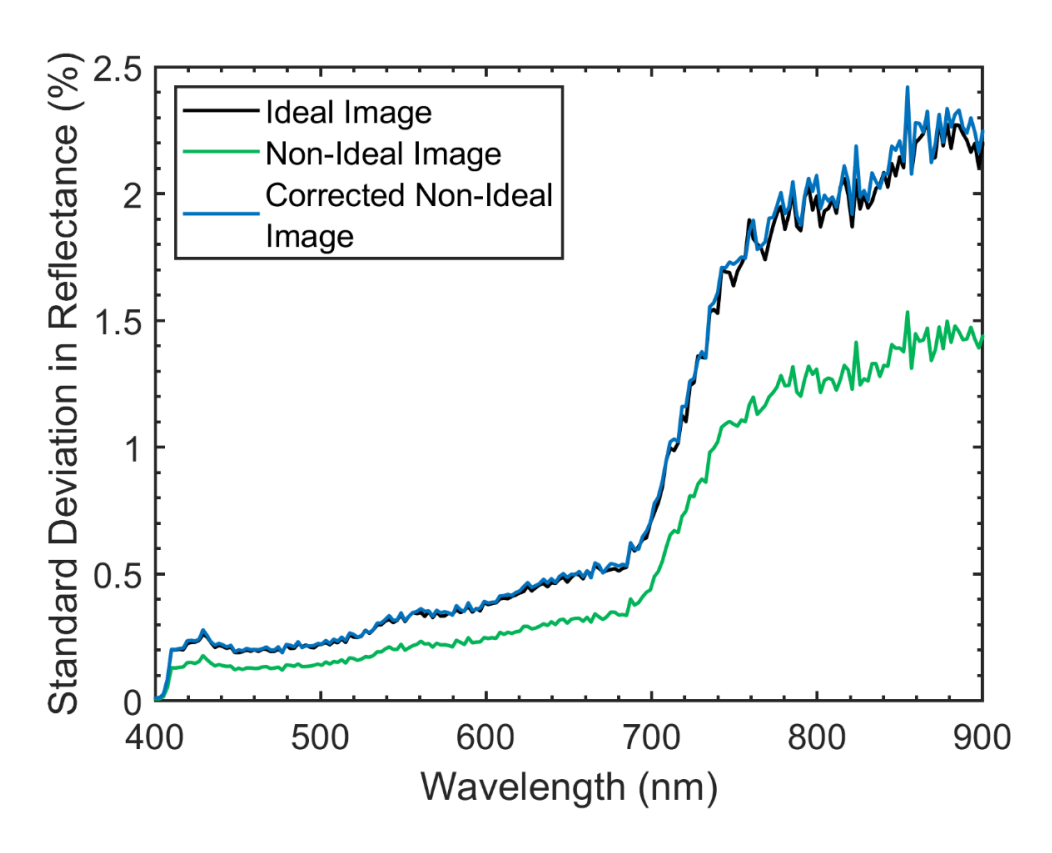


Figure 4.9. The standard deviation in each spectral band of the ideal (uniform point spread function), non-ideal (Compact Airborne Spectrographic Imager 1500 point spread function) and corrected non-ideal image. The corrected non-ideal image was generated by applying the developed deconvolution algorithm. The attenuation in the standard deviation of the non-ideal image suggests that sensor blurring eliminated some of the natural variability observed in the ideal image. The natural variability in each spectral band of the ideal image was restored from the non-ideal image by applying the deconvolution algorithm.

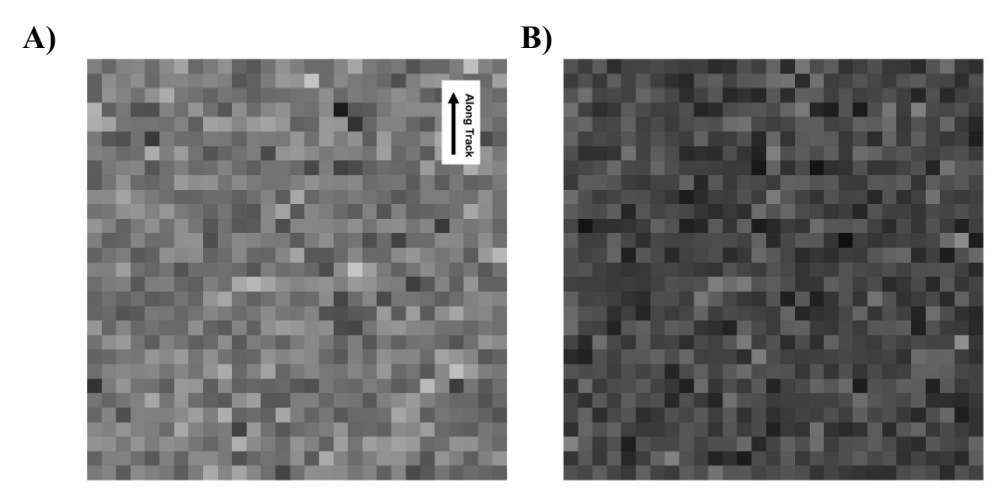


Figure 4.10. The Euclidean distance (in units of reflectance) between the ideal imagery and both the non-ideal (plot **A**) and corrected non-ideal (plot **B**) images. The grayscale display is linearly stretched between 10% and 20%. After the application of the deconvolution algorithm, the Euclidean distance between the ideal and non-ideal imagery decreased by an average of 1.91%.

4.3.4. Algorithm Application to Real–World HSI Data

After applying the deconvolution algorithm to the HSI data, both images were qualitatively sharper (**Figure 4.11** and **Figure 4.12**). The spectrum from the 7 adjacent across track pixels for each of the studied edges in the Mer Bleue and Airport imagery were displayed in **Figure 4.13**. Pixel 4 was the closest to the studied edge. The pixel number represents the order of each adjacent pixel in the across track direction. In plots **A** and **B**, pixels 1–3 represented spectra from the calibration tarp while pixels 5–7 represented spectra from vegetation at the Mer Bleue Peatland. In plots **C** and **D**, pixels 1–3 represented spectra from the concrete while pixels 5–7 represented spectra from asphalt from the airport. Plots **A** and **C** are from the original imagery, while plots **B** and **D** are from the deconvolved imagery. In both the Mer Bleue and Airport imagery, the spectra from pixels 3 and 5 were closer to the spectra of their respective materials after the application of the deconvolution algorithm. In particular, the spectrum from pixel 5 dropped in magnitude, aligning with that of pixels 6 and 7 in both sets of imagery. Quantitatively, the deconvolution algorithm increased the maximum change in reflectance per pixel across the two studied edges by a relatively constant factor of 1.4 (**Figure 4.14**).

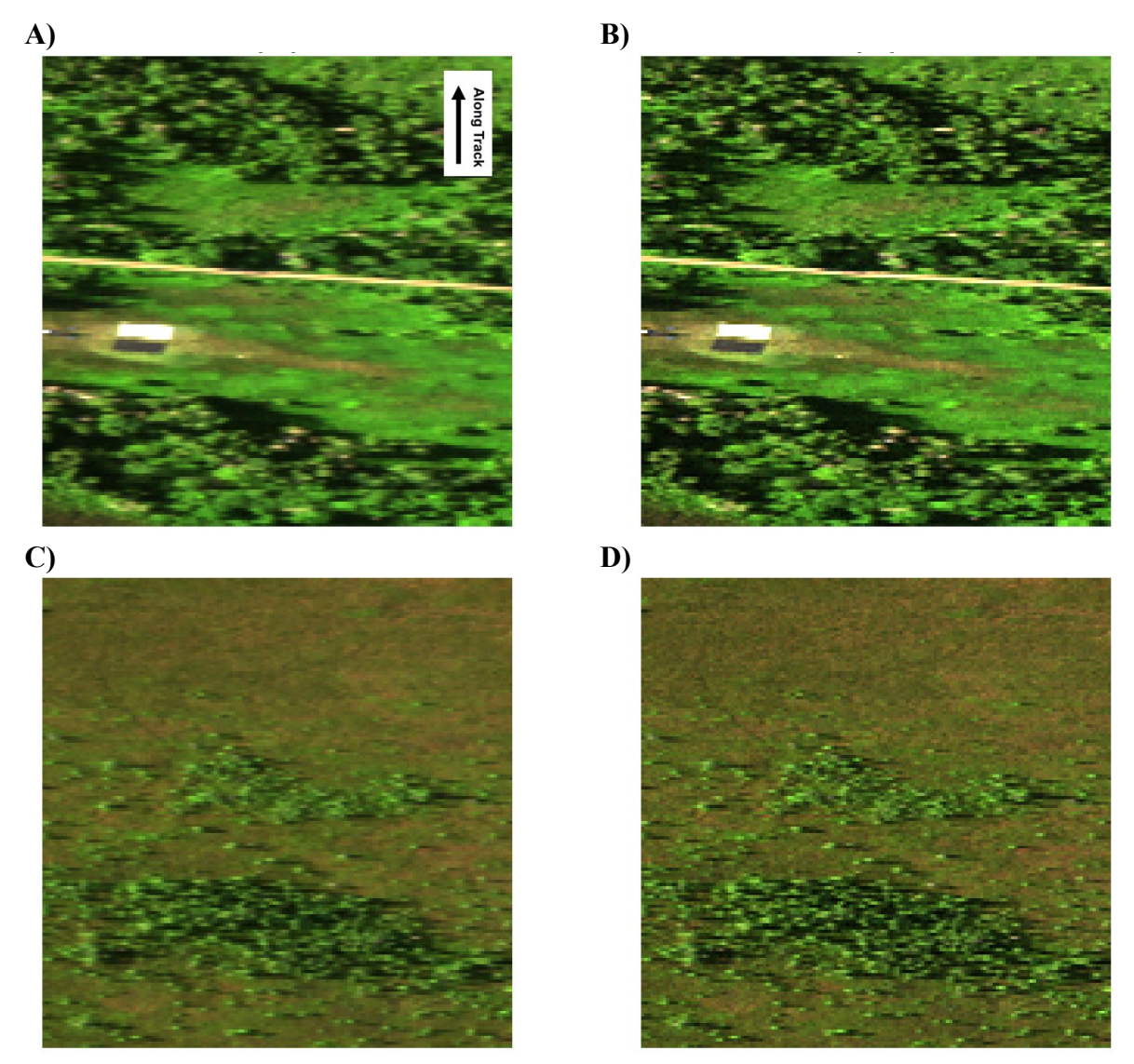


Figure 4.11. Hyperspectral imaging data over the Mer Bleue Peatland before and after the application of the deconvolution algorithm. The images are displayed in true colour (Red = $639.5 \text{ nm} \pm 1.2 \text{ Green} = 551.0 \text{ nm} \pm 1.2, \text{ Blue} = 460.1 \text{ nm} \pm 1.2$). In the display, all three bands are linearly stretched between 0% and 12%. Panels (A) and (C) display the original imagery. Panels (B) and (D) represent the same two scenes after the deconvolution algorithm was applied. Both images were qualitatively sharpened by the deconvolution algorithm.

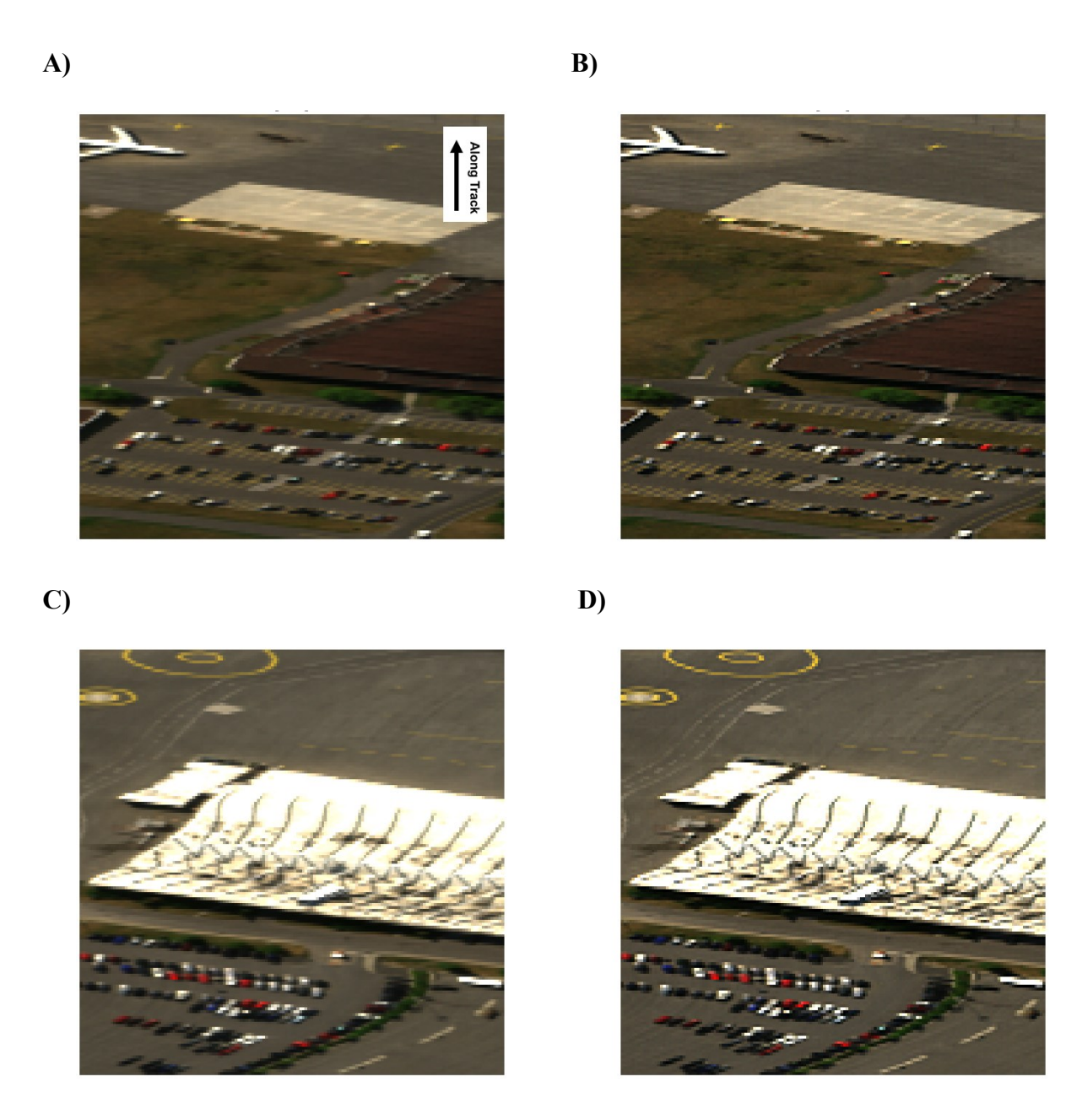


Figure 4.12. Hyperspectral imaging data over the Macdonald–Cartier International Airport (Ottawa, Ontario, Canada) before and after the application of the developed deconvolution algorithm. The images are displayed in true colour ($Red = 639.5 \text{ nm} \pm 1.2$, Green = $551.0 \text{ nm} \pm 1.196$, Blue = $460.1 \text{ nm} \pm 1.2$). In the display, all three bands are linearly stretched between 0% and 40%. Panels (**A**) and (**C**) display the original imagery. Panels (**B**) and (**D**) represent the same two scenes after the deconvolution algorithm was applied. Both images were qualitatively sharpened by the deconvolution algorithm.

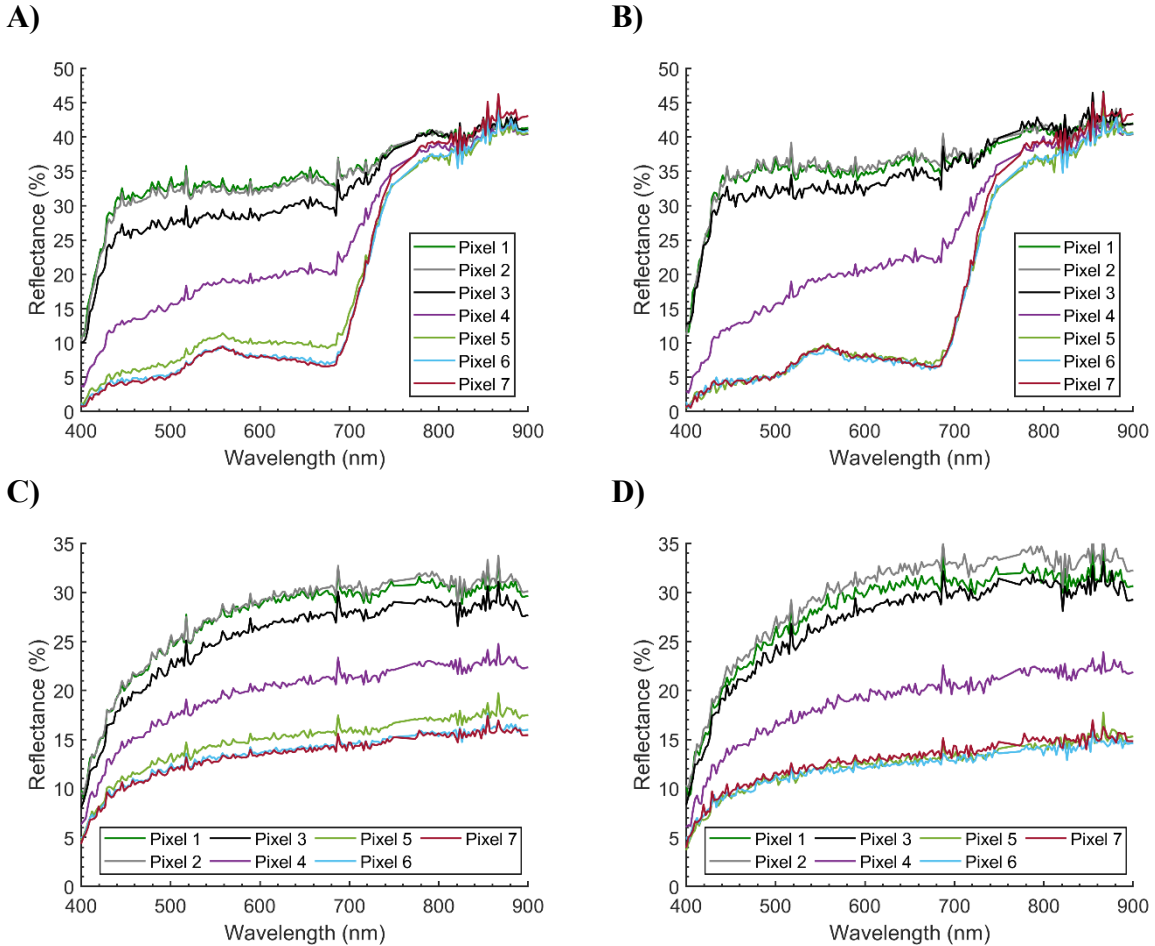


Figure 4.13. A,B) The 7 adjacent across track pixels to the edge of the calibration tarp in the Mer Bleue imagery before (plot A) and after (plot B) the deconvolution algorithm was applied. Pixel 4 was the closest to the studied edge. The pixel number represents the order of each adjacent pixel in the across track direction. Pixels 1–3 represented spectra from the calibration tarp while pixels 5–7 represented spectra from vegetation. C,D) The 7 adjacent across track pixels to the edge of the concrete—asphalt transition at the calibration site within the airport imagery before (plot C) and after (plot D) the deconvolution algorithm was applied. Pixel 4 was the closest to the studied edge. Pixels 1–3 represented spectra from the concrete while pixels 5–7 represented spectra from asphalt. In both the Mer Bleue and Airport imagery, the spectra from pixels 3 and 5 were closer to the spectra of their respective materials after the application of the deconvolution algorithm. In particular, spectra from pixel 5 dropped in magnitude, aligning with that of pixels 6 and 7 in both sets of imagery. This suggests that the algorithm mitigated influences from neighbouring pixel materials.

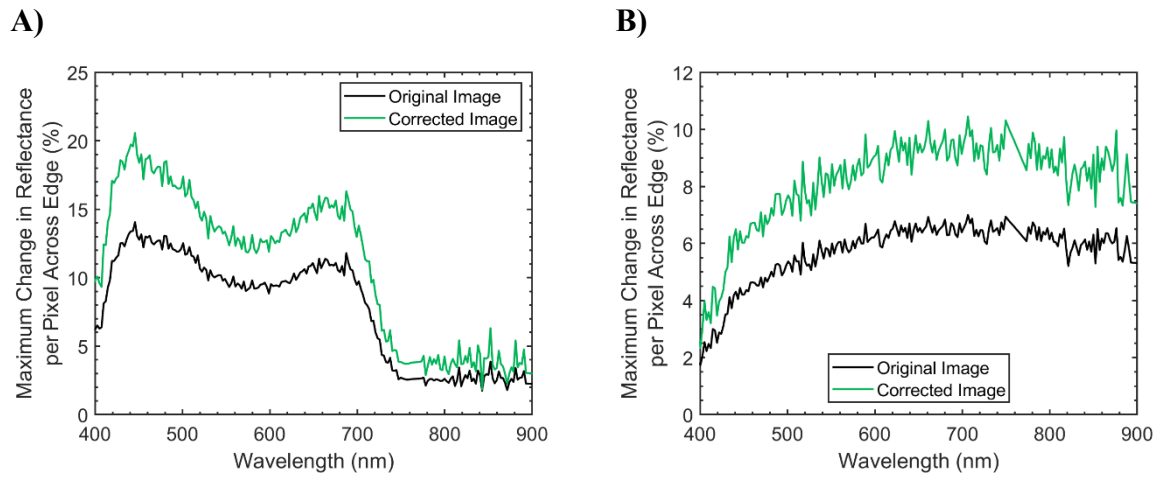


Figure 4.14. A) The maximum change in reflectance per pixel across the edge of the calibration tarp in the Mer Bleue imagery. B) The maximum change in reflectance per pixel across the edge along the border of the concrete—asphalt transition at the calibration site within the airport imagery. The larger the number, the sharper the change from the two materials that defined the edge. The corrected image was generated by applying the developed deconvolution algorithm to the real—world Compact Airborne Spectrographic Imager 1500 (CASI) data. The corrected imagery was sharper than the original imagery. The imagery was sharpened by the developed deconvolution algorithm.

When applying the *CC* based algorithm to the vegetation region of interest from the CASI data, there were several differences in the correlation structure between the imagery before and after the application of the deconvolution algorithm (**Figure 4.15**). Most notably, the algorithm decreased correlation levels in both the across track and along track directions from 0.998 to 0.994 while increasing the standard deviation in the system approximately by a factor of 3. In the along track direction, spatial correlations decreased marginally along with pixel displacement. This trend held in the across—track, however, there was also a sinusoidal trend that repeated every four pixels (~2 m). This sinusoidal feature dampened by a pixel displacement of 5 in the original imagery. In the corrected imagery, this sinusoidal structure was far more prominent, dampening at a pixel displacement of 12.

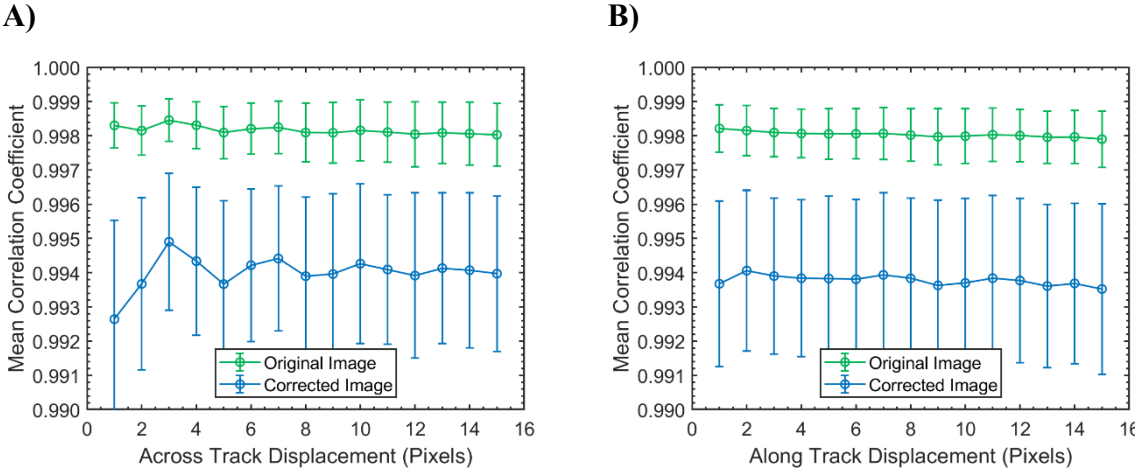


Figure 4.15. The mean correlation coefficient as a function of pixel displacement in the across track (plot A) and along track (plot B) direction of the vegetation region of interest from the Mer Bleue CASI imagery. The bars around each mean give the 1–sigma window. The mean and standard deviation quantified the strength and variability of the spatial correlations present within each image. The corrected image was generated by applying the developed deconvolution algorithm to the real—world Mer Bleue Compact Airborne Spectrographic Imager 1500 (CASI) data. In general, the deconvolution algorithm decreased the observed spatial correlations while increasing spatial variability. After applying the developed deconvolution algorithm, the micro—spatial patterns of vegetation could be observed more clearly in the across track direction. The micro—spatial patterns of vegetation could not be observed in the along track.

The mean and standard deviation of the vegetation plot in the original and corrected imagery is displayed in **Figure 4.16**. The mean values for each spectral band between the original and corrected image within the vegetation pixels were not significantly different (two–sample t–test with unequal variances applied separately for each spectral band; p–values > 0.855). The mean spectra were essentially identical, with an extremely small root–mean–square deviation (<0.0035%) relative to the range of the data (31.2%). The variances between the two simulated datasets for each spectral band were significantly different (F–test for equal variances applied separately for each spectral band; p–values < 6.143E–37).

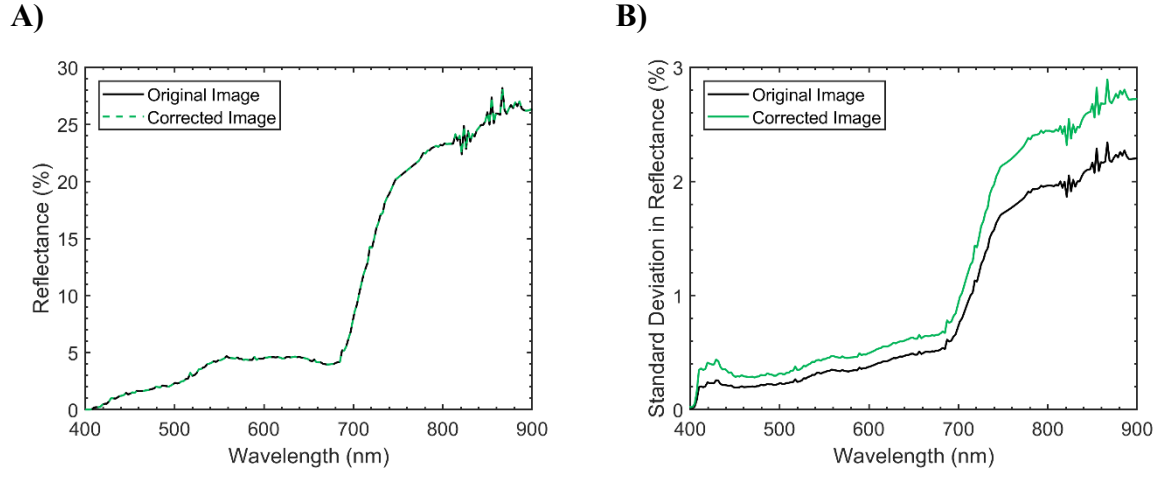


Figure 4.16. The mean (plot A) and standard deviation (plot B) of the vegetation region of interest from the Mer Bleue imagery. The corrected image was generated by applying the developed deconvolution algorithm to the real—world Mer Bleue Compact Airborne Spectrographic Imager 1500 (CASI) data. The standard deviation valued measured the variability in each spectral band. Although there was no difference in the mean, the standard deviation increased after applying the deconvolution algorithm. This increase likely occurred as the deconvolution reintroduced some of the lost natural variations in each spectral band.

4.4. Discussion

The objective of this study was to characterize and mitigate sensor–generated blurring effects in airborne HSI data with simple and intuitive tools, emphasizing the importance of point spread functions. By studying the derived CASI PSF_{net} it was possible to understand the potential implications of sensor induced blurring effects in general.

The CASI *PSF*_{net} was roughly Gaussian in shape, extending two pixels in the across track and one pixel in the along track before reaching a value of approximately zero. The spread of this function meant that approximately 45% of the signal in the spectrum from each CASI pixel originated from materials within the spatial boundaries of neighboring pixels (**Figure 4.5**). Although these values may seem quite large, it is important to recognize that they are not unreasonable for all imaging spectrometers. For instance, based on the 2D Gaussian *PSF*_{net} (full—width at half—maximum of 28 m in the across track and 32 m in the along track (Markham et al. 2018)) for each Landsat 8 Operational Land Imager pixel (bands 1–7), only ~57.7% of the signal originates from materials within the spatial boundaries of each pixel. This value is almost identical to that of the CASI.

With the ideal (perfectly uniform PSF_{net} over pixel boundaries) and non–ideal (CASI PSF_{net}) simulated images, the effects of sensor induced blurring could be quantified. From the basic

second—order image statistics, sensor induced blurring reduced the spectral variability, as measured by the standard deviation, in the simulated scene by 31.1%—38.9% for all spectral bands. Given the importance of second—order statistics in the analysis of high dimensional data (Lee and Landgrebe, 1993), the change in standard deviation exemplifies the information loss associated with sensor blurring. The *CC* based method further investigated this loss of information, while verifying the detective and corrective capabilities of the developed algorithms.

The CASI PSF_{net} modified the spatial correlation structure of the image. In particular, spatial correlations substantially increased for closely neighbouring pixels displaced by 2 in the across track and 1 in the along track. These results directly reflect the structure of the CASI PSF_{net} . Although the PSF_{net} did not extend spatially more than 2 pixels, spatial correlations were saturated for all pixel displacements. These saturated correlations showcase that local sensor blurring can have global impacts on HSI data.

The standard deviation in the calculated CCs indicated that sensor induced blurring attenuated the natural spatial variability in the image. Once again, this trend held on a global scale but was more prominent locally. In fact, sensor induced blurring reduced the variability, as measured by the standard deviation, in the spatial correlation structure of the imaged scene by 54.0%–75.4% for all pixel displacements. As expected, these findings suggest that sensor generated spatial correlations act to mask and distort the spatial dynamics of the imaged scene while removing natural variations.

It is important to note that, despite only observing deviations in the CCs from the 3rd_4th decimal places, the *CC* based method was still sensitive to the simulated blurring effects, especially the saturated correlations and the asymmetry between the across track and along track spatial correlations. With this in mind, the *CC* based algorithm can be applied to assess the effectiveness of deconvolution algorithms that attempt to mitigate sensor–generated spatial correlations. This was exemplified by the developed deconvolution algorithm.

When applied to the non-ideal dataset, the deconvolution algorithm brought the spectral variability, as measured by the standard deviation, within 6.8% of the spectral variability in the ideal image. In fact, there was no significant difference in the spectral variance between the ideal and corrected non-ideal datasets. This finding suggests that the deconvolution algorithm

recovered some of the information that was attenuated by sensor blurring. A closer examination of the algorithm's performance with the *CC* based method revealed similar conclusions.

In the corrected non-ideal image, the standard deviation values around the calculated mean CCs were relatively constant, similar in magnitude to those observed in the ideal simulated image. In fact, the spatial structure in the along track of the ideal image was almost completely recovered from the non-ideal image. A similar statement can be made in the across track for pixel displacements > 2. Although the algorithm decreased the mean CC for neighbouring pixels separated by < 3 in the across—track, it did not completely restore the spatial structure. At a pixel displacement of 1, there were still elevated correlation levels. In addition, the algorithm introduced an artificial decorrelation at a pixel displacement of 2 in the across–track. This decorrelation was a consequence of the pure pixel assumption. Although these artifacts may be problematic for some applications, it is important to recognize that deconvolution is an ill-posed problem; information will always be lost in a blurred image and thus it is impossible to perfectly eliminate sensor blurring effects, especially at the attenuated high frequencies (Chaudhuri et al., 2014). In fact, many algorithms suffer from difficulties in restoring high-frequency spatial structures in HSI data (Henrot et al., 2013). Despite introducing this decorrelation, the equalized spatial correlation levels revealed that the algorithm restored the spatial structure of the dataset to some degree. A similar conclusion could be drawn from the standard deviation of the calculated CC values. The deconvolution algorithm brought the variability in the spatial correlation structure of the non-ideal imagery within 23.3% of the spatial variability in the ideal imagery.

To ensure that the increase of spatial and spectral variability was linked to a decrease of difference between the ideal and non-ideal simulated images, Euclidean distance metrics were calculated. As shown in **Figure 4.10**, the Euclidean distance between the ideal and non-ideal imagery decreased by an average of 1.91% after the application of the deconvolution algorithm. Along with these findings, the increased spectral and spatial variability continue to suggest that the simple deconvolution algorithm is restoring some of the information that was lost to sensor blurring.

To assess the deconvolution algorithm further, it was applied to real—world HSI data. When applied to both real—world HSI datasets, there was a qualitative increase in image sharpness (**Figure 4.11** and **Figure 4.12**). In the airport imagery, this was evident from the abundant high

contrast edges produced by man—made structures like roads, buildings, cars and parking lots. Although there were fewer high contrast materials in the Mer Bleue imagery, the calibration tarps and tree crowns clearly showcased the sharpening effect of the deconvolution algorithm. These observations were supported quantitatively by analyzing the edge of a calibration tarp in the Mer Bleue imagery and the edges of the calibration site in the airport imagery. In **Figure 4.13**, the spectra of the adjacent 7 pixels to each of the studied edges were displayed. In both the Mer Bleue and Airport imagery, the spectra from the pixels immediately neighbouring the edge pixel were closer to the spectra of their respective materials after the application of the deconvolution algorithm, indicating that the imagery had been sharpened. This finding was supported by **Figure 4.14**, where the horizontal profile across the two edges increased in slope (an in extension image sharpness) by an approximate factor of 1.4 after the application of the deconvolution algorithm.

To showcase an application of the developed algorithms, the CC based method was applied to the vegetation region of interest (Figure 4.4) in the Mer Bleue image to analyze the spatial correlation structure of the plot before and after the deconvolution was applied. In the original imagery, spatial correlations decreased marginally over space in both the across track and along track. This decrease likely corresponded with changes in the peatland over large spatial scales. With a priori knowledge of the micro spatial patterns in the vegetation and surface elevation (Figure 4.1) (Arroyo-Mora et al., 2018a; Arroyo-Mora et al., 2018b; Eppinga et al., 2008; Lafleur et al., 2005), it was possible to observe a subtle sinusoidal structure in the correlation plots that repeated every 4 pixels (2 m) in the across—track. The period of this sinusoidal structure agreed with the spatial scale of the patterns in surface vegetation and microtopography (2–4m) (Belyea and Baird, 2006; Malhotra et al., 2016; Wilson, 2012). These trends were not apparent in the along track. However, this was to be expected based on the Nyquist sampling theorem; the sampling frequency in the along track direction (0.5 cycles per m) was less than the frequency of the patterns in surface vegetation and microtopography (0.25–0.5 cycles per m) multiplied by 2 and thus undetectable. After applying the deconvolution algorithm, there was an overall decrease in the spatial correlations. The simulation results suggested that this decrease was due to the attenuation of sensor induced correlations. The sinusoidal structure in the across track was more prominent after the deconvolution algorithm was applied. These results suggest that the deconvolution algorithm highlighted the patterns in microtopography and, in extension,

vegetation composition. In this particular ecosystem, the microtopography is important as it covaries with surface vegetation, water table position and carbon uptake from the atmosphere (Malhotra et al., 2016).

Although more sophisticated deconvolution algorithms exist (Chaudhuri et al., 2014; Fang et al., 2017; Henrot et al., 2013; Jackett et al., 2011), they may rely on a higher level of mathematical understanding to implement. Without a fundamental understanding of a method, its implementation can lead to inaccurate interpretations. This may be problematic for end–users, who often do not have the appropriate information to implement these methodologies effectively. The presented method is intuitive; the algorithm is based on the principles of the classical linear spectral unmixing model and is thus simple to understand and implement. Despite using a wavelength–independent *PSF*_{opt} that was derived based on a theoretical calculation as opposed to an empirical estimation, the algorithm was capable of sharping real–world HSI data. With a more rigorous characterization of the optical blurring that accounts for the wavelength dependence of the point spread function, the performance of the deconvolution algorithm could be improved, resulting in sharper imagery and a spatial correlation structure more representative of the imaged scene.

Before applying the developed deconvolution algorithm, it is critical to consider the implications and validity of the pure pixel assumption made in Equation 8. Given that HSI may be characterized by sensor blurring and noise that varies as a function of wavelength, these assumptions may not be realistic for real—world spectral imagery. They are, however, reasonable to simplify the system since the spatial variability within each pixel is often non—constant and unknown. Similar pure pixel assumptions have been made in other deconvolution studies (e.g., (Huang et al., 2002; Townshend et al., 2000)) at the satellite level. This is encouraging since the pure pixel assumption is more likely to hold for airborne systems that collect data at higher spatial resolution (<3 m). That being said, end—users must be aware that the assumption may lead to anomalies in the deconvolved data.

As previously mentioned, the pure pixel assumption resulted in artificial decorrelations at pixel displacements from 1–2 pixels in the across–track. Such artifacts are potentially problematic for certain applications, likely showing overestimated contrast along edges. Despite this, the real–world imagery was sharpened with promising results. When analyzing the

sharpening effects on a pixel—by—pixel basis (**Figure 4.13**), there was little evidence that showed any overestimated contrast in the imagery. That being said, given the construction of the algorithm, overestimated contrast is possible. Furthermore, this algorithm has no constraints on the positivity of the deconvolved imagery. Since negative reflectance has no real—world significance, edges between extremely high reflectance and low reflectance materials may need to be checked for non—positive anomalies. Furthermore, low signal and excessive noise in the data may negatively affect the performance of the algorithm, also resulting in negative values. As such, the application of this algorithm may not be ideal for low signal to noise ratio bands.

This work focused on developing a simplistic approach to deconvolution, which is a complex and ill–posed problem. To satisfy this objective, the pure pixel assumption was necessary, despite the potential for introducing data anomalies. In this study, there is ample evidence to suggest that the algorithm is effective at mitigating sensor–generated blurring effects within the data. With this in mind, if sensor blurring is the major obstacle for a particular application, the developed methodologies should be sufficient to observe noticeable improvements. From that point, more complex deconvolution algorithms (e.g., Chaudhuri et al., 2014; Fang et al., 2017; Henrot et al., 2013; Jackett et al., 2011) can be implemented if the developed algorithm is introducing too many artifacts in the HSI data.

From both the simulated and real—world HSI data, sensor induced blurring effects were found to mask and distort the natural spatial dynamics of the imaged scene. These blurring effects directly corresponded with the structure of the PSF_{net} . From this work, it is clear that sensor induced blurring effects are not always identical in the across track and along track directions. The same can be said for the raw pixel sizes. In fact, for pushbroom sensors, pixels are inherently more rectangular than square. Although it is possible to obtain nearly identical pixel resolutions in the across track and along track directions, technical restraints may make it difficult. For instance, the resolution in the along track is determined by the integration time and platform speed, both of which have impacts on other aspects of the data (signal to noise ratio, positional accuracy, etc.), especially for low altitude platforms such as unmanned aerial systems (Arroyo-Mora et al., 2019). This implies that HSI data characterize the scene on a slightly different scale in the across track than the along track directions, with different blurring levels. Given the scale—dependent nature of many natural phenomena, patterns could be observable in one spatial

dimension, but not the other. This was exemplified by the Mer Bleue imagery, in which the micro–spatial patterns in surface vegetation could be detected in the across–track, but not the along track. Without considering the *PSF*_{net} and the heading of the data acquisition flight, sensor induced blurring effects could be mistaken for directional trends in the data. Similarly, scale–dependent phenomena observable in either the across track or along track directions could lead to assumptions of directionality to a trend where none exists.

Given the importance of sensor point spread functions, when applying HSI data, it may be critical to analyze the imagery in its original sensor geometry, pre–geocorrection. Many geocorrective methods operate by resampling the raw HSI data on a linear grid with a nearest neighbour resampling technique (Warren et al., 2014). As such, the location of each point in the raw imagery is shifted and the original sensor geometry is lost to some degree. Consequently, the natural spatial correlations of a scene are likely to be distorted even further as sensor–generated spatial correlations are shifted to fit the pre–specified linear grid. Further research into the spatial correlation structure of HSI data post geocorrection would give insight into the cumulative effects of sensor–generated spatial correlations.

Overall, the described methodology provides a framework to characterize and mitigate the implications of sensor induced blurring; by generating a simulated dataset with known blurring, it is possible to understand the degree to which sensor blurring (and the associated artificial spatial correlations) will affect real—world HSI data. At the satellite level, there exists a rich body of literature that characterizes and discusses the implications of sensor point spread functions on a wide array of remote sensing tasks such as classification (Huang et al., 2002), sub—pixel feature detection (Radoux et al., 2016) and spectral unmixing (Wang et al., 2018). Unfortunately, the implications of sensor point spread functions have yet to be fully investigated to the same degree at the airborne level. This may be problematic as sensor—generated blurring effects may be more prominent for airborne platforms (Schläpfer et al., 2007).

4.5. Conclusions

The presented work developed two simple and intuitive algorithms to characterize and mitigate sensor–generated spatial correlations while emphasizing the implications of sensor point spread functions. The first algorithm applied the *CC* to observe and quantify spatial correlations. The algorithm was able to characterize the structure of spatial correlations. Sensor blurring was

found to increase spatial correlations and decrease the variance in the system. The second algorithm developed in the study used a theoretically derived PSF_{net} to mitigate sensor–generated spatial correlations in HSI data. The CC-based algorithm showed that sensor blurring generated spatial correlations that removed 54.0%–75.4% of the natural variability in the spatial correlation structure of the simulated HSI data. Sensor blurring effects were also shown to remove 31.1%— 38.9% of the spectral variability. The deconvolution algorithm mitigated the observed sensor generated spatial correlations while restoring a large portion of the natural spectral and spatial variability of the scene. In the real-world I data, the deconvolution algorithm quantitatively and qualitatively sharpened the imagery, decreasing levels of spatial correlation within the imagery that were likely caused by sensor induced blurring effects. As a result of this effect, the natural spatial correlations within the imagery were enhanced. The presented work substantiates the implications of sensor-generated spatial correlations while providing a framework to analyze the implications of sensor blurring for specific applications. Point spread functions are shown to be crucial variables to complement traditional parameters such as pixel resolution and geometric accuracy. The developed tools are simple and intuitive. As a result, they can be readily applied by end-users of all expertise levels to consider the impact of sensor-generated blurring, and by extension, spatial correlations, HSI applications.

4.6. References

Aiazzi, B., Selva, M., Arienzo, A., & Baronti, S. (2019). Influence of the system MTF on the on-board lossless compression of hyperspectral raw data. *Remote Sensing*, 11, 791

Arroyo-Mora, J., Kalacska, M., Soffer, R., Moore, T., Roulet, N., Juutinen, S., Ifimov, G., Leblanc, G., & Inamdar, D. (2018a). Airborne hyperspectral evaluation of maximum gross photosynthesis, gravimetric water content, and CO₂ uptake efficiency of the Mer Bleue ombrotrophic peatland. *Remote Sensing*, 10, 565

Arroyo-Mora, J.P., Kalacska, M., Inamdar, D., Soffer, R., Lucanus, O., Gorman, J., Naprstek, T., Schaaf, E.S., Ifimov, G., & Elmer, K. (2019). Implementation of a UAV–hyperspectral pushbroom imager for ecological monitoring. *Drones*, *3*, 12

Arroyo-Mora, J.P., Kalacska, M., Soffer, R., Ifimov, G., Leblanc, G., Schaaf, E.S., & Lucanus, O. (2018b). Evaluation of phenospectral dynamics with Sentinel-2A using a bottom-up approach in a northern ombrotrophic peatland. *Remote Sensing of Environment, 216*, 544-560

Babey, S., & Anger, C. (1989). A Compact Airborne Spectrographic Imager (CASI). In: *Proceedings of the IGARSS '89 Quantitative Remote Sensing: An Economic Tool for the Nineties* (pp. 1028-1031)

Belyea, L.R., & Baird, A.J. (2006). Beyond "the limits to peat bog growth": Cross-scale feedback in peatland development. *Ecological Monographs*, 76, 299-322

- Bergen, K.M., Brown, D.G., Rutherford, J.F., & Gustafson, E.J. (2005). Change detection with heterogeneous data using ecoregional stratification, statistical summaries and a land allocation algorithm. *Remote Sensing of Environment, 97*, 434-446
- Berk, A., Anderson, G.P., Bernstein, L.S., Acharya, P.K., Dothe, H., Matthew, M.W., Adler-Golden, S.M., Chetwynd Jr, J.H., Richtsmeier, S.C., & Pukall, B. (1999). MODTRAN4 radiative transfer modeling for atmospheric correction. In: *Proceedings of the Optical Spectroscopic Techniques and instrumentation for atmospheric and space research III* (pp. 348-353): International Society for Optics and Photonics
- Bioucas-Dias, J.M., Plaza, A., Camps-Valls, G., Scheunders, P., Nasrabadi, N., & Chanussot, J. (2013). Hyperspectral remote sensing data analysis and future challenges. *IEEE Geoscience and Remote Sensing Magazine*, 1, 6-36
- Chang, G., Mahoney, K., Briggs-Whitmire, A., Kohler, D., Mobley, C., Lewis, M., Moline, M., Boss, E., Kim, M., & Philpot, W. (2004). The new age of hyperspectral oceanography. *Oceanography*, 71, 16-23
- Chaudhuri, S., Velmurugan, R., & Rameshan, R. (2014). Chapter 2 Mathematical background. In: *Blind Image Deconvolution: Methods and Convergence*: Springer International Publishing
- Cloutis, E.A. (1996). Review article hyperspectral geological remote sensing: evaluation of analytical techniques. *International Journal of Remote Sensing*, 17, 2215-2242
- Cocks, T., Jenssen, R., Stewart, A., Wilson, I., & Shields, T. (1998). The HyMapTM airborne hyperspectral sensor: The system, calibration and performance. In: *Proceedings of the 1st EARSeL workshop on Imaging Spectroscopy* (pp. 37-42): EARSeL
- Dale, L.M., Thewis, A., Boudry, C., Rotar, I., Dardenne, P., Baeten, V., & Pierna, J.A.F. (2013). Hyperspectral imaging applications in agriculture and agro-food product quality and safety control: A review. *Applied Spectroscopy Reviews*, 48, 142-159
- Eismann, M.T. (2012). Hyperspectral remote sensing. In: *Hyperspectral Remote Sensing*. Bellingham: SPIE
- Eppinga, M.B., Rietkerk, M., Borren, W., Lapshina, E.D., Bleuten, W., & Wassen, M.J. (2008). Regular surface patterning of peatlands: Confronting theory with field data. *Ecosystems*, 11, 520-536
- Fang, H., Luo, C., Zhou, G., & Wang, X. (2017). Hyperspectral image deconvolution with a spectral-spatial total variation regularization. *Canadian Journal of Remote Sensing*, 43, 384-395
- Green, R.O., Eastwood, M.L., Sarture, C.M., Chrien, T.G., Aronsson, M., Chippendale, B.J., Faust, J.A., Pavri, B.E., Chovit, C.J., & Solis, M. (1998). Imaging spectroscopy and the airborne visible/infrared imaging spectrometer (AVIRIS). *Remote Sensing of Environment*, 65, 227-248
- Heiskanen, J. (2006). Tree cover and height estimation in the Fennoscandian tundra—taiga transition zone using multiangular MISR data. *Remote Sensing of Environment*, 103, 97-114
- Henrot, S., Soussen, C., & Brie, D. (2013). Fast positive deconvolution of hyperspectral images. *IEEE Transactions on Image Processing*, 22, 828-833

- Hu, W., Xue, J., & Zheng, N. (2012). PSF estimation via gradient domain correlation. *IEEE Transactions on Image Processing*, 21, 386-392
- Huang, C., Townshend, J.R., Liang, S., Kalluri, S.N., & DeFries, R.S. (2002). Impact of sensor's point spread function on land cover characterization: assessment and deconvolution. *Remote Sensing of Environment*, 80, 203-212
- Inamdar, D., Leblanc, G., Soffer, R.J., & Kalacska, M. (2018). The Correlation Coefficient as a Simple Tool for the Localization of Errors in Spectroscopic Imaging Data. *Remote Sensing*, 10, 231
- Jackett, C., Turner, P., Lovell, J., & Williams, R. (2011). Deconvolution of MODIS imagery using multiscale maximum entropy. *Remote sensing letters*, 2, 179-187
- Kalacska, M., Arroyo-Mora, J., Soffer, R., Roulet, N., Moore, T., Humphreys, E., Leblanc, G., Lucanus, O., & Inamdar, D. (2018). Estimating peatland water table depth and net ecosystem exchange: A comparison between satellite and airborne imagery. *Remote Sensing*, 10
- Kalacska, M., & Bell, L. (2006). Remote sensing as a tool for the detection of clandestine mass graves. *Canadian Society of Forensic Science Journal*, 39, 1-13
- Kalacska, M.E., Bell, L.S., Sanchez-Azofeifa, G.A., & Caelli, T. (2009). The application of remote sensing for detecting mass graves: an experimental animal case study from Costa Rica. *Journal of Forensic Sciences*, *54*, 159-166
- Koch, B. (2010). Status and future of laser scanning, synthetic aperture radar and hyperspectral remote sensing data for forest biomass assessment. *ISPRS Journal of Photogrammetry and Remote Sensing*, 65, 581-590
- Kruse, F.A., Richardson, L.L., & Ambrosia, V.G. (1997). Techniques developed for geologic analysis of hyperspectral data applied to near-shore hyperspectral ocean data. In: *Proceedings of the Fourth International Conference on Remote Sensing for Marine and Coastal Environments* (p. 19)
- Lafleur, P.M., Hember, R.A., Admiral, S.W., & Roulet, N.T. (2005). Annual and seasonal variability in evapotranspiration and water table at a shrub-covered bog in southern Ontario, Canada. *Hydrological processes*, 19, 3533-3550
- Lafleur, P.M., Roulet, N.T., Bubier, J., Frolking, S., & Moore, T.R. (2003). Interannual variability in the peatland-atmosphere carbon dioxide exchange at an ombrotrophic bog. *Global Biogeochemical Cycles*, 17, 13
- Leblanc, G., Kalacska, M., & Soffer, R. (2014). Detection of single graves by airborne hyperspectral imaging. *Forensic Science International*, 245, 17-23
- Lee, C., & Landgrebe, D.A. (1993). Analyzing high-dimensional multispectral data. *IEEE Transactions on Geoscience and Remote Sensing*, 31, 792-800
- Lee Rodgers, J., & Nicewander, W.A. (1988). Thirteen ways to look at the correlation coefficient. *The American Statistician*, 42, 59-66
- Malhotra, A., Roulet, N.T., Wilson, P., Giroux-Bougard, X., & Harris, L.I. (2016). Ecohydrological feedbacks in peatlands: an empirical test of the relationship among vegetation, microtopography and water table. *Ecohydrology*, *9*, 1346-1357

- Markham, B.L. (1985). The Landsat sensors' spatial responses. *IEEE Transactions on Geoscience and Remote Sensing*, 864-875
- Markham, B.L., Arvidson, T., Barsi, J.A., Choate, M., Kaita, E., Levy, R., Lubke, M., & Masek, J.G. (2018). Landsat Program. In: S. Liang (Ed.), *Comprehensive Remote Sensing* (pp. 27-90). Oxford: Elsevier
- Migdall, S., Klug, P., Denis, A., & Bach, H. (2012). The additional value of hyperspectral data for smart farming. In: *Proceedings of IGARSS 2012* (pp. 7329-7332): IEEE
- Murphy, R.J., Monteiro, S.T., & Schneider, S. (2012). Evaluating classification techniques for mapping vertical geology using field-based hyperspectral sensors. *IEEE Transactions on Geoscience and Remote Sensing*, 50, 3066-3080
- Pearlman, J.S., Barry, P.S., Segal, C.C., Shepanski, J., Beiso, D., & Carman, S.L. (2003). Hyperion, a space-based imaging spectrometer. *IEEE Transactions on Geoscience and Remote Sensing*, 41, 1160-1173
- Peng, G., Ruiliang, P., Biging, G.S., & Larrieu, M.R. (2003). Estimation of forest leaf area index using vegetation indices derived from hyperion hyperspectral data. *IEEE Transactions on Geoscience and Remote Sensing*, 41, 1355-1362
- Puttonen, E., Suomalainen, J., Hakala, T., & Peltoniemi, J. (2009). Measurement of reflectance properties of asphalt surfaces and their usability as reference targets for aerial photos. *IEEE Transactions on Geoscience and Remote Sensing*, 47, 2330-2339
- Radoux, J., Chomé, G., Jacques, D.C., Waldner, F., Bellemans, N., Matton, N., Lamarche, C., d'Andrimont, R., & Defourny, P. (2016). Sentinel-2's potential for sub-pixel landscape feature detection. *Remote Sensing*, *8*, 488
- Rauchmiller, R.F., & Schowengerdt, R.A. (1988). Measurement of the landsat thematic mapper modulation transfer function using an array of point sources. *Optical Engineering*, 27, 334-343, 310
- Ryan, J.P., Davis, C.O., Tufillaro, N.B., Kudela, R.M., & Gao, B.-C. (2014). Application of the hyperspectral imager for the coastal ocean to phytoplankton ecology studies in Monterey Bay, CA, USA. *Remote Sensing*, 6, 1007-1025
- Schläpfer, D., Nieke, J., & Itten, K.I. (2007). Spatial PSF nonuniformity effects in airborne pushbroom imaging spectrometry data. *IEEE Transactions on Geoscience and Remote Sensing*, 45, 458-468
- Schowengerdt, R.A. (2006). 3.4. Spatial Response. In: *Remote Sensing: Models and Methods for Image Processing*: Elsevier
- Schowengerdt, R.A., Antos, R.L., & Slater, P.N. (1974). *Measurement of the Earth Resources Technology Satellite (ERTS-1) multi-spectral scanner OTF from operational imagery*. SPIE
- Simms, D.M., Waine, T.W., Taylor, J.C., & Juniper, G.R. (2014). The application of time-series MODIS NDVI profiles for the acquisition of crop information across Afghanistan. *International Journal of Remote Sensing*, *35*, 6234-6254

- Smith, M.-L., Martin, M.E., Plourde, L., & Ollinger, S.V. (2003). Analysis of hyperspectral data for estimation of temperate forest canopy nitrogen concentration: comparison between an airborne (AVIRIS) and a spaceborne (Hyperion) sensor. *IEEE Transactions on Geoscience and Remote Sensing*, 41, 1332-1337
- Soffer, R.J., Ifimov, G., Arroyo-Mora, J.P., & Kalacska, M. (2019). Validation of airborne hyperspectral imagery from laboratory panel characterization to image quality assessment: Implications for an arctic peatland surrogate simulation site. *Canadian Journal of Remote Sensing*, 45, 476-508
- Tarrant, P., Amacher, J., & Neuer, S. (2010). Assessing the potential of Medium-Resolution Imaging Spectrometer (MERIS) and Moderate-Resolution Imaging Spectroradiometer (MODIS) data for monitoring total suspended matter in small and intermediate sized lakes and reservoirs. *Water Resources Research*, 46
- Torres-Rua, A., Ticlavilca, A., Bachour, R., & McKee, M. (2016). Estimation of surface soil moisture in irrigated lands by assimilation of landsat vegetation indices, surface energy balance products, and relevance vector machines. *Water*, 8, 167
- Townshend, J., Huang, C., Kalluri, S., Defries, R., Liang, S., & Yang, K. (2000). Beware of per-pixel characterization of land cover. *International Journal of Remote Sensing*, 21, 839-843
- Turner, W., Spector, S., Gardiner, N., Fladeland, M., Sterling, E., & Steininger, M. (2003). Remote sensing for biodiversity science and conservation. *Trends in ecology & evolution*, 18, 306-314
- van der Meer, F.D., van der Werff, H.M.A., van Ruitenbeek, F.J.A., Hecker, C.A., Bakker, W.H., Noomen, M.F., van der Meijde, M., Carranza, E.J.M., Smeth, J.B.d., & Woldai, T. (2012). Multi- and hyperspectral geologic remote sensing: A review. *International Journal of Applied Earth Observation and Geoinformation*, 14, 112-128
- Wang, Q., Shi, W., & Atkinson, P.M. (2018). Enhancing spectral unmixing by considering the point spread function effect. *Spatial Statistics*, 28, 271-283
- Warren, M.A., Taylor, B.H., Grant, M.G., & Shutler, J.D. (2014). Data processing of remotely sensed airborne hyperspectral data using the Airborne Processing Library (APL): Geocorrection algorithm descriptions and spatial accuracy assessment. *Computers & Geosciences*, 64, 24-34
- Wilson, P. (2012). The Relationship among Micro-topographical Variation, Water Table Depth and Biogeochemistry in an Ombrotrophic Bog. In: McGill University Libraries
- Yao, H., Tang, L., Tian, L., Brown, R., Bhatnagar, D., & Cleveland, T. (2011). Using hyperspectral data in precision farming applications. *Hyperspectral Remote sensing of vegetation*, 591-607
- Zhang, Z., & Moore, J.C. (2015). Remote Sensing. In: Z. Zhang, & J.C. Moore (Eds.), *Mathematical and Physical Fundamentals of Climate Change* (pp. 111-124). Boston: Elsevier

4.7. Author Contributions

Conceptualization, D.I., M.K, G.L. and J.P.A.—M.; methodology, D.I., M.K, G.L. and J.P.A.—M.; validation, D.I..; formal analysis, D.I.; investigation, D.I.; resources, M.K, G.L, J.P.A.—M.;

data curation, D.I., M.K, G.L. and J.P.A. –M.; writing—original draft preparation, D.I.; writing—review and editing, D.I., M.K, G.L. and J.P.A. –M.; visualization, D.I.; supervision, M.K and G.L.; project administration, M.K.; funding acquisition, D.I, M.K, G.L. and J.P.A. –M.

4.8. Acknowledgments

The authors would like to thank Stephen Achal (formerly of ITRES Research Limited) for information regarding the CASI point spread functions; Dr. Ronald Resmini and Sion Jennings for feedback on the manuscript; and Raymond Soffer, Dr. Nigel Roulet and Dr. Tim Moore for productive discussions. The authors would like to express their appreciation to Defence Research and Development Canada Valcartier for the loan of the CASI instrument and the calibration tarps. The authors would also like to thank the three anonymous reviewers who provided critical feedback on the manuscript.

Connecting Statement (Chapter 4 to Chapter 5)

Chapter 4 developed novel algorithms to characterized sensor generated spatial correlations that were caused by the overlap in the spatial response of neighbouring pixels. The study highlighted that pixels are not square; based on the sensor net point spread function, the spatial response to any given pixel extends past the square boundaries given by the spatial resolution and is non-uniform. When adopting a raster data structure, even under ideal conditions, less than 55% of the signal originates from within the spatial boundaries of a square pixel. The work in chapter 4 is supported by Appendix 7.1, which presents a workflow to account for the spatial point spread function in simulation efforts. This appendix substantiates the importance of considering point spread functions in flight planning, data fusion and data cross-validation efforts. Overall, chapters 4 and 7.1 show that the dimensions of each square pixel in georeferenced raster end products misrepresent the spatial properties of each spectral measurement and thus should be supplemented by sensor point spread functions for optimal data analytics.

Chapter 5 expands on chapters 4 and 7.1, further exploring the manner in which the raster data model misrepresents hyperspectral imaging data. The research explores the negative consequences of assuming that pixels are uniformly distributed across the imaged scene. Specifically, chapter 5 quantifies pixel loss, pixel duplication and pixel shifting errors that are introduced while generating georeferenced HSI raster end products. In the chapter, an alternative point cloud based data representation is proposed for data analytics. This Directly-Georeferenced Hyperspectral Point Cloud data format not only preserves the spatial-spectral data integrity of hyperspectral imaging data (zero pixel loss, pixel duplication and pixel shifting) but is stored at a fraction of the file size. In various applications (e.g., classification, spectra geo-location, target detection), the DHPC outperformed the conventional raster data product due to its ability to preserve spatial-spectral data integrity.

5. The Directly-Georeferenced Hyperspectral Point Cloud (DHPC): Preserving the Integrity of Hyperspectral Imaging Data

Deep Inamdar ¹, Margaret Kalacska ^{1,*}, J. Pablo Arroyo-Mora ² and George Leblanc ^{2,1}

- ¹ Applied Remote Sensing Laboratory, Department of Geography, McGill University, Montréal, QC H3A 0B9, Canada; deep.inamdar@mail.mcgill.ca (D.I.)
- ² Flight Research Laboratory, National Research Council of Canada, Ottawa, ON K1A 0R6, Canada; juanpablo.arroyomora@nrc-cnrc.gc.ca (J.P.A.-M.); George.Leblanc@nrc-cnrc.gc.ca (G.L.)
- * Correspondence: Margaret.kalacska@mcgill.ca; Tel.: +1-514-398-4347; Fax: +1-514-398-7437

This chapter is published in *Frontiers in Remote Sensing*, 2, 9 under the terms and conditions of the Creative Commons Attribution (CC BY) license (http://creativecommons.org/licenses/by/4.0/).

Minor modifications have been made with respect to formating style.

DOI: https://doi.org/10.3389/frsen.2021.675323

Abstract

The raster data model has been the standard format for hyperspectral imaging (HSI) over the last four decades. Unfortunately, it misrepresents HSI data because pixels are not natively square nor uniformly distributed across imaged scenes. To generate end products as rasters with square pixels while preserving spectral data integrity, the nearest neighbor resampling methodology is typically applied. This process compromises spatial data integrity as the pixels from the original HSI data are shifted, duplicated and eliminated so that HSI data can conform to the raster data model structure. Our study presents a novel hyperspectral point cloud data representation that preserves the spatial-spectral integrity of HSI data more effectively than conventional square pixel rasters. This Directly- Georeferenced Hyperspectral Point Cloud (DHPC) is generated through a data fusion workflow that can be readily implemented into existing processing

workflows used by HSI data providers. The effectiveness of the DHPC over conventional square pixel rasters is shown with four HSI datasets. These datasets were collected at three different sites with two different sensors that captured the spectral information from each site at various spatial resolutions (ranging from ~1.5 cm to 2.6 m). The DHPC was assessed based on three data quality metrics (i.e., pixel loss, pixel duplication and pixel shifting), data storage requirements and various HSI applications. All of the studied raster data products were characterized by either substantial pixel loss (~50–75%) or pixel duplication (~35–75%), depending on the resolution of the resampling grid used in the nearest neighbor methodology. Pixel shifting in the raster end products ranged from 0.33 to 1.95 pixels. The DHPC was characterized by zero pixel loss, pixel duplication and pixel shifting. Despite containing additional surface elevation data, the DHPC was up to 13 times smaller in file size than the corresponding rasters. Furthermore, the DHPC consistently outperformed the rasters in all of the tested applications which included classification, spectra geo- location and target detection.

Based on the findings from this work, the developed DHPC data representation has the potential to push the limits of HSI data distribution, analysis and application.

Keywords: spatial data integrity, spectral data integrity, nearest neighbor resampling, pixel loss, pixel duplication, pixel shifting, data fusion, geometric correction

5.1. Introduction

In the era of machine learning, the wealth of spatial-spectral information provided by hyperspectral imaging (HSI) data presents a unique opportunity to model and understand complex dynamics in a variety of applications (Eismann, 2012). For instance, airborne long-wave infrared HSI data have been successfully used for mineral exploration, mining and geohazard monitoring through the detection of rock forming and alteration minerals (Riley and Hecker, 2013). In vegetation studies for example, visible and near-infrared airborne HSI data have been used with thermal imagery for the early detection of Xylella fastidiosa, a pathogenic floral bacterium (Poblete et al., 2020). The success of these applications, in addition to many others, rely on the use of various cutting- edge analytical techniques that have been specifically developed to exploit HSI data and its unique properties. For instance, the high dimensionality of HSI data can be leveraged using deep feature extraction techniques (Chen et al., 2016; Rasti et al., 2020) that transform raw data in a hierarchical fashion to a lower dimensional data

representation composed of new variables that are more discriminant, abstract and robust. Challenges from spectral mixing in HSI data can be minimized using dictionary learning-based unmixing approaches (Hong et al., 2019; Liu et al., 2019) to understand the material composition of a single pixel. Even in the presence of signal noise, targets of interest can readily be detected using ensemble learning techniques (Zhao et al., 2019; Sun et al., 2020) and classified using graph convolutional neural networks (Qin et al., 2019; Hong et al., 2020a).

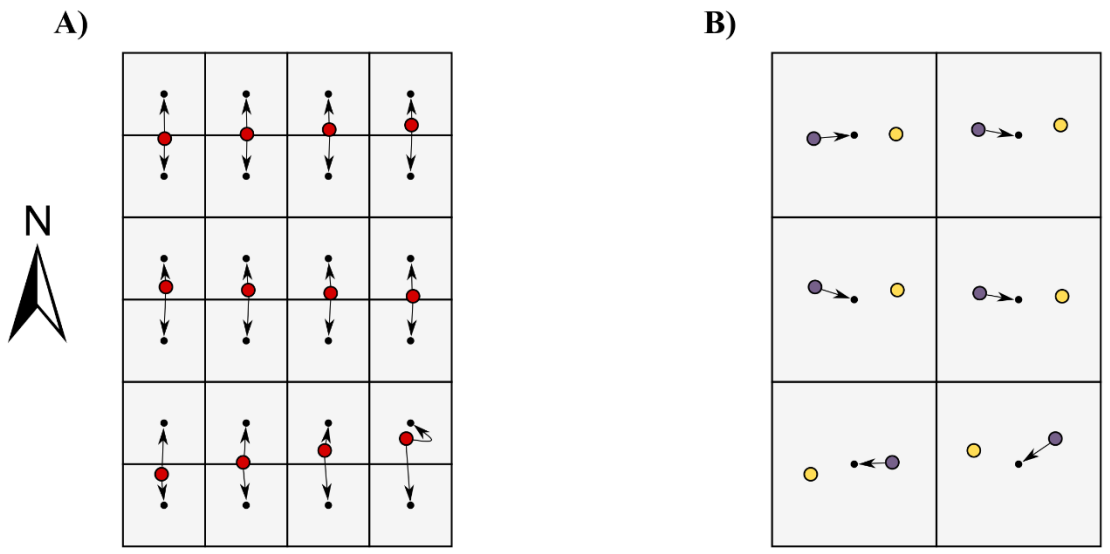
In order to obtain spatially coherent HSI data that optimally preserves the captured spectral information from the conventional sensor types (e.g., pushbroom and whiskbroom) used on unmanned aerial systems (UAS) (e.g., Lucieer et al., 2014; Arroyo-Mora et al., 2019; Arroyo-Mora et al., 2021) and manned airborne platforms (e.g., Kalacska et al., 2016), the geometric correction is essential. In the geometric correction, each pixel of acquired HSI data is located in a real-world coordinate space at the intersection of an input digital surface model (DSM) and a straight line that is projected from the sensor position at the pixel dependent look direction (Müller et al., 2002; Schroth, 2004; Yeh and Tsai, 2011; Lenz et al., 2014). The look direction describes the angle from which incoming electromagnetic radiation is observed by a particular pixel of the imager (Müller et al., 2002). It is calculated by accounting for the roll, pitch and yaw while simultaneously considering the focal geometry and boresight misalignment of the imaging system (Müller et al., 2002; Warren et al., 2014). The DSMs used to geometrically correct HSI data are typically derived from either Light Detection and Ranging (LiDAR) (Liu, 2008), radar altimetry (Leslie, 2018) or Structure-from-Motion photogrammetry (Westoby et al., 2012).

Due to various factors (e.g., lens distortion, sensor movement, rugged terrains) pixels in the imagery are not uniformly spaced over the imaged scene after the geometric correction (Galbraith et al., 2003; Vreys et al., 2016). To correct for this non-uniformity, the geometrically corrected data are often resampled on a north- oriented linear grid. Each cell in this grid is typically separated by an equal distance in both the easting and northing directions, leading to a raster with square pixels (Shlien, 1979; Richards and Jia, 1999; Warren et al., 2014).

When spatially resampling HSI data, the nearest neighbor resampling method is conventionally applied (Roy, 2000; Williams et al., 2017). In this technique, the spectrum for each cell in the pre-specified linear grid is determined by the nearest spectrum from the geometrically corrected imaging data that are being resampled (Shlien, 1979). Since this

resampling process does not change the value recorded in any given spectrum, the nearest neighbor methodology preserves spectral data integrity (Schläpfer et al., 2007). Nonetheless, the nearest neighbor method can compromise spatial data integrity. For instance, nearest neighbor resampling can lead to a blocky appearance due to pixel duplication if oversampling occurs (Arif and Akbar, 2005). Likewise, if the data are undersampled during nearest neighbor resampling, pixels can be lost all together, eliminating valid spectral information (Arif and Akbar, 2005). Even if pixel duplication and loss are near zero, nearest neighbor resampling shifts the position of each pixel (Shlien, 1979; Roy, 2000), altering the calculated location of each spectral measurement.

In many of the popular sensor designs (e.g., pushbroom and whiskbroom) the spatial characteristics of collected HSI data are often different between the cross track and along track directions (Inamdar et al., 2020). Therefore, it is difficult to select a spatial resolution for the resampling grid used in the nearest neighbor methodology. **Figure 5.1** illustrates this issue, showing the spatial resampling process for theoretical HSI data. In this example, the pixel spacing in the cross track is half that of the along track. If the imagery is resampled to the cross track pixel spacing, there would likely be a substantial amount of pixel duplication due to oversampling in the along track (**Figure 5.1A**). In the alternative case where the imagery is resampled to the along track pixel spacing, there would be a considerable amount of pixel loss due to undersampling in the cross track (**Figure 5.1B**). The impact of pixel loss and duplication on remote sensing applications has not been addressed in the literature. Regardless of the method, resampling will affect the spatial integrity of HSI datasets so that the end product fits a raster data structure (Shlien, 1979).



Square Pixel Resampling Approach
Resulting in Pixel Duplication (Oversampling)

Square Pixel Resampling Approach Resulting in Pixel Loss (Undersampling)

- Properly Sampled Hyperspectral Data Point
- Lost Hyperspectral Data Point
- Duplicated Hyperspectral Data Point

Figure 5.1. Pixel loss and pixel duplication during nearest neighbor spatial resampling. Consider spatially resampling a hyperspectral imaging dataset (given by the colored circles) acquired along an approximate true north heading where the pixel spacing in the cross track is half that of the along track. To generate a rasterized data product (given by the grey raster grid and the small black dots which designate the center of each cell), the data must be resampled on a north-oriented grid. Panels (A) and (B) show two resampling grids that could be used for the nearest neighbor resampling.

Instead of the conventional raster data structure, hyperspectral data can be represented as a point cloud, where each spectrum has a distinct position in a three-dimensional space. Hyperspectral point clouds have been extensively discussed in the remote sensing literature. Hyperspectral point cloud generation methodologies can be grouped into three main categories (Brell et al., 2019): 1) physical measurements that collect simultaneous hyperspectral and surface elevation data from a single sensor (e.g., Vauhkonen et al., 2013), 2) photogrammetric ranging with multiple full-frame hyperspectral images (e.g., Oliveira et al., 2019) and 3) data fusion that synergistically integrates surface elevation data with conventional HSI data (e.g., Brell et al., 2019). With physical measurements, it is critical to recognize that a single airborne sensor is not capable of collecting both high quality spectral and elevation data (Brell et al., 2019), especially at fine spectral-spatial resolutions. With photogrammetric ranging, the data storage requirements

can pose operational and computational difficulties, especially at high spatial resolutions (< 3 cm) over large extents since a large volume of data are collected due to the necessity of multiple images with significant overlap. There can also be fundamental issues with photogrammetric ranging hyperspectral point cloud generation related to spectral data integrity depending on the manner in which the spectral information is assigned to each calculated elevation point (Aasen et al., 2015). Data fusion utilizing separate surface elevation and HSI datasets are generally the most feasible, however, their spectral and spatial alignment is challenging due to different sampling strategies, interaction with surface objects and fundamental differences in sensor characteristics (e.g., spectral-spatial point spread functions, illumination sources and viewing angles) (Brell et al., 2016; Brell et al., 2017; Brell et al., 2019).

Despite the abundance of hyperspectral point cloud generation methods, raster datasets have remained the standard for HSI data for over 40 years (Vane et al., 1984; Wilkinson, 1996; Goetz, 2009). This is likely due to the aforementioned difficulties with hyperspectral point cloud generation approaches: they can be difficult to implement, computationally expensive, result in large file sizes and compromise spatial-spectral data integrity. Interestingly, when generating conventional raster images, a hyperspectral point cloud is generated as each hyperspectral pixel is assigned an easting, northing and elevation value during the geometric correction (Müller et al., 2002; Lenz et al., 2014). This point cloud information is rarely analyzed by end users, who are provided with the elevation removed, resampled HSI products in raster format. A data fusion workflow that is implemented via the geometric correction would be straightforward to implement in existing processing protocols. The lack of spatial resampling in such a data product would also mean that the point cloud would preserve the spatial-spectral integrity of HSI data more effectively than rasters.

The objective of our study is to propose a hyperspectral point cloud data representation that preserves the spatial-spectral integrity of HSI data more effectively than conventional square pixel raster end products. This data representation, the Directly- Georeferenced Hyperspectral Point Cloud (DHPC), is generated through a novel data fusion workflow that can be implemented with the same tools used to generate conventional rasters. Our work herein first describes four HSI datasets that we use to generate both raster and DHPC end products. This description incudes an overview of the implemented raster data processing workflow and the

developed DHPC data fusion workflow. After, we assess the DHPC and raster data products based on three spatial integrity data quality metrics (i.e., pixel loss, pixel duplication and pixel shifting) and data storage requirements, which is an important parameter for data distribution. Finally, we assess the practical implications of the data quality metrics by comparing the DHPC end products against the conventional raster end products in common HSI applications including classification, spectra geo-location and target detection. Overall, our study proposes an alternative data representation to the conventional raster data model that has the potential to push the limitations of data distribution, analysis and application in HSI.

5.2. Materials and Methods

5.2.1. Data Collection and Processing

5.2.1.1. Study Areas

The study analyzed HSI data collected at three field sites with different topographic features: the Mer Blue Peatland (MBP), the Cowichan Garry Oak Preserve (CGOP) and the Parc National du Mont- Mégantic (MMG). These sites are important climate change and conservation study areas. The MBP is a ~8,500 year old ombrotrophic bog in Ottawa, Ontario, Canada (Lafleur et al., 2001). It is characterized by a hummock-hollow microtopography that corresponds with spatial patterns in vegetation and hydrology (Malhotra et al., 2016). A hollow is a wetter lowlying area that is dominated by Sphagnum spp. mosses, while a hummock is a drier elevated mound rising from the surface with a dense cover of vascular plants in addition to mosses (Lafleur et al., 2005; Eppinga et al., 2008). The CGOP is located near Duncan, British Columbia, Canada. The site is an endangered Garry Oak Meadow with an open forest and an understory composed of native grasses and herbaceous vegetation. At this site, there is a difference in elevation (>10 m) between the top of the canopy and the understory. The MMG field site is located in southern Québec, Canada. The site is composed of mixed northern hardwood and boreal forest stands. The elevation gradient at this site is relatively large in comparison to the other two sites, changing by more than 600 m within the 10 km² area surrounding the peak of the mountain (Savage and Vellend, 2015).

5.2.1.2. Hyperspectral Imaging Data

HSI data were acquired with two hyperspectral imagers: the micro-Compact Airborne Spectrographic Imager (µCASI-1920, ITRES, Calgary, AB, Canada) and the Compact Airborne Spectrographic Imager (CASI-1500, ITRES, Calgary, AB, Canada). The imagers were mounted

on different airframes and captured spectral information at different spatial scales (\sim 1.5–3 cm and \sim 0.5–2.5 m, respectively) over the visible-near infrared portion of the electromagnetic spectrum. The μ CASI- 1920 was mounted on a DJI Matrice 600 Pro UAS. It is a variable framerate pushbroom imager that collects spectral data across a 34.21° field of view over 288 spectral bands (401–996 nm) on a silicon-based focal plane array (Arroyo-Mora et al., 2019). The CASI-1500 was mounted in a Twin Otter fixed-wing aircraft. It is a variable frame rate, grating-based, pushbroom imager with a 39.8° field of view that collects spectral information over 288 spectral bands (366–1,053 nm) with a silicon-based charged coupled device detector (Soffer et al., 2019). Both μ CASI-1920 and CASI-1500 HSI data were collected over the MBP. μ CASI- 1920 data were collected at the CGOP site and CASI-1500 data were collected at the MMG site. **Table 5.1** lists the parameters associated with both the μ CASI-1920 and CASI-1500 datasets. The CGOP and MMG HSI data represented terrains with large elevation gradients relative to the sensor altitude and nominal pixel sizes of the imagery.

The raw hyperspectral data were radiometrically and atmospherically corrected. The radiometric correction was implemented with proprietary software developed by the sensor manufacturer while the atmospheric correction was done using ATCOR4 [as described in Soffer et al. (2019)]. The MMG imagery further had a Lambert + Statistical-Empirical BRDF topographic correction applied (Richter and Schläpfer, 2020).

Table 5.1. Parameters for the hyperspectral imaging data acquired over the Mer Bleue Peatland (MBP), the Cowichan Garry Oak Preserve (CGOP) and the Parc National du Mont- Mégantic (MMG) with the μCASI-1920 and the CASI-1500. Nominal altitudes are reported as height above ground level.

Parameter	MBP MBP		CGOP	MMG
	(μCASI-1920)	(CASI-1500)	(μCASI-1920)	(CASI-1500)
Date (dd-mm-yyyy)	15-07-2019	15-07-2019	15-05-2019	18-07-2019
Image Start Time (hh.mm.ss GMT)	15.44.49	15.44.38	18.33.41	15.06.34
Latitude of Flight Line Centre (DD)	45.4102	45.4014	48.8080	45.4588
Longitude of Flight Line Centre (DD)	-75.5157	-75.5156	-123.6305	-71.1516
Nominal Heading (°)	156	341	165	171
Nominal Altitude (m)	45	1133	60	2325
Nominal Speed (m/s)	2.7	41.6	2.7	53.5
Integration Time (ms)	9	48	9	48
Frame Time (ms)	11	48	11	48
Cross Track Pixel Resolution (cm)	1.5	55	2.0	113
Cross Track Pixel Spacing (cm)	1.5	55	2.0	113
Along Track Pixel Resolution (cm)	2.4	198	2.4	257
Along Track Pixel Spacing (cm)	3.0	198	3.0	257

5.2.1.3. Conventional Hyperspectral imaging Data (Square Pixel Raster)

To generate conventional HSI end products (georeferenced raster with square pixels), the radiometrically and atmospherically corrected data were first geometrically corrected and then spatially resampled. The geometric correction was completed with proprietary software from the sensor manufacturer using the onboard inertial navigation system data (position and attitude). The DSMs used for the geometric correction are described in section 5.2.1.5. Conventional square pixel raster images were generated for each HSI dataset by spatially resampling the geometrically corrected HSI data on a north- oriented linear grid using a nearest neighbor methodology. Since there was a discrepancy between the cross track and along track pixel spacing of the collected HSI data, each HSI dataset was resampled on two different grids.

Adjacent grid cells were separated by the cross track pixel spacing in the first resampling grid and the along track pixel spacing in the second resampling grid. Since the along track spacing was consistently larger than that of the cross track, the first resampling grid oversampled the data while the second undersampled the data to generate raster data products with square pixels. In total 8 imaging data sets were generated (two images for each of the HSI datasets described in **Table 5.1**).

5.2.1.4. Directly-Georeferenced Hyperspectral Point Cloud (DHPC)

The DHPC data fusion workflow implements a standard geometric correction processing protocol to create the point cloud (**Figure 5.2**). The workflow has three major inputs: the atmospherically corrected HSI data, the inertial navigation data of the sensor (position and attitude) and a DSM of the area covered by the HSI data.

The first step in the DHPC data fusion workflow modifies the input DSM, blurring it through convolution with the point spread function of the imaging sensor. This modification makes the spatial properties of the DSM more consistent with the collected HSI data; each point in the blurred DSM corresponds to the average elevation of the objects/terrain that would contribute to a single HSI pixel.

In the second and final step of the data fusion workflow, the HSI data in its original sensor geometry is projected onto the blurred DSM. This was practically done by applying the geometric correction described in section 5.2.1.3, using the blurred DSM instead of the original. As a result of the blurred DSM, each HSI pixel receives the average surface elevation of the materials contributing to it. With the real-world position (northing, easting, averaged surface elevation) of each pixel from the imagery in its original sensor geometry, the DHPC is complete. In our study, each point in the DHPC data product was referred to as a "pixel". Following the described workflow, a DHPC was generated for each of the HSI datasets from **Table 5.1**.

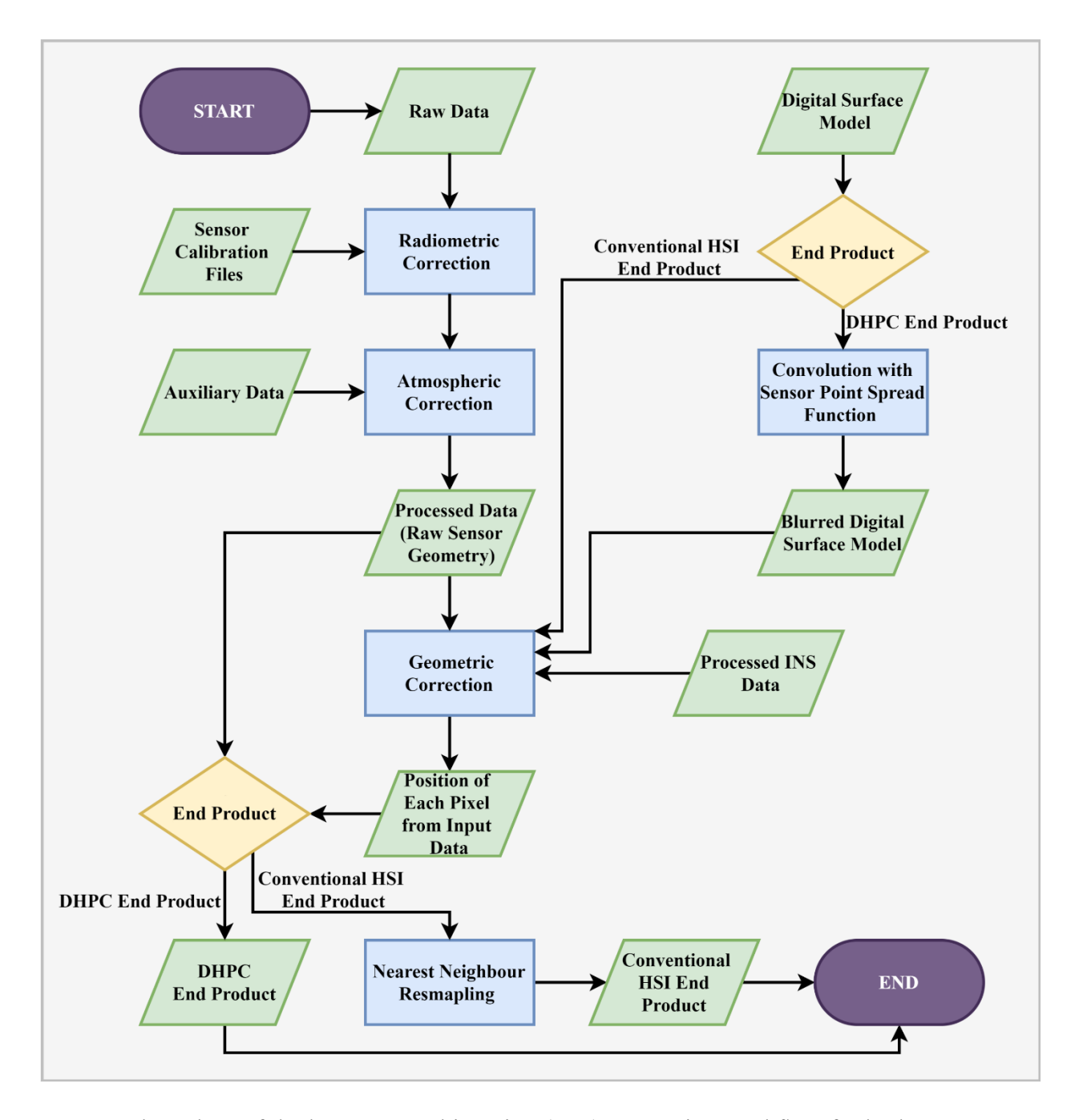


Figure 5.2. Flow chart of the hyperspectral imaging (HSI) processing workflow for both conventional rasterized hyperspectral imaging end products and the Directly-Georeferenced Hyperspectral Point Cloud (DHPC).

5.2.1.5. Digital Surface Models

The DSMs used to geometrically correct the µCASI-1920 data were generated by using a Structure-from-Motion Multiview Stereo (SfM-MVS) workflow from RGB photography (Kalacska et al., 2017; Kalacska et al., 2020). In this workflow (Lucanus and Kalacska, 2020) geo-tagged aerial photographs were collected on June 6th, 2019 (for MBP) and May 11th, 2019

(for CGOP) over the area covered by the μCASI-1920 imagery, with a Canon EOS 5D Mark III equipped with a Canon EF 24–70 mm f/2.8 L II USM lens set to a focal length of 24 mm. All photographs included the geolocation and altitude of the UAS, as recorded by an EMLID Reach M+ GNSS module. The collected raw GNSS data were postprocessed with RTKLIB (Takasu and Yasuda, 2009) using local base station data collected from a EMLID Reach RS+ GNSS module that was receiving incoming corrections from a commercial NTRIP (Networked Transport of Radio Technical Commission for Maritime Services via Internet Protocol) casting service (Smartnet North America, Atlanta) on an RTCM3-iMAX (Radio Technical Commission for Maritime Individualized Master Auxiliary) mount point that used both GPS and GLONASS constellations. The SfM-MVS workflow was implemented using Pix4D Mapper Pro [see Kalacska et al. (2020) for details], ultimately generating a DSM at a spatial resolution of 0.69 cm for the MBP and 1.52 cm for the CGOP.

For the MBP CASI-1500 data, airborne LiDAR data collected for the National Capital Commission in 2009 (density 2–4 pts m²) (Arroyo-Mora et al., 2018b) were used to generate a DSM at a spatial resolution of 0.5 m. Based on ground observations and peat growth modeling, the MBP has been estimated to grow <0.5 m over the last millennium (Frolking et al., 2010). Given this slow growth rate, the LiDAR data collected in 2009 is still appropriate to apply to the peatland.

For the MMG CASI-1500 data, the study used airborne LiDAR data collected in 2018 by the Ministry of Forests, Wildlife and Parks of Québec as part of the province-wide LiDAR sensor data acquisition project (density 2.5 pts m2) (Le ministère des Fore^ts, de la Faune et des Parcs, 2021). The dataset was provided as a DSM at a spatial resolution of 1 m.

5.2.2. Data Assessment Metrics

Three spatial data quality metrics were calculated for each DHPC and square pixel raster end product: pixel loss (PL), pixel duplication (PD) and root mean square error in the radial direction (RMSE_r). PL (%) is the total percentage of pixels from the original HSI dataset that were not used in the final data product. PD (%) is the total percentage of pixels in the final data product that are duplicates. The RMSE_r gives a measure of the average distance (cm) the location of each pixel (as determined from the geometric correction) was shifted while generating the final end product. Assuming a uniform pixel spacing in the cross track and along track directions, it is

possible to derive theoretical PL and PD values (see Theoretical Pixel Loss and Pixel Duplication Derivation) for any given HSI dataset from nominal flight parameters alone. Following this derivation, theoretical PL (PLH) and PD (PDH) values were calculated for each of the resampled and DHPC datasets and compared to the measured values. In addition to the described spatial data quality metrics, data storage requirements for each DHPC and square pixel raster end product were also calculated.

5.2.2.1. Pixel Loss

The PL was calculated according to Mulcahy (2000) (Eq. 1):

$$PL = \left(1 - \frac{U_{I_r}}{T_{I_0}}\right) \times 100\%,\tag{1}$$

where the following holds: U_{I_r} represents the number of unique spectra in the analyzed data product (I_r) and T_{I_0} represents the number of total spectra in the original imagery from which I_r was derived. PL is given as a percentage, indicating the total percentage of pixels from the original HSI dataset that were not used in the final data product.

5.2.2.2. Pixel Duplication

The PD was calculated according to Mulcahy (2000) (Equation 2):

$$PD = \left(1 - \frac{U_{I_r}}{T_{I_r}}\right) \times 100\%,\tag{2}$$

where the following holds: U_{I_r} represents the number of unique spectra in the analyzed data product (I_r) while T_{I_r} represents the total number of spectra in I_r . PD is given as a percentage, indicating the total portion of pixels in I_r that are duplicates of one another.

5.2.2.3. Horizontal Linear Root Mean Square Error in Radial Direction

The RMSE_r was calculated according to American Society for Photogrammetric Engineering Remote Sensing (2015) (Equation 3):

$$RMSE_{r} = \sqrt{\frac{\sum_{i=1}^{i=n} ([P_{r,North}(S_{r}(i)) - P_{o,North}(S_{r}(i))]^{2} + [P_{r,East}(S_{r}(i)) - P_{o,East}(S_{r}(i))]^{2})}_{n}},$$
(3)

where the following holds: $S_r(i)$ represents the spectrum from the ith pixel of the analyzed data product (I_r) ; $P_{r,North}(S_r(i))$ represents the northing position of $S_r(i)$ in I_r ; $P_{r,East}(I_r(i))$, represents the easting position of $S_r(i)$ in I_r ; n represents the total number of spectrum in I_r ; P_o ,

 $North(S_r(i))$ represents the original northing position of $S_r(i)$ as calculated during the geometric correction; and $P_{o, East}(S_r(i))$ represents the original easting position of $S_r(i)$ as calculated during the geometric correction. The RMSE_r gives a measure of the average distance (cm) the location of each pixel (as determined by the geometric correction) is shifted in the final data product.

5.2.2.4. Theoretical Pixel Loss and Pixel Duplication Derivation

This section derives the theoretical PL (PL_H) and PD (PD_H) of a hypothetical HSI dataset (I_o) collected with uniform pixel spacing in the cross track and along track directions. In this section, I_o was assumed to be collected over an area with length W in the cross track direction and length L in the along track direction. Furthermore, the cross track pixel spacing ($P_{s_{cross}}$) was assumed to be smaller than that of the along track pixel spacing ($P_{s_{along}}$). The total number of spectra in I_o (T_{I_o}) was approximated by the following:

$$T_{I_0} = (L/Ps_{along})(W/Ps_{cross}). \tag{4}$$

The theoretical PL and PD values were calculated for the two resampling approaches investigated in our study. The first resampling grid oversampled I_o (resampling resolution equal to the cross track pixel spacing) while the second undersampled I_o (resampling resolution equal to the along track pixel spacing). The total number of pixels in the resampled dataset can be calculated from:

$$T_{I_r} = (L/R_r)(W/R_r), \tag{5}$$

where R_r is the resolution of the resampled image (I_r) .

Considering the first scenario (dataset is oversampled), it is assumed that there is no PL (PL_H = 0 %) since R_r is always equal to or smaller than pixel spacing throughout I_o . To derive PD_H, the number of total (T_{I_r}) and unique (U_{I_r}) spectra within the resampled image (I_r) must be calculated. Since there is no PL, U_{I_r} is equal to T_{I_o} .

Starting from the PD formula given in section 5.2.2.2, the derivation follows:

$$PD_H = \left(1 - \frac{U_{l_r}}{T_{l_r}}\right) \times 100\%$$
 (6)

$$PD_{H} = \left(1 - \frac{\left(L/Ps_{along}\right)(W/Ps_{cross})}{\left(L/Ps_{cross}\right)(W/Ps_{cross})}\right) \times 100\% \tag{7}$$

$$PD_H = \left(1 - \frac{Ps_{cross}}{Ps_{along}}\right) \times 100\%. \tag{8}$$

Considering the second scenario (dataset is undersampled), it is assumed that there is no PD (PD_H = 0 %) since the resampling resolution is always equal to or greater than the pixel spacing throughout I_o . To derive PL_H, T_{I_o} and U_{I_r} are required. Since there is no PD, U_{I_r} is equal to T_{I_r}

Starting from the PL formula given in 5.2.2.1, the derivation follows:

$$PL_H = \left(1 - \frac{U_{l_r}}{T_{l_o}}\right) \times 100\%$$
 (9)

$$PL_{H} = \left(1 - \frac{\left(L/Ps_{along}\right)\left(W/Ps_{along}\right)}{\left(L/Ps_{along}\right)\left(W/Ps_{cross}\right)}\right) \times 100\% \tag{10}$$

$$PL_{H} = \left(1 - \frac{Ps_{cross}}{Ps_{along}}\right) \times 100\%. \tag{11}$$

The theoretical PL and PD of the DHPCs required no derivation; since pixels were not resampled after the geometric correction, there should be zero PL_H or PD_H.

5.2.3. Hyperspectral Imaging Data Applications

To compare the DHPC to the two resampled data products, two applications were tested with the MBP μ CASI-1920 imagery. The first was a simple classification problem, differentiating two microforms (hummocks and hollows) in the MBP. The second μ CASI-1920 application aimed to approximate the potential error in biomass estimation for hummocks and hollows (based on the classification results).

Two applications were also assessed for the MBP CASI-1500 data. The first located unique spectra within pre-specified vegetation plots. This application was based on common HSI end user requirements of matching ground control data (e.g., vegetation species counts) with HSI data (Arroyo-Mora et al., 2018a). The second CASI-1500 application was a sub-pixel target detection exercise.

5.2.3.1. Hummock and Hollow Classification (µCASI-1920)

Hummocks and hollows were classified from the MBP μCASI-1920 HSI data using a linear discriminant analysis (LDA) classification (Fisher, 1936). An independent classification model

was trained and validated for each of the resampled µCASI-1920 images and the DHPC, resulting in nine different classification models. Each of the models were differentiated by the utilized training dataset (oversampled raster, undersampled raster or DHPC) and training variables (elevation only, spectral reflectance only or elevation and spectral reflectance). The surface elevation data for the rasterized data products were provided during geometric correction by resampling the surface elevation value associated with each pixel. The performance of each model was measured by the overall accuracy, producer's accuracy and user's accuracy metrics calculated on the validation dataset. The training and validation datasets for each model were generated based on both elevation and spectral data with domain knowledge of the MBP. In this process, trees were masked by removing the upper 2 percentile of the surface elevation distribution in each dataset. The surface elevation data were then detrended by removing the median surface elevation in a 10x10 m area around each pixel. Potential hummocks were identified as the 75–90th percentile of the detrended surface elevation data. Potential hollows were identified as the bottom 5th percentile. The identified hummocks and hollows were further filtered to remove bright (i.e., man-made objects) and low (i.e., shadows) reflectance objects. In this filtering, hummock and hollow labels that fell within the top and bottom 5 percentile of the spectral data at 600 nm were removed. Half of the remaining hollow labels were randomly selected and designated as training data. The other 50 % of hollow labels were designated as validation data. An equal number of hummock data points were randomly selected and designated as training data and validation data. A minimum of 60,000 training and validation data points were used for each of the models.

5.2.3.2. Biomass Error Estimation for Hummocks and Hollows (µCASI-1920)

To assess the impact of resampling and the DHPC on a basic modeling question, our study investigated how classification errors could affect total aboveground biomass estimation. The biomass of hummocks and hollows were assumed to be Gaussian in nature. For hummocks, this Gaussian distribution was defined by a mean value of 527 g/m² and a standard deviation (SD) of 43 g/m². For hollows, this Gaussian distribution was defined by a mean value of 431 g/m² and a SD of 147 g/m². Each of these biomass distributions (mean and SD) were based on ground data from the MBP reported in Bubier et al. (2003).

A biomass value was randomly generated for each observation in the validation dataset based on its actual microform label. For instance, if an observation was actually labeled a hummock, it would be randomly assigned a biomass value from the previously defined hummock biomass distribution function. The mean of the randomly generated biomass values was calculated separately for hummocks and hollows based on the predicted labels in the validation dataset. In a perfect classification, the mean biomass of predicted hummocks and hollows would be nearly identical to the values used for the field-based biomass distributions. As such, to quantify the error in the biomass estimation for hummocks and hollows due to misclassification, the difference between the mean of the predicted and actual biomass distributions ($\Delta B_{\mu,mf}$) was calculated for both hummocks ($\Delta B_{\mu,hk}$) and hollows ($\Delta B_{\mu,hw}$).

5.2.3.3. Geo-locating Spectra from Pre-Specified Vegetation Plots (CASI-1500)

One-hundred virtual 3 x 3 m vegetation plots were randomly placed across the MBP (uniform probability distribution over space). The mean number of spectra and unique spectra per plot were calculated in both the raster data sets and the DHPC generated from the CASI-1500. A pixel spectrum was located within a plot if its center was within the spatial boundaries of the plot. The percentage of these spectra located outside the plots before rasterization were calculated. The tested datasets were evaluated by identifying the mean number of unique spectra per plot that fell within its spatial boundaries before and after rasterization.

5.2.3.4. Detecting Sub-Pixel Targets (CASI-1500)

A target detection analysis was conducted on each of the MBP CASI-1500 datasets. One-thousand artificial targets were randomly placed across the MBP (uniform probability distribution over space). In sub-pixel detection applications, the position of a target within a pixel's field of view and the sensor point spread function are of utmost importance (Radoux et al., 2016). As such, this application assumed that a target can be detected within a pixel of the imagery in its raw sensor geometry (pre-rasterization) if the point spread function of the pixel was greater than a pre-defined threshold value at the location of the target. The study tested threshold values ranging from 0.15 to 0.85 in increments of 0.05. The higher the threshold, the more difficult it was for a target to be detected within any given pixel of the imagery in its original sensor geometry. Based on this target detection, the false discovery rate and false negative rate were then calculated for each of the oversampled, undersampled and DHPC products. A pixel was a true positive if the detected target was within its spatial boundaries. For the rasterized data product, the spatial boundaries were given by their pixel boundaries. For the

DHPC, the boundaries were given by the full width at half maximum (FWHM) of the sensor point spread function.

5.3. Results

5.3.1. Hyperspectral Imaging Data Assessment

5.3.1.1. Terrain with Small Elevation Gradient Relative to Sensor Altitude and Nominal Pixel Size

The MBP HSI data are displayed in **Figure 5.3** and **Figure 5.4**. **Table 5.2** records the RMSE_r, PL, PD, PL_H, PD_H and file size of the raster and point cloud datasets. The oversampled MBP data products were large in file size (30.90 Gb for μCASI-1920 and 40.36 Gb for CASI-1500) and characterized by high PD (50.25% for μCASI-1920 and 77.70% for CASI-1500). The PD for the oversampled CASI- 1500 dataset was relatively large in comparison to the theoretical value (PD_H 72.22%). The undersampled MBP data products were small (7.77 Gb for μCASI-1920 and 2.57 Gb for CASI-1500) and characterized by a large PL (51.09% for μCASI-1920 and 72.32% for CASI-1500). The RMSE_r for the resampled μCASI-1920 and CASI-1500 were 1.1 cm and 66.7 cm, respectively. The DHPC products for the MBP had a small file size (4.55 Gb for μCASI-1920 and 3.05 Gb for CASI-1500) and were characterized by zero PL, PD and RMSE_r. Supplementary Video S1, S2 show the DHPCs in three dimensions.

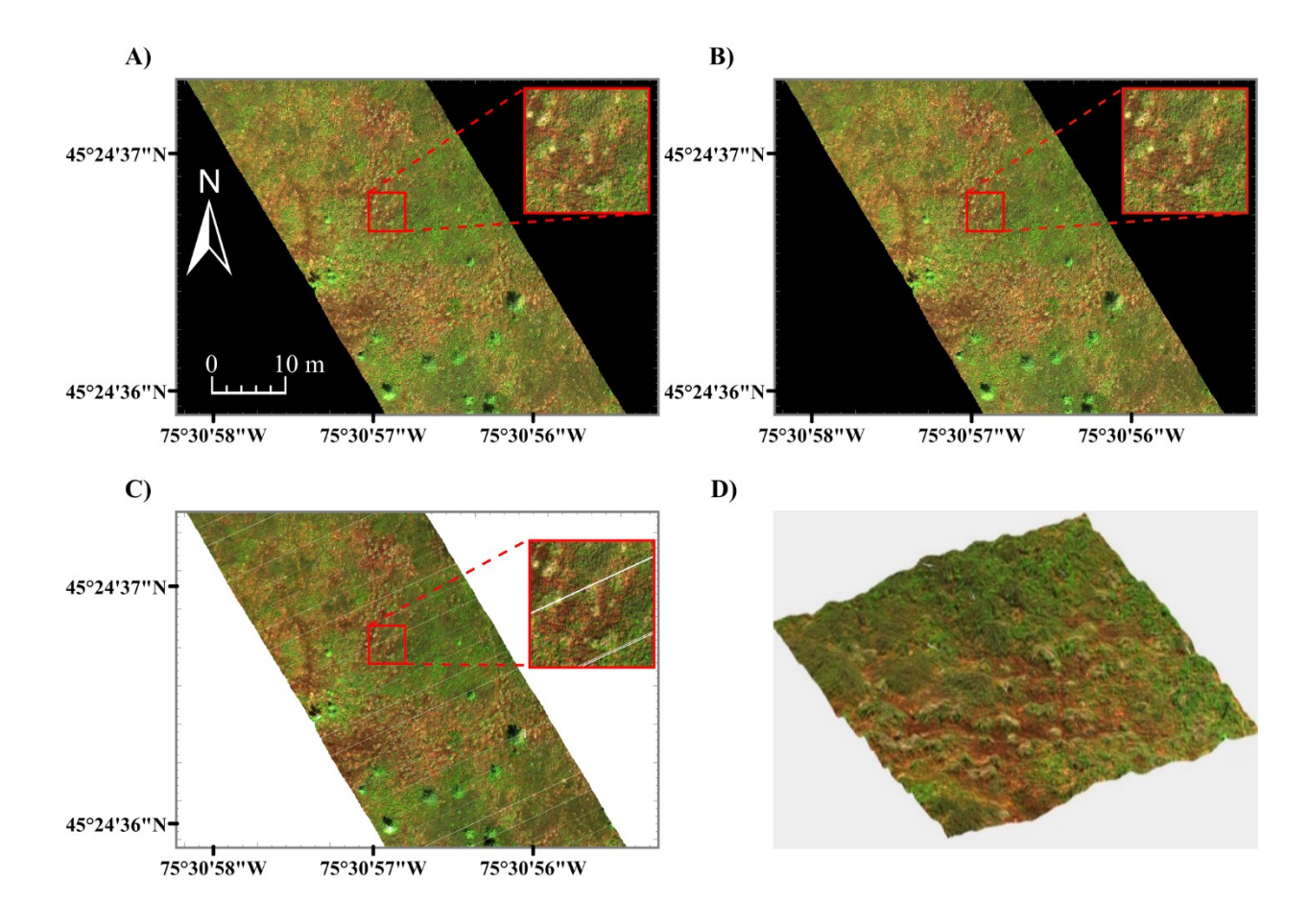


Figure 5.3. Hyperspectral imaging data (R = 639.6 nm, G = 550.3 nm, B = 459.0 nm) from the μ CASI-1920 over the Mer Bleue Peatland. Panels (A, B) are rasterized hyperspectral imaging datasets resampled to 1.5×1.5 cm (A) and 3×3 cm (B). Panel (C) represents the Directly-Georeferenced Hyperspectral Point Cloud (DHPC) viewed from above. Panel (D) displays a video still of the DHPC in a 12×12 m region around the image zoom center. In all panels, each displayed band is linearly stretched between 0 and 12%. The full video can be seen in Supplementary Video S1. The white stripes in the DHPC [clearly visible in the image zoom of panel (C)] represent areas on the ground that were not sampled by the hyperspectral imager during data acquisition. These gaps are not present in the raster images (A, B) as they are interpolated over with duplicated pixels from the edges of the stripes during the nearest neighbor resampling.

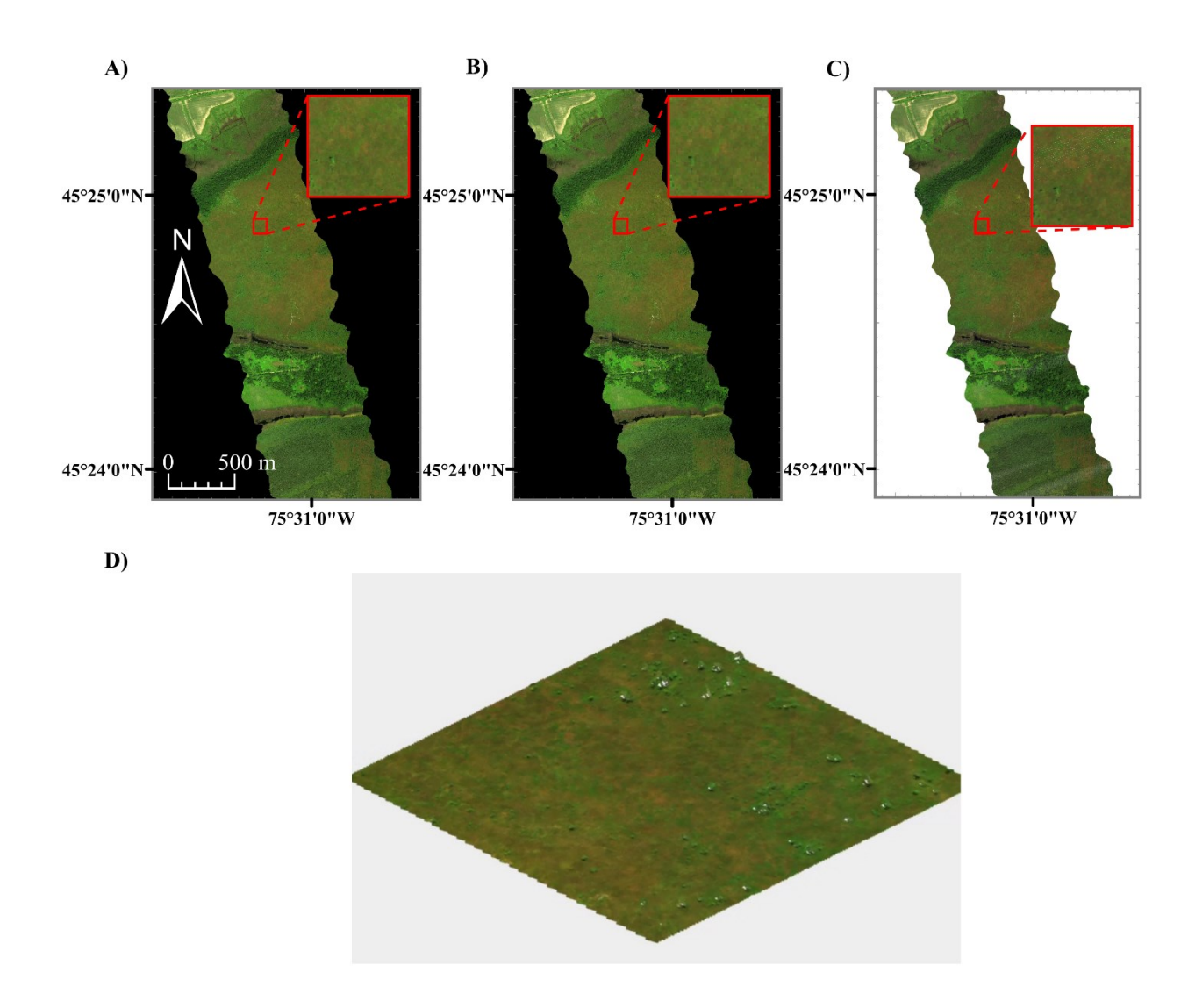


Figure 5.4. Hyperspectral imaging data (R = 640.8 nm, G = 549.9 nm, B = 459.0 nm) for the CASI-1500 over the Mer Bleue Peatland. Panels (A, B) are rasterized hyperspectral imaging datasets resampled to 50×50 cm (A) and 200×200 cm (B) grids. Panel (C) represents the Directly-Georeferenced Hyperspectral Point Cloud (DHPC) viewed from above. Panel (D) displays a video still of the DHPC in a 240×240 m region surrounding the image zoom center. The full video can be seen in Supplementary Video S2. In all panels, each displayed band is linearly stretched between 0 and 12%.

Table 5.2. The file size, pixel loss (PL), pixel duplication (PD), theoretical pixel loss (PL_H), theoretical pixel duplication (PD_H) and horizontal root mean square error (RMSE_r) in the radial direction for the μ CASI-1920 and CASI-1500 data over the Mer Bleue Peatland. These data include the resampled hyperspectral imaging datasets and the Directly-Georeferenced Hyperspectral Point Clouds (DHPC).

Dataset (Pixel Size)	File Size (Gb)	PL _H (%)	PD _H (%)	PL (%)	PD (%)	RMSEr
						(cm)
Resampled μCASI-1920 Data (1.5 x 1.5 cm)	30.90	0	50.00	1.15	50.25	1.1
Resampled μCASI-1920 Data (3 x 3 cm)	7.77	50.00	0.00	51.09	1.61	1.1
μCASI-1920 DHPC	4.55	0.00	0.00	0.00	0.00	0.0
Resampled CASI-1500 Data (50 x 50 cm)	40.36	0.00	72.22	0.8576	77.70	66.7
Resampled CASI-1500 Data (200 x 200 cm)	2.57	72.22	0.00	72.32	0.43	66.7
CASI-1500 DHPC	3.05	0.00	0.00	0.00	0.00	0.0

5.3.1.2. Terrain with Large Elevation Gradient Relative to Sensor Altitude and Nominal Pixel Size

The CGOP and MMG HSI data are displayed in **Figure 5.5** and **Figure 5.6**, respectively. **Table 5.3** records the RMSE_r, PL, PD, PL_H, PD_H and file size of the raster and point cloud datasets. The oversampled CGOP and MMG data products were large in file size (24.40 Gb for CGOP and 30.67 Gb for MMG) and characterized by high PD (34.29% for CGOP and 59.76% for MMG). The oversampled CGOP dataset also had a relatively large PL of 11.09% in comparison to the theoretical value (PL_H 0.00%). The undersampled CGOP and MMG data products were small in file size (10.89 Gb for CGOP and 5.54 Gb for MMG) and characterized by high PL (46.69% for CGOP and 58.12% for MMG). The PL for the undersampled CGOP dataset was relatively large in comparison to the theoretical value (PL_H 33.33%). The undersampled MMG and CGOP data products also had relatively high PD (11.49% for CGOP and 5.52% for MMG) in comparison to the theoretical value (PD_H = 0.00%). The RMSE_r for the resampled CGOP and MMG data were 3.9 cm and 86.6 cm, respectively. The DHPC products

for the CGOP and MMG sites had a small file size (10.16 Gb for CGOP and 4.73 Gb for MMG) and were characterized by zero PL, PD and RMSE_r. Supplementary Video S3, S4 show the DHPCs in three dimensions.

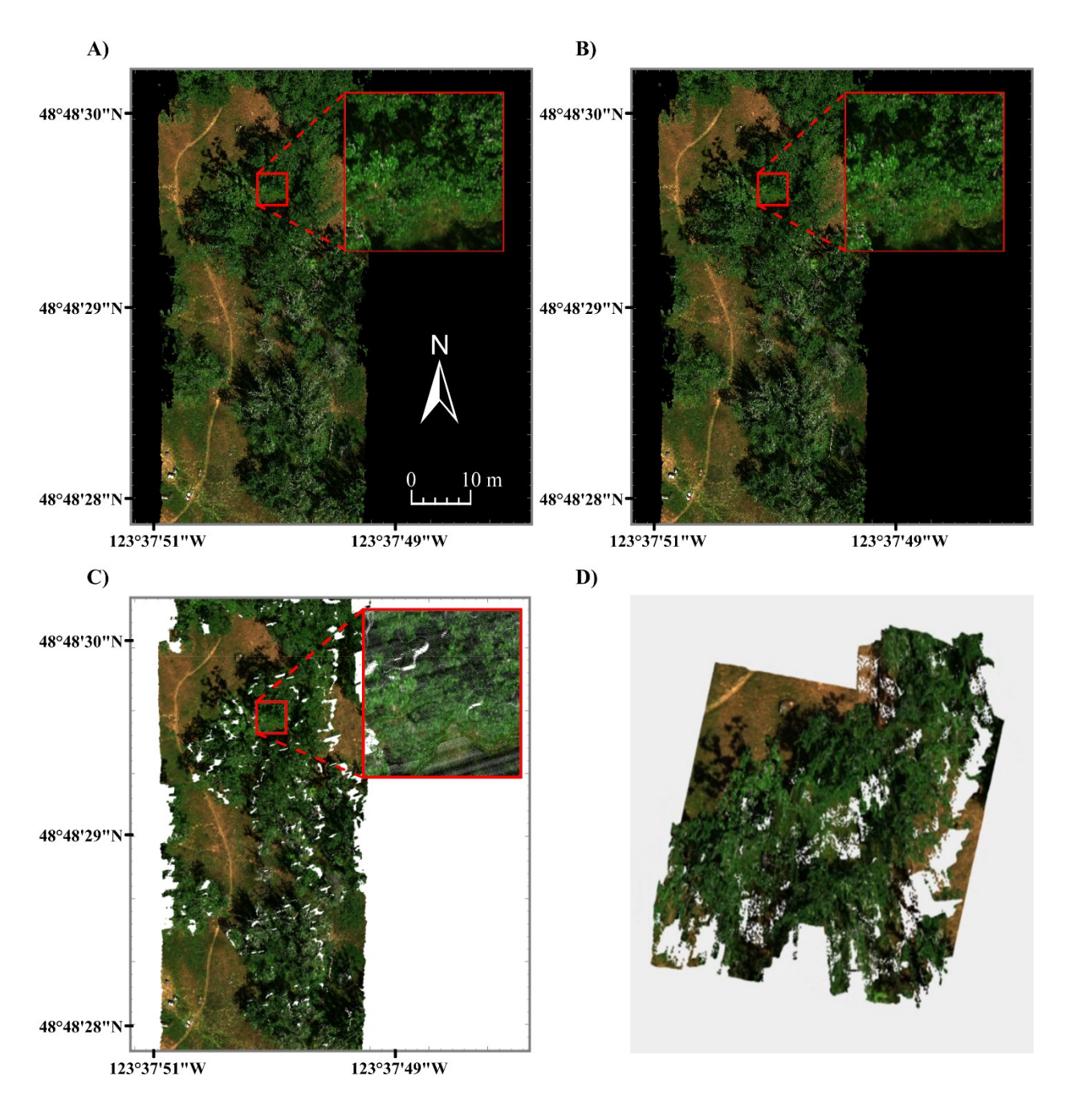


Figure 5.5. Hyperspectral imaging data (R = 639.6 nm, G = 550.3 nm, B = 459.0 nm) from the μ CASI-1920 over the Cowichan Garry Oak Preserve. Panels (A, B) are rasterized hyperspectral imaging datasets resampled to 2×2 cm (A) and 3×3 cm (B) grids. Panel (C) represents the Directly-Georeferenced Hyperspectral Point Cloud (DHPC) viewed from above. Panel (D) displays a video still of the DHPC in a D4 × D4 m region surrounding the image zoom center. The full video can be seen in Supplementary Video S3. In all panels, each displayed band is linearly stretched between 0 and 22%. The white stripes in the DHPC [clearly visible in the image zoom of panel (D2) represent areas on the ground that were not sampled by the hyperspectral imager during data acquisition. These gaps are not present in the raster images

(A, B) as they are interpolated over with duplicated pixels from the edges of the stripes during the nearest neighbor resampling.

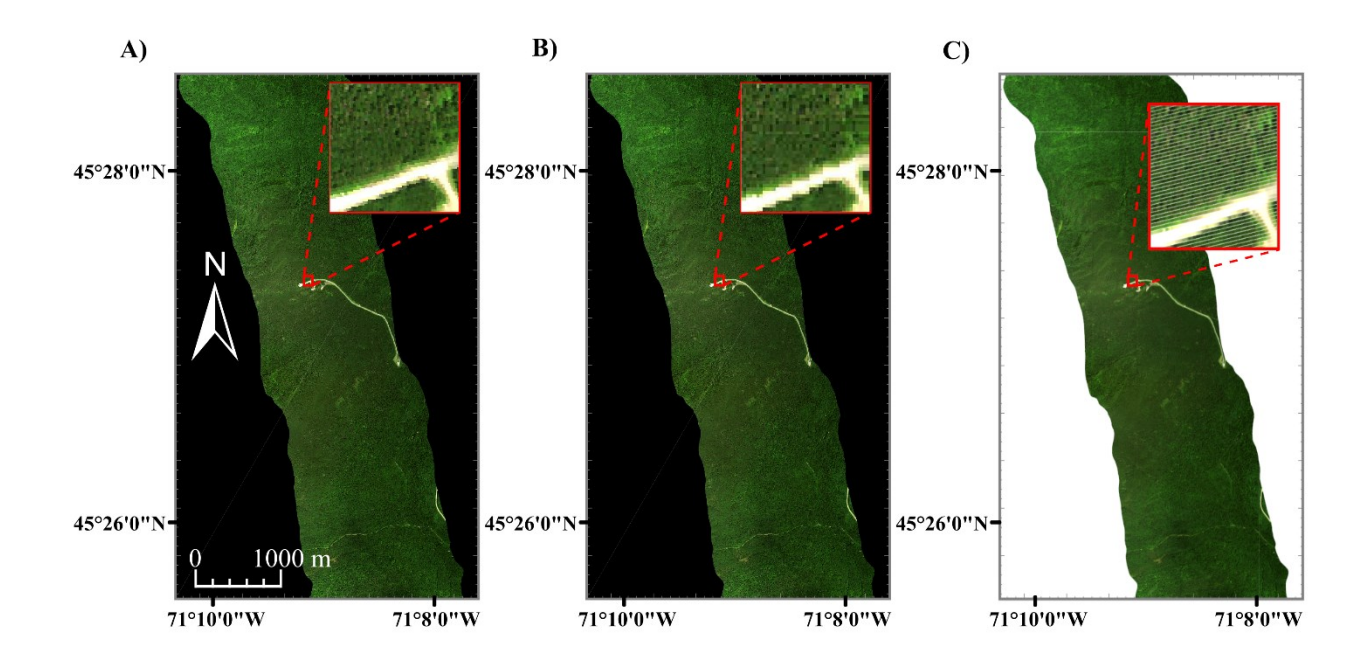




Figure 5.6. Hyperspectral imaging data (R = 640.8 nm, G = 549.9 nm, B = 459.0 nm) for the CASI-1500 over the Parc National du Mont- Mégantic. Panels (A, B) are rasterized hyperspectral imaging datasets resampled to 110×110 cm (A) and 260×260 cm (B) grids. Panel (C) represents the Directly-Georeferenced Hyperspectral Point Cloud (DHPC) viewed from above. Panel (D) displays a video still of the DHPC. The full video can be seen in Supplementary Video S4. In all panels, each displayed band is linearly stretched between 0 and 12%. The white stripes in the DHPC represent areas on the ground that were not sampled by the hyperspectral imager during data acquisition. The white stripes in the DHPC [clearly visible in the image zoom of panel (D)] represent areas on the ground that were not sampled by the hyperspectral imager during data acquisition. These gaps are not present in the raster images

(A, B) as they are interpolated over with duplicated pixels from the edges of the stripes during the nearest neighbor resampling.

Table 5.3. The file size, pixel loss (PL), pixel duplication (PD), theoretical pixel loss (PL_H), theoretical pixel duplication (PD_H) and horizontal root mean square error (RMSE_r) in the radial direction for the μ CASI-1920 data from the Cowichan Garry Oak Preserve and the CASI-1500 data from the Parc National du Mont-Mégantic. These data include the resampled hyperspectral imaging datasets and the Directly-Georeferenced Hyperspectral Point Clouds (DHPC).

Dataset (Pixel Size)	File Size (Gb)	PL _H (%)	PD _H (%)	PL (%)	PD (%)	RMSEr
						(cm)
Resampled μCASI-1920 Data (2 x 2 cm)	24.40	0.00	33.33	11.09	34.29	3.9
Resampled μCASI-1920 Data (3 x 3 cm)	10.89	33.33	0.00	46.69	11.49	3.9
μCASI-1920 DHPC	10.16	0.00	0.00	0.00	0.00	0.0
Resampled CASI-1500 Data (110 x 110 cm)	30.67	0.00	56.11	0.36	59.76	86.6
Resampled CASI-1500 Data (260 x 260 cm)	5.54	56.11	0.00	58.12	5.52	86.6
CASI-1500 DHPC	4.73	0.00	0.00	0.00	0.00	0.0

5.3.2. Hyperspectral Imaging Data Applications

5.3.2.1. Hummock and Hollow Classification

The three models trained on the spectral data alone had the lowest overall classification accuracies (83.3–83.7%) (**Table 5.4**). Importantly, there was a discrepancy in these models between producer's accuracy and user's accuracy. For hollows, the user's accuracies ranged from 86.3 to 86.8%. These values were higher than the producer's accuracies which ranged from 79.1 to 79.6%. The opposite trend was observed for hummocks where the user's accuracy ranged from 80.8 to 81.2% while the producer's accuracy ranged from 87.4 to 87.9%. The models trained on the surface elevation data alone had overall accuracies of 85.8–86.5%. As with the spectral models, there was a discrepancy between user's accuracy and producer's accuracy. In hollows, the user's and producer's accuracies were valued at 82.4–83.0% and 91.1–91.8%,

respectively. For hummocks, the user's accuracy and producer's accuracies were valued at 90.0–90.8% and 80.5–81.2%, respectively. The classification models trained on both the spectral and elevation data had the highest overall accuracy, user's accuracy and producer's accuracy values ranging from 90.0 to 91.3% for both hummocks and hollows. Although all classification accuracies were relatively constant when comparing models trained with identical variables, the DHPC based classification had higher overall accuracies by 0.3–0.7%.

Table 5.4. Accuracy results for the hummock-hollow classification models (μ CASI-1920 hyperspectral imaging (HSI) data from the Mer Bleue Peatland). Each of the models were differentiated by the training dataset and training variables. The training datasets included the Directly-Georeferenced Hyperspectral Point Cloud (DHPC) in addition to the three resampled hyperspectral images. The superscripts^{S, E} corresponded to the inclusion of the spectral reflectance and surface elevation, respectively.

Classification Model (Pixel Size)	Overall Accuracy (%)	Hollow User's accuracy (%)	Hollow Producer's accuracy (%)	Hummock User's accuracy (%)	Hummock Producer's accuracy (%)
Resampled HSI Data ^E (1.5 x 1.5cm)	85.90	82.39	91.31	90.26	80.48
Resampled HSI Data ^E (3 x 3cm)	85.84	82.45	91.07	90.03	80.62
DHPC Data ^E	86.52	83.03	91.80	90.84	81.24
Resampled HSI Data ^S (1.5 x 1.5cm)	83.35	86.42	79.14	80.76	87.57
Resampled HSI Data ^S (3 x 3cm)	83.30	86.29	79.17	80.76	87.43
DHPC Data ^S	83.72	86.76	79.60	81.15	87.85
Resampled HSI Data ^{S, E} (1.5 x 1.5cm)	90.87	91.20	90.47	90.55	91.27
Resampled HSI Data S, E (3 x 3cm)	90.63	91.10	90.06	90.17	91.21
DHPC Data ^{S, E}	91.24	91.32	91.14	91.16	91.34

The output classification map over a 12 x 12 m plot for each model is shown in **Figure 5.7**. When trained on spectral data alone (e.g., **Figure 5.7H**), the classification tracked hummocks and hollows observable in the RGB image (**Figure 5.7J**). Isolated hummock pixels were observed in hollow patches within the classification. The opposite was also observed, with isolated hollow pixels within hummock patches. These isolated pixels qualitatively decreased when using elevation data in addition to spectral data (e.g., **Figure 5.7I**), leading to a higher spatial coherency. There were few isolated pixels in the classification model trained on the surface elevation data alone. Nevertheless, there were clear areas of misclassification. For instance, in the north-west corner of the displayed classification map (e.g., **Figure 5.7G**), the entire region was classified as hummocks, despite the presence of hollows that can be seen in the RGB image (see **Figure 5.7J**) and surface elevation map (see **Figure 5.7K**).

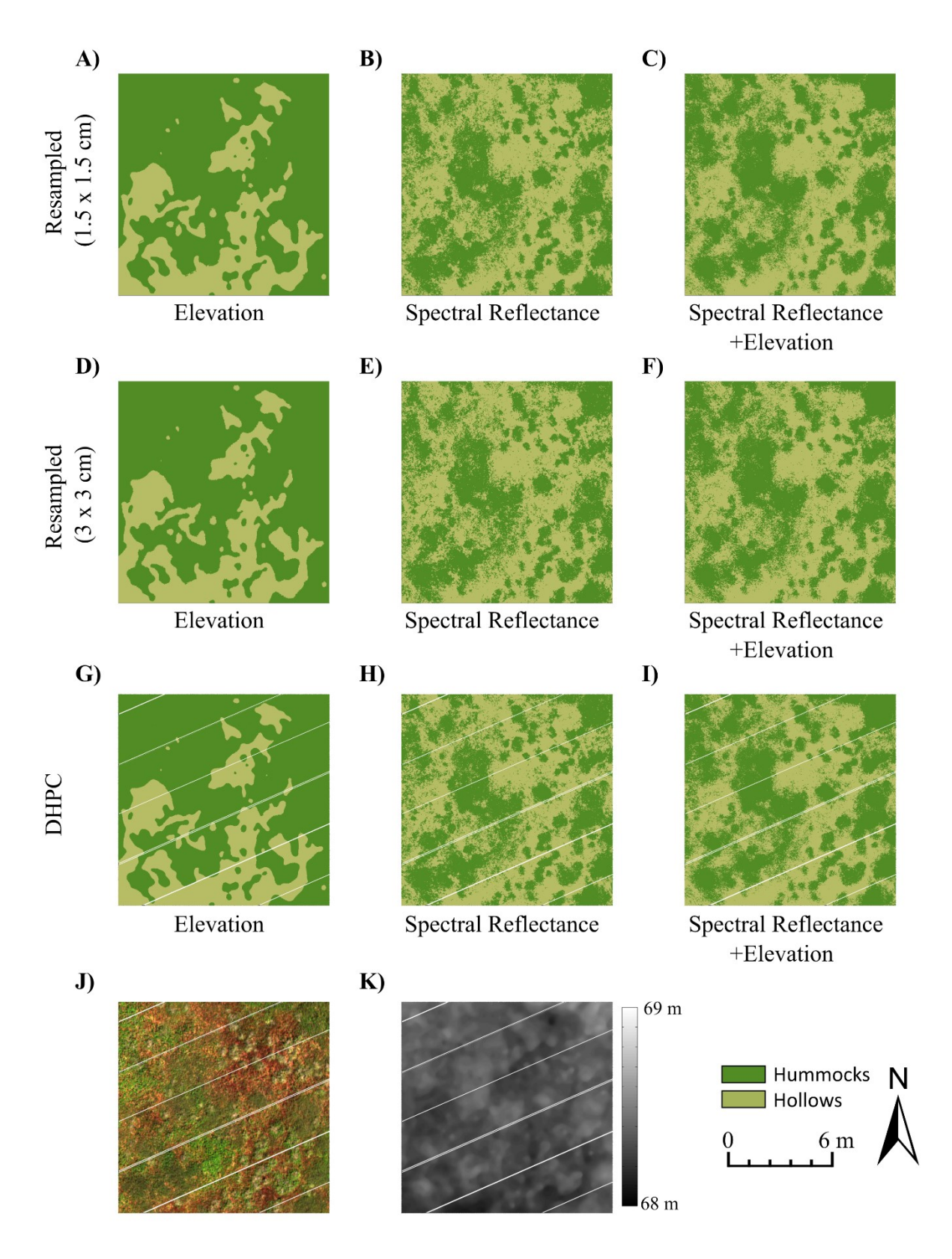
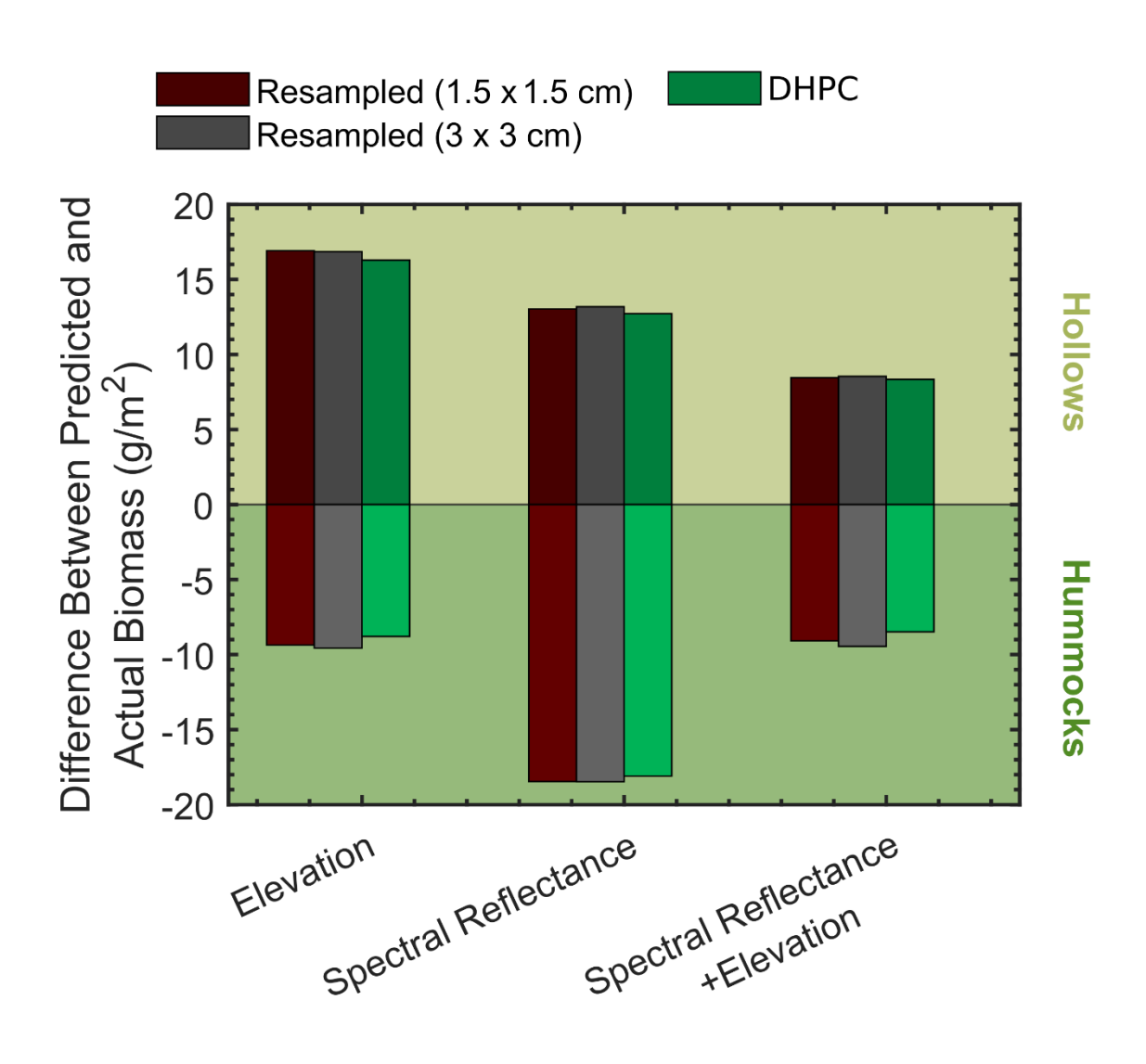


Figure 5.7. Panels (A-I) display sample hummock-hollow classification maps (12×12 m plot) generated from each of the trained models (μ CASI-1920 HSI data from the Mer Bleue Peatland).

The μ CASI-1920 HSI data included the Directly-Georeferenced Hyperspectral Point Cloud (DHPC) in addition to the two resampled hyperspectral images. The hyperspectral dataset used to generate each panel is given by the row titles. The training variables used to generate each classification model were displayed in the subtitle below each panel. An RGB image (R = 639.6 nm, G = 550.3 nm, B = 459.0 nm, linearly stretched between 0 and 12%) and surface elevation map (linearly stretched from 68 to 69 m) were generated by viewing the DHPC from directly above and are displayed in panels (J) and (K), respectively. The hummocks appear green in panel (J) while hollows appear red. The white stripes in the DHPC data derivatives (G-K) represent areas on the ground that were not sampled by the hyperspectral imager during data acquisition. These gaps are not present in the raster data derivatives (A-F) as they are interpolated over with duplicated pixels from the edges of the stripes.

5.3.2.2. Biomass Error Estimation

The differences between the mean of the predicted and actual biomass distribution for both hummocks ($\Delta B_{\mu,hk}$) and hollows ($\Delta B_{\mu,hw}$) are displayed in **Figure 5.8** (for exact values see Supplementary Table S1). The hollow distribution had a positive $\Delta B_{\mu,hw}$ for all of the classification models. The opposite trend was observed in hummocks ($\Delta B_{\mu,hk}$ <0). $\Delta B_{\mu,hw}$ ranged from 12.72 to 13.18 g/m² for all models trained with the spectral data alone. $\Delta B_{\mu,hk}$ ranged from -18.09 to -18.47 g/m² for all models trained with the spectral data alone. The models trained on the elevation data alone had the largest $\Delta B_{\mu,hw}$ values (16.29–16.91 g/m²). In comparison to these values, the magnitude of the $\Delta B_{\mu,hk}$ values when using elevation data alone were relatively small (8.79–9.56 g/m²). When using the classification models that incorporated both spectral and elevation information, both $\Delta B_{\mu,hw}$ and $\Delta B_{\mu,hk}$ decreased in magnitude; $\Delta B_{\mu,hw}$ was equal to 8.34–8.54 g/m² while $\Delta B_{\mu,hk}$ ranged from -8.48 to -9.45 g/m². Although all classification accuracies were relatively constant when comparing models trained with identical variables, the magnitude of $\Delta B_{\mu,hw}$ and $\Delta B_{\mu,hk}$ for the DHPC based classifications were always lower by 0.07–0.97 g/m².



Training Variables

Figure 5.8. Biomass estimation errors (difference between mean of predicted and actual biomass) for the developed hummock hollow classification models for the μCASI-1920 hyperspectral imaging data from the Mer Bleue Peatland. This data included the Directly-Georeferenced Hyperspectral Point Cloud (DHPC) in addition to the two resampled hyperspectral images. Each of the models were differentiated by the training dataset (given by bar colours) and training variables. The bars above 0 correspond to hollow biomass estimation errors while the bars below correspond to hummocks.

5.3.2.3. Geo-Locating Spectra from Pre-Specified Vegetation Plots

The mean and SD of the number of CASI-1500 spectra located per vegetation plot is shown in **Figure 5.9** (for exact values see Supplementary Table S2). For all resampled data products, spectra that were originally located outside the plot ended up within the boundaries of the plot after rasterization. The highest mean number of spectra located per plot (36.00) was acquired

when oversampling the data. Approximately 62% of the identified spectra were duplicates of one another as there were only a mean of 13.56 unique spectra per plot. Approximately 38% of these unique spectra on average were from outside of the actual plots before rasterization. The lowest mean number of spectra located per plot (2.26) was acquired when undersampling the data. 100% of the located spectra were unique. On average, 40% of the spectra were originally from outside of the actual plots before rasterization. When using the DHPC, it was possible to locate a mean of 8.46 unique spectra per plot. With this technique, there was zero duplication in these spectra. Furthermore, none of the located spectra were originally from outside the actual plots.

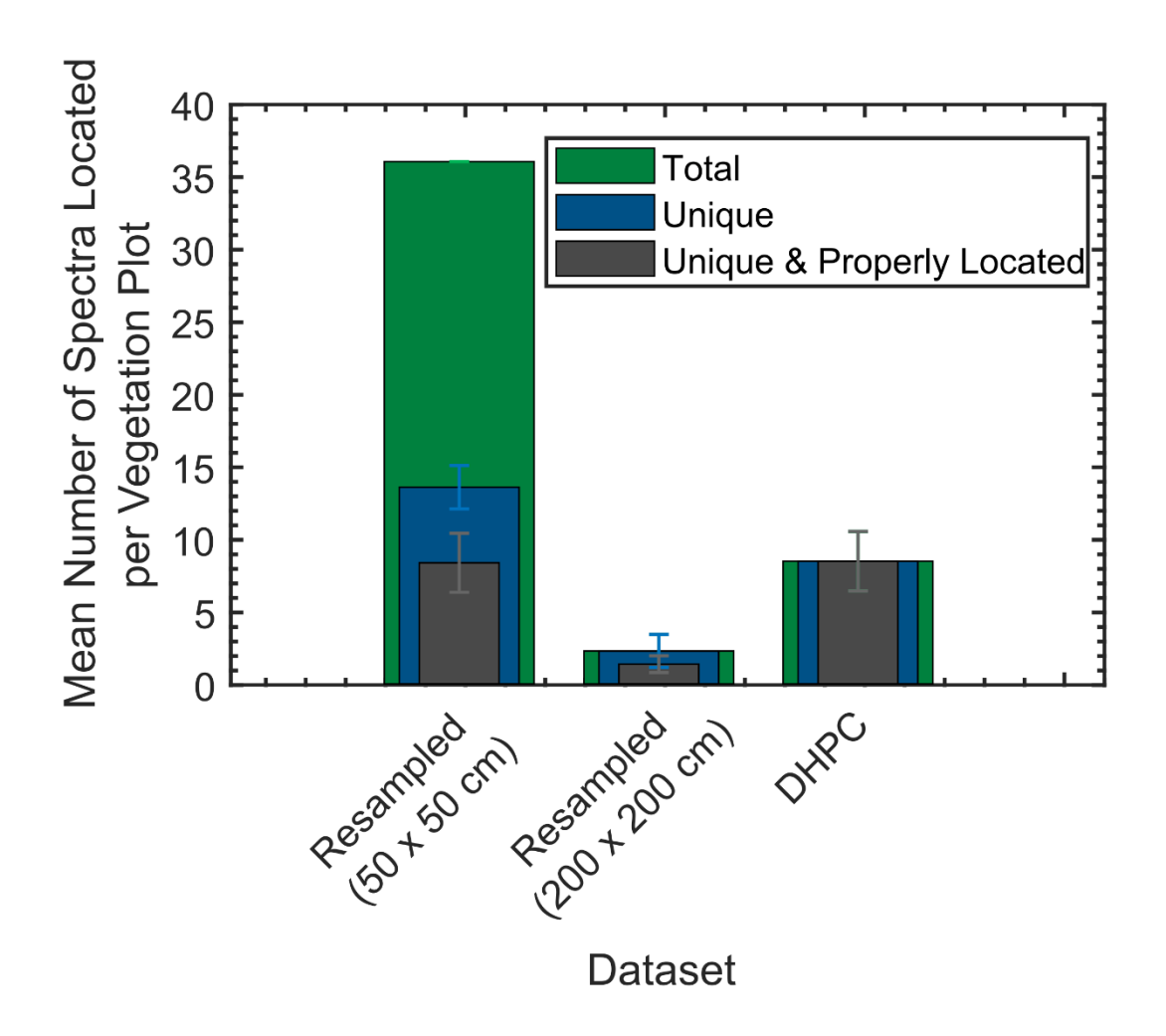


Figure 5.9. The mean and SD of the number of spectra, number of unique spectra and number of unique spectra properly located per each 3×3 m virtual vegetation plot (n = 100) from the Mer Bleue Peatland CASI-1500 data. The CASI-1500 data included the Directly-Georeferenced Hyperspectral Point Cloud (DHPC) in addition to the two resampled hyperspectral images. The error bars give the 1-sigma window around each mean value. Properly located spectra refer to those which were contained within each plot before and after rasterization (in the case of the resampled data products).

5.3.2.4. Detecting Sub-Pixel Targets

The results of the sub-pixel target detection (n=1,000 targets) are displayed in **Figure 5.10**. The total number of identified targets decreased as the threshold value increased. The total number of targets identified were identical for the oversampled data product and the DHPC, decreasing from 1,000 at a threshold of 0.15 to 402 at a threshold value of 0.85. The undersampled data products detected 577 targets at a threshold of 0.15 and 88 at a threshold of 0.85. The false discovery rate decreased linearly as the applied threshold value increased for all data products. The false discovery rate of the oversampled data products decreased from 90% at

a threshold value of 0.15 to 80% at a threshold value of 0.85. These false discovery rates were consistently larger than that of the undersampled data and the DHPC by an average of 50% and 69%, respectively. For all data products, the false negative rate increased linearly as the applied threshold value increased. The false negative rate was consistently largest for the undersampled data product increasing from 67% to 93% as the threshold value changed from 0.15 to 0.85. These false negative rates were consistently larger than that of the oversampled data and the DHPC by an average of 53% and 64%, respectively.

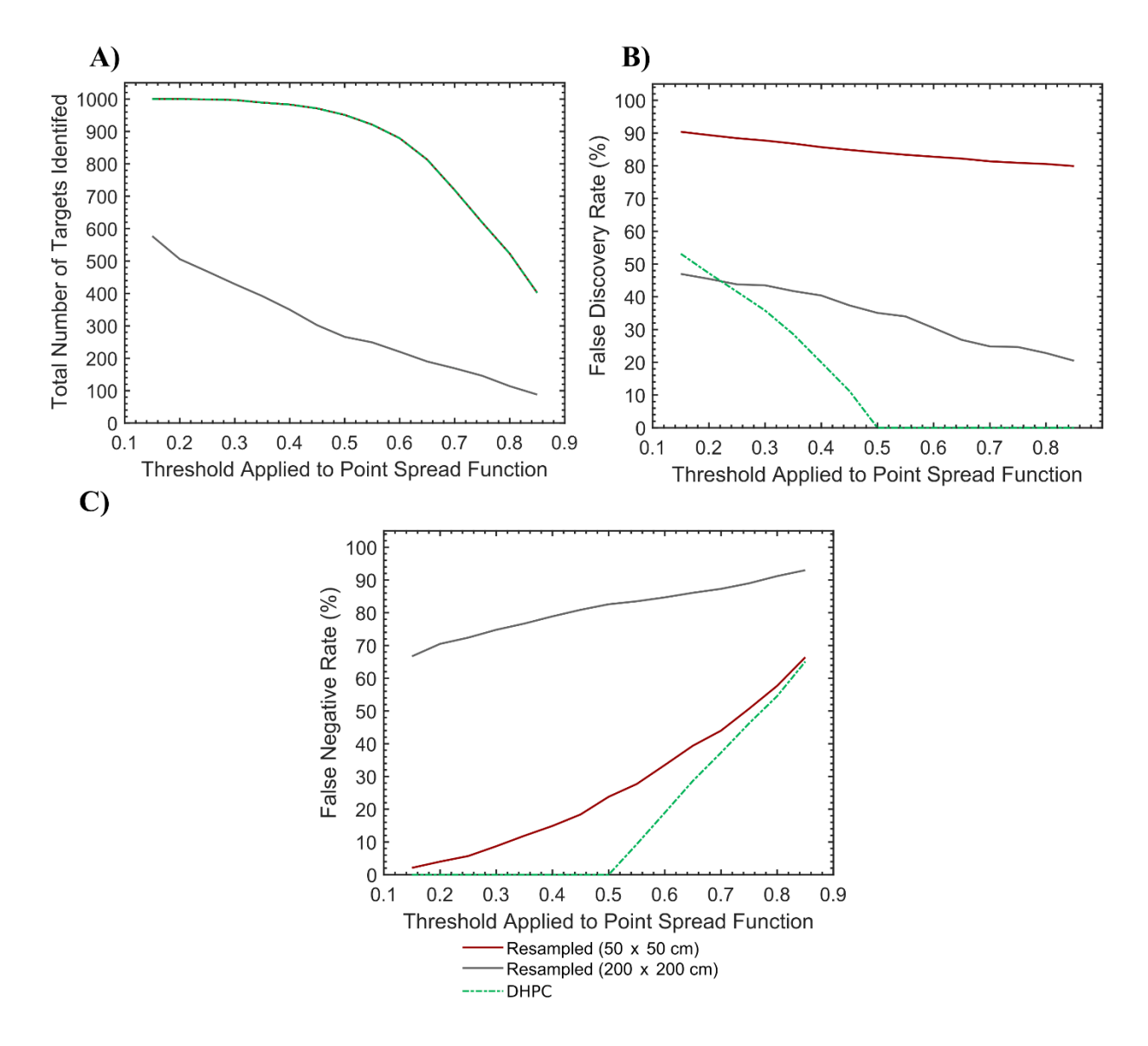


Figure 5.10. Target detection results from the CASI-1500 hyperspectral imaging data over the Mer Bleue Peatland. Artificial targets (n = 1,000) were randomly placed within the scene. The CASI-1500 data included the Directly-Georeferenced Hyperspectral Point Cloud (DHPC) in addition to the two resampled hyperspectral images. Panel (A) displays the number of targets (out of a maximum 1,000) identified in the target detection. Panel (B) and (C) give the false discovery and false negative rates, respectively.

5.4. Discussion

Our study presents a novel hyperspectral point cloud data representation which preserves the spatial integrity of HSI data (i.e., zero PL, PD and pixel shifting). Because the data fusion workflow does not modify the spectra from the original HSI data, the DHPC also preserves spectral data integrity. Although the raster datasets preserved spectral data integrity with the nearest neighbor methodology, spatial data integrity was compromised due to PL, PD and pixel

shifting from the resampling. For the raster data products, there was a trade-off between PD and PL that was dependant on the resolution of the implemented resampling grid; oversampling resulted in substantial PD (~35–75%) while undersampling led to substantial PL (~50–75%) (Table 5.2 and Table 5.3). The PL and PD were primarily caused by the uneven pixel spacing between the cross track and along track directions. While it may be possible to collect data with nearly identical pixel spacing in the cross track and along track, there are practical limitations that make it difficult. For example, the pixel spacing in the along track is dependent on the integration time, frame time and platform speed, all of which have impacts on other aspects of the data such as the signal to noise ratio and positional accuracy (Arroyo-Mora et al., 2019; Inamdar et al., 2020). The PL and PD caused by nearest neighbor resampling have been analyzed in a limited number of remote sensing studies (e.g., Kimerling, 2002; Kollasch, 2005; Williams et al., 2017), with only one focusing on HSI data (Williams et al., 2017). However, it was outside the scope of these studies to quantify the negative effects of PD and PL.

In the resampled MBP and MMG data, the calculated PL and PD metrics were only marginally larger than the theoretical expectations (PD_H and PL_H) (**Table 5.2** and **Table 5.3**). The PD and PL in the CGOP rasters exceeded theoretical expectations by up to $\sim 13\%$. The elevated PD and PL were likely a result of non-uniform pixel spacing due to differences in surface elevation across the scene. In the CGOP there was a difference in pixel spacing between the top of the canopy (~ 1.5 cm in cross track) and the understory (~ 2.0 cm in cross track). As such, even when resampling to 2.0 cm, the data were being undersampled at the top of the canopy, leading to PL. Due to the elevation of the surface relative to the sensor altitude, tall objects (e.g., treetop) blocked the view of lower lying regions of the imagery (e.g., ground below the canopy), leading to areas on the ground that were not imaged (data holes seen in Figure 5.5C). Such gaps are not present in the resampled images (Figure 5.5A,B) as they have been interpolated over with duplicated pixels from the edges, increasing PD values. The conservative assumptions made in section 5.2.2.4 while deriving PD_H and PL_H likely mean that these metrics can be used to approximate the lower boundary of PL and PD. As such, PD_H and PL_H are valuable for flight planning efforts, allowing data collectors to avoid PL and PD in their datasets.

Regardless of whether the HSI dataset was undersampled or oversampled, pixel shifting was large in the studied rasters (RMSE $_r$ = ~0.33–1.33 pixels in the raster MBP and MMG data) in comparison to the DHPC. The RMSE $_r$ values were, however, less than half the pixel spacing in the along and cross track directions and thus consistent with studies performed at the satellite level that quantify pixel shifting due to nearest neighbor resampling (e.g., Tan et al., 2006; Roy et al., 2016). Pixel shifting due to nearest neighbor resampling has been noted to negatively affect various applications [e.g., aligning multi-temporal datasets (Tan et al., 2006), change detection (Roy, 2000), classification (Alcantara et al., 2012) and biophysical parameter estimation (Tian et al., 2002)]. The exceptionally large RMSE $_r$ values (~1.30–1.95 pixels) in the CGOP was likely caused by the non-uniform pixel spacing across the scene due to large changes in elevation between treetops and ground below canopy relative to the sensor altitude.

In the DHPC data products (**Figure 5.3**–**Figure 5.6**), the observable white stripes represented areas on the ground that were not sampled by the hyperspectral imager during data acquisition. Such gaps in the imagery were likely caused by non-uniform sensor movement (e.g., sudden platform movement from changes in wind direction) between consecutive integration periods. It is important to recognize that these gaps are a true characteristic of the HSI data itself and are not data artifacts. Such gaps are not present in the resampled images as they have been interpolated over with duplicated pixels from the edges of the stripes. This example shows how the raster data model misrepresents HSI data as neighboring pushbroom HSI pixels in the along track direction are not uniformly spaced across the entire image.

In an ideal HSI end product, each pixel from the HSI data in its original sensor geometry should be sampled once. Since each pixel has identical data storage requirements (Johnson and Jajodia, 1998), an ideal HSI end product would have a file size roughly equal to that of the HSI data before the geometric correction (e.g., 4.09 Gb for the MBP μCASI-1920 data). In the rasterized data products, NoData pixels are abundant along the edges of the imagery (black pixels along the edges of **Figure 5.6A,B**). These additional NoData pixels contribute to the overall files size of raster data products (Lutes, 2005), increasing the data storage requirements. PD in the oversampled datasets led to a larger number of pixels, resulting in larger file sizes than in the ideal scenario (e.g., 30.90 Gb for the MBP μCASI-1920 data). Although the PL in the undersampled data product meant that many pixels were lost from the original HSI data in its

raw sensor geometry (theoretically leading to smaller files sizes than in the ideal scenario), there were generally more pixels overall due to the presence of the NoData pixels. As such, even the undersampled datasets often had larger file sizes (e.g., 7.77 Gb for the MBP μCASI-1920 data) than in the ideal scenario. Even with its additional elevation data, the data storage requirements of the DHPC were only slightly larger than in the ideal scenario (e.g., 4.55 Gb for the MBP μCASI-1920 DHPC). The small file size was due to the absence of PD and NoData pixels along the edges of the imagery, making the DHPC ideal for data distribution. This is important given the data requirements of HSI, especially for high spatial resolution applications (Arroyo-Mora et al., 2019).

The DHPC outperformed the raster data products in the four studied applications. In the hummock-hollow classification, models trained with spectral data alone had the lowest overall accuracy (~83%) and a discrepancy between user's accuracy and producer's accuracy. The discrepancy meant that there was a large portion of hollow pixels that were misclassified as hummocks, explaining why the magnitude of $\Delta B_{\mu,hk}~(\sim\!18~g/~m^2)$ was larger than $\Delta B_{\mu,hw}~(\sim\!13$ g/m²) in the biomass error calculation. Models trained with the surface elevation data alone had an intermediate overall accuracy (~86%). The discrepancy between user's accuracy and producer's accuracy in these models meant that the magnitude of $\Delta B_{\mu,hk}~(\sim\!9~g/m^2)$ was smaller than that of $\Delta B_{\mu,hw}$ (~17 g/m²) since a large portion of hummock pixels were being misclassified as hollows. The classification models trained on both the spectral and elevation data had high overall accuracy, user's accuracy and producer's accuracy for both hummocks and hollows (\sim 91%), leading to relatively low errors in biomass estimation (magnitude of \sim 9 g/m²). These findings show that the integration of surface elevation and spectral information can lead to improved results for classification problems, agreeing with a number of other studies (e.g., Elaksher, 2008; Vauhkonen et al., 2013; Brell et al., 2019; Sothe et al., 2019; Hong et al., 2020b). For instance, Sothe et al. (2019) improved the overall accuracy of tree species classification of tropical forests by > 10% by using elevation data in addition to spectral information.

The DHPC based classification consistently had higher overall accuracies by 0.3–0.7% which led to lower biomass estimation errors by 0.07–0.97 g/m². The higher accuracies were likely due to the reduced levels of PL and PD, the latter of which has been found to impede classification

accuracy (Chowdhury and Alspector, 2003). Based on the microform spatial distribution in the 19 km² region of MBP (Arroyo-Mora et al., 2018a), by implementing the DHPC, the aboveground biomass estimation of hollows (~12.7% area coverage) and hummocks (~51.2% area coverage) would be improved by 179–1,504 kg and 3,415–9,437 kg, respectively. Such a systematic increase in biomass estimation performance is biologically important since above ground biomass is one of the primary sources of carbon to peat soil and thus impacts the ability of peatlands to mitigate the effects of climate change by sequestering carbon (Moore et al., 2002).

In the geo-location application, a substantial portion of the located spectra in the raster data products originated from outside the plot before resampling (~40%). These spectra were only brought within the plot due to the pixel shifting from resampling. If these spectra were used as training data in any remote sensing application, this could mean that a substantial amount of the training data would not be valid, potentially leading to error unrelated to the applied algorithm (Tan et al., 2006). When using the DHPC, 0% of the identified spectra were originally from outside the plots. By maximizing the total number of unique spectra located per plot, the DHPC should lead to improved performance in applications that rely on accurately matching field data to collected imagery [e.g., biophysical parameter estimation (Zhu et al., 2013) and classification (Alcantara et al., 2012)].

In the sub-pixel target detection application, a trade-off was observed between false discovery and false negative rates (**Figure 5.10B,C**). Such a trade-off is commonly discussed in the target detection literature (e.g., Han et al., 2014); false negatives increase while false discoveries decrease as target detection thresholds become more strict. The false discovery and false negative rates were linked to the PD and PL metrics (**Figure 5.11**). False discoveries were created when each true positive pixel was duplicated during resampling. Likewise, PL led to false negatives as true positive pixels were lost during resampling. These principles explain why the oversampled data product had a large false discovery rate and a low false negative rate while the opposite was observed in the undersampled data product. The DHPC minimized both false discovery rates (19% and 69% smaller on average than the undersampled and oversampled rasters, respectively) and false negative rates (11% and 64% smaller on average than the oversampled and undersampled rasters, respectively). The reduced error rates could allow

individuals following up on target detection maps to identify more targets with less searching power, reducing cost and minimizing physical and environmental risks, [e.g., landmine detection (Makki et al., 2017) and invasive species detection (Pengra et al., 2007)]. In target detection applications where the precise location of a target is necessary, it may be problematic to use HSI data that is spatially resampled with the nearest neighbor approach. Further research should investigate the performance of target detection algorithms before and after spatial resampling.

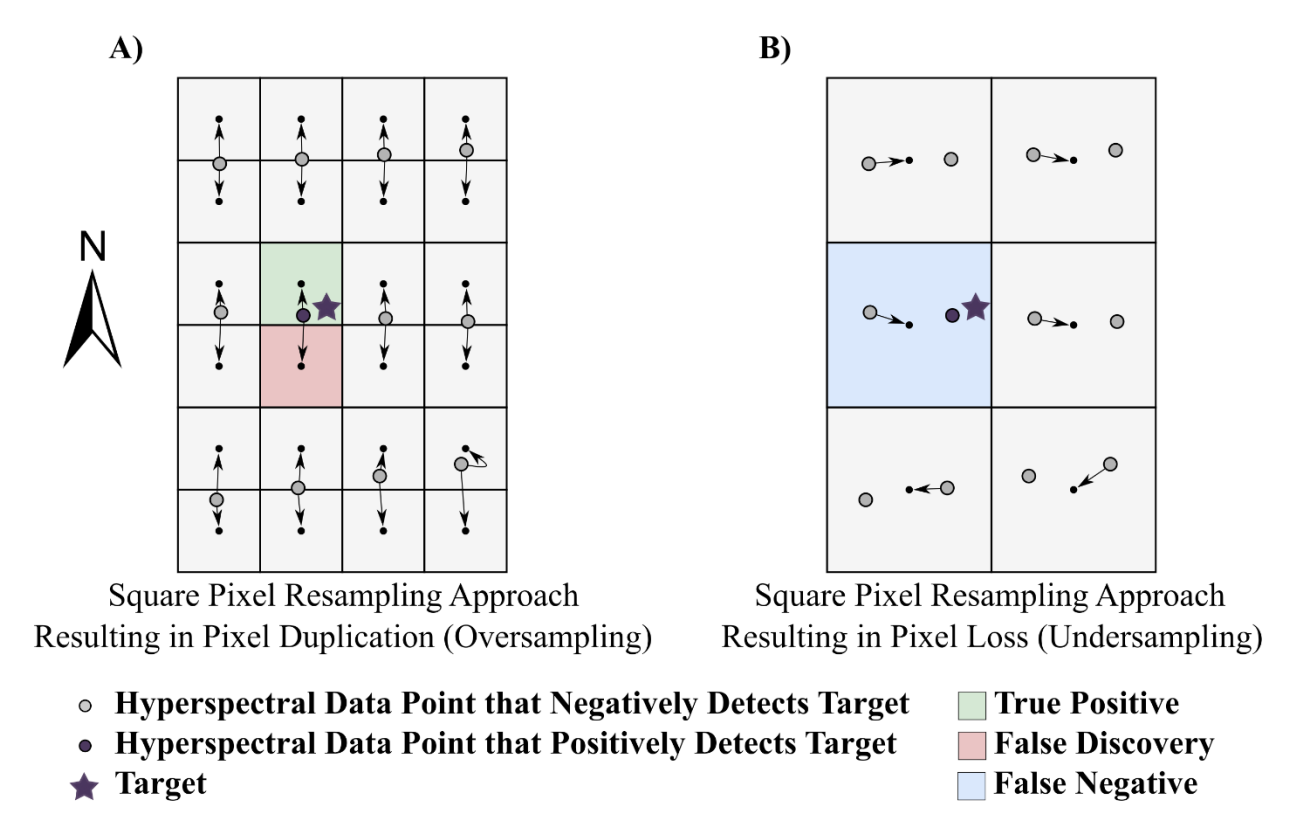


Figure 5.11. False discoveries and false negatives caused by pixel loss and pixel duplication in a target detection exercise. Consider spatially resampling a hyperspectral imaging dataset (given by the colored circles) acquired along an approximate true north heading where the pixel spacing in the cross track is half that of the along track. To generate a rasterized data product (given by the raster grid and the small black dots which designate the center of each cell), the data must be resampled on a north-oriented grid. In this scene there is one target of interest (purple star) that can be detected by the hyperspectral data point represented by the purple circle. Panel (A) shows that pixel duplication can cause false discoveries while panel (B) shows that pixel loss can cause false negatives.

In signature matched target detection algorithms, error metrics are often theoretically calculated based on the modeled probability distributions of the background and target signals. For reliable error metrics, the modeled distributions must accurately describe the data (Manolakis et al., 2016). There must also be a statistically significant number of target and

background pixels. The availability of such datasets are often limited in the literature (Manolakis et al., 2013). In the theoretical target detection, the PSF was used as a detection statistic, fundamentally representing the horizontal distance from each pixel center to the nearest target. Since the location of each simulated target was known, it was possible to calculate error metrics from the target detection results, as opposed to modeled probability distributions. Such a target detection workflow is valuable in understanding the limitations of sub-pixel target detection and the variables that control it (e.g., size and position of a target within a pixel).

Aside from preserving spatial-spectral data integrity and the minimal data storage requirements, the DHPC is advantageous over other existing hyperspectral point clouds as its data fusion workflow can be implemented with the same tools used to process conventional raster end products. Additionally, the DHPC can use HSI and DSM data from a variety of different data sources and thus is not limited by any particular sensor. Furthermore, by convolving the DSM by the hyperspectral sensor PSF during the data fusion workflow, the spatial characteristics of the elevation data become more consistent with that of the HSI data. As such, the elevation information encoded in each pixel of the DHPC actually corresponds to the footprint of the spectral information, leading to a more spatially coherent data fusion. This convolution may come at the cost of fine spatial scale elevation information. Although there are hyperspectral point clouds that can preserve fine spatial scale elevation information, they can come at the cost of spectral data integrity, especially over spectrally and spatially heterogeneous terrains (Brell et al., 2019). Further research into the performance of the DHPC against other point cloud data representations is advised.

In this work, we developed a hyperspectral point cloud that preserves the spatial-spectral integrity of HSI data more effectively than conventional rasterized square pixel end products. Our DHPC methodology has been shown to produce no pixel shift, duplication or loss. Despite containing additional surface elevation data, the DHPC file size was up to 13 times smaller than the corresponding rasterized datasets. This is favorable for data distribution, especially since the DHPC generation workflow can be easily implemented with pre-existing processing protocols. Importantly, the DHPC consistently outperformed raster data products in various remote sensing applications (classification, target detection, spectra geolocation). Overall, our research shows

that the developed DHPC data representation has the potential to push the limits of HSI data distribution, analysis and application.

5.5. References

- Aasen, H., Burkart, A., Bolten, A., & Bareth, G. (2015). Generating 3D hyperspectral information with lightweight UAV snapshot cameras for vegetation monitoring: From camera calibration to quality assurance. *ISPRS Journal of Photogrammetry and Remote Sensing*, 108, 245-259
- Alcantara, C., Kuemmerle, T., Prishchepov, A.V., & Radeloff, V.C. (2012). Mapping abandoned agriculture with multi-temporal MODIS satellite data. *Remote Sensing of Environment*, 124, 334-347
- American Society for Photogrammetric Engineering Remote Sensing (2015). ASPRS positional accuracy standards for digital geospatial data (Edition 1, Version 1.0., November, 2014). *Photogrammetric Engineering & Remote Sensing*, 81, A1-A26
- Arif, F., & Akbar, M. (2005). Resampling air borne sensed data using bilinear interpolation algorithm. In: *Proceedings of the 2005 IEEE International Conference on Mechatronics*. (pp. 62-65). Taipei: IEEE
- Arroyo-Mora, J.P., Kalacska, M., Inamdar, D., Soffer, R., Lucanus, O., Gorman, J., Naprstek, T., Schaaf, E.S., Ifimov, G., & Elmer, K. (2019). Implementation of a UAV–Hyperspectral Pushbroom Imager for Ecological Monitoring. *Drones, 3*, 12
- Arroyo-Mora, J.P., Kalacska, M., Løke, T., Schläpfer, D., Coops, N.C., Lucanus, O., & Leblanc, G. (2021). Assessing the impact of illumination on UAV pushbroom hyperspectral imagery collected under various cloud cover conditions. *Remote Sensing of Environment, 258*, 112396
- Arroyo-Mora, J.P., Kalacska, M., Soffer, R., Ifimov, G., Leblanc, G., Schaaf, E.S., & Lucanus, O. (2018a). Evaluation of phenospectral dynamics with Sentinel-2A using a bottom-up approach in a northern ombrotrophic peatland. *Remote Sensing of Environment*, 216, 544-560
- Arroyo-Mora, J.P., Kalacska, M., Soffer, R., Moore, T., Roulet, N., Juutinen, S., Ifimov, G., Leblanc, G., & Inamdar, D. (2018b). Airborne hyperspectral evaluation of maximum gross photosynthesis, gravimetric water content, and CO₂ uptake efficiency of the Mer Bleue ombrotrophic peatland. *Remote Sensing*, 10, 565
- Brell, M., Rogass, C., Segl, K., Bookhagen, B., & Guanter, L. (2016). Improving sensor fusion: A parametric method for the geometric coalignment of airborne hyperspectral and LiDAR Data. *IEEE Transactions on Geoscience and Remote Sensing*, 54, 3460-3474
- Brell, M., Segl, K., Guanter, L., & Bookhagen, B. (2017). Hyperspectral and LiDAR intensity data fusion: A framework for the rigorous correction of illumination, anisotropic effects, and cross calibration. *IEEE Transactions on Geoscience and Remote Sensing*, 55, 2799-2810
- Brell, M., Segl, K., Guanter, L., & Bookhagen, B. (2019). 3D hyperspectral point cloud generation: Fusing airborne laser scanning and hyperspectral imaging sensors for improved

- object-based information extraction. ISPRS Journal of Photogrammetry and Remote Sensing, 149, 200-214
- Bubier, J.L., Bhatia, G., Moore, T.R., Roulet, N.T., & Lafleur, P.M. (2003). Spatial and temporal variability in growing-season net ecosystem carbon dioxide exchange at a large peatland in Ontario, Canada. *Ecosystems*, 353-367
- Chowdhury, A., & Alspector, J. (2003). Data duplication: an imbalance problem? In: *ICML'2003 Workshop on Learning from Imbalanced Data Sets (II)* (pp. 1-10). Washington, DC: ICML
- Chen, Y., Jiang, H., Li, C., Jia, X., & Ghamisi, P. (2016). Deep feature extraction and classification of hyperspectral images based on convolutional neural networks. *IEEE Transactions on Geoscience and Remote Sensing*, *54*, 6232-6251
- Eismann, M.T. (2012). Hyperspectral Remote Sensing. In: *Hyperspectral Remote Sensing*. Bellingham: SPIE
- Elaksher, A.F. (2008). Fusion of hyperspectral images and LiDAR-based DEMs for coastal mapping. *Optics and Lasers in Engineering, 46*, 493-498
- Eppinga, M.B., Rietkerk, M., Borren, W., Lapshina, E.D., Bleuten, W., & Wassen, M.J. (2008). Regular surface patterning of peatlands: Confronting theory with field data. *Ecosystems*, 11, 520-536
- Fisher, R.A. (1936). The use of multiple measurements in taxonomic problems. *Annals of Eugenics*, 7, 179-188
- Frolking, S., Roulet, N.T., Tuittila, E.-S., Bubier, J.L., Quillet, A., Talbot, J., & Richard, P. (2010). A new model of Holocene peatland net primary production, decomposition, water balance, and peat accumulation. *Earth System Dynamics*, *1*,1-21
- Galbraith, A.E., Theiler, J.P., & Bender, S.C. (2003). Resampling methods for the MTI coregistration product. In: *Algorithms and Technologies for Multispectral, Hyperspectral, and Ultraspectral Imagery IX* (pp. 283-293). Orlando: International Society for Optics and Photonics
- Goetz, A.F.H. (2009). Three decades of hyperspectral remote sensing of the Earth: A personal view. *Remote Sensing of Environment*, 113, S5-S16
- Han, J., Zhou, P., Zhang, D., Cheng, G., Guo, L., Liu, Z., Bu, S., & Wu, J. (2014). Efficient, simultaneous detection of multi-class geospatial targets based on visual saliency modeling and discriminative learning of sparse coding. *ISPRS Journal of Photogrammetry and Remote Sensing*, 89, 37-48
- Hong, D., Gao, L., Yao, J., Zhang, B., Plaza, A., & Chanussot, J. (2020a). Graph Convolutional networks for hyperspectral image classification. *IEEE Transactions on Geoscience and Remote Sensing*, 1-13
- Hong, D., Gao, L., Yokoya, N., Yao, J., Chanussot, J., Du, Q., & Zhang, B. (2020b). More diverse means better: Multimodal deep learning meets remote-sensing imagery classification. *IEEE Transactions on Geoscience and Remote Sensing*, 1-15
- Hong, D., Yokoya, N., Chanussot, J., & Zhu, X.X. (2019). An augmented linear mixing model to address spectral variability for hyperspectral unmixing. *IEEE Transactions on Image Processing*, 28, 1923-1938

- Inamdar, D., Kalacska, M., Leblanc, G., & Arroyo-Mora, J.P. (2020). Characterizing and mitigating sensor generated spatial correlations in airborne hyperspectral imaging data. *Remote Sensing*, 12, 641
- Johnson, N.F., & Jajodia, S. (1998). Exploring steganography: Seeing the unseen. *Computer*, 31, 26-34
- Kalacska, M., Arroyo-Mora, J.P., Soffer, R., & Leblanc, G. (2016). Quality control assessment of the mission airborne carbon 13 (MAC-13) hyperspectral imagery from Costa Rica. *Canadian Journal of Remote Sensing*, 42, 85-105
- Kalacska, M., Chmura, G.L., Lucanus, O., Bérubé, D., & Arroyo-Mora, J.P. (2017). Structure from motion will revolutionize analyses of tidal wetland landscapes. *Remote Sensing of Environment*, 199, 14-24
- Kalacska, M., Lucanus, O., Arroyo-Mora, J.P., Laliberté, É., Elmer, K., Leblanc, G., & Groves, A. (2020). Accuracy of 3D Landscape Reconstruction without Ground Control Points Using Different UAS Platforms. *Drones*, 4, 13
- Kimerling, A.J. (2002). Predicting data loss and duplication when resampling from equalangle grids. *Cartography and Geographic Information Science*, 29, 111-126
- Kollasch, R.P. (2005). Increasing the detail of land use classification: The Iowa 2002 land cover product In: *Proceedings of the Global priorities in Land and Remote Sensing Conference: PECORA* (pp. 1-9). Sioux Falls: American Society for Photogrammetry and Remote Sensing
- Lafleur, P.M., Hember, R.A., Admiral, S.W., & Roulet, N.T. (2005). Annual and seasonal variability in evapotranspiration and water table at a shrub-covered bog in southern Ontario, Canada. *Hydrological Processes*, 19, 3533-3550
- Lafleur, P.M., Roulet, N., & Admiral, S. (2001). Annual cycle of CO2 exchange at a bog peatland. *Journal of Geophysical Research: Atmospheres*, 106, 3071-3081
- Le ministère des Forêts, d.l.F.e.d.P. (2021). LiDAR Modèles numériques (terrain, canopée, pente) Données Québec. In d.l.F.e.d.P. Le ministère des Forêts (Ed.), *Le ministère des Forêts, de la Faune et des Parcs*. Québec City: Les Publications du Québec
- Lenz, A., Schilling, H., Perpeet, D., Wuttke, S., Gross, W., & Middelmann, W. (2014). Automatic in-flight boresight calibration considering topography for hyperspectral pushbroom sensors. In: *2014 IEEE Geoscience and Remote Sensing Symposium* (pp. 2981-2984). Quebec City: IEEE
- Leslie, R.V. (2018). Microwave Sensors. In: S. Liang (Ed.), *Comprehensive Remote Sensing* (pp. 435-474). Oxford: Elsevier
- Liu, X. (2008). Airborne LiDAR for DEM generation: some critical issues. *Progress in Physical Geography*, 32, 31-49
- Liu, Y., Guo, Y., Li, F., Xin, L., & Huang, P. (2019). Sparse dictionary learning for blind hyperspectral unmixing. *IEEE Geoscience and Remote Sensing Letters*, 16, 578-582
- Lucanus, O., & Kalacska, M. (2020). UAV DSLR photogrammetry with PPK processing. protocols.io. DOI: dx.doi.org/10.17504/protocols.io.bjm2kk8e

- Lucieer, A., Malenovský, Z., Veness, T., & Wallace, L. (2014). HyperUAS—imaging spectroscopy from a multirotor unmanned aircraft system. *Journal of Field Robotics*, *31*, 571-590
- Lutes, J. (2005). Resourcesat-1 geometric accuracy assessment. In: *ASPRS 2005 Annual Conference* (pp. 1-12). Baltimore: American Society for Photogrammetric Engineering Remote Sensing
- Makki, I., Younes, R., Francis, C., Bianchi, T., & Zucchetti, M. (2017). A survey of landmine detection using hyperspectral imaging. *ISPRS Journal of Photogrammetry and Remote Sensing*, 124, 40-53
- Malhotra, A., Roulet, N.T., Wilson, P., Giroux-Bougard, X., & Harris, L.I. (2016). Ecohydrological feedbacks in peatlands: an empirical test of the relationship among vegetation, microtopography and water table. *Ecohydrology*, *9*, 1346-1357
- Manolakis, D., Pieper, M., Truslow, E., Cooley, T., Brueggeman, M., & Lipson, S. (2013). *The remarkable success of adaptive cosine estimator in hyperspectral target detection.* SPIE
- Manolakis, D.G., Lockwood, R.B., & Cooley, T.W. (2016). Hyperspectral data exploitation. In: *Hyperspectral Imaging Remote Sensing: Physics, Sensors, and Algorithms* (pp. 551-620). Cambridge: Cambridge University Press
- Moore, T.R., Bubier, J.L., Frolking, S.E., Lafleur, P.M., & Roulet, N.T. (2002). Plant biomass and production and CO2 exchange in an ombrotrophic bog. *Journal of Ecology*, 90, 25-36
- Mulcahy, K.A. (2000). Two new metrics for evaluating pixel-based change in data sets of global extent due to projection transformation. *Cartographica*, 37, 1-11
- Müller, R., Lehner, M., Muller, R., Reinartz, P., Schroeder, M., & Vollmer, B. (2002). A program for direct georeferencing of airborne and spaceborne line scanner images. *International Archives of Photogrammetry Remote Sensing and Spatial Information Sciences*, 34, 148-153
- Oliveira, R.A., Tommaselli, A.M.G., & Honkavaara, E. (2019). Generating a hyperspectral digital surface model using a hyperspectral 2D frame camera. *ISPRS Journal of Photogrammetry and Remote Sensing*, 147, 345-360
- Pengra, B.W., Johnston, C.A., & Loveland, T.R. (2007). Mapping an invasive plant, Phragmites australis, in coastal wetlands using the EO-1 Hyperion hyperspectral sensor. *Remote Sensing of Environment*, 108, 74-81
- Poblete, T., Camino, C., Beck, P.S.A., Hornero, A., Kattenborn, T., Saponari, M., Boscia, D., Navas-Cortes, J.A., & Zarco-Tejada, P.J. (2020). Detection of Xylella fastidiosa infection symptoms with airborne multispectral and thermal imagery: Assessing bandset reduction performance from hyperspectral analysis. *ISPRS Journal of Photogrammetry and Remote Sensing*, 162, 27-40
- Qin, A., Shang, Z., Tian, J., Wang, Y., Zhang, T., & Tang, Y.Y. (2019). Spectral–spatial graph convolutional networks for semisupervised hyperspectral image classification. *IEEE Geoscience and Remote Sensing Letters*, 16, 241-245
- Radoux, J., Chomé, G., Jacques, D.C., Waldner, F., Bellemans, N., Matton, N., Lamarche, C., d'Andrimont, R., & Defourny, P. (2016). Sentinel-2's potential for sub-pixel landscape feature detection. *Remote Sensing*, *8*, 488

- Rasti, B., Hong, D., Hang, R., Ghamisi, P., Kang, X., Chanussot, J., & Benediktsson, J.A. (2020). Feature extraction for hyperspectral imagery: The evolution from shallow to deep: overview and toolbox. *IEEE Geoscience and remote sensing magazine*, 8, 60-88
 - Richards, J.A., & Jia, X. (1999). Remote sensing digital image analysis. Springer
- Richter, R., & Schläpfer, D. (2020). ATCOR-4 User Guide, Version 7.3.0, March 2020. In: *Atmospheric/Topographic Correction for Airborne Imagery*. Wessling: DLR German Aerospace Center
- Riley, D.N., & Hecker, C.A. (2013). Mineral mapping with Airborne hyperspectral thermal infrared remote sensing at Cuprite, Nevada, USA. In: C. Kuenzer, & S. Dech (Eds.), *Thermal Infrared Remote Sensing: Sensors, Methods, Applications* (pp. 495-514). Dordrecht: Springer Netherlands
- Roy, D.P. (2000). The impact of misregistration upon composited wide field of view satellite data and implications for change detection. *IEEE Transactions on Geoscience and Remote Sensing*, 38, 2017-2032
- Roy, D.P., Li, J., Zhang, H.K., & Yan, L. (2016). Best practices for the reprojection and resampling of Sentinel-2 Multi Spectral Instrument Level 1C data. *Remote sensing letters*, 7, 1023-1032
- Savage, J., & Vellend, M. (2015). Elevational shifts, biotic homogenization and time lags in vegetation change during 40 years of climate warming. *Ecography*, 38, 546-555
- Schläpfer, D., Nieke, J., & Itten, K.I. (2007). Spatial PSF nonuniformity effects in airborne pushbroom imaging spectrometry data. *IEEE Transactions on Geoscience and Remote Sensing*, 45, 458-468
- Schroth, R. (2004). Direct geo-referencing in practical applications. In: *ISPRS WG1/5 Workshop about Theory, Technology and Realities of Inertial/GPS Sensor Orientation* (pp. 1-5). Castelldefels: International Society for Photogrammetry and Remote Sensing
- Shlien, S. (1979). Geometric correction, registration, and resampling of Landsat imagery. *Canadian Journal of Remote Sensing*, *5*, 74-89
- Soffer, R.J., Ifimov, G., Arroyo-Mora, J.P., & Kalacska, M. (2019). Validation of airborne hyperspectral imagery from laboratory panel characterization to image quality assessment: implications for an arctic peatland surrogate simulation site. *Canadian Journal of Remote Sensing*, 45, 476-508
- Sothe, C., Dalponte, M., Almeida, C.M.d., Schimalski, M.B., Lima, C.L., Liesenberg, V., Miyoshi, G.T., & Tommaselli, A.M.G. (2019). Tree species classification in a highly diverse subtropical forest integrating UAV-based photogrammetric point cloud and hyperspectral data. *Remote Sensing*, 11, 1338
- Sun, X., Qu, Y., Gao, L., Sun, X., Qi, H., Zhang, B., & Shen, T. (2020). Target detection through tree-structured encoding for hyperspectral images. *IEEE Transactions on Geoscience and Remote Sensing*, 1-17
- Takasu, T., & Yasuda, A. (2009). Development of the low-cost RTK-GPS receiver with an open source program package RTKLIB. In: *International symposium on GPS/GNSS* (pp. 4-6). Jeju Island: International Convention Center Jeju Korea

- Tan, B., Woodcock, C.E., Hu, J., Zhang, P., Ozdogan, M., Huang, D., Yang, W., Knyazikhin, Y., & Myneni, R.B. (2006). The impact of gridding artifacts on the local spatial properties of MODIS data: Implications for validation, compositing, and band-to-band registration across resolutions. *Remote Sensing of Environment*, 105, 98-114
- Tian, Y., Woodcock, C., Wang, Y., Privette, J., Shabanov, N., Zhou, L., Zhang, Y., Buermann, W., Dong, J., & Veikkanen, B. (2002). Multiscale analysis and validation of the MODIS LAI product I. Uncertainty assessment. *Remote Sensing of Environment*, 83, 414-430
- Vane, G., Goetz, A.F., & Wellman, J.B. (1984). Airborne imaging spectrometer: A new tool for remote sensing. *IEEE Transactions on Geoscience and Remote Sensing*, 6, 546-549
- Vauhkonen, J., Hakala, T., Suomalainen, J., Kaasalainen, S., Nevalainen, O., Vastaranta, M., Holopainen, M., & Hyyppa, J. (2013). Classification of Spruce and pine trees using active hyperspectral LiDAR. *IEEE Geoscience and Remote Sensing Letters*, 10, 1138-1141
- Vreys, K., Iordache, M.-D., Biesemans, J., & Meuleman, K. (2016). Geometric correction of APEX hyperspectral data. *Miscellanea Geographica*, 20, 11-15
- Warren, M.A., Taylor, B.H., Grant, M.G., & Shutler, J.D. (2014). Data processing of remotely sensed airborne hyperspectral data using the Airborne Processing Library (APL): Geocorrection algorithm descriptions and spatial accuracy assessment. *Computers & Geosciences*, 64, 24-34
- Westoby, M.J., Brasington, J., Glasser, N.F., Hambrey, M.J., & Reynolds, J.M. (2012). 'Structure-from-Motion' photogrammetry: A low-cost, effective tool for geoscience applications. *Geomorphology*, 179, 300-314
- Wilkinson, G. (1996). A review of current issues in the integration of GIS and remote sensing data. *International Journal of Geographical Information Science*, 10, 85-101
- Williams, M.D., Kerekes, J.P., & Aardt, J.V. (2017). Application of abundance map reference data for spectral unmixing. *Remote Sensing*, *9*, 793
- Yeh, C.-K., & Tsai, V.J. (2011). Self-calibrated direct geo-referencing of airborne pushbroom hyperspectral images. In: 2011 IEEE International Geoscience and Remote Sensing Symposium (pp. 2881-2883). Vancouver: IEEE
- Zhao, R., Shi, Z., Zou, Z., & Zhang, Z. (2019). Ensemble-based cascaded constrained energy minimization for hyperspectral target detection. *Remote Sensing*, 11, 1310
- Zhu, Z., Bi, J., Pan, Y., Ganguly, S., Anav, A., Xu, L., Samanta, A., Piao, S., Nemani, R.R., & Myneni, R.B. (2013). Global data sets of vegetation leaf area index (LAI) 3g and fraction of photosynthetically active radiation (FPAR) 3g derived from global inventory modeling and mapping studies (GIMMS) normalized difference vegetation index (NDVI3g) for the period 1981 to 2011. *Remote Sensing*, 5, 927-948

5.6. Author Contribution

Conceptualization, D.I., M.K., methodology, D.I., M.K, G.L. and J.P.A.-M.; validation, D.I.; formal analysis, D.I.; investigation, D.I.; resources, M.K., G.L, J.P.A.-M.; data curation, D.I.,

M.K., G.L. and J.P.A.-M.; writing—original draft preparation, D.I.; writing—review and editing, D.I., M.K., G.L. and J.P.A.-M.; visualization, D.I.

5.7. Acknowledgements

The authors would like to thank Raymond Soffer and Stephen Achal for information regarding the sensor point spread functions and Dr. Ronald Resmini and Dr. Nigel Roulet for discussions that improved the study. The authors express their appreciation to Defence Research and Development Canada Valcartier for the loan of the CASI-1500 instrument. The authors would like to thank the Ministry of Forests, Wildlife and Parks of Québec for their digital surface model from the MMG field site, to the National Capital Commission for access to MBP and for the LiDAR point cloud of the site, the Nature Conservancy of Canada for access to CGOP and SEPAQ for access to MMG.

5.8. Supplementary Material

The Supplementary Material for this chapter can be found online at: https://www.frontiersin.org/articles/10.3389/frsen.2021.675323/full#supplementary-material.

Connecting Statement (Chapter 5 to Chapter 6)

Chapter 5 developed and validated a novel hyperspectral point cloud data representation (the Directly-Georeferenced Hyperspectral Point Cloud (DHPC)) that preserves the spatial-spectral integrity of HSI data more effectively than conventional square pixel raster end products. Although the article theoretically presents all of the information needed to carry out the DHPC generation workflow, its practical implementation may not be approachable for all end users. Detailed information on the practical implementation (e.g., code, high-level explanations, documentation) of the DHPC data fusion workflow was published in *MethodsX* and can be found in Appendix 7.2. Chapter 6 provides a discussion of the thesis findings, acknowledging the limitations of the research and providing future directions to expand on the presented work. Chapter 6 also summarizes all of the presented work and their significance to the field.

6. Discussion and Conclusion

6.1. Discussion of Research

The popularity of HSI has increased substantially over the past ten years, as airborne and spaceborne HSI systems have become more prevalent. At the airborne level, there is a wide array of HSI instruments that operate on remotely piloted aircraft systems (RPAS) (e.g., HySpex Mjolnir (Arroyo-Mora et al., 2021), ITRES µCASI-1920 (Arroyo-Mora et al., 2019)) and manned fixed-wing aircrafts (e.g., AVIRS-NG (Hamlin et al., 2011), APEX (Vreys et al., 2016a)). Currently, there are several operational spaceborne HSI systems (e.g., DESIS (Alonso et al., 2019), EnMAP (Guanter et al., 2015)) that have replaced early generation systems such as Hyperion (Pearlman, 2003). More than 10 HSI satellites are planned to be launched over the next 15 years alone (e.g., HyspIRI, FLORIS, CHIME, OCI, SBG) (Qian, 2021; Chandra et al., 2022). The widescale availability of HSI data is promising to end users from various fields as these data can provide invaluable economic, environmental and social insight into some of the most challenging problems that the Earth and its inhabitants face (e.g., climate change, national defense, food security, biodiversity conservation). In HSI processing efforts, raster end products have remained the standard input and output format for over 40 years (Goetz, 2009; Vane et al., 1984; Wilkinson, 1996). Although the raster data model has been pivotal to how multivariate data are displayed and represented, it is a heritage of the old computing era (Lim, 2008) and misrepresents HSI data on a fundamental level during data analytics. The use of the raster data model requires end users to implicitly assume that all HSI pixels are: 1) directly comparable, 2) square and 3) uniformly distributed across the image scene. Due to various factors (e.g., sensor design, rugged terrains, illumination conditions), these assumptions do not hold for HSI data and can lead to issues in data analytics. This dissertation identified limitations in the raster model and developed a novel data representation methodology that results in a new paradigm for HSI conceptualization that has the potential to revolutionize data analysis and application.

Hyperspectral imagers (like all measurement devices) are affected by errors (e.g., dead pixels, spectral smile artifacts) that appear in various spectral bands and spatial pixels (Schläpfer et al., 2007). To confidently analyze the spectra from different pixels and understand changes in spectral information across the imaged scene, the location of these imaging errors must be determined. Chapter 3 leveraged the correlation coefficient to develop a quality assessment

methodology that can be readily implemented by end users, even without advanced image analysis tools. Specifically, the novel approach allows end users to quickly locate common non-linear errors in the spectral and spatial domain and understand the comparability of pixels across the sensor FOV. Despite best processing practices, it is virtually impossible to correct all imaging errors. Thus, not all pixels in any final georeferenced end product are directly comparable. The variance introduced by a single error could severely influence results obtained from linear techniques such as the principal component analysis. For instance, Ramsey et al. (2005) used Hyperion data to detect Chinese tallow, an invasive tree species that causes losses in native habitats and harvestable land. In the study, Hyperion reflectance data were used to derive percentage occurrences of senescing foliage, canopy shadows, green vegetation, yellow foliage and red tallow (a surrogate for Chinese tallow). In these data derivatives, image-related striping errors could be seen in three of the five canopy composition images, potentially resulting in inaccurate values that could have been mistaken for natural phenomena. With this in mind, if a target of opportunity is available (e.g., asphalt road), the comparability of pixels across the field of view should be assessed using the techniques developed in chapter 3.

In general, the impact of located imaging errors can be minimized via flight planning and data processing. For instance, in the flight planning tool developed by Naprstek and Inamdar (2022), the 160 pixels on either edge of the uCASI-1920 were ignored when calculating the distance from adjacent flight lines as these pixels were noticeably blurred when compared to pixels from the center of the FOV. Factored into flight planning, this meant HSI data collected from adjacent flight lines would have contiguous spatial coverage, even when ignoring the problematic edge pixels in data analytics. For errors isolated in specific spectral and spatial locations, problematic pixels can be removed in post-processing without substantial loss in information content. At the very least, errors should be documented in the metadata to potentially reduce the possibility of end users confusing imaging errors with physically significant phenomena in the scene.

The work from chapter 3 also has important implications for data analysis by showcasing the importance of analyzing HSI data in its raw sensor geometry. The developed quality assessment technique cannot be directly applied to georeferenced raster end products as the sensor geometry is lost, and errors are masked after being randomly shifted and duplicated during nearest

neighbour resampling. The loss of sensor geometry also makes it more difficult to understand the differences in spatial characteristics (e.g., PSFs, resolution, pixel spacing) between the across track and along track directions of HSI data.

In HSI, spatial PSFs are important data parameters that are typically ignored by data providers and end users in favour of less informative metrics such as pixel resolution. Chapter 4 substantiated the importance of PSFs in understanding the physical significance of a pixel. Pixels are not square (Smith, 1995); by ignoring the true geometry of spectral measurements from each pixel, HSI data can be misinterpreted, leading to false conclusions about the studied scene. For instance, the HSI data from chapter 4 over the Mer Bleue Peatland could detect the hummockhollow microtopography in the cross track, but not the along track direction. This was due to the discrepancy in the width of the sensor PSF between the cross track and along track directions. Without actual knowledge of the peatland, end users might believe that the spatial variability in the observed scene was present in one dimension but not the other. This interpretation would hinder our understanding of the ecosystem from the imagery, thus substantiating the importance of recognizing that imaging pixels are not square. Using the data simulation workflow from Appendix 7.1, and a modified spatial autocorrelation methodology, it was possible to show that the overlap in the PSF of neighbouring pixels reduces the spectral and spatial variability observed in the scene. The reduction in variability is problematic as it is associated with information loss (Lee and Landgrebe, 1993) and thus negatively affects various remote sensing tasks such as classification (Huang et al., 2002), sub-pixel feature detection (Radoux et al., 2016) and spectral unmixing (Wang et al., 2018). The work in Appendix 7.1 further showcased the importance of accounting for spatial PSFs when performing tasks such as data cross-validation, flight planning and data fusion.

Based on the analysis in chapter 4, <60% of the signal to a spectrum originates from materials within the spatial boundaries defined by the pixel resolution (e.g., only 57.8 % of the signal to each Landsat 8 Operational Land Imager pixel (bands 1-7) originates within the square pixel spatial boundaries (Inamdar et al., 2020)). This is caused by how pixel resolution is defined by FWHM. FWHM as pixel resolution only has physical significance if PSFs take the form of well-defined functions (Gaussian, rectangular pulse, Airy function). Since net PSFs can vary substantially depending on data acquisition parameters, FWHM has a different physical

interpretation for each dataset. As such, FWHM is somewhat arbitrary and can lead end users to make inappropriate assumptions during data applications. This issue is compounded by the fact that the pixel resolution of georeferenced raster end products can differ substantially from the FWHM. For instance, based on the spatial characteristics of the geometrically corrected CASI imagery from Appendix 7.1, < 36 % of the signal to each measured spectrum originates from the square spatial boundaries defined by the final pixel resolution (1 m). This value will likely be even lower when accounting for pixel shifting due to resampling. These observations have important implications for HSI data applications as the utility and performance of remote sensing technologies depend greatly on establishing rigorous relationships with field measurements. For instance, Pau et al. (2022) attributed poor relationships between HSI data collected by the National Ecological Observation Network (NEON) and certain ecological variables (e.g., leaf area index, total biomass) to differences in scale. Such a discrepancy in scale could be avoided by making plot size decisions based on the PSF instead of conventional parameters such as spatial resolution (Schweiger, 2020). Ideally, the PSF should always be consulted in addition to pixel resolution when characterizing the spatial properties of any given spectrum. For this to be possible, future HSI efforts should append sensor PSFs as metadata to all end products. Furthermore, whenever pixel resolution is used to describe the spatial properties of a system, it should be accompanied by additional parameters that give the value real physical significance (e.g., percent signal contribution to a pixel). For instance, the metadata of the CASI imagery analyzed in chapter 4 should document that ~55% of the signal from each pixel originated from the area within the spatial boundaries defined by the pixel resolution.

By highlighting issues in the rasterization process used to generate square pixel end products and developing an alternative HSI data representation (DHPC) to overcome the described limitations of the raster data model, the work from chapter 5 will potentially lead to significant improvements in the way that HSI data are processed, analyzed and applied. In chapter 5, rasterization via nearest neighbour resampling was shown to introduce substantial levels of pixel loss, duplication and shifting, especially in areas with large elevational gradients relative to pixel size. These resampling errors negatively affect data applications, especially when applications rely on accurately georeferenced spectra (e.g., sub-pixel target detection). The developed DHPC represents georeferenced HSI in its raw sensor geometry after the geometric correction, including additional elevation data. The elevation information encoded in the DHPC is

particularly important for applications dependent on structural information. For instance, Komoske et al. (2022) show that the spectral properties related to leaf and canopy function traits and forest health must be leveraged simultaneously with LiDAR-derived forest structure measures to map biodiversity accurately. As such, implementing the DHPC instead of conventional rasters would likely lead to improved biodiversity estimation. Although other point cloud data representations exist (as highlighted in section 2.5.2), they can be difficult to implement, computationally expensive, result in large file sizes and compromised spatial-spectral data integrity. The DHPC can be implemented via the same processing protocols and computational resources as conventional raster end products. Thus, the processing implementation of the DHPC is approachable for current users and data providers. Given its minimal data storage requirements, the DHPC is ideal for data distribution and analysis. For example, when using analytical tools with local memory constraints (e.g., MATLAB), data are loaded to random access memory (RAM). A compact data representation is important since files larger than the available RAM must be parsed and continually loaded from local storage to memory, which is not ideal for performance (Schilling and Harris, 2011). By eliminating resampling errors (pixel duplication, loss and shifting), which are problematic for data analytics (e.g., subpixel target detection, geolocation), the DHPC preserves spatial-spectral data integrity and thus can improve results in multiple applications (e.g., target detection, spectra geolocation, classification).

Up to this point, the discussion has addressed the main aspects directly related to the dissertation objectives and findings. However, the work from this dissertation also has important implications for various general aspects of remote sensing and Earth observation, such as: uncertainty budgets, data intercomparability, data acquisition and processing, metadata documentation and data distribution, which will be discussed herein.

This dissertation makes fundamental contributions to reducing the overall uncertainties in the spectral domain (radiance or reflectance) and spatial domain (spectra location) of HSI data. HSI data uncertainties are a function of the instrument, calibration, data acquisition and processing uncertainties. Using best practices, instrument and calibration uncertainties can result in a radiometric uncertainty of < 2 % (Kopp, 2017). Additionally, calibration and processing uncertainties arise due to spectral smile and keystone corrections (see section 2.4.1 for more

information). When using radiative transfer modelling for atmospheric compensation, uncertainties in various factors (e.g., visibility, water vapour, aerosol type, radiometric calibration quality, spectral smile and keystone) affect reflectance spectra (Cairns, 2003; Boucher, 2002; Richter and Schläpfer, 2020). If ground spectroscopy data over known reference materials are used to fine-tune atmospheric correction approaches, atmospheric and radiometric uncertainties can be reduced (Richter and Schläpfer, 2020). In such cases, additional instrument and calibration uncertainties from the utilized ground spectrometer are introduced. When using best practices, atmospheric correction uncertainties can be <5 %. For instance, ATCOR4 reports accuracies of < 4 % for high reflectance targets (> 40%) and accuracies of < 2 % for low reflectance targets (< 10%) (Richter and Schläpfer, 2020). Practically, uncertainties in reflectance from atmospheric compensation are larger than those reported and vary drastically depending on data acquisition practices, the atmosphere and the imaged scene. By identifying and removing errors in HSI systems using the approach developed in chapter 3, instrument and atmospheric compensation uncertainties can potentially be reduced. Using the developed DHPC and accounting for sensor PSFs, it would be possible to ensure that the ground spectroscopy data used to fine-tune atmospheric compensation methodologies are spatially coherent with the HSI data (no contributions from non-calibration materials), further minimizing overall uncertainties.

By calculating pixel shifting, chapter 5 assessed spatial uncertainty due to the use of nearest neighbour resampling. The magnitude of the uncertainties due to pixel shifting can be on the same order of magnitude as the other sources of spatial uncertainties, such as those imposed by the technical limitations of the inertial navigation system (INS) (e.g., pixel shifting was equal to 0.87 m for MMG data, see chapter 5.3.1). By using the DHPC, the uncertainty due to spatial resampling is eliminated as the data are analyzed in raw sensor geometry, pre-rasterization. Thus, the DHPC results in more spatially accurate information. Although spatial and spectral uncertainties are often analyzed separately from one another, they are interdependent. For instance, pixel duplication, loss and shifting from resampling will affect reflectance spectra in raster end products and thus affect uncertainty values calculated via comparison with an independent reference source (i.e., ground spectroscopy data). As such, the reduction in spatial uncertainties from the use of the DHPC is likely associated with a reduction in spectral uncertainties.

The work from this dissertation has important implications for data intercomparability. Data intercomparability is fundamental to applications that rely on the output from multiple data sources. For instance, global, regional and local vegetation assessments use multiple data sources (e.g., Landsat 8 and Sentinel-2) to monitor vegetation dynamics over time and space (Moravec et al., 2021). Data intercomparability is also critical in the cross-validation of satellite data products using in situ data collected at the ground level and airborne HSI data collected at the airborne level (Arroyo-Mora et al., 2018b). For instance, the Quality Assurance for Earth Observation (QA4EO) initiative aims to validate spaceborne (Sentinel-2) spectrographic imaging data using RPAS HSI data (Hyspex Mjolnir VS-620) and manned fixed-wing aircraft HSI data (CASI and SASI), in addition to in situ ground spectroscopy data. This dissertation highlights two important factors that could potentially affect sensor intercomparability. Firstly, some sensor-related errors, such as dead pixels, should be removed; otherwise, differences between sensors could be artificially inflated. Secondly, it is critical to ensure that all compared data are spatially coherent. When comparing datasets collected at different spatial scales, it is important to spatially degrade the finer-resolution dataset based on the spatial response function of the coarser-resolution dataset using tools like the developed SR² workflow. Otherwise, sensors will be comparing information from different areas on the ground and, by extension, materials. When comparing datasets collected on similar spatial scales, there will always be differences in spatial response functions, meaning that measurements from different sensors will always correspond to different areas on the ground. The spatial mismatch is amplified by resampling errors due to pixel shifting, duplication and loss. By representing HSI data as a point cloud representation with spatial dimensions defined by the sensor PSF, it is possible to assess data intercomparability between different sensors. Specifically, the overlap in PSFs between the closest points in the compared data products can be calculated and used as a metric of spatial coherency between sensors. By filtering out points of low spatial coherency, intercomparability between different sensors in the spatial domain can be ensured.

In general, HSI data acquisition should be planned based on the intended use of the data. In many scenarios, it is unclear what spatial-spectral resolutions are required. In these cases, RPAS HSI paired with data simulation can be used to understand the spatial-spectral resolution requirements of a given data application (as shown in section 7.1). To avoid differences in spatial characteristics between the cross track and along track directions of HSI data, missions should be

planned to generate pixels with a similar resolution and spacing in both spatial dimensions. Although ideal, this can be technically challenging since the resolution in the along track is determined by the integration time and platform speed, both of which have impacts on other aspects of the data (signal to noise ratio, positional accuracy, etc.), especially for low altitude platforms such as unmanned aerial systems (Arroyo-Mora et al., 2019). On that note, the DHPC is highly recommended, as discrepancies between the cross track and along track spatial dynamics can lead to excessive pixel loss and duplication (e.g., up to 78 % in imagery analyzed in chapter 5) in square pixel raster end products. If square pixel raster end products are being used in data analytics, it is critical to collect HSI data so that it is compatible with the raster data model. Specifically, pixels should be spatially summed to ensure that the spatial PSF is square. To minimize pixel loss and duplication in square pixel raster end products, it is also critical to minimize the angular misalignment between the resampling grid and the flight line heading. For instance, assuming that the pixel spacing in the cross track and along track directions is equal to 1 m, data products would theoretically have > 15 % pixel duplication and loss if there is a misalignment of 45 degrees between the flight line heading and the resampling grid. As such, missions should be planned so that the flight line heading is in one of the cardinal directions. Given BRDF effects, airspace restrictions, wind directions and area coverage requirements, it may not always be possible to collect HSI data in a cardinal direction. In these situations, it may be important to resample the data on a grid that is aligned with the flight line heading to minimize pixel loss and duplication.

In addition to data acquisition (including flight planning) and processing, the work from this dissertation also has important implications for metadata documentation and data distribution. Despite the increased availability of HSI data in general, it is critical to recognize that there is currently no standard for HSI, though this is slowly changing. In particular, the IEEE Geoscience and Remote Sensing Society is developing a standard for the characterization and calibration of ultraviolet through shortwave infrared (250 nm to 2500 nm) HSI devices (Skauli et al., 2021). Until a comprehensive and widely accepted standard is fully developed, end users must ensure that they are making informed decisions when purchasing, analyzing and applying HSI data. Ideally, manufacturers and data providers should strive for transparency, providing informative metadata that characterize end products (e.g., PSFs, data acquisition parameters, sensor calibration, processing parameters). Metadata should include uncertainty measurements of

spectra geolocation and retrieved reflectance whenever possible so that end users can understand the limitations of HSI for various applications. In addition to improved metadata, HSI data at various pre-processing levels (e.g., radiometrically corrected, atmospherically corrected, geometrically corrected, spatially resampled) should be given by data providers along with all utilized auxiliary data products (e.g., INS data, calibration files, data processing reports). When direct georeferencing methodologies are used in HSI processing, the position (easting, northing, elevation) of each pixel from the original sensor geometry is an intermediate data product of particular interest as it allows end users to generate vector-based data representations like the DHPC. Although most data providers do not currently give this information, future spaceborne HSI efforts such as NASA's Earth Surface Mineral Dust Source Investigation (EMIT) and Surface Biology and Geology (SBG) initiative may adopt a similar approach to the DHPC for improved data analytics (Philip Townsend, Pers. Comm., 2022).

6.2. Impact of Research

By improving the quality of remotely sensed imaging data while simultaneously lowering the barrier to entry, this dissertation represents a major technological advancement that will allow policymakers to make more confident and reliable decisions that address important societal, environmental and economic issues. The research from this dissertation has already been implemented in the scientific literature with promising results. For instance, Rowan et al. (2021) implemented the DHPC for the target detection of submerged aquatic vegetation in the water surrounding the Long Sault Parkway in Ontario, Canada. Submerged aquatic vegetation is critical to study as it provides valuable ecosystem services, is a significant global carbon sink helping to mitigate climate change (Fourqurean et al., 2012) and helps improve water quality by limiting phytoplankton concentration and reducing turbidity (Dennison et al., 1993; Wolter et al., 2005). In Rowan et al. (2021), the DHPC allowed ground truth data to be accurately associated with reflectance spectra extracted from the HSI data during target detection. Rowan et al. (2021) recommended using the DHPC for future submerged aquatic vegetation monitoring and mapping efforts due to its ability to improve data quality. The DHPC was also implemented by Wallis et al. (2023) to assess the relationship between spectral reflectance derived from HSI and forest carbon content in the Parc national du Mont Mégantic in Quebec, Canada. Since forest clearings account for an estimated 12-15% of global greenhouse gas emissions (van der Werf, 2009), forest carbon content is critical to study when understanding climate change. In Wallis et al.

(2023), the analyzed VNIR and SWIR imagery were collected across a large elevation gradient (elevation changes by > 600 m within the 10 km² area surrounding the peak of the mountain). Raster end products were avoided as they were characterized by substantial pixel duplication (up to 60%), pixel loss (up to 58%) and pixel shifting (0.866 m), partially due to the elevation gradient. In this work, the DHPC was also ideal for associating HSI spectra with ground data due to the lack of resampling errors. By explicitly defining the spatial extent of each spectrum from the DHPC with the sensor PSF, it is possible to understand how materials are sampled across the entire scene. This will ensure end users have a firm understanding of the spatial coverage and any holes that may arise due to data acquisition and sampling strategies. An understanding of spatial coverage is fundamental as it shows how well insights derived from Earth observation represent the studied area of interest (e.g., how accurately HSI-derived forest carbon content estimates represent an area).

The DHPC has also been adopted by the Canadian Airborne Biodiversity Observatory (CABO) project, a national initiative using HSI to understand the changes in plant biodiversity and its relation to land use change, climate change, invasive species and nitrogen deposition across Canadian ecosystems. The CABO project will provide all collected HSI data (> 200 images) in DHPC data format to ensure optimal data quality. Future investigators using the CABO data will have the opportunity to use the DHPC data representation in meaningful data applications (such as the work described in Wallis et al. (2023)).

The research from this dissertation has also led to important contributions to industry and government. For instance, the error detection methodology implemented in chapter 3 led to the identification of fundamental errors (e.g., cross track illumination effects, striping artifacts, dead pixels) in spectrographic imaging data collected and processed with ITRES (Calgary, AB, Canada) products, including the CASI and SASI sensors and their data processing programs. The provided input improved the ITRES processing programs, allowing the company to enhance their product. The research from this dissertation has also had various impacts in government. For instance, the nominal PSF derivation established in chapter 4 and implemented in the code from chapters 7.1-7.2 have been integrated into the Hyperspectral Planning Tool (HYPlanT) (Naprstek and Inamdar, 2022) that was developed for the CABO project. This tool is also in use by the National Research Council of Canada, Flight Research Laboratory (FRL) to estimate

parameters such as pixel size, pixel spacing and spatial response functions based on nominal flight parameters. The FLR is also implementing the SR² workflow (chapter 7.1) in the QA4EO initiative described earlier.

HSI is an extremely technical field that calls on concepts from remote sensing theory, mathematics, physics and computer science. Without a firm understanding of such concepts, end users new to HSI may have difficulties working with the data, creating a high barrier to entry into the field. This barrier to entry is problematic as novel end users without a sufficient background in HSI analytics may be unable to successfully extract information relevant to the application of interest, potentially leading them to disregard the field altogether. The work presented in this dissertation lowers the barrier to entry for incoming end users from fields outside of remote sensing. The developed techniques were designed to allow end users of all expertise levels to understand HSI data on a fundamental level. With such an understanding, novel end users can confidently apply HSI data to various problems. The DHPC is stored in text file format as a list of multivariate observations (including elevation, reflectance values, position and other desired variables such as off-nadir look angle) that researchers in various fields are comfortable manipulating. This makes the DHPC more approachable to a wider array of scientists. Overall, by lowering the barrier to entry, data applications will expand drastically as end users from different fields have the domain knowledge to implement HSI techniques in new, creative and exciting ways (Cavender-Bares et al., 2022). This will undoubtedly contribute to solving Earth's most challenging problems, such as climate change, national defense, food security and biodiversity conservation using HSI data.

6.3. Limitations and Future Directions of Research

Despite the various advantages of the developed DHPC data format, some challenges must be addressed before the remote sensing community at large uses the data format. To date, various data processing and analysis methodologies have been built around the raster data format (Bioucas-Dias et al., 2013; Signoroni et al., 2019). Before the DHPC data format can be used in such cases, these workflows must be modified to use vectorized data. In some cases, such modifications could require major changes that can be difficult to implement (Tomlin, 1990), particularly when analyzing spatial information via operations such as convolution. Although there are analogous convolution operators that work on vector data (e.g., Thomas et al., 2019),

they can be difficult to implement and more computationally expensive when compared to raster-based techniques. These added difficulties may dissuade end users from using the DHPC data format. However, it is important to recognize that in many cases, only minor modifications must be made to processing workflows. This was exemplified by Rowan et al. (2021), who were able to modify the water compensation workflow reported in Inamdar et al. (2022) to use a DHPC input instead of a raster data input as per the original algorithm. Interestingly, the first step in many processing workflows is to vectorize the imaging data (Charmisha et al., 2018; Rasti et al., 2020; Rasti et al., 2014). For example, autoencoder and recurrent neural network deep learning techniques often require vectorized inputs (Rasti et al., 2020). Using the DHPC in these cases, the workflow can be implemented more efficiently as an initial vectorization step would not be required. With this in mind, HSI data processing may be more computationally efficient for the DHCP than conventional raster end products in certain situations.

The DHPC was not tested with spaceborne data. This is problematic given the importance of spaceborne data acquisition to scaling local and regional observations acquired from HSI data at the airborne level. Although not explicitly tested, some literature showcases the utility of the DHPC at the spaceborne level. As discussed in section 2.5.3, Kristóf and Pataki (2009) developed a vector-based data product for MODIS multispectral data that used swath reflectance (MOD02) and geolocation (MOD03) products to calculate the footprint of each observation and to represent and process them as rectangular polygons. Kristóf (2015) further tested the MODIS vector data representation, showcasing its practical importance for time series applications. Since the DHPC is fundamentally similar to the MODIS vector data representation, the work from Kristóf and Pataki (2009) and Kristóf (2015) suggests that the DHPC will likely allow for improved data applications (e.g., time series analysis) at the spaceborne level.

Although structural information is fundamental to many data applications (e.g., mapping biodiversity), high-quality elevation information is not always available. This presents an issue for the DHPC, especially since the accuracy of the spectra geolocation is dependent on high-quality surface elevation data (Beekhuizen, 2011). For areas with small elevation gradients relative to pixel size, a flat elevation model can be used during the generation of DHPC data products without a large loss in spatial accuracy. For areas with large elevation gradients relative to spatial resolution, a flat elevation model may be inappropriate and could improperly locate

spectra during the geometric correction, especially along the edges of the FOV. It is important to recognize that this issue would equally affect the geometric accuracy of raster end products generated from direct georeferencing approaches (which would have pixel loss, duplication and shifting errors in addition to geometric accuracy errors). Although using a flat elevation model during the generation of the DHPC may be problematic for areas with large elevation gradients relative to spatial resolution, it is still advised over raster end products as it eliminates pixel duplication, loss and shifting.

The variability in data application performance between the raster and vector data models agrees with Wade et al. (2003), who show that when the phenomenon of interest is small relative to the pixel size, vector-based data representations outperform raster-based methods. This explains why the performance of the subpixel target detection from chapter 5 improved substantially when using the DHPC over raster end products. Despite the effectiveness of the DHPC, it is unlikely that the data representation will always outperform the rasterized datasets. Certain applications may be invariant to factors such as pixel shifting, duplication and loss. For instance, although pixel duplication and loss modify the spatial dynamics of the raw imagery, they theoretically do not affect basic first and second-order statistics like mean and standard deviation (Schläpfer et al., 2007). As such, applications that exploit this information (e.g., Laliberté et al. (2020), which exploits variance to partition plant spectral diversity into alpha and beta diversity) may not be substantially affected by pixel loss and duplication.

In this dissertation, the developed algorithms were programmed in MATLAB. MATLAB is one of the most popular programming platforms for HSI efforts and was utilized in this dissertation as it is a high-level language that can carry out matrix math effectively. However, MATLAB is monetarily expensive. To solve this issue, the tools developed in this dissertation will be packaged and distributed as stand-alone programs (as part of the CABO project) that can be applied by end users of all expertise levels, further lowering the barrier to entry. This form of distribution does, however, mean that higher level programmers may not be able to modify the developed tools without completely rewriting them. To solve this problem, it may be beneficial to rewrite all the algorithms using a free programming language such as Python or R. When releasing individual scripts, it is critical to use a version control platform such as GitHub.

6.4. Conclusion

The goal of Earth observation within the context of environmental science, conservation and protection is to: 1) Help society observe and monitor the Earth; 2) Understand and predict the physical interactions between society and the Earth; and 3) Provide decision-makers with the necessary information to understand the consequences that political and economic decisions could have on the Earth and its inhabitants (Goryl, 2018). By highlighting limitations in the raster end products commonly utilized for Earth observation efforts, this dissertation identifies limitations in how spatial phenomena across the planet are observed and analyzed. Using the developed DHPC data representation, it is possible to overcome these limitations. Specifically, the DHPC data representation bridges the gap between in situ ground truth and HSI data by providing a clear physical interpretation of the collected spectral information. This contribution is critical to ensuring data intercomparability, which is fundamental when scaling up ground observations to model global phenomena using information from multiple data sources. This dissertation also lowers the barrier to entry to HSI by developing various algorithms (e.g., data analytics, data quality assessment, spatial autocorrelation analysis, image sharpening, data simulation, data fusion, flight planning) that can be readily implemented by end users of all expertise levels. This contribution will make HSI more approachable to a wider array of users, allowing them to solve important problems such as climate change, national defense, food security and biodiversity conservation. For example, the United Nations Biodiversity Conference (COP15) sets out to define a global biodiversity framework that specifies regional, national and global actions that will mitigate biodiversity loss across Earth. Before actions can be taken, biodiversity must be measured and mapped. HSI data has been shown as a strong tool for the assessment of biodiversity in vegetation (e.g., Asner and Martin, 2016) and wildlife (e.g., Kolman, 2021). The insight from this dissertation has the potential to improve biodiversity measures and maps derived from HSI data. Specifically, the tools and findings from this dissertation will ensure that biodiversity maps derived from multiple sensors are intercomparable, allowing for more accurate temporal studies of biodiversity change over time. By improving our ability to accurately match ground data to HSI data, the findings from this dissertation will also improve the quality of biodiversity maps, providing better information for decision-makers to make policies and take action.

7. Appendix

7.1. Spatial Response Resampling (SR²): Accounting for the Spatial Point Spread Function in Hyperspectral Image Simulation

Deep Inamdar ¹, Margaret Kalacska ^{1,*}, Patrick Osei Darko¹, George Leblanc ^{2,1} and J. Pablo Arroyo-Mora ²

This chapter has been submitted to *MethodsX*. Minor modifications have been made from the original submission with respect to formating style.

Abstract

With the increased availability of hyperspectral imaging (HSI) at various scales (0.03-30 m), the role of simulation is becoming increasingly important in data analysis and applications. There are few commercially available tools to spatially degrade imagery based on the spatial response of a coarser resolution sensor. Instead, HSI data are typically spatially degraded using nearest neighbour, pixel aggregate or cubic convolution approaches. Without accounting for the spatial response of the simulated sensor, these approaches yield unrealistically sharp images. This article describes the spatial response resampling (SR²) workflow, a novel approach to degrade HSI data based on the spatial response of a coarser resolution sensor. The workflow is open source and widely available for personal, academic or commercial use with no restrictions. The importance of the SR² workflow is shown with three practical applications (data cross-validation, flight planning and data fusion of separate VNIR and SWIR images).

¹ Applied Remote Sensing Laboratory, Department of Geography, McGill University, Montréal, QC H3A 0B9, Canada; deep.inamdar@mail.mcgill.ca (D.I.)

² Flight Research Laboratory, National Research Council of Canada, Ottawa, ON K1A 0R6, Canada; George.Leblanc@nrc-cnrc.gc.ca (G.L.); juanpablo.arroyomora@nrc-cnrc.gc.ca (J.P.A.-M.)

^{*} Correspondence: Margaret.kalacska@mcgill.ca; Tel.: +1-514-398-4347; Fax: +1-514-398-7437

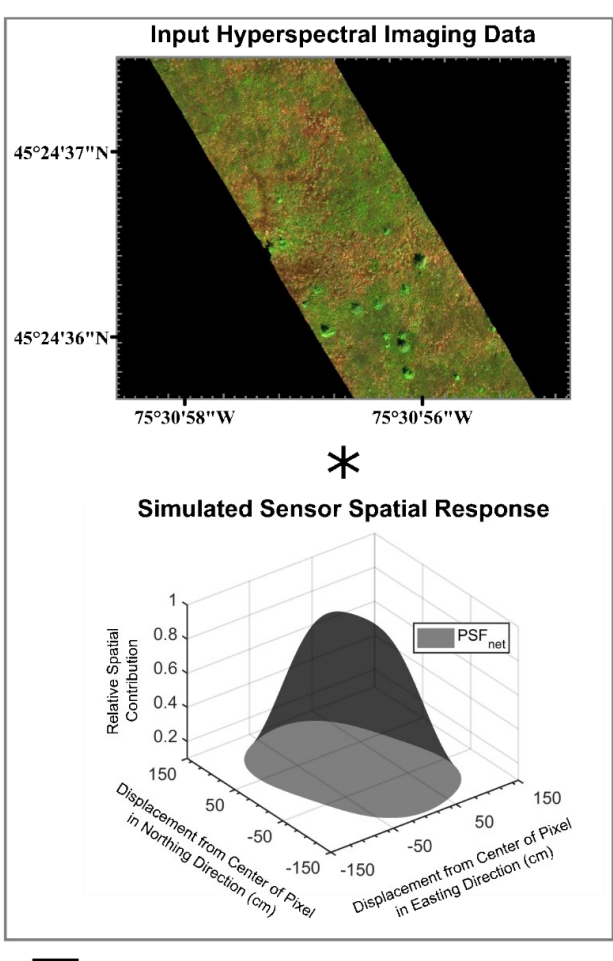
- The SR² workflow derives the point spread function of a specified HSI sensor based on nominal data acquisition parameters (e.g., integration time, altitude, speed), convolving it with a finer resolution HSI dataset for data simulation.
- \bullet To make the workflow approachable for end users, we provide a MATLAB function that implements the SR^2 methodology.

Keywords: Spatial Resampling, Simulation, Data Cross-Validation, Flight Planning, Data Fusion, Point Spread Function, Spatial Response, Pushbroom, MATLAB

Graphical Abstract

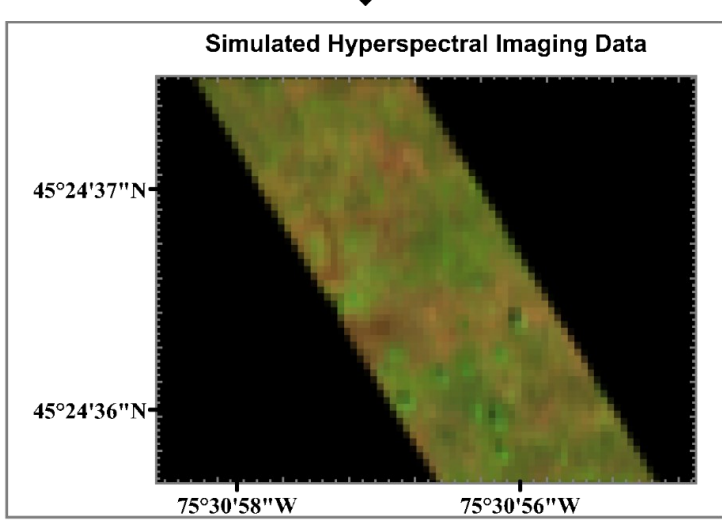
Simulated Data Acquisition Parameters			
and Sensor Characteristics			

and delisor dilaracteristics							
Input Parameters							
Total Number of Cross Track Pixels	1500						
Effective Number of Cross Track Pixels	1496						
Sensor Field of View (°)	39.9						
Nominal Flight Line Heading (° True North)	341						
Nominal Altitude (m ft)	1133 3717						
Nominal Speed (m/s kn)	41.6 80.9						
Integration Time (ms)	48						
Optical Point Spread Function FWHM (pixels)	1.1						
Cross Track Summing (pixel)	2						









7.1.1. Background

Over the past three decades, the abundance of spatial-spectral information captured by remotely sensed hyperspectral imaging (HSI) data has been actively exploited for various applications (Eismann, 2012). The utility of HSI data will only increase as remotely piloted aerial system (RPAS) (e.g., HySpex Mjolnir (Arroyo-Mora et al., 2021), ITRES μCASI-1920 (Arroyo-Mora et al., 2019), Specim Aisa KESTREL 10 (Kaňuk et al., 2018), etc.), airborne (e.g., AVIRS-NG (Hamlin et al., 2011), ITRES CASI (Babey and Anger, 1993), APEX (Vreys et al., 2016)) and spaceborne (e.g., DESIS (Alonso et al., 2019), SHALOM (Feingersh and Dor, 2015), Carbon Mapper (Shivers et al., 2021), EnMAP (Guanter et al., 2015)) imagers become more prevalent. With the increased availability of optical remotely sensed data at various spatial and spectral resolutions, the role of simulation is becoming increasingly important in data analysis and application. Specifically, data simulation is a valuable tool for sensor optimization and development (Guanter et al., 2009), flight planning (Zhao et al., 2019), data cross validation and calibration (Teillet et al., 2001) and algorithm development (Castaldi et al., 2016), amongst others. Many of the popular remote sensing data analytics software (e.g., ENVI (Harris Geospatial Solutions inc., Broomfield, CO, USA), CATALYST Professional (PCI Geomatics, Markham, Ontario, Canada) provide tools to simulate the spectral characteristics of a coarser spectral resolution sensor based on its spectral response. In the spatial domain, HSI data simulation is typically carried out via pixel aggregate, nearest neighbor, bilinear and cubic convolution spatial resampling techniques. Although these approaches can simulate imagery at any desired pixel size, it is important to recognize that pixel size does not accurately represent the spatial characteristics of the spectrum collected by coarser resolution imagers.

The PSF maps the relative response of a single pixel as a function of displacement from the center of the pixel (Inamdar et al., 2020). Hyperspectral PSFs generally follow a gaussian shape. Correspondingly, the spectrum from any given pixel is not equally representative of the materials within its conventionally square pixel boundaries. A substantial portion of the signal to each pixel (> 40 %) originates from materials outside the pixel boundaries defined by the spatial resolution (Inamdar et al., 2020). When spatially resampling imagery for data simulation, it is not appropriate to use a simple average or a nearest neighbour approach as the characteristics of the simulated sensor are ignored. Instead, spatial resampling should be conducted using a weighted

average based on the PSF of the simulated sensor. For instance, in the end-to-end simulation approach described by Blonski et al. (2000), the spatial response of the simulated sensor was accounted for by convolving a synthetic HSI scene with the spatial PSF. Inamdar et al. (2020) adopted a similar approach, convolving a theoretically derived PSF with a synthetic dataset to understand the importance of the spatial response. In this work, the overlap in the PSF of adjacent pixels was shown to lead to image blurring that reduced the natural spatial and spectral variance of the simulated scene. It is important to capture this loss of variance in simulation efforts. Otherwise, the simulated imagery will be unrealistically sharp, affecting downstream applications. For example, without accounting for the sensor PSF in flight planning efforts, simulated imagery might detect features of interest that cannot be observed in real imagery. This may lead end users to select inappropriate data acquisition parameters during aerial campaigns. Without accounting for sensor PSFs, it can also be difficult to compare, combine and apply imagery collected across various spatial scales. This is problematic given the increased availability of RPAS, airborne and spaceborne HSI data (Aasen et al., 2018; Transon et al., 2018). For instance, in many applications, it is desirable to have full-range HSI data. Due to technological and monetary restrictions, collecting full-range HSI data from a single sensor at a high spectral resolution is not generally feasible. Instead, the spectra from separate HSI datasets covering different portions of the electromagnetic spectrum need to be fused into one coherent signal. To ensure that the spectra from various data are optimally fused, it is critical to account for discrepancies in spatial scale between the utilized sensors. In this process, one image must be spatially degraded to match the spatial characteristics of the other image. Without accounting for discrepancies in spatial properties, any derived full-range spectrum would be unusable in conventional spectroscopy analyses such as material identification and characterization.

Expanding on the methodology implemented by Inamdar et al. (2020), the objective of this study was to develop a spatial resampling workflow that accounts for the spatial response of a specified sensor. The developed spatial response resampling (SR²) workflow degrades spatial resolution HSI data to the spatial characteristics of a coarser resolution sensor. In this workflow, the PSF of the simulated sensor is first derived with nominal data acquisition parameters (altitude, speed, integration time, etc.). Afterward, the derived PSF is convolved with the input HSI data. The output is then spatially degraded to the resolution of the simulated sensor with a nearest neighbour resampling technique. A MATLAB (Mathworks, Natick, MA, USA)

implementation of the described workflow is provided in this manuscript. This MATLAB script can be used as-is or adapted as needed. In three practical example applications of the developed SR² workflow, we show the importance of accounting for the sensor PSF when spatially resampling fine resolution HSI data for simulation. In the first example, the workflow is applied for HSI data cross-validation. This example shows the potential of using RPAS-HSI to bridge the gap between *in situ* spectroscopy data and coarser resolution HSI data. In the second example, the workflow is applied to aid in data acquisition planning. In this example, the simulation workflow establishes suitable scales and, by extension, data acquisition parameters for identifying a feature of interest. The final example application shows how the workflow can be implemented for data fusion between sensors that capture spectral information in different portions of the electromagnetic spectrum. This example generates a single full-range image from a VNIR and SWIR HSI dataset.

7.1.2. Method Workflow

Following the methodology briefly outlined by Inamdar et al. (2020), the SR² simulation workflow derives the net PSF (PSF_{net}) of a specified sensor, convolving it with a finer resolution HSI dataset (**Figure 7.1**). Before describing the SR² workflow, it is necessary to define the terminology surrounding the spatial properties of HSI systems. In this work, the pixel resolution is defined by the full width at half maximum of the sensor PSF. The nominal pixel resolution is defined by the ground-projected instantaneous field of view (IFOV) (units of meters), which is the ground distance covered by a single pixel in the cross track direction. Pixel size refers to the spatial dimensions of each square pixel in the geometrically corrected raster end product. With these definitions in mind, the workflow can be broken into three steps:

- 1. Derive PSF_{net} in two dimensions as a function of pixel displacement in the easting and northing directions
- 2. Convolve PSF_{net} from step 1 with input HSI data
- 3. Spatially resample input HSI data to the pixel size of the simulated sensor with a nearest neighbour resampling technique.

The PSF_{net} derivation in step 1 follows the calculations from Inamdar et al. (2020), with a slight modification to account for cross track pixel summing. In this process, the optical PSF (PSF_{opt}), motion PSF (PSF_{mot}) and detector PSF (PSF_{det}) are first derived. After, the cross track

PSF_{net} is generated by convolving the PSF_{opt} and PSF_{det} while the along track PSF_{net} is obtained by convolving the PSF_{opt}, PSF_{mot} and PSF_{det}. In many data processing streams, adjacent cross track pixels are summed to boost signal levels and equalize spatial resolution between the cross track and along track directions (Epperson and Denton, 1989). In these scenarios, the cross track PSF_{net} must be modified to account for the degree to which data summing is applied. The PSF_{net} in the cross track direction at summing level $s \ge 2 \mid s \in \mathbb{Z}$ can be defined by the following expression:

$$PSF_{net,s}(x) = \begin{cases} \sum_{k=1}^{k=\frac{S}{2}} PSF_{net}\left(x + (k - \frac{1}{2}) * rx\right) + PSF_{net}\left(x - (k - \frac{1}{2}) * rx\right), & if \ s \ge 2 | s \in 2\mathbb{Z} \\ \\ PSF_{net}(x) + \sum_{k=1}^{k=\frac{S-1}{2}} PSF_{net}(x + k * rx) + PSF_{net}(x - k * rx), & otherwise \end{cases}$$
(1)

where rx is equal to the nominal pixel resolution in the cross track direction (width of the PSF_{det}), x is the cross track displacement from the pixel center and $PSF_{net}(x)$ is the unsummed PSF_{net} in the cross track direction. The total PSF_{net} in two dimensions is then derived by vector multiplication of the PSF_{net} in the cross track (after data summing) and along track directions. To complete step 1, the total PSF_{net} is reparametrized as a function of pixel displacement in the easting and northing directions via matrix rotation by the nominal flight line heading (° True North). To generate the convolution kernel for step 2, the total PSF_{net} is spatially degraded to the same pixel size as the input HSI data. This is accomplished by spatially integrating the PSF_{net} in intervals equal to the pixel size of the input HSI data. The output matrix (referred to as the convolution kernel) is normalized to sum to unity. The kernel is then convolved with the input HSI data, blurring it based on the spatial characteristics of the simulated sensor. In the blurred HSI data, each pixel represents the average spectra that would contribute to a single pixel of the simulated sensor. It is important to note that the pixel size of the input HSI data does not change after convolution. To complete the simulation workflow, the blurred HSI data are spatially subset to the same pixel size as the simulated sensor using a nearest neighbour spatial resampling technique. A flow chart of the described workflow is shown in Figure 7.1.

Although step 3 can be conducted in most commercially available geospatial software (e.g., ENVI's Resize function, ArcMap's (Esri, Redlands, CA, USA) Resample function), steps 1-2 may be challenging to implement for end users that are unfamiliar with PSFs and convolution.

This work presents a MATLAB function (HSI_BLUR.m) that carries out steps 1-2 of the data simulation workflow to make the workflow more approachable for end users of all expertise levels.

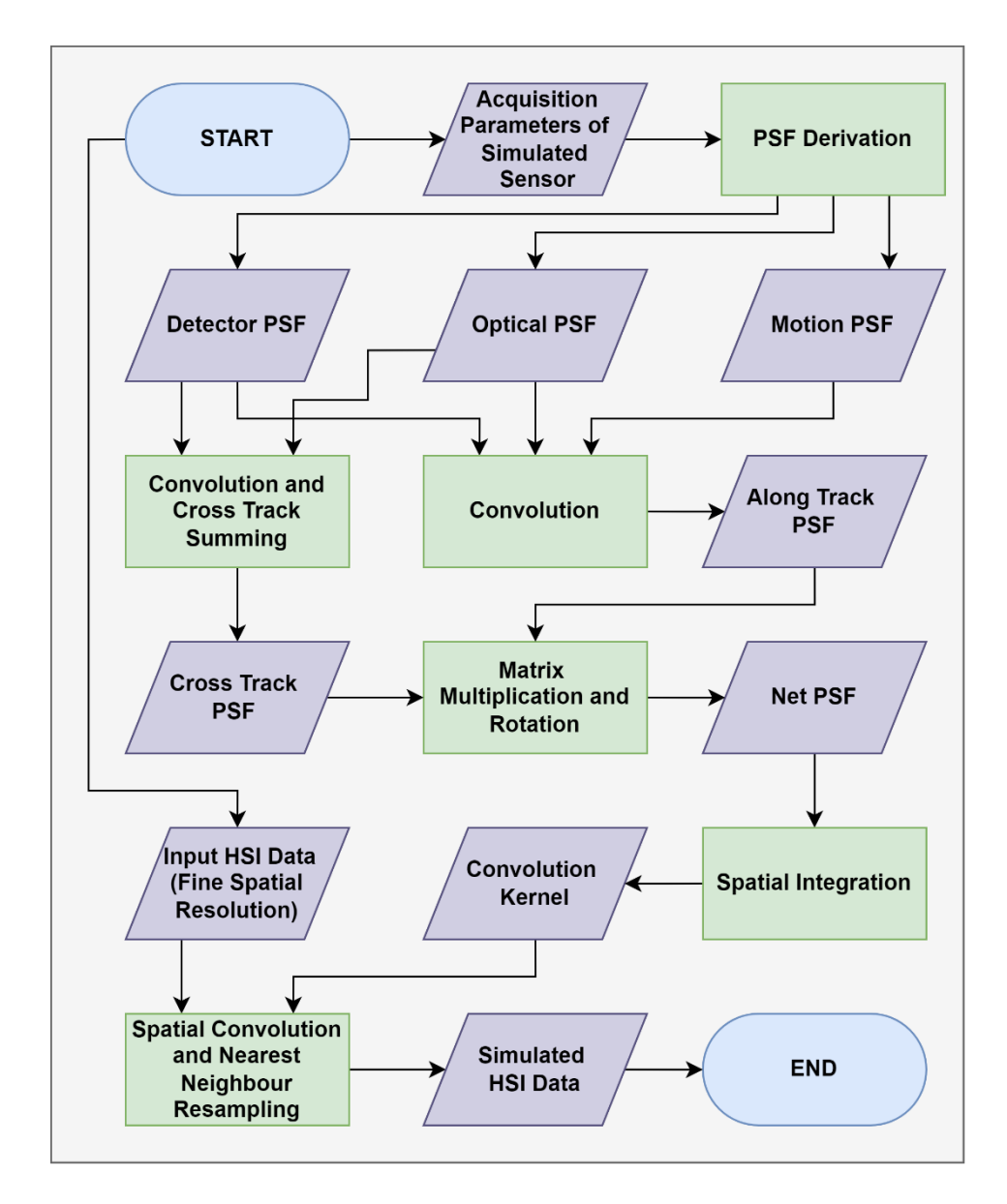


Figure 7.1. Flowchart of the Spatial Response Resampling (SR^2) workflow. The workflow degrades fine spatial resolution hyperspectral imaging (HSI) data to the spatial characteristics of a coarser resolution sensor.

7.1.3. MATLAB Function

The developed MATLAB function is based on the DHPC_DSM_BLUR.m function developed in Inamdar et al. (2021b). The purpose of the DHPC_DSM_BLUR.m function was to

convolve a digital surface model with the PSF of a coarser resolution HSI dataset for data fusion. Although not necessarily for data fusion, on a fundamental level, the SR² workflow aims to accomplish the same task. However, instead of spatially degrading a DSM (1 band image), the workflow degrades an HSI dataset. Additional modifications have been made to the original DHPC_DSM_BLUR.m function to account for spatial summing in the cross track direction. As such, the PSF calculations are more robust and can simulate a wider array of HSI sensors.

The HSI_BLUR MATLAB function carries out four tasks: 1) derive hyperspectral PSF of the simulated sensor; 2) derive convolution kernel from PSF based on the characteristics of the input HSI data; 3) convolve input HSI dataset by convolution kernel, 4) output blurred imagery as ENVI standard data format. The HSI_BLUR.m function description defines the input and output parameters of the workflow.

```
%%% Input Parameters
  % flight line heading... Heading of simulated sensor (True North Heading in
degrees, e.g., north=0, east=90, south=180, west=270).
  % FOV_deg...
% pix_tot...
% alt...
                            Field of view of simulated sensor (degrees).
                            Number of cross track pixels in simulated sensor.
                            Nominal altitude (m above ground level) of simulated
sensor during data acquisition.
  % speed... Nominal speed (m/s) of simulated sensor during data
acquisition.
                            Integration time (s) of simulated sensor during data
  % it...
acquisition.
  % cross track sum Summing factor of simulated sensor in cross track
direction
  % FWHM opt... Full width at half maximum (pixels) of simulated
sensor's optical point spread function (PSF). If unknown please enter 1.
  % IMG_loc...
                            String with fold path of the input hyperspectral
imaging dataset.
  % IMG name... Name of the input hyperspectral imaging dataset
(must be *.dat). Please DO NOT Include the ".dat" Extension.
  %%%Output Parameters
                    Hyperspectral imaging dataset blurred through
     IMG conv...
convolution with simulated sensor PSF
  % PSF tot 3d... PSF of simulated sensor. The PSF is a function of
spatial displacement from pixel Center (m) in the Easting and Northing directions
  % x c dist...
                    Displacement values associated with columns of
PSF tot 3d in Easting direction (m)
     y c dist...
                            Displacement values associated with rows of
PSF tot 3d in Northing direction (m)
```

The PSF derivation (task 1) follows the calculations presented in Inamdar et al. (2020) using the implementation from Inamdar et al. (2021b). In this process, the nominal pixel size of the simulated sensor (without considering pixel summing) is first calculated based on the field of view, number of cross track pixels, integration time and speed.

```
%%%Derive nominal pixel sizes of simulated sensor
pix_size_x=alt*tand(FOV_deg/2)/(pix_tot/2); %nominal cross track resolution (m)
pix_size_y=max(speed*it,pix_size_x); %nominal along track resolution (m)
dt=round(min([pix_size_x pix_size_y])/150,1,'significant'); % spatial resolution
to which PSF is calculated
```

Next, the rectangular pulse detector PSF and gaussian optical PSF are calculated and convolved with one another to derive the net PSF in the cross track direction. It is important to note that, at this point, the net cross track PSF does not consider the dynamics of spatial pixel summing.

```
%%% Derive Cross Track PSF of simulated sensor
%%%% Derive Gaussian Optical PSF of simulated sensor
muPDF=0; % Mean of Gaussian Distribution for Optical PSF
FWHM_x=FWHM_opt*pix_size_x; %FWHM of Gaussian Distribution for Optical PSF
sigmaPDF=FWHM_x/(2*sqrt(2*log(2))); %Standard Deviation of Gaussian for Optical
PSF
    op_pdx=makedist('Normal',muPDF,sigmaPDF); %Generate PSF
    num_vals=round(pix_size_x*2/dt);
    x=-num_vals*dt:dt:num_vals*dt; % Displacement from pixel center (m) at which the
Optical PSF will be calculated
    op_x_f=pdf(op_pdx,x); %Calculate value of Optical PSF

    %%% Derive Rectangular Pulse Detector PSF of simulated sensor
    step_f=x>=-pix_size_x/2& x<=pix_size_x/2;

    %%% Derive Net Cross Track PSF of simulated sensor normalized by the maximum
    x_c_spr=conv(op_x_f,step_f)/max(conv(op_x_f,step_f));</pre>
```

Afterward, the net cross track PSF is convolved with a derived rectangular pulse motion PSF. The result of this convolution is the net PSF in the along track direction.

```
%%% Derive Along Track PSF of simulated sensor
num_vals=round(it*speed/dt);
y=num_vals*dt:-dt:-num_vals*dt; % Displacement from pixel center (m) at which
the along track PSF will be calculated

%%%% Derive motion PSF of simulated sensor
step_f_2=y>=-it*speed/2& y<=it*speed/2;

%%%% Derive Net Along Track PSF of simulated sensor normalized by the maximum
y_c_spr=conv(x_c_spr,step_f_2)/max(conv(x_c_spr,step_f_2));</pre>
```

Next, the cross track net PSF is spatially summed as per the setup of the simulated sensor.

```
%%%% Handle cross track summing
   if cross track sum>1
   dist inc pix=cross track sum-1;
   addon2=ceil(pix size x*dist inc pix/2/dt);
   x \min = \min(abs(x c dist));
   x len orig=length(x c spr);
   x c dist=x min-addon2*dt-(x len orig-1)/2*dt:dt:x min+addon2*dt+(x len orig-
1)/2*dt;
   x spr new=zeros(1,length(x c dist));
   if rem(cross track sum, 2) == 0
       center pt=(-pix size x/2-(cross track sum/2-
1) *pix size x):pix size x: (pix size x/2+(cross track sum/2-1) *pix size x);
       center pt=-pix size x*(cross track sum-
1)/2:pix size x:pix size x*(cross track sum-1)/2;
   index center pt = knnsearch(x c dist',center pt');
   for i=1:cross track sum
       start indx=index center pt(i)-(x len orig-1)/2;
       end indx=index_center_pt(i)+(x_len_orig-1)/2;
       x spr new(start indx:end indx) = x spr new(start indx:end indx) + x c spr;
   x_spr_new=x_spr_new/max(x_spr_new);
   x c spr=x spr new;
   end
```

The net PSF in 2-dimensions is derived through vector multiplication of the cross track and along track net PSFs. The rows and columns of the resultant matrix correspond with the along track and cross track displacement (in meters) from the center of the pixel. Since the rows and columns of the input HSI data correspond to the northing and easting directions, respectively, the net PSF must be rotated by the flight line heading of the simulated sensor before convolution. After rotation, task 1 is completed.

```
%%% Calculate Net PSF of simulated sensor in 2-dimensions (along track x cross
track)
    PSF_tot_3d_no_rot=y_c_spr'*x_c_spr;

    %%% Rotate PSF by flight line heading so that PSF of the simulated sensor is
north oriented
    PSF_tot_3d=imrotate(PSF_tot_3d_no_rot,-flight_line_heading,'bilinear','crop');

To complete task 2, the input HSI data must first be imported, and the pixel
size must be extracted.

%%% Read input HSI dataset and extract pixel size
    Filename=[IMG_loc IMG_name '.dat'];
    Filename_2=[IMG_loc IMG_name '.hdr'];
    info = enviinfo(Filename_2);
    data=hypercube(Filename,Filename_2);
    pix_size_IMG= data.Metadata.MapInfo.PixelSize(1);
```

To generate the convolution kernel and complete task 2, the rotated net PSF is spatially integrated in intervals equal to the input HSI dataset pixel size and normalized to sum to unity.

```
%%% Generate Convolution Kernel by integrating PSF of simulated sensor
size_kernel=ceil(max(x_c_dist)/pix_size_IMG)*2+1; %calculate size of convolution
kernel

conv_ker=ones(size_kernel,size_kernel);
x_vec=-pix_size_IMG*size_kernel/2:pix_size_IMG:pix_size_IMG*(size_kernel/2-1);
y_vec=fliplr(x_vec);

for i= 1:size_kernel
x_indx=(x_vec(i)<x_c_dist & x_c_dist<(x_vec(i)+pix_size_IMG));
    for j=1:size_kernel
        y_indx=(y_vec(j)+pix_size_IMG>y_c_dist & y_c_dist>y_vec(j));
        conv_ker(j,i)=sum(sum(PSF_tot_3d(y_indx,x_indx)))/sum(sum(PSF_tot_3d));
end
end

%%%% Normalize convolution kernel to sum to 1
conv_ker=conv_ker/sum(sum(conv_ker));
```

Afterward, the input HSI dataset is convolved with the derived kernel, blurring the imagery based on the PSF of the simulated sensor (completing task 3).

```
%% Convolve input HSI dataset by Convolution Kernel
IMG_conv=data.DataCube;

for i=1:info.Bands
IMG_conv(:,:,i)=conv2(data.DataCube(:,:,i),conv_ker,'same');
i/info.Bands*100
end
```

Task 4 is completed by saving the blurred HSI dataset to a new ENVI standard file (Harris Geospatial Solutions, 2022) in the same location as the input HSI dataset. This new file is named after the input HSI dataset, appended with "_conv".

```
%% Output input HSI dataset to ENVI Standard File
Filename=[IMG_loc IMG_name '_conv'];
newhcube = assignData(data, ':',':','IMG_conv);
enviwrite(newhcube,Filename);
```

Below, we provide an example MATLAB code that generates a blurred HSI dataset by calling HSI BLUR.m.

```
% Define Input Parameters
   FOV deg=39.86;
   pix tot=1500;
   alt=1130;
   speed=41.15;
   it=48/1000;
   FWHM opt=1.1
   IMG_loc='H:\HSI_Blur\'
   IMG name='Input HSI' %Name of DSM (must be *.dat). Please do not include the
".dat" extention.
   flight line heading=341.4650; %heading of the hyperspectral imager
   cross track sum=2;
   % Run Function
   [IMG_conv, PSF_tot_3d, x_c_dist, y_c_dist] =
HSI BLUR(flight line heading, FOV deg, pix tot, alt, speed, it, cross track sum, FWHM opt,
IMG loc, IMG name);
```

It is important to note that the provided MATLAB function does not apply the final nearest neighbour spatial resampling stage of the workflow. As previously mentioned, this can be done in most commercially available image analysis software (e.g., the Resize function from ENVI or the Resample function in ArcMap).

7.1.4. Example Applications of the Spatial Response Resampling Workflow

In this work, we give three practical example applications of the SR² workflow to show the importance of accounting for the sensor PSF when spatially resampling HSI data to simulate the spatial characteristics of a coarser resolution sensor. These applications use HSI data collected from two field sites: The Mer Bleue Peatland (MBP) in Ontario, Canada and the Puerto Jiménez Airport (PJA) in Puntarenas, Costa Rica. The MBP is a ~8500-year-old ombrotrophic bog characterized by a hummock-hollow microtopography (Lafleur et al., 2001). A hollow microform is at or below the water table in the peatland and is primarily composed of exposed

mosses (e.g., *Sphagnum* spp.), while a hummock microform is an elevated mound in the peatland surface where vascular plants densely cover the underlying mosses (Eppinga et al., 2008; Lafleur et al., 2005). In the MBP, hummocks and hollows differ in absolute elevation by as much as 0.30 m and are separated by an approximate horizontal distance of 1–2 m (Belyea and Baird, 2006; Malhotra et al., 2016). In peatlands, hummock-hollow microtopography provides diversity in ecohydrological structure and biogeochemical function that is integral to the negative feedbacks that maintain the long-term stability of peatland carbon (Belyea and Malmer, 2004; Eppinga et al., 2008; Malhotra et al., 2016; Moore et al., 2019). As such, characterization of hummock-hollow microtopography is critical to understanding and modeling complex hydrological and biogeochemical processes, in addition to validating satellite-derived products such as water table depth and net ecosystem exchange (Arroyo-Mora et al., 2018; Kalacska et al., 2018; Kalacska et al., 2021). The PJA is located on the Osa peninsula and contains many urban features (e.g., roads and buildings). The PJA was a validation site for the Mission Airborne Carbon 13 (MAC-13) project, an initiative to derive aboveground biomass/carbon estimates in five highly diverse ecosystems in Costa Rica (Kalacska et al., 2016).

HSI data were collected using three pushbroom hyperspectral imagers: the micro-Compact Airborne Spectrographic Imager (μCASI-1920, ITRES, Calgary, AB, Canada), the Compact Airborne Spectrographic Imager (CASI-1500, ITRES, Calgary, AB, Canada) and the Shortwave Airborne Spectrographic Imager (SASI-640, ITRES, Calgary, AB, Canada). The μCASI-1920 and the CASI-1500 collect spectral information in the VNIR from 450 to 900 nm, while the SASI-640 collects spectral information in the SWIR from 900 to 1900 nm. Because the μCASI-1920 was mounted on a DJI Matrice 600 Pro RPAS, it is capable of collecting finer spatial resolution data (< 5 cm) (Arroyo-Mora et al., 2019) than the CASI-1500 and SASI-640 sensors, which are mounted in a Twin Otter fixed-wing manned aircraft. This study specifically analyzes μCASI-1920 and CASI-1500 data collected from the MBP in addition to CASI-1500 and SASI-640 data from the PJA (see Figure 7.2). The data acquisition parameters and sensor properties associated with each dataset are given in Table 7.1. Before application, all HSI data were radiometrically corrected, atmospherically compensated and geometrically corrected using software developed by the sensor manufacturer and ATCOR4 (ReSe, Wil, Switzerland), as described by Soffer et al. (2019) and Osei Darko et al. (2021).

The first example application shows the utility of the SR^2 workflow for data cross-validation. Specifically, the CASI-1500 imagery from the MBP was cross-validated using the μ CASI-1920 data. In the second example application, the SR^2 workflow was applied for flight planning. In this example, the simulation workflow used the μ CASI-1920 data to establish appropriate CASI-1500 data acquisition parameters for identifying hummocks and hollows within the MBP. The final example application shows how the SR^2 workflow can be implemented for data fusion between sensors that capture spectral information in different portions of the electromagnetic spectrum. In this application, the CASI-1500 data from the PJA was fused with the SASI-640 data to generate a spatially coherent full-range spectrum.

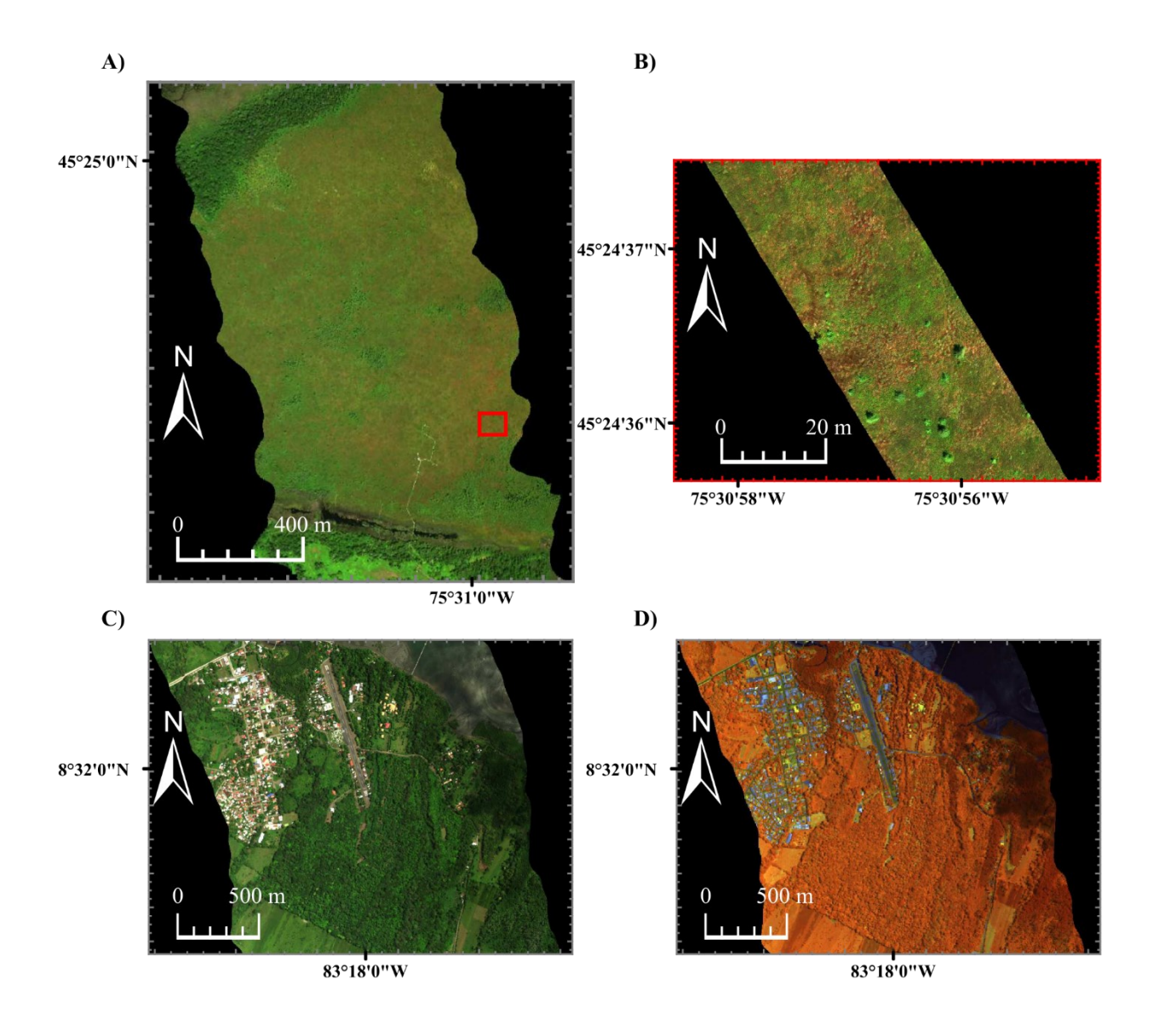


Figure 7.2. The hyperspectral imaging data used to show the utility of the developed Spatial Response Resampling (SR²) workflow. CASI-1500 and μ CASI-1920 data were collected over the Mer Bleue Peatland (MBP), while CASI-1500 and SASI-640 data were collected over the Puerto Jiménez Airport (PJA). A) Hyperspectral imaging data collected over the MBP with the CASI-1500 (R=640.8 nm, G=549.9 nm, B=459.0 nm, linearly scaled from 0 to 12 %). The red box shows the location where the μ CASI-1920 data was collected. B) Hyperspectral imaging data collected over the MBP with the μ CASI-1920 (R=639.6 nm, G=550.3 nm, B=459.0 nm, linearly scaled from 0 to 12 %). C) Hyperspectral imaging data collected over the PJA with the CASI-1500 (R=641.2 nm, G=550.3 nm, B=458.3 nm, linearly scaled from 0 to 20 %). D) Hyperspectral imaging data collected over the PJA with the SASI-640 (R=1240.1 nm and linearly scaled from 0 to 60 %, G=1540.7 nm and linearly scaled from 0 to 50 %, B=1846.0 nm and linearly scaled from 0 to 30 %).

Table 7.1. Parameters for the hyperspectral imaging data acquired over the Mer Bleue Peatland (MBP) and Puerto Jiménez Airport (PJA) with the SASI-644, CASI-1500 and μ CASI-1920.

Parameter	MBP MBP		PJA	PJA
	(μCASI-1920)	(CASI-1500)	(CASI-1500)	(SASI-640)
Date (dd-mm-yyyy)	15-07-2019	15-07-2019	29-04-2013	29-04-2013
Image start time (hh.mm.ss GMT)	15.44.49	15.44.38	15.07.55	15.07.55
Total Number of Cross Track Pixels	1920	1500	1500	644
Effective Number of Cross Track Pixels	1833	1496	1493	640
Sensor Field of View (°)	34.21	39.9	39.9	39.7
Nominal Flight Line Heading (° True North)	156	341	343	343
Nominal Altitude (m ft)	45 148	1133 3717	2586 8484	2586 8484
Nominal Speed (m/s kn)	2.7 5.2	41.6 80.9	61.7 120.0	61.7 120.0
Integration Time (ms)	9	48	32	4.1
Full width at half maximum of Optical Point Spread Function (pixels)	1.1	1.1	1.1	1.1
Cross Track Summing (pixel)	1	2	1	1
Nominal Cross Track Pixel Resolution	0.03	1.1	1.25	2.9
Nominal Along Track Pixel Resolution	0.03	1.97	1.99	2.9
Pixel Size of Georeferenced Raster (m)	0.03	1.0	1.25	3.5

7.1.4.1. Data Cross-Validation Application

In the remote sensing literature, cross-validation is a process whereby a measurement with known uncertainty is used to assess the accuracy of an independent measurement. Typically, *in situ* data collected at the ground level is used to cross-validate measurements collected at the airborne level, which can then be used to cross-validate spaceborne measurements. Cross-

validation of *in situ* and imaging spectroscopy data at the airborne and spaceborne levels requires a detailed understanding of the measurement process, the involved spatial-spectral scales and the processing applied to the data (Hueni et al., 2017). Depending on the sampling strategy and the characteristics of the target (size, spectral variability), it can be difficult to acquire *in situ* data that is spatially coherent with airborne imaging spectroscopy data. Additional problems arise in cross-validation efforts as it is difficult to collect *in situ* data that samples materials across the spatial extent covered by airborne sensors. RPAS-HSI data presents a potential solution to bridge the gap between airborne HSI data and *in situ* data via cross-validation. This study analyzes the utility of the SR² workflow in cross-validating higher altitude airborne HSI data with finer resolution RPAS-HSI data.

The μ CASI-1920 dataset was input to the SR² workflow to simulate the MBP CASI-1500 data with the flight parameters in **Table 7.1**. The PSF associated with the MBP CASI-1500 data can be seen in **Figure 7.3**. The simulated image was compared to a conventional data simulation approach where the μ CASI-1920 imagery was spatially degraded using a pixel aggregate averaging approach. In this comparison, the mean and standard deviation of each spectral band were calculated for the two degraded μ CASI-1920 datasets and the original CASI-1500 dataset. For comparability, the CASI-1500 data were spatially subset to the area covered by the μ CASI-1920 imagery before calculating the mean and standard deviation of each spectral band.

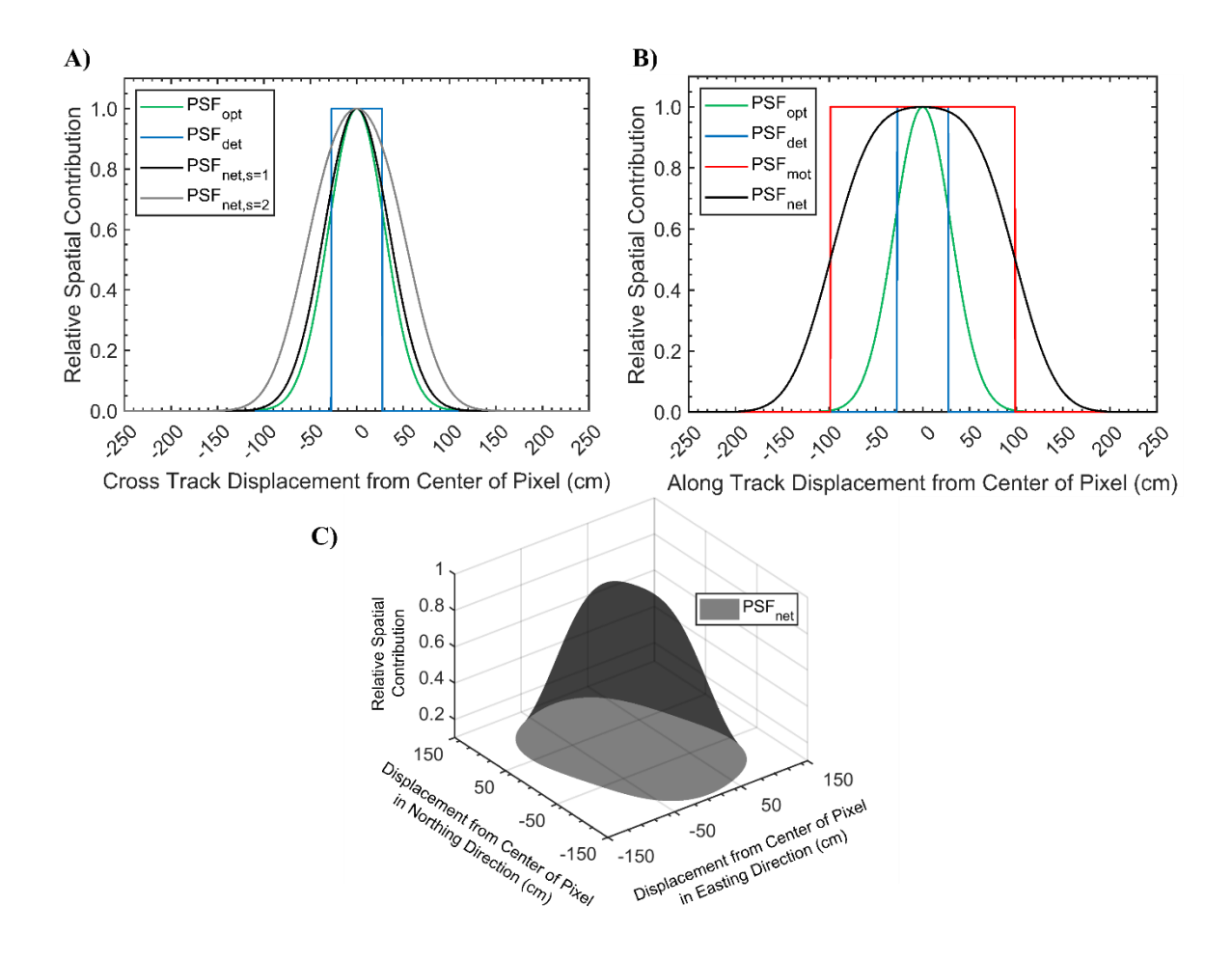


Figure 7.3. The point spread function (PSF) for the CASI-1500 data collected over the Mer Bleue Peatland. A) The optical PSF (PSF_{opt}), detector PSF (PSF_{det}) and net PSF (PSF_{net}) in the cross track direction (unsummed and summed PSFs are designated by the s=1 and s=2 tags, respectively). B) The PSF_{opt}, PSF_{det}, motion PSF (PSF_{mot}) and PSF_{net} in the along track direction. C) The PSF_{net} as a function of displacement from the center of the pixel in the easting and northing directions. The grid in the x-y plane corresponds to the pixel size in the final georeferenced end product. When studying the PSF_{net} in panel C, less than 37% of the signal originates within the square spatial boundaries defined by pixel size in the final data end product.

Figure 7.4A-D shows the original CASI-1500 and μCASI-1920 imagery, in addition to the two simulated data products. The mean reflectance spectra (**Figure 7.4E**) of the two simulated data products were consistent with the mean spectrum of the CASI-1500 imagery. The standard deviation (**Figure 7.4F**) in the reflectance spectra of the conventional data simulation end product was 45.86 % larger on average than the standard deviation measured from the original CASI-1500 data (ranging from 23.37 % to 76.91 %) (see **Figure 7.4H**). The standard deviation in the reflectance spectra of the SR² data simulation end product was only 22.65 % larger on

average than the standard deviation measured from the CASI-1500 data (ranging from 6.29 % to 42.62 %) (see Figure 7.4H). Inamdar et al. (2020) show that the overlap in the sensor PSF of adjacent pixels results in spatial autocorrelation that changes observed spectral variance. If the spatial properties of the degraded µCASI-1920 imagery are perfectly consistent with that of the CASI-1500, then the standard deviation in the reflectance spectrum should be identical. It is important to recognize that the standard deviation values calculated for the original and simulated CASI-1500 data will never be identical due to factors such as jitter, increased noise levels, viewing geometries and other sensor-related phenomena, in addition to intrinsic properties of the observed matter such as material bidirectional reflectance distribution functions. However, the observed reduction in the standard deviation implies that the simulated dataset output from the SR² workflow was more spatially consistent with the CASI-1500 data than the conventional data product. If the conventional data simulation product was used in data crossvalidation efforts, the additional variation in the reflectance spectra could contribute to the overall errors. The additional errors would unnecessarily increase the overall uncertainty in the CASI-1500 data during cross-validation efforts. Overall, the SR² workflow ensured that all data used in cross-validation efforts were spatially consistent for data validation efforts.

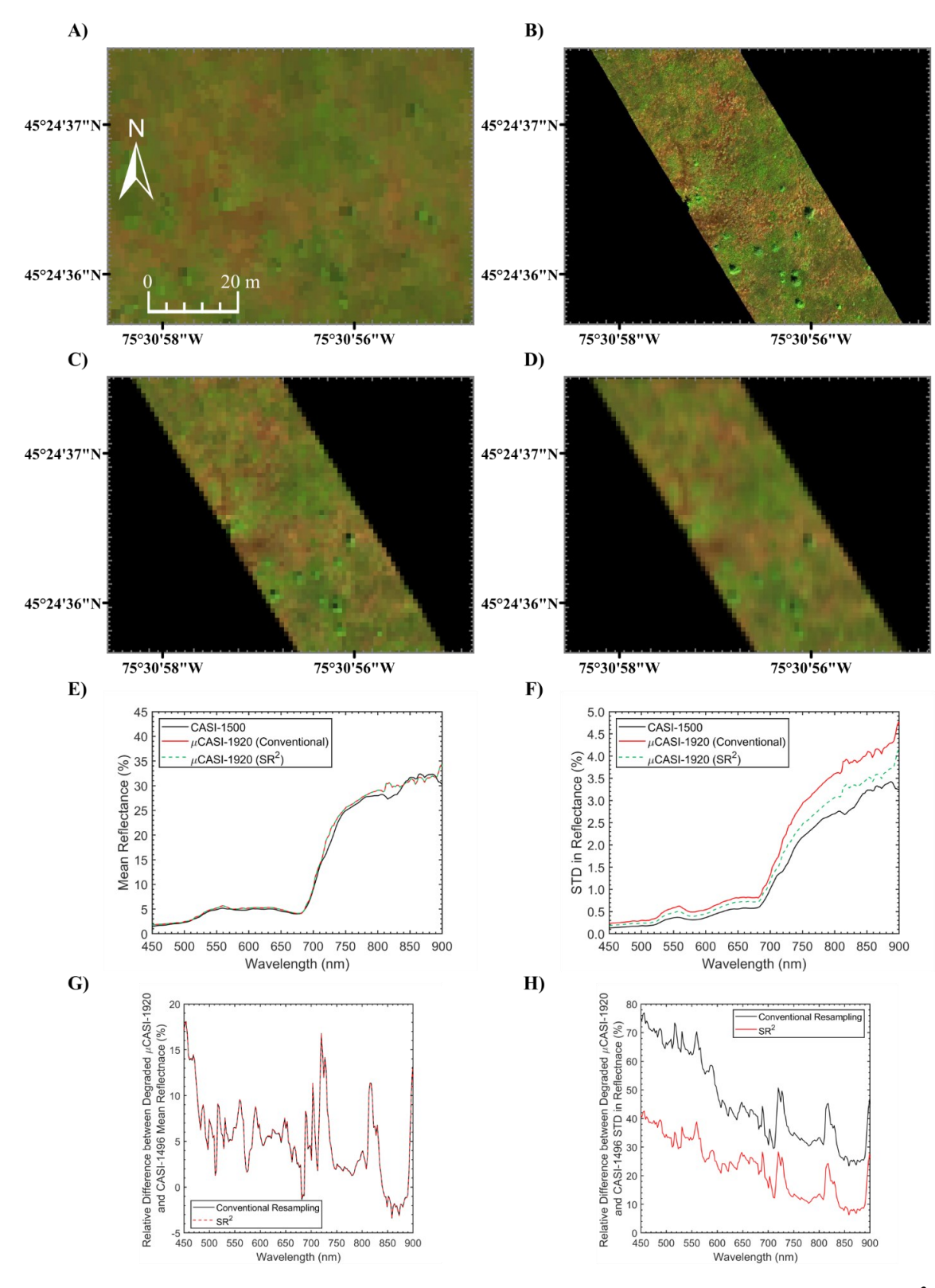


Figure 7.4. Example data cross-validation application of the Spatial Response Resampling (SR^2) workflow. A) Spatial subset of the Mer Bleue Peatland (MBP) CASI-1500 hyperspectral imaging data (R=640.8 nm, G=549.9 nm, B=459.0 nm, linearly scaled from 0 to 12 %). B) Original

 $\mu CASI-1920$ hyperspectral imaging data collected over the MBP (R=639.6 nm, G=550.3 nm, B=459.0 nm, linearly scaled from 0 to 12 %). C) Spatially degraded μ CASI-1920 hyperspectral imaging data (R=639.6 nm, G=550.3 nm, B=459.0 nm, linearly scaled from 0 to 12 %) generated using conventional resampling methodologies (pixel aggregate method). D) Spatially degraded μ CASI-1920 hyperspectral imaging data (R=639.6 nm, G=550.3 nm, B=459.0 nm, linearly scaled from 0 to 12 %) generated using the SR² workflow. E) The mean of each spectral band from the two spatially degraded µCASI-1920 images and the original CASI-1500 imagery, spatially subset to cover the same extent. F) The standard deviation in each spectral band from the two spatially degraded µCASI-1920 images and the CASI-1500 imagery, spatially subset to cover the same extent. G) Relative difference in the calculated mean reflectance spectrum between the original CASI-1500 imagery and the two spatially degraded µCASI-1920 images. H) Relative difference between the calculated standard deviation in reflectance of the original CASI-1500 imagery and the two spatially degraded µCASI-1920 images. The simulated data product generated using the SR² workflow was the most spatially consistent with the CASI-1500 imagery. The mean in the reflectance was consistent between the two simulated data products and the CASI-1500 data. The standard deviation calculated for the simulated imagery derived from the SR² workflow was the closest to that of the CASI-1500 imagery, indicating that the datasets are characterized by similar levels of sensor blurring.

7.1.4.2. Flight Planning Application

HSI acquisition is monetarily expensive, requiring considerable effort from experts during flight planning and data acquisition (Arroyo-Mora et al., 2019). As a result, it is practically infeasible to test multiple data acquisition parameters to determine how to optimally collect data for a specific scientific question. The SR² workflow presents a solution to this problem, showing an example where fine resolution HSI data can be used to identify optimal data acquisition parameters to collect coarser resolution HSI data capable of identifying a user-defined target with minimal mixing. In the flight planning example application, the SR² workflow used the μCASI-1920 data to establish appropriate CASI-1500 data acquisition parameters for identifying hummocks and hollows within the MBP. As previously mentioned, the hummock-hollow microtopography is key to understanding and modeling complex hydrological and biogeochemical processes, in addition to validating satellite-derived products such as water table depth and net ecosystem exchange (Arroyo-Mora et al., 2018; Kalacska et al., 2018; Kalacska et al., 2021).

In the flight planning data application, the μ CASI-1920 imagery was spatially degraded using the SR² workflow based on the characteristics of the CASI-1500 sensor with various data acquisition parameters (see **Table 7.2**). Each set of data acquisition parameters was selected to

simulate data that the CASI-1500 could potentially acquire at various nominal spatial resolutions (0.25 m, 0.5 m, 0.75 m, 1.00 m, 1.25 m, 1.50 m). **Figure 7.5** shows the spatially degraded μCASI-1920 datasets that simulated various flight configurations of the CASI-1500. At 25 cm, the hummock-hollow microtopography could be clearly observed. As progressively coarser resolution CASI-1500 images were simulated, the hummock-hollow microtopography was more difficult to identify qualitatively.

The detectability of hummocks and hollows was analyzed by extracting spectra from a small (~1 m) example hummock and hollow at the MBP (see Figure 7.6A). Hollows are mainly composed of exposed *Sphagnum* mosses. As such, the spectral properties of hollows differ from hummocks (Bubier et al., 1997; Vogelmann and Moss, 1993), which are composed of *Sphagnum* mosses densely covered by vascular plants. The predominant difference between *Sphagnum* moss and vascular plant reflectance is in the location and magnitude of the green peak, the red edge inflection point and the magnitude of reflectance in the near infrared (Bubier et al., 1997; Harris et al., 2005; Vogelmann and Moss, 1993). This is due to differences in pigmentation and cell and canopy structure (Bubier et al., 1997; Harris et al., 2005; Vogelmann and Moss, 1993).

Figure 7.6B-C shows the spectra extracted from the example hollow and hummock within each simulated scene. The difference between the hollow and hummock spectra at each scale was normalized by the standard deviation in each band of the utilized HSI data. The absolute value of the normalized difference is representative of separability between the example hummock and hollow as a function of wavelength in units of standard deviations (STD) (see Figure 7.6E).

At fine spatial resolutions, mixing in the hummock and hollow spectra was less prominent. For instance, the hollow spectrum at scale 1 (see **Figure 7.6B**) was representative of *Sphagnum* mosses such as *Sphagnum divinum*, with a notable shift in the green peak towards longer wavelengths and high reflectance in the near infrared likely due to low near-surface moisture content. Similarly, the hummock spectrum at scale 1 was representative of vascular plants, with a red absorption feature from ~650-680 nm (see **Figure 7.6C**) that was not observable in the hollow spectrum. As the resolution became coarser, mixing between hummocks and hollows was more prominent and the difference between the example spectrum from each microform decreased (**Figure 7.6D-E**). For example, over the spectral range of the red absorption feature

typically observed in vascular plants (~650-680 nm), the difference in reflectance between the example hollow and hummock spectrum was 3.24 % on average at scale 1, ranging from 3.10 to 3.36 %. The corresponding normalized difference was equal to 3.40 STD on average, ranging from 3.25-3.52 STD. At scale 6, the difference between the hummock and hollow spectrum over the same spectral range was only 0.49 % on average, ranging from 0.47 % to 0.52 %. The corresponding normalized difference was equal to 0.77 STD on average, ranging from 0.73 -0.81 STD. This practically implies that hummocks and hollows were more than 4 times as separable at scale 1 when compared to scale 5 over the 680-700 nm spectral range. Given the generally low separability of hummocks and hollows at scales 3-6 (normalized difference between hummock and hollow spectrum < 1.36 STD, see **Figure 7.6E**), the flight parameters from scales 1-2 were the most suitable for aerial campaigns interested in the microtopography at the MBP.

When selecting flight parameters, it is critical to consider logistical constraints. For instance, although an integration time of 6 ms may be technically possible, it would require on-chip summing in the spectral domain which may result in suboptimal data applications. Similarly, high altitudes may not be practically feasible. Overall, the simulation workflow is useful in determining the data acquisition parameters necessary to detect features of interest.

Table 7.2. Tested CASI-1500 data acquisition parameters for degrading the μ CASI-1920 at multiple spatial scales. The different spatial scales were acquired by modifying sensor altitude and integration time. The bolded entries indicate the parameters that were varied between scales. It is important to note that it is not feasible to maintain such precise altitudes over long durations at the airborne level with manned aircrafts.

Parameter	Scale 1	Scale 2	Scale 3	Scale 4	Scale 5	Scale 6
Number of Cross Track Pixels	1500	1500	1500	1500	1500	1500
Sensor Field of View (°)	39.86	39.86	39.86	39.86	39.86	39.86
Nominal Flight Line Heading (° True North)	0	0	0	0	0	0
Nominal Altitude (m ft)	517 1696	1034 3392	1551 5088	2068 6785	2575 8448	3092 10144
Nominal Speed (m/s kn)	41 80	41 80	41 80	41 80	41 80	41.15 80
Integration Time (ms)	6	12	18	24	30	36
Full width at half maximum of Optical Point Spread Function (pixels)	1.1	1.1	1.1	1.1	1.1	1.1
Cross Track Summing (pixel)	1	1	1	1	1	1
Swath (m)	375	750	1125	1500	1867	2242
Nominal Pixel Resolution (m)	0.25	0.5	0.75	1.0	1.25	1.50

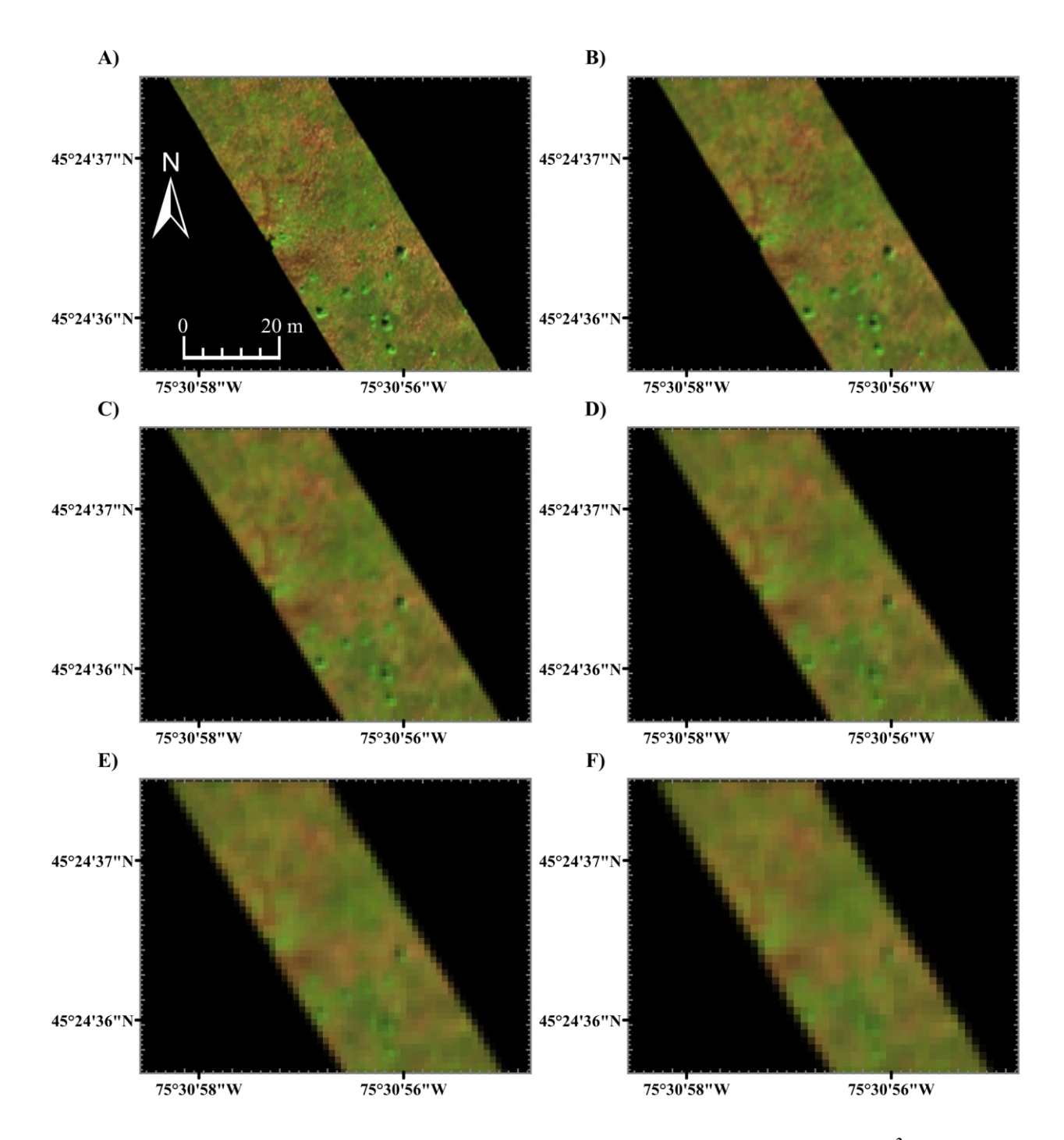


Figure 7.5. Example flight planning application of the Spatial Response Resampling (SR^2) workflow. A-F) Spatially degraded μ CASI-1920 hyperspectral imaging data (R=639.6 nm, G=550.3 nm, B=459.0 nm, linearly scaled from 0 to 12 %) generated using the SR^2 workflow with the data acquisition parameters in **Table 7.2**. Panels A-F correspond with simulations of the scene at scale 1 (0.25 m), scale 2 (0.50 m), scale 3 (0.75 m), scale 4 (1.0 m), scale 5 (1.25 m) and scale 6 (1.5 m), respectively. In general, the hummocks appear green in color while hollows appear red. Users can analyze these datasets to understand the required spatial resolution for

their particular application. In this case, the microtopography of the Mer Bleue peatland becomes less observable at coarser resolutions.

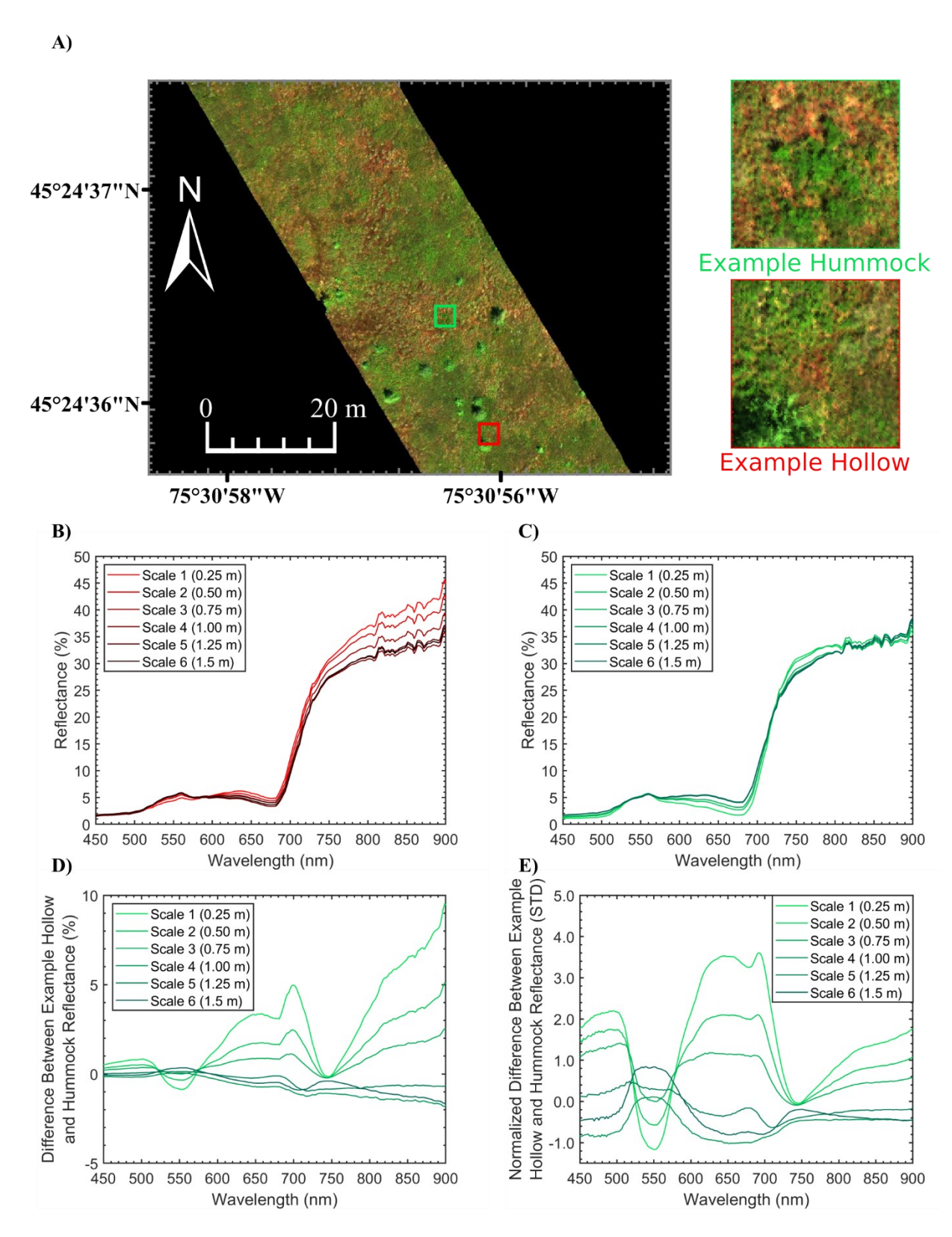


Figure 7.6. Hummock and hollow spectra extracted from the spatially degraded μ CASI-1920 hyperspectral imaging data generated using the SR^2 workflow with the data acquisition

parameters in **Table 7.2**. A) Original µCASI-1920 hyperspectral imaging data (R=639.6 nm, G=550.3 nm, B=459.0 nm, linearly scaled from 0 to 12%). The analyzed example hummock and hollow were identified in the image. In general, the hummocks appear green in color while hollows appear red. Panels B and C show the example hollow and hummock spectra, respectively. Panel D shows the difference between the hollow and hummock spectra at different spatial scales. Panel E shows the normalized difference between the hollow and hummock spectra at different spatial scales in units of standard deviation (STD). These values were obtained by dividing the difference spectrum in panel D by the standard deviation in each spectral band of the image from which the spectra were obtained. The absolute value of the normalized difference is representative of separability between the example hummock and hollow as a function of wavelength. As the spatial scale becomes coarser, hummock and hollow reflectance spectra become more similar due to mixing with neighbouring endmembers. For instance, at fine spatial resolutions, the sphagnum from the hollow spectra can be observed by the shifted green peak and the high NIR reflectance. At scale 3-6, these characteristics were lost, and the spectra were more consistent with the example hummock.

7.1.4.3. Data Fusion of VNIR and SWIR Imagery

Inamdar et al. (2021a) developed a data fusion approach that synergistically integrated surface elevation data into HSI data. In their work, a fine spatial resolution digital surface model was convolved with the PSF of a coarser resolution HSI dataset to make the elevation and spectral data more spatially consistent. Following the same logic, the SR² workflow can be used for data fusion between sensors that capture spectral information in different portions of the electromagnetic spectrum (e.g., visible near infrared (VNIR) and shortwave infrared (SWIR)) at different spatial scales. In this example application, the CASI-1500 and SASI-640 data collected over the PJA were fused to generate a full-range (450 nm to 1900 nm) image.

Due to differences in sensor characteristics, the spatial resolution of the SASI-640 imagery (2.9 m) was coarser than that of the CASI imagery (1.25 m). To ensure that the reflectance spectrum was spatially coherent between the VNIR and SWIR during data fusion, the CASI imagery (1.25 m) needed to be spatially degraded. As such, the CASI-1500 data was input to the data simulation workflow and spatially degraded based on the spatial response of the SASI-640 derived from the flight parameters in **Table 7.1**. To generate a full-range data product after the simulation workflow, the spatially degraded CASI-1500 image and unmodified SASI-640 image were stacked via ENVI using a nearest neighbour resampling technique. To showcase the utility of the SR² workflow in data fusion, the derived full-range data product was compared against a conventional full-range data product generated by stacking the unmodified CASI-1500 and SASI-640 data using a nearest neighbour resampling technique in ENVI. The two data products were initially evaluated by observing the mean and standard deviation in the reflectance

spectrum from two 280 m x 280 m (80 x 80 pixels) regions of interest (forest and urban) in the fused data products.

Figure 7.7A-F shows the studied ROIs from the two generated full-range products in the VNIR and SWIR. As seen in Figure 7.7G-H, the difference between the mean VNIR reflectance spectra in the conventional and SR² data products was marginal (< 0.12 %). This was expected as convolution theoretically has no effects on first-order statistics such as mean (Inamdar et al., 2020) over large enough regions. Figure 7.7I-J shows that the conventional full-range data product had a larger standard deviation than the SR² workflow derivative. The offset in standard deviation between the VNIR and SWIR was larger in the conventional full-range product (3.02 % and 2.58 % for the forest and urban ROIs, respectively) than in the SR² derivative (0.58 % and 0.28 % for the forest and urban ROIs, respectively). Based on the results previously discussed by Inamdar et al. (2020), this implies that the spatial properties of the CASI-1500 data are more consistent with that of the SASI-640 when using the SR² workflow. To expand on this analysis, the absolute offset in reflectance spectra between the VNIR and SWIR for the two studied fullrange data products was calculated on a pixel-by-pixel basis (see Figure 7.8) over the studied ROIs. The VNIR reflectance spectra derived from the SR² workflow were more consistent with the SWIR data. As seen in the violin plots from Figure 7.8G-H, the mean absolute difference in reflectance across the transition between the VNIR and SWIR in the SR² full-range end product was 4.08 % and 3.06 % for the forest and urban ROIs, respectively. These values were much smaller than those recorded for the conventional full-range product, which was 7.72 % and 7.25 % for the forest and urban ROIs, respectively. Visual inspection of the violin plots also reveals that the distribution of the offset between the VNIR and SWIR portions skews closer to zero for the SR² data derivative than the conventional end product.

To gain some insight into the cause of the VNIR-SWIR offset, **Figure 7.8I-J** shows spectra of various features (tree canopy, shaded tree canopy, building and road) within the two example ROIs. In the conventional full-range product, the spectra were inconsistent between the VNIR and SWIR (see **Figure 7.8I**). For instance, in the shaded tree canopy spectra, the VNIR spectra appeared to be from a shaded canopy exclusively, while the SWIR spectra appeared to be a mixture of the shaded canopy and the unshaded surrounding materials. The discrepancy in the material composition of the shaded canopy spectrum resulted in a large offset of 26.56 %

between the VNIR and SWIR portions of the electromagnetic spectrum. In the full-range product generated using the SR² workflow, the shaded canopy VNIR spectrum was consistent with the SWIR; the offset between the VNIR and SWIR portions of the electromagnetic spectrum was <0.3% (see Figure 7.8J). These results imply that the large mean absolute offset in the conventional full-range product (7.72 % and 7.25 % for the forest and urban ROIs, respectively) was due to discrepancies in scale and, by extension, pixel material composition between the CASI-1500 and SASI-640 data. Without applying the SR² workflow, the derived full-range HSI product cannot be effectively utilized for spectroscopy analyses. Similar arguments can be made by studying the building and tree canopy spectra. Although the SR² workflow did not improve the road spectra in Figure 7.8I-J, it is crucial to recognize that the extracted pixel was surrounded by other road pixels. As such, the pixel material composition to each spectrum did not change when applying the SR² workflow. This implies that the SR² workflow is critical in heterogeneous areas. Overall, the SR² workflow was shown to be an effective method to ensure that the VNIR and SWIR portions of the spectra from the full-range HSI datasets are representative of similar areas on the ground.

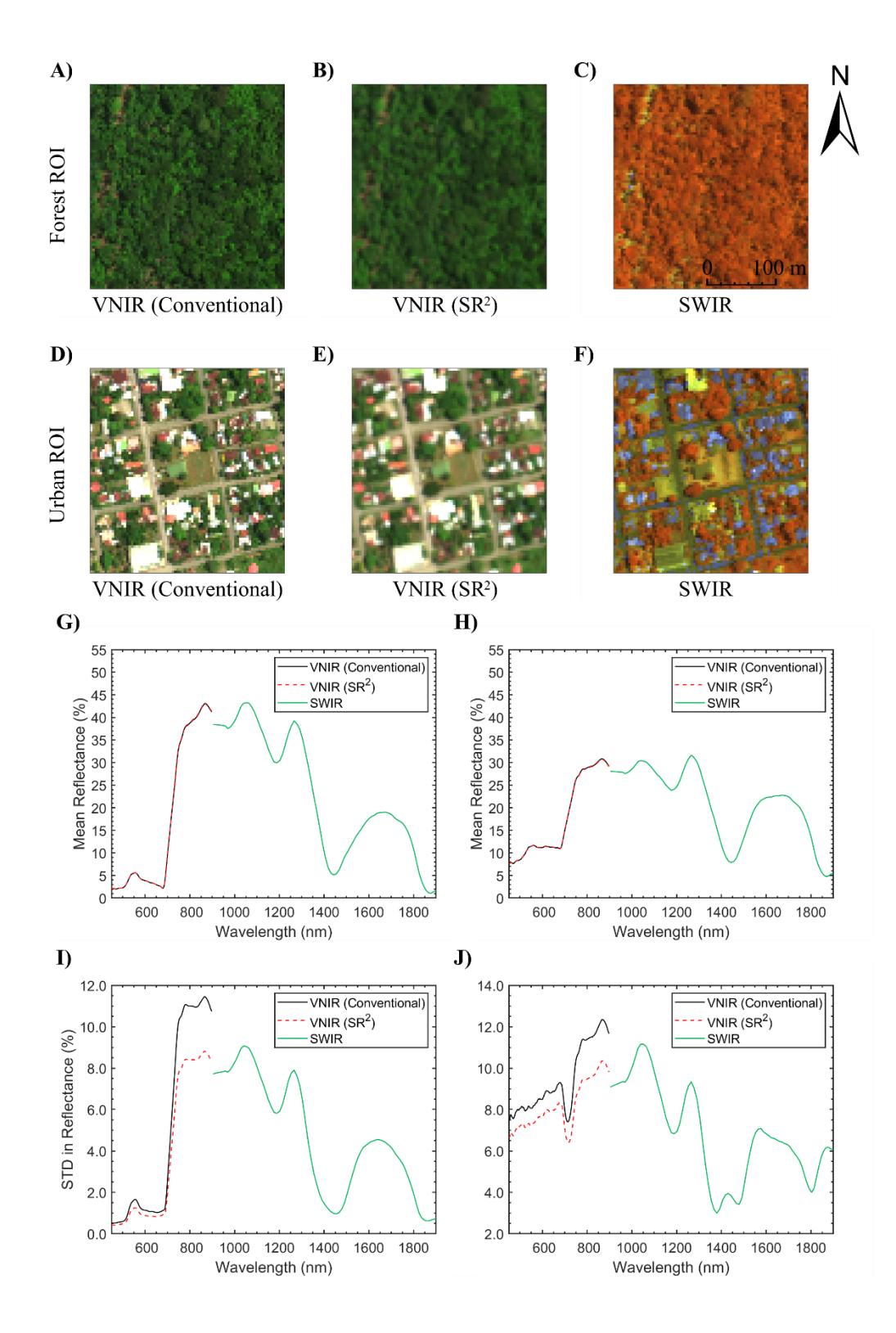


Figure 7.7. Example data fusion application of the spatial response resampling (SR^2) workflow for generating a full-range image from separate VNIR and SWIR hyperspectral imagery. The two tested full-range data products were the same in the shortwave infrared (SWIR) and only distinguishable in the visible near infrared (VNIR). The conventional full-range data product

was generated using a nearest neighbour resampling technique, while the novel data fusion approach used the SR^2 technique described in this study. A-C) the forest region of interest in the VNIR (R=641.2~nm, G=550.3~nm, B=458.3~nm, linearly scaled from 0 to 20 %) and the SWIR (R=1240.1~nm and linearly scaled from 0 to 60 %, G=1540.7~nm and linearly scaled from 0 to 50 %, B=1846.0~nm and linearly scaled from 0 to 30 %) for both full-range data products. D-F) The urban region of interest in the VNIR and SWIR (RGB display identical to the forest region of interest) for both full-range products. G) The mean reflectance spectrum from the conventional and SR^2 full-range end products over the forest region of interest. H) The mean reflectance spectrum from the conventional and SR^2 full-range end products over the urban region of interest. Subplots I and J display the standard deviation in the reflectance spectrum shown in subplots G and H, respectively. The offset between the VNIR and SWIR in subplots I and J shows that the SR^2 workflow is critical in ensuring that the merged SASI-640 imagery and CASI-1500 imagery are spatially consistent.

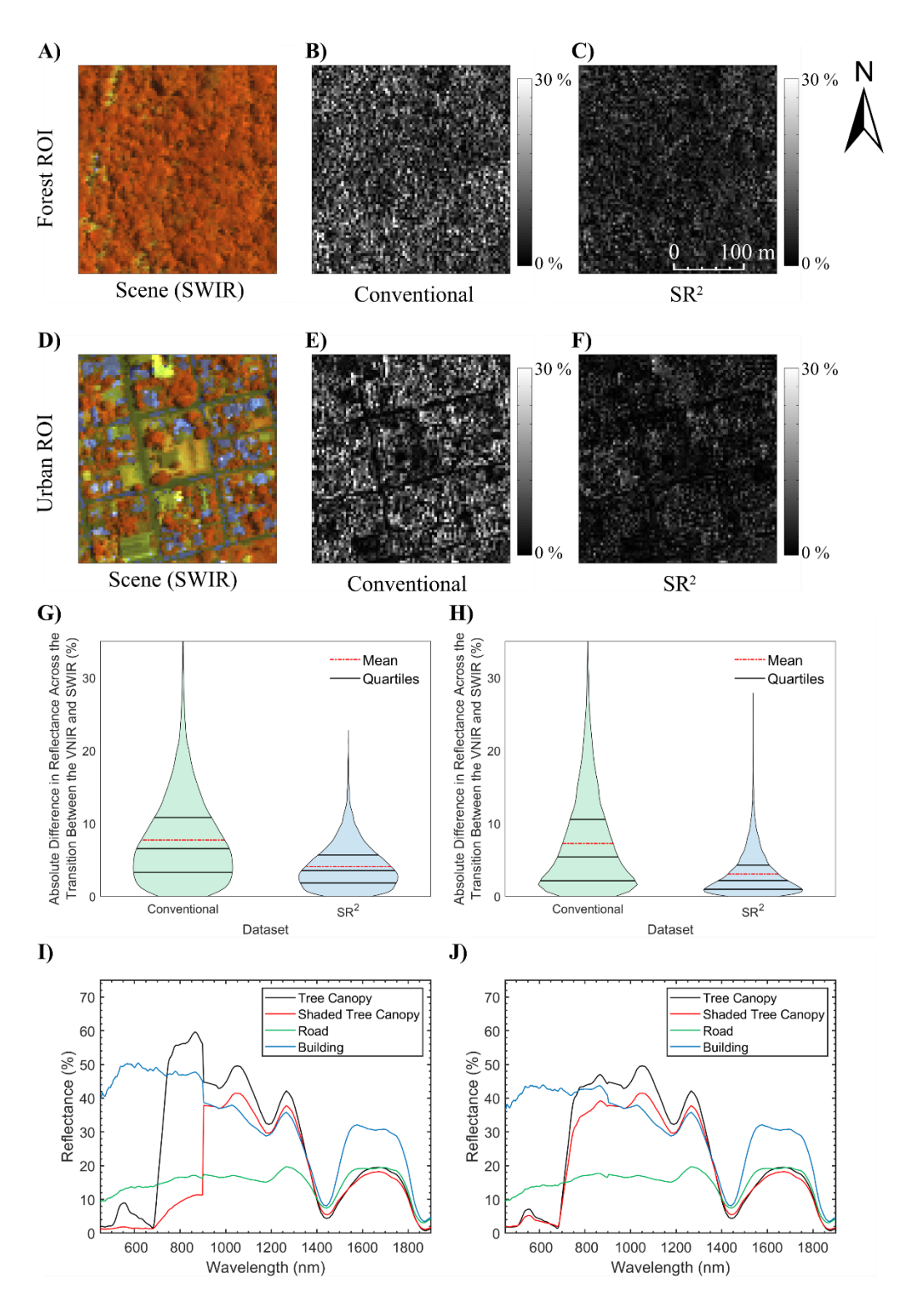


Figure 7.8. Example data fusion application of the spatial response resampling (SR^2) workflow for generating a full-range image from separate VNIR and SWIR hyperspectral imagery. The two tested full-range data products were the same in the shortwave infrared (SWIR) and only distinguishable in the visible near infrared (VNIR). The conventional full-range data product

was generated using a nearest neighbour resampling technique, while the novel data fusion approach used the SR² technique described in this study. A) The forest region of interest (ROI) in the SWIR (R=1240.1 nm and linearly scaled from 0 to 60 %, G=1540.7 nm and linearly scaled from 0 to 50 %, B=1846.0 nm and linearly scaled from 0 to 30 %). Panels B and C show the absolute difference in reflectance across the transition between the VNIR and SWIR for the two studied full-range data products in the forest ROI. D) The urban ROI in the SWIR (displayed identically to panel A). Panels E and F show the absolute difference in reflectance across the transition between the VNIR and SWIR for the two studied full-range data products in the urban ROI. G) Violin plot (includes mean and quartiles) of the absolute difference in reflectance across the transition between the VNIR and SWIR for the two studied full-range data products in the forest ROI. H) Violin plot (includes mean and quartiles) of the absolute difference in reflectance across the transition between the VNIR and SWIR for the two studied full-range data products in the urban ROI. I) Spectra from various materials extracted from the conventional data fusion end product within the studied ROIs. J) Spectra from various materials extracted from the SR² data fusion end product within the studied ROIs. The offset between the VNIR and SWIR in the conventional full-range data product would leave the spectra unusable in spectroscopy analyses such as material identification and characterization.

7.1.5. References

Aasen, H., Honkavaara, E., Lucieer, A., & Zarco-Tejada, P.J. (2018). Quantitative remote sensing at ultra-high resolution with UAV spectroscopy: A review of sensor technology, measurement procedures, and data correction workflows. *Remote Sensing*, 10, 1091

Alonso, K., Bachmann, M., Burch, K., Carmona, E., Cerra, D., de los Reyes, R., Dietrich, D., Heiden, U., Hölderlin, A., Ickes, J., Knodt, U., Krutz, D., Lester, H., Müller, R., Pagnutti, M., Reinartz, P., Richter, R., Ryan, R., Sebastian, I., & Tegler, M. (2019). Data products, quality and validation of the DLR Earth Sensing Imaging Spectrometer (DESIS). *Sensors*, 19, 4471

Arroyo-Mora, J.P., Kalacska, M., Inamdar, D., Soffer, R., Lucanus, O., Gorman, J., Naprstek, T., Schaaf, E.S., Ifimov, G., & Elmer, K. (2019). Implementation of a UAV–hyperspectral pushbroom imager for ecological monitoring. *Drones*, *3*, 12

Arroyo-Mora, J.P., Kalacska, M., Løke, T., Schläpfer, D., Coops, N.C., Lucanus, O., & Leblanc, G. (2021). Assessing the impact of illumination on UAV pushbroom hyperspectral imagery collected under various cloud cover conditions. *Remote Sensing of Environment*, 258, 112396

Arroyo-Mora, J.P., Kalacska, M., Soffer, R., Ifimov, G., Leblanc, G., Schaaf, E.S., & Lucanus, O. (2018). Evaluation of phenospectral dynamics with Sentinel-2A using a bottom-up approach in a northern ombrotrophic peatland. *Remote Sensing of Environment*, 216, 544-560

Babey, S., & Anger, C. (1993). Compact Airborne Spectrographic Imager (CASI): A progress review. In: *Proceedings of the Society of Photo-Optical Instrumentation Engineers,* 1937 (pp. 152-163): SPIE

Belyea, L.R., & Baird, A.J. (2006). Beyond "the limits to peat bog growth": Cross-scale feedback in peatland development. *Ecological Monographs*, 76, 299-322

- Belyea, L.R., & Malmer, N. (2004). Carbon sequestration in peatland: Patterns and mechanisms of response to climate change. *Global Change Biology*, 10, 1043-1052
- Blonski, S., Cao, C., Gasser, J., Ryan, R., Zanoni, V., & Stanley, T. (2000). Satellite hyperspectral imaging simulation. In: *Proceedings of the International Symposium on Spectral Sensing Research (ISSSR)* 1999: US Corps of Engineers.
- Bryant, R.G., & Baird, A.J. (2003). The spectral behaviour of sphagnum canopies under varying hydrological conditions. *Geophysical Research Letters*, 30, 1134
- Bubier, J.L., Rock, B.N., & Crill, P.M. (1997). Spectral reflectance measurements of boreal wetland and forest mosses. *Journal of Geophysical Research: Atmospheres*, 102, 29483-29494
- Castaldi, F., Palombo, A., Santini, F., Pascucci, S., Pignatti, S., & Casa, R. (2016). Evaluation of the potential of the current and forthcoming multispectral and hyperspectral imagers to estimate soil texture and organic carbon. *Remote Sensing of Environment, 179*, 54-65
- Eismann, M.T. (2012). Hyperspectral Remote Sensing. In: *Hyperspectral Remote Sensing*. Bellingham: SPIE
- Epperson, P.M., & Denton, M.B. (1989). Binning spectral images in a charge-coupled device. *Analytical Chemistry*, 61, 1513-1519
- Eppinga, M.B., Rietkerk, M., Borren, W., Lapshina, E.D., Bleuten, W., & Wassen, M.J. (2008). Regular surface patterning of peatlands: Confronting theory with field data. *Ecosystems*, 11, 520-536
- Feingersh, T., & Dor, E.B. (2015). SHALOM–a commercial hyperspectral space mission. In: Qian, S (Ed.), *Optical payloads for space missions*: John Wiley & Sons, LTD. (pp.247-263)
- Guanter, L., Kaufmann, H., Segl, K., Foerster, S., Rogass, C., Chabrillat, S., Kuester, T., Hollstein, A., Rossner, G., Chlebek, C., Straif, C., Fischer, S., Schrader, S., Storch, T., Heiden, U., Mueller, A., Bachmann, M., Mühle, H., Müller, R., Habermeyer, M., Ohndorf, A., Hill, J., Buddenbaum, H., Hostert, P., Van der Linden, S., Leitão, P.J., Rabe, A., Doerffer, R., Krasemann, H., Xi, H., Mauser, W., Hank, T., Locherer, M., Rast, M., Staenz, K., & Sang, B. (2015). The ENMAP spaceborne imaging spectroscopy mission for Earth observation. *Remote Sensing*, *7*, 8830-8857
- Guanter, L., Segl, K., & Kaufmann, H. (2009). Simulation of optical remote-sensing scenes with application to the ENMAP hyperspectral mission. *IEEE Transactions on Geoscience and Remote Sensing*, 47, 2340-2351
- Hamlin, L., Green, R.O., Mouroulis, P., Eastwood, M., Wilson, D., Dudik, M., & Paine, C. (2011). Imaging spectrometer science measurements for terrestrial ecology: AVIRIS and new developments. In: *2011 Aerospace Conference* (pp. 1-7)
- Harris, A., Bryant, R., & Baird, A. (2005). Detecting near-surface moisture stress in spp. *Remote Sensing of Environment*, 97, 371-381
- Harris Geospatial Solutions (2022). Envi image files. https://www.l3harrisgeospatial.com/docs/enviimagefiles.html

- Hueni, A., Damm, A., Kneubuehler, M., Schläpfer, D., & Schaepman, M.E. (2017). Field and airborne spectroscopy cross validation—some considerations. *IEEE Journal of Selected Topics in Applied Earth Observations and Remote Sensing*, 10, 1117-1135
- Inamdar, D., Kalacska, M., Arroyo-Mora, J.P., & Leblanc, G. (2021a). The Directly-Georeferenced Hyperspectral Point Cloud: Preserving the integrity of hyperspectral imaging data. *Frontiers in Remote Sensing*, *2*, 675323
- Inamdar, D., Kalacska, M., Leblanc, G., & Arroyo-Mora, J.P. (2020). Characterizing and mitigating sensor generated spatial correlations in airborne hyperspectral imaging data. *Remote Sensing*, 12, 641
- Inamdar, D., Kalacska, M., Leblanc, G., & Arroyo-Mora, J.P. (2021b). Implementation of the Directly-Georeferenced Hyperspectral Point Cloud. *MethodsX*, 8, 101429
- Kalacska, M., Arroyo-Mora, J., Soffer, R., Roulet, N., Moore, T., Humphreys, E., Leblanc, G., Lucanus, O., & Inamdar, D. (2018). Estimating peatland water table depth and net ecosystem exchange: A comparison between satellite and airborne imagery. *Remote Sensing*, 10, 687
- Kalacska, M., Arroyo-Mora, J.P., & Lucanus, O. (2021). Comparing uas LiDAR and structure-from-motion photogrammetry for peatland mapping and Virtual Reality (vr) visualization. *Drones*, 5, 36
- Kalacska, M., Arroyo-Mora, J.P., Soffer, R., & Leblanc, G. (2016). Quality control assessment of the Mission Airborne Carbon 13 (mac-13) hyperspectral imagery from Costa Rica. *Canadian Journal of Remote Sensing*, 42, 85-105
- Kaňuk, J., Gallay, M., Eck, C., Zgraggen, C., & Dvorný, E. (2018). Technical report: Unmanned helicopter solution for survey-grade LiDAR and hyperspectral mapping. *Pure and Applied Geophysics*, 175, 3357-3373
- Lafleur, P., Roulet, N., & Admiral, S. (2001). Annual cycle of CO2 exchange at a bog peatland. *Journal of Geophysical Research: Atmospheres*, 106, 3071-3081
- Lafleur, P.M., Hember, R.A., Admiral, S.W., & Roulet, N.T. (2005). Annual and seasonal variability in evapotranspiration and water table at a shrub-covered bog in southern Ontario, canada. *Hydrological processes*, 19, 3533-3550
- Malhotra, A., Roulet, N.T., Wilson, P., Giroux-Bougard, X., & Harris, L.I. (2016). Ecohydrological feedbacks in peatlands: An empirical test of the relationship among vegetation, microtopography and water table. *Ecohydrology*, *9*, 1346-1357
- Moore, P.A., Lukenbach, M.C., Thompson, D.K., Kettridge, N., Granath, G., & Waddington, J.M. (2019). Assessing the peatland hummock–hollow classification framework using high-resolution elevation models: Implications for appropriate complexity ecosystem modeling. *Biogeosciences*, 16, 3491-3506
- Osei Darko, P., Kalacska, M., Arroyo-Mora, J.P., & Fagan, M.E. (2021). Spectral complexity of hyperspectral images: A new approach for mangrove classification. *Remote Sensing*, 13, 2604
- Shivers, S., Guido, J., Duren, R., Asner, G., Green, R.O., Ardila, D.R., Ayasse, A., de Belloy, M., Cusworth, D., & Lai-Norling, J. (2021). Carbon Mapper: A new public-private hyperspectral constellation. In: *AGU Fall Meeting 2021*: AGU

Soffer, R.J., Ifimov, G., Arroyo-Mora, J.P., & Kalacska, M. (2019). Validation of airborne hyperspectral imagery from laboratory panel characterization to image quality assessment: Implications for an arctic peatland surrogate simulation site. *Canadian Journal of Remote Sensing*, 45, 476-508

Teillet, P.M., Fedosejevs, G., Gauthier, R.P., O'Neill, N.T., Thome, K.J., Biggar, S.F., Ripley, H., & Meygret, A. (2001). A generalized approach to the vicarious calibration of multiple earth observation sensors using hyperspectral data. *Remote Sensing of Environment*, 77, 304-327

Transon, J., D'Andrimont, R., Maugnard, A., & Defourny, P. (2018). Survey of hyperspectral earth observation applications from space in the Sentinel-2 context. *Remote Sensing*, 10, 157

Vogelmann, J.E., & Moss, D.M. (1993). Spectral reflectance measurements in the genus sphagnum. *Remote Sensing of Environment*, 45, 273-279

Vreys, K., Iordache, M.-D., Bomans, B., & Meuleman, K. (2016). Data acquisition with the apex hyperspectral sensor. *Miscellanea Geographica*, 20, 5-10

Zhao, H., Cui, B., & Jia, G. (2019). A flight direction design method for airborne spectral imaging considering the anisotropy reflectance of the target in rugged terrain. *Sensors*, 19, 2715

7.1.6. Author Contributions

Conceptualization, D.I., M.K., P.O.D.; methodology, D.I., M.K. J.P.A.-M., P.O.D.; validation, D.I.; formal analysis, D.I.; investigation, D.I.; resources, M.K., G.L, J.P.A.-M.; data curation, D.I., M.K.; writing—original draft, D.I.; writing—review and editing, D.I., M.K., G.L., J.P.A.-M., P.O.D.; visualization, D.I.

7.1.7. Acknowledgement

This work was funded by the Natural Sciences and Engineering Research Council of Canada (NSERC), the Fonds de Recherche du Québec – Nature et Technologies (FQRNT), the Canadian Airborne Biodiversity Observatory (CABO), the Lorne Trottier Fellowship and the Dr. and Mrs. Milton Leong Fellowship in Science. The PJA imagery was provided by the MAC-13 project funded by the Canadian Space Agency FAST-AO program. The authors would like to thank Stephen Achal (Pi4Lab) for information regarding the sensor point spread functions and Raymond Soffer for conversations that helped develop the ideas presented in this work.

7.1.8. Supplemental Material

The supplementary HSI BLUR MATLAB script can be found below:

```
function [IMG conv, PSF tot 3d, x c dist, y c dist ] =
HSI BLUR(flight line heading, FOV deg, pix tot, alt, speed, it, cross track sum, FWHM opt,
IMG loc, IMG name)
%% HSI BLUR (Blur Hyperspectral Imaging Data to the Spatial Characteristics of a
Specified Sensor)
% [IMG conv, PSF tot 3d, x c dist, y c dist] =
HSI BLUR (flight line heading, FOV deg, pix tot, alt, speed, it, cross track sum, FWHM opt,
IMG loc, IMG name)
%%% Input Parameters
% flight line heading... Heading of simulated sensor (True North Heading in
degrees, e.g., north=0, east=90, south=180, west=270).
% FOV deg...
                          Field of view of simulated sensor (degrees).
% pix_tot...
                           Number of cross track pixels in simulated sensor.
% alt...
                          Nominal altitude (m above ground level) of simulated
sensor during data acquisition.
% speed...
                          Nominal speed (m/s) of simulated sensor during data
acquisition.
% it...
                          Integration time (s) of simulated sensor during data
acquisition.
                          Summing factor of simulated sensor in cross track
% cross track sum
direction
% FWHM opt...
                          Full width at half maximum (pixels) of simulated
sensor's optical point spread function (PSF). If unknown please enter 1.
                          String with fold path of the input hyperspectral
% IMG loc...
imaging dataset.
% IMG name...
                          Name of the input hyperspectral imaging dataset (must
be *.dat). Please DO NOT Include the ".dat" Extension.
%%%Output Parameters
% IMG conv...
                          Hyperspectral imaging dataset blurred through
convolution with simulated sensor PSF
% PSF tot 3d... PSF of simulated sensor. The PSF is a function of
spatial displacement from pixel Center (m) in the Easting and Northing directions
                          Displacement values associated with columns of
% x c dist...
PSF tot 3d in Easting direction (m)
% y_c_dist...
                          Displacement values associated with rows of PSF tot 3d
in Northing direction (m)
% *** After running HSI BLUR, the blurred HSI dataset will be saved ***
% *** to the same location as the input image as a *.dat file. The
                                                                      ***
% *** output image will be named after the input image with "conv"
                                                                      ***
\mbox{\%} *** appended to the file name.
%%% Description
% HSI BLUR is used to blur an input HSI dataset to simulate the spatial
% characteristics of another sensor.
%%% Copyright: Deep Inamdar, deep.inamdar@mail.mcgill.ca
%%% Applied Remote Sensing Laboratory, Department of Geography, McGill University
                                                                    Code Segment 1 of 4
```

```
%% Derive PSF
%%%Derive nominal pixel sizes of simulated sensor
pix size x=alt*tand(FOV deg/2)/(pix tot/2); %nominal cross track resolution (m)
pix size y=max(speed*it,pix size x); %nominal along track resolution (m)
dt=round(min([pix_size_x pix_size_y])/150,1,'significant'); % spatial resolution to
which PSF is calculated
%%% Derive Cross Track PSF of simulated sensor
%%%% Derive Gaussian Optical PSF of simulated sensor
muPDF=0; % Mean of Gaussian Distribution for Optical PSF
FWHM x=FWHM opt*pix size x; %FWHM of Gaussian Distribution for Optical PSF
sigmaPDF=FWHM x/(2*sqrt(2*log(2))); %Standard Deviation of Gaussian for Optical PSF
op_pdx=makedist('Normal', muPDF, sigmaPDF); %Generate PSF
num vals=round(pix size x*2/dt);
x=-num\ vals*dt:dt:num\ vals*dt; % Displacement from pixel center (m) at which the
Optical PSF will be calculated
op x f=pdf(op pdx,x); %Calculate value of Optical PSF
%%%% Derive Rectangular Pulse Detector PSF of simulated sensor
step_f=x>=-pix_size_x/2& x<=pix_size_x/2;</pre>
%%%% Derive Net Cross Track PSF of simulated sensor normalized by the maximum
x c spr=conv(op x f, step f)/max(conv(op x f, step f));
%%%% Derive cross track displacement values associated with the Net PSF of
simulated sensor
x \min = \min(abs(x));
addon x=(length(x c spr)-1)/2;
x c dist=x min-addon x*dt:dt:x min+addon x*dt;
%%% Derive Along Track PSF of simulated sensor
num vals=round(it*speed/dt);
y=num vals*dt:-dt:-num vals*dt; % Displacement from pixel center (m) at which the
along track PSF will be calculated
%%%% Derive motion PSF of simulated sensor
step_f_2=y>=-it*speed/2& y<=it*speed/2;</pre>
%%%% Derive Net Along Track PSF of simulated sensor normalized by the maximum
y c spr=conv(x c spr, step f 2)/max(conv(x c spr, step f 2));
%%%% Derive along track displacement values associated with the Net PSF of
simulated sensor
y \min = \min(abs(y));
addon_y=(length(y_c_spr)-1)/2;
y c dist=y min+addon y*dt:-dt:y min-addon y*dt;
                                                                       Code Segment 2 of 4
```

```
%%%% Handle cross track summing
if cross track sum>1
dist inc pix=cross track sum-1;
addon2=ceil(pix size x*dist inc pix/2/dt);
x \min = \min(abs(x c dist));
x len orig=length(x_c_spr);
x c dist=x min-addon2*dt-(x len orig-1)/2*dt:dt:x min+addon2*dt+(x len orig-
1)/2*dt;
x spr new=zeros(1,length(x c dist));
if rem(cross track sum, 2) == 0
   center pt=(-pix size x/2-(cross track sum/2-
1) *pix size x):pix size x:(pix size x/2+(cross track sum/2-1) *pix size x);
   center pt=-pix size x*(cross track sum-
1)/2:pix_size_x:pix_size_x*(cross_track_sum-1)/2;
index center pt = knnsearch(x c dist',center pt');
for i=1:cross track sum
    start_indx=index_center_pt(i)-(x_len_orig-1)/2;
    end indx=index center pt(i)+(x len orig-1)/2;
    x_spr_new(start_indx:end_indx)=x_spr_new(start_indx:end_indx)+x_c_spr;
x spr new=x spr new/max(x spr new);
x_c_spr=x_spr_new;
end
%%% Make x c spr same spatial dimensions as y c spr by padding edges
if length(y c spr)>length(x c spr)
    x c spr=padarray(x c spr, [0 (length(y c spr)-length(x c spr))/2], 'both');
        x_c_dist=fliplr(y_c_dist);
elseif length(x_c_spr)>length(y_c_spr)
    y c spr=padarray(y c spr,[0 (length(x c spr)-length(y c spr))/2],'both');
        y c dist=fliplr(x c dist);
end
%%% Calculate Net PSF of simulated sensor in 2-dimensions (along track x cross
PSF_tot_3d_no_rot=y_c_spr'*x_c_spr;
%%% Rotate PSF by flight line heading so that PSF of the simulated sensor is north
oriented
PSF_tot_3d=imrotate(PSF_tot_3d_no_rot,-flight_line_heading,'bilinear','crop');
                                                                      Code Segment 3 of 4
```

```
%% Derive Convolution Kernel for input HSI dataset
%%% Read input HSI dataset and extract pixel size
Filename=[IMG_loc IMG_name '.dat'];
Filename 2=[IMG loc IMG name '.hdr'];
info = enviinfo(Filename 2);
data=hypercube(Filename, Filename 2);
pix size IMG= data.Metadata.MapInfo.PixelSize(1);
%%% Generate Convolution Kernel by integrating PSF of simulated sensor
size kernel=ceil(max(x c dist)/pix size IMG)*2+1; %calculate size of convolution
kernel
conv ker=ones(size kernel, size kernel);
x vec=-pix size IMG*size kernel/2:pix size IMG:pix size IMG* (size kernel/2-1);
y_vec=fliplr(x_vec);
for i= 1:size kernel
   x_{indx} = (x_{vec(i)} < x_{c_dist} & x_{c_dist} < (x_{vec(i)} + pix_{size_IMG}));
    for j=1:size kernel
       y_indx=(y_vec(j)+pix_size_IMG>y_c_dist & y_c_dist>y_vec(j));
       conv ker(j,i)=sum(sum(PSF tot 3d(y indx,x indx)))/sum(sum(PSF tot 3d));
end
%%%% Normalize convolution kernel to sum to 1
conv ker=conv ker/sum(sum(conv ker));
%% Convolve input HSI dataset by Convolution Kernel
IMG conv=data.DataCube;
for i=1:info.Bands
IMG conv(:,:,i)=conv2(data.DataCube(:,:,i),conv ker,'same');
i/info.Bands*100
end
%% Output input HSI dataset to ENVI Standard File
Filename=[IMG_loc IMG_name '_conv'];
newhcube = assignData(data, ':',':',':',IMG_conv);
enviwrite(newhcube, Filename);
end
                                                                          Code Segment 4 of 4
```

7.2. Implementation of the Directly-Georeferenced Hyperspectral Point Cloud (DHPC)

Deep Inamdar ¹, Margaret Kalacska ^{1,*}, George Leblanc ^{2,1} and J. Pablo Arroyo-Mora ²

This chapter is published in *MethodsX*, 8, 101429 under the terms and conditions of the Creative Commons Attribution (CC BY) license (http://creativecommons.org/licenses/by/4.0/). Minor modifications have been made with respect to formating style.

DOI: https://doi.org/10.1016/j.mex.2021.101429

Abstract

Before pushbroom hyperspectral imaging (HSI) data can be applied in remote sensing applications, it must typically be preprocessed through radiometric correction, atmospheric compensation, geometric correction and spatial resampling procedures. After these preprocessing procedures, HSI data are conventionally given as georeferenced raster images. The raster data model compromises the spatial-spectral integrity of HSI data, leading to suboptimal results in various applications. Inamdar et al. (2021) developed a point cloud data format, the Directly-Georeferenced Hyperspectral Point Cloud (DHPC), that preserves the spatial-spectral integrity of HSI data more effectively than rasters. The DHPC is generated through a data fusion workflow that uses conventional preprocessing protocols with a modification to the digital surface model used in the geometric correction. Even with the additional elevation information, the DHPC is still stored with file sizes up to 13 times smaller than conventional rasters, making it ideal for data distribution. Our article aims to describe the DHPC data fusion workflow from Inamdar et al. (2021), providing all the required tools for its integration in pre-existing processing

¹ Applied Remote Sensing Laboratory, Department of Geography, McGill University, Montréal, QC H3A 0B9, Canada; deep.inamdar@mail.mcgill.ca (D.I.)

² Flight Research Laboratory, National Research Council of Canada, Ottawa, ON K1A 0R6, Canada; George.Leblanc@nrc-cnrc.gc.ca (G.L.); juanpablo.arroyomora@nrc-cnrc.gc.ca (J.P.A.-M.)

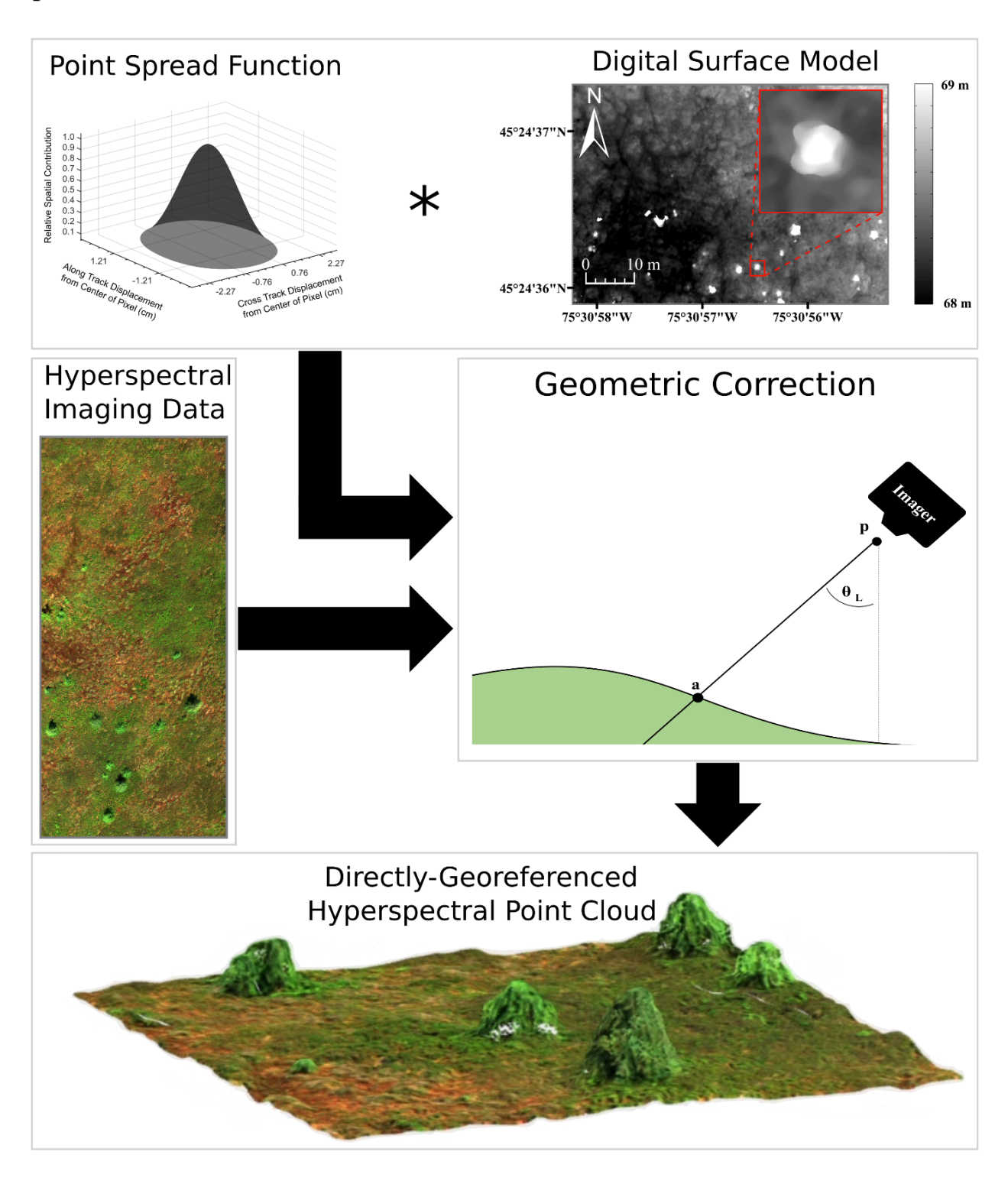
^{*} Correspondence: Margaret.kalacska@mcgill.ca; Tel.: +1-514-398-4347; Fax: +1-514-398-7437

workflows. This includes a MATLAB script that can be readily applied to carry out the modification that must be made to the digital surface model used in the geometric correction. The MATLAB script first derives the point spread function of the HSI data and then convolves it with the digital surface model input in the geometric correction. By breaking down the MATLAB script and describing its functions, data providers can readily develop their own implementation if necessary. The derived point spread function is also useful for characterizing HSI data, quantifying the contribution of materials to the spectrum from any given pixel as a function of distance from the pixel center. Overall, our work makes the implementation of the DHPC data fusion workflow transparent and approachable for end users and data providers.

- Our article describes the Directly-Georeferenced Hyperspectral Point Cloud (DHPC) data fusion workflow, which can be readily implemented with existing processing protocols by modifying the input digital surface model used in the geometric correction.
- We provide a MATLAB function that performs the modification to the digital surface model required for the DHPC workflow. This MATLAB script derives the point spread function of the hyperspectral imager and convolves it with the digital surface model so that the elevation data are more spatially consistent with the hyperspectral imaging data as collected.
- We highlight the increased effectiveness of the DHPC over conventional raster end products in terms of spatial- spectral data integrity, data storage requirements, hyperspectral imaging application results and site exploration via virtual and augmented reality.

Keywords: Hyperspectral point cloud, Spectral data integrity, Spatial data integrity, Data fusion

Graphical Abstract



7.2.1. Background

Over the last four decades, the abundance of high quality spectral-spatial information captured by pushbroom hyperspectral imaging (HSI) data has been shown to be invaluable in a variety of remote sensing applications (e.g., classification, change detection, modeling, etc.) (Eismann, 2021). Before such HSI data products can be effectively used, they must typically undergo radiometric correction, atmospheric compensation, geometric correction and spatial resampling methodologies. The end product is a georeferenced raster image. The raster data model is the most common end product data format in HSI (Vane et al., 1984; Wilkinson, 1996; Goetz, 2009). However, it is important to recognize that the raster model mispresents HSI data. For instance, hyperspectral pixels are not square, as they appear in rasters (Smith, 1995). In reality, the spatial contribution to the spectrum from a single pixel is non-uniform and extends into the spatial boundaries of neighbouring pixels (Inamdar et al., 2020). Furthermore, hyperspectral pixels are not uniformly distributed over the imaged scene as they appear in rasters due to various factors such as sensor design, sensor orientation and rugged terrains (Vreys et al., 2016). In raster data end products, pixels appear to be uniformly distributed due to the use of spatial resampling (Shlien, 1979), which can compromise spatial-spectral data integrity and lead to suboptimal results in HSI applications (Inamdar et al., 2021).

Inamdar et al. (2021) developed a point cloud HSI data representation, the Directly-Georeferenced Hyperspectral Point Cloud (DHPC), that preserves spatial-spectral data integrity more effectively than raster data end products. The DHPC is generated through a data fusion workflow that primarily uses existing processing protocols (i.e., standard radiometric correction, atmospheric compensation and geometric correction protocols). As such, it can readily be adapted and applied by data providers without large modifications to their existing processes. Our work herein first summarizes the results from Inamdar et al. (2021), which substantiates the effectiveness of the DHPC over conventional square pixel rasters. Next, we describe the DHPC data fusion workflow, illustrating its similarity to conventional preprocessing workflows. We highlight a necessary modification that must be made to these conventional preprocessing workflows to generate the DHPC, providing a novel MATLAB function to carry out this step. In the following section, we break down and fully explain the MATLAB function so that data providers can readily develop their own implementation. In the final section of this work, we provide an example of the DHPC and the intermediate data products that were used to derive it.

Overall, our work aims to describe the DHPC data fusion workflow and provide all the required tools for its integration into pre-existing processing workflows.

7.2.2. Method Effectiveness

The effectiveness of the DHPC was substantiated over square pixel rasters by Inamdar et al. (2021) based on three spatial integrity data quality metrics (i.e., pixel loss, pixel duplication and pixel shifting), data storage requirements and multiple common HSI applications (i.e., classification, spectra geo-location and target detection). The study (Inamdar et al., 2021) analyzed four different HSI datasets that were collected at three field sites with two hyperspectral sensors producing data at various spatial scales (~1.5 cm to 2.6 m). Since the spectral information is not modified in the DHPC data fusion workflow, the data product preserved spectral data integrity. Furthermore, the DHPC also preserved spatial data integrity with zero pixel loss, pixel duplication and pixel shifting. In comparison, the rasters preserved the spectral data integrity at the expense of substantial pixel loss (\sim 50–75%) or pixel duplication (\sim 35–75%), depending on the resampling grid resolution used in the nearest neighbour methodology. Furthermore, pixel shifting was relatively large in comparison to the DHPC, ranging from 0.33 to 1.95 pixels. In terms of data storage requirements, the DHPC had a file size that was smaller than the rasters by up to a factor of 13. In all the studied applications, the DHPC consistently outperformed the rasters. For instance, in the target detection application, false discovery and false negative rates were up to 69 % lower in the DHPC than in the studied raster datasets. Overall, the DHPC is ideal for the analysis, distribution and application of HSI data.

Although not mentioned in Inamdar et al. (2021), the DHPC is also effective for site exploration via virtual (VR) and augmented (AR) reality. This is particularly useful for remote field work, which often has high logistical costs (e.g., travel, food, lodging) that limit the number of individuals that can be involved. By navigating a DHPC in VR or AR, users can study the field conditions of remote sites in a cost-effective (Kalacska et al., 2021) and repeatable manner (Le Mouélic et al., 2020; Liberatore and Wagner, 2021). For fragile ecosystems, VR/AR visualization of the DHPC also allows multiple users to analyze the same field site without disturbing the natural dynamics of the system. VR/AR visualization of the DHPC makes the analyzed field site more accessible for individuals that might not have the funding, time or permission to study the site firsthand. Without the structural information provided by the

elevation data, the same level of immersion cannot be obtained with conventional rasters, which are viewed in two-dimensions (Kalacska et al., 2021; Liberatore and Wagner, 2021).

7.2.3. Method Workflow

The data fusion workflow for the DHPC is shown in Figure 7.9. In the first phase of the DHPC data fusion workflow, the input DSM is blurred through convolution with the HSI sensor point spread function (PSF). The PSF describes the spatial contribution to a single pixel of the HSI data as a function of distance from the center of the pixel (Inamdar et al., 2020). As such, the convolution step makes the elevation data spatially consistent with the HSI data. After the convolution, each point in the blurred DSM corresponds to the average elevation of the objects/terrain that would contribute to a single HSI pixel. In the second phase, the radiometrically and atmospherically corrected HSI data are geometrically corrected using the blurred DSM and the inertial navigation system data of the sensor recorded during HSI data acquisition. As a result of the geometric correction, the northing, easting and elevation of each pixel of the HSI data is calculated at the intersection between the blurred DSM and a straight line that is projected from the sensor position at the pixel dependent look direction (Figure 7.10). Because the blurred DSM is used in the geometric correction, each HSI pixel receives the average surface elevation of the objects/terrain contributing to it. With the projected coordinate system position (northing, easting and averaged surface elevation) the DHPC is complete. The general steps for generating the DHPC are:

- 1. Apply radiometric correction methodology to HSI data in raw sensor geometry (OPTIONAL).
- Apply atmospheric compensation methodology to the HSI data from step 1 (OPTIONAL).
- 3. Derive PSF of the HSI data.
- 4. Generate blurred DSM by convolving the input DSM with the derived PSF.
- 5. Apply geometric correction methodology to the HSI data from step 2 using the blurred DSM.

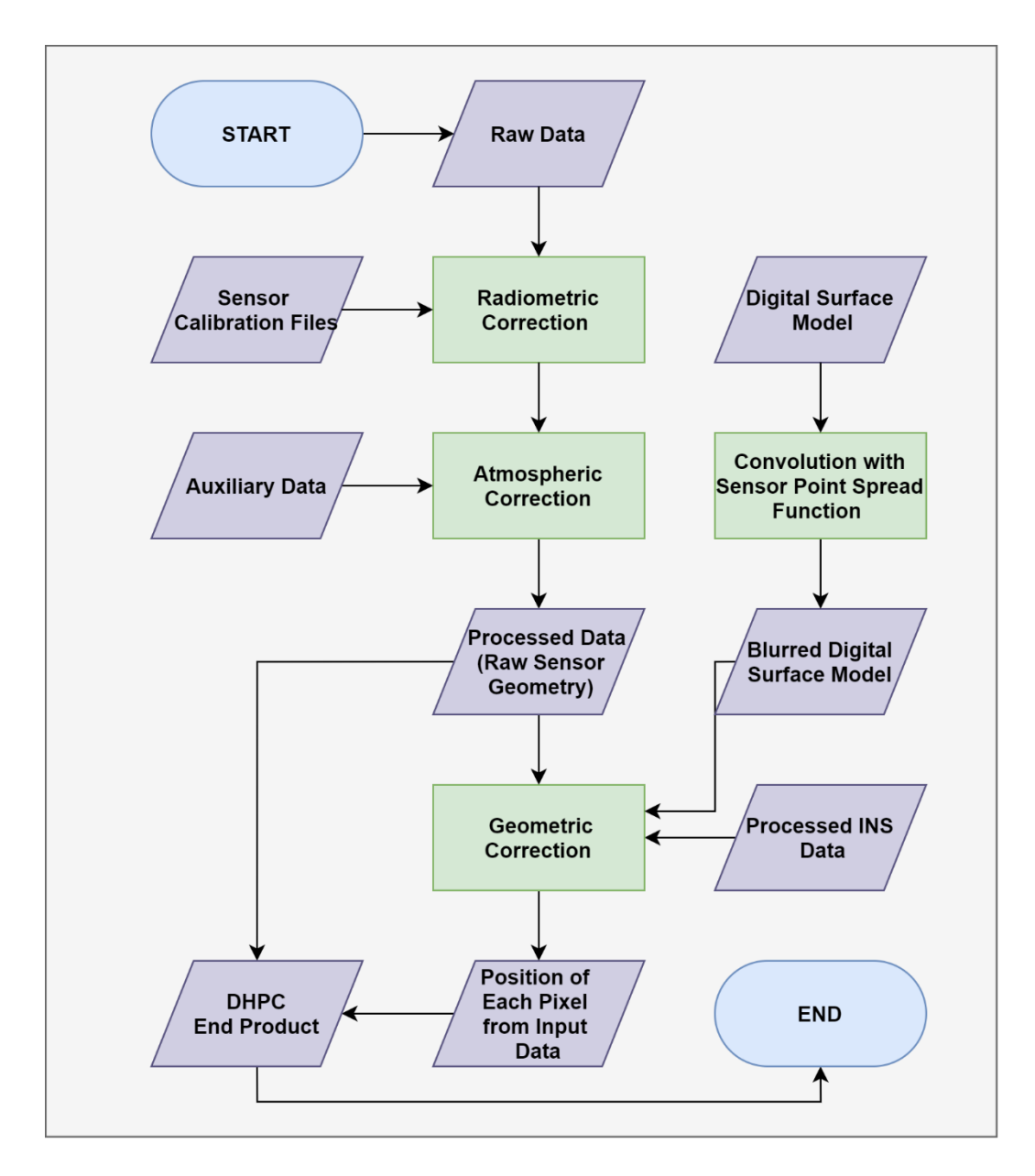


Figure 7.9. Flow chart of the hyperspectral imaging (HSI) processing workflow for the Directly-Georeferenced Hyperspectral Point Cloud (DHPC). Adapted from Inamdar et al. (2021).

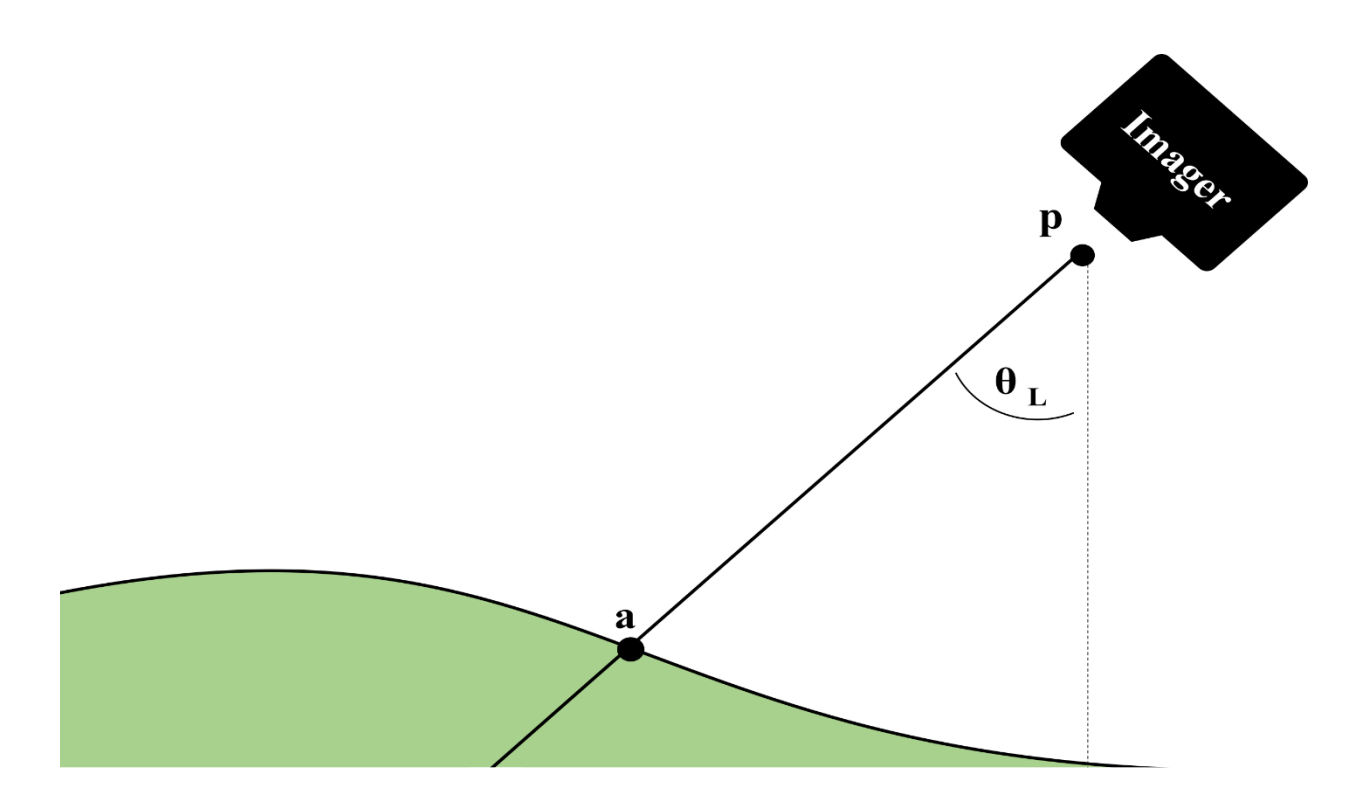


Figure 7.10. Schematic of the geometric correction. With a known sensor position (p) and look direction (θ L) the position of each pixel in the image space can be located in a real-world coordinate space. The pixel is located at the intersection (a) of the input digital surface model (shown in green) and a straight line that is projected at the pixel dependent look direction from the sensor position. The look direction is the angle at which incoming electromagnetic radiation is observed by any given pixel of the hyperspectral imager (Müller et al., 2002). The look direction is calculated from the attitude, focal geometry and boresight misalignment of the sensor during data acquisition (Müller et al., 2002; Warren et al., 2014).

The DHPC data fusion workflow is not limited by any particular software; data processing can be completed with the user's software of choice. Steps 1, 2 and 5 above are implemented in conventional HSI data processing workflows. As a result, data providers have pre-existing protocols to complete these steps. Steps 1 and 2 are optional because the DHPC can be used to represent the raw DN (if steps 1 and 2 are omitted) or radiance (if step 2 is omitted) data if desired. Steps 3–4 are not typically implemented in conventional data preprocessing protocols. As such, these steps represent a necessary modification that must be made to conventional preprocessing protocols to generate the DHPC. Because it can be practically difficult to derive the PSF of the input HSI data and convolve it with the input DSM, we provide a MATLAB function (see DHPC_DSM_BLUR.m in supplementary material) to carry out steps 3–4. In the following section we break down this script, describing the most important code segments and their function.

7.2.4. MATLAB Function

The presented MATLAB function (DHPC_DSM_BLUR.m) carries out four main tasks: 1) derive hyperspectral PSF; 2) derive convolution kernel for DSM; 3) convolve input DSM by convolution kernel; 4) output blurred DSM as ENVI standard data format. The inputs and outputs to the function are outlined in the function description:

```
%%% Input Parameters
   % flight line heading... Heading of hyperspectral imager (True North Heading in
degrees, e.g., north=0, east=90, south=180, west=270).
   % FOV_deg... Field of view of hyperspectral imager (degrees).
% pix_tot... Number of cross track pixels in hyperspectral imager.
   % alt... Nominal altitude (m above ground level) of hyperspectral imager.
% speed... Nominal speed (m/s) of hyperspectral imager.
   % it... Integration time (s) of hyperspectral imager.
% FWHM_opt... Full width at half maximum (pixels) of optical point spread
function (PSF). If unknown please enter 1.
   % DSM_loc... String with folder path of the input digital surface model
(DSM).
   % DSM_name... Name of DSM (must be *.dat). Please DO NOT Include the ".dat"
Extension.
   %%%Output Parameters;
   % DSM_conv... DSM Blurred through Convolution with Hyperspectral Imager PSF % PSF_tot_3d... PSF as a Function of Hyperspectral Imager as a Function of
Spatial Displacement from Pixel Center (m)
  % x c dist... Displacement values associated with Columns of PSF tot 3d in
easting direction (m)
  % y_c_dist...
                            Displacement values associated with Rows of PSF tot 3d in
Northing direction (m)
```

Task 1 is completed following the derivation from Inamdar et al. (2020). In the MATLAB function, the net cross track PSF is derived by convolving the Gaussian optical PSF with the rectangular pulse detector PSF.

```
%%% Derive Cross Track PSF

%%% Derive Gaussian Optical PSF
muPDF=0; % Mean of Gaussian Distribution for Optical PSF
FWHM_x=FWHM_opt*pix_size_x; %FWHM of Gaussian Distribution for Optical PSF
sigmaPDF=FWHM_x/(2*sqrt(2*log(2))); %Standard Deviation of Gaussian for Optical PSF
L8pdx=makedist('Normal',muPDF,sigmaPDF); %Generate PSF
num_vals=round(pix_size_x*2/dt);
x=-num_vals*dt:dt:num_vals*dt; % Displacement from pixel center (m) at which the
Optical PSF will be calculated
L8p_x_f=pdf(L8pdx,x); %Calculate value of Optical PSF

%%% Derive Rectangular Pulse Detector PSF
step_f=x>=-pix_size_x/2& x<=pix_size_x/2;

%%%% Derive Net Cross Track PSF normalized by the maximum
x_c_spr=conv(L8p_x_f,step_f)/max(conv(L8p_x_f,step_f));</pre>
```

Next, the net along track PSF is derived by convolving the net cross track PSF by the rectangular pulse motion PSF.

```
%%% Derive Along Track PSF
num_vals=round(it*speed/dt);
y=num_vals*dt:-dt:-num_vals*dt; % Displacement from pixel center (m) at which the along track PSF will be calculated

%%%% Derive motion PSF
step_f_2=y>=-it*speed/2& y<=it*speed/2;

%%%% Derive Net Along Track PSF normalized by the maximum
y_c_spr=conv(x_c_spr,step_f_2)/max(conv(x_c_spr,step_f_2));</pre>
```

With the net cross track and along track PSFs, the net PSF in 2-dimensions can be derived through vector multiplication. The two dimensions of the resultant matrix correspond with the cross track (columns) and along track (rows) displacement from the center of the pixel. To convolve the PSF with the north-oriented DSM, the 2-dimensional PSF must be rotated by the flight line heading.

```
%%% Calculate Net PSF in 2-dimensions (along track x cross track)
PSF_tot_3d_no_rot=y_c_spr'*x_c_spr;

%%% Rotate PSF by flight line heading so that PSF is north oriented
PSF_tot_3d=imrotate(PSF_tot_3d_no_rot,-flight_line_heading,'bilinear','crop');
```

To complete task 2, the input DSM must first be imported and the pixel size must be extracted.

```
%%% Read DSM and extract pixel size
Filename=[DSM_loc DSM_name '.dat'];
Filename_2=[DSM_loc DSM_name '.hdr'];
info = enviinfo(Filename_2);
data=hypercube(Filename, Filename_2, [1000]);
pix_size_dsm= data.Metadata.MapInfo.PixelSize(1);
```

To derive the convolution kernel, the PSF must be spatially integrated in intervals equal to the DSM pixel size in the northing and easting direction. The kernel must also be normalized to sum to unity so that the average elevation of the convolved DSM is identical to that of the original DSM.

```
%%% Generate Convolution Kernel by integrating PSF

size_kernel=ceil(max(x_c_dist)/pix_size_dsm)*2+1; %calculate size of convolution
kernel

conv_ker=ones(size_kernel,size_kernel);
    x_vec=-pix_size_dsm*size_kernel/2:pix_size_dsm:pix_size_dsm*(size_kernel/2-1);
    y_vec=fliplr(x_vec);

for i= 1:size_kernel
    x_indx=(x_vec(i)<x_c_dist & x_c_dist<(x_vec(i)+pix_size_dsm));
    for j=1:size_kernel
        y_indx=(y_vec(j)+pix_size_dsm>y_c_dist & y_c_dist>y_vec(j));
        conv_ker(j,i)=sum(sum(PSF_tot_3d(y_indx,x_indx)))/sum(sum(PSF_tot_3d));
    end
end

%%%% Normalize convolution kernel to sum to 1
    conv_ker=conv_ker/sum(sum(conv_ker));
```

Afterwards, the kernel is convolved with the input DSM (task 3), blurring it based on the characteristics of the hyperspectral sensor PSF.

```
%% Convolve DSM by Convolution Kernel

DSM_conv=conv2(data.DataCube,conv_ker,'same');
```

The final lines of the function write the blurred DSM to a new ENVI standard file (task 4). This file is saved in the same location as the original DSM. The blurred DSM is named after the original DSM, with an appended "conv.dat".

```
%% Output DSM to ENVI File
Filename=[DSM_loc DSM_name '_conv'];
newhcube = assignData(data, ':',':',DSM_conv);
enviwrite(newhcube,Filename);
```

Below, we provide an example MATLAB code that can be used to call the MATLAB function and generate the blurred DSM.

```
%%% Define Input Parameters
flight_line_heading=156;
FOV_deg=34.21/180*pi;
pix_tot=1833;
alt=45;
speed=2.7;
it=9/1000;
FWHM_opt=1.01
DSM_loc='D:\Hyperspectral_Point_Cloud\methods_x\'
DSM_name='MB_DSM'

%%% Run Function
[DSM_conv,PSF_tot_3d,x_c_dist,y_c_dist] = DHPC_DSM_BLUR(flight_line_heading,...
FOV_deg,pix_tot,alt,speed,it,FWHM_opt,DSM_loc,DSM_name);
```

With the blurred DSM, the DHPC data fusion workflow can be readily implemented using pre-existing processing workflows. Although there is no explicit need to output the derived PSF, it is provided by the MATLAB function to quantify the spatial contribution of the objects/terrain within any pixel. Overall, the presented MATLAB function makes the implementation of the DHPC data fusion workflow approachable for end users and data providers.

7.2.5. Example Dataset

Here, we provide an example of the DHPC generated in Inamdar et al. (2021) from the Mer Bleue Peatland. Peatlands are important study areas due to their ability to sequester atmospheric carbon and mitigate the effects of climate change. The HSI data (see Table 7.3 for details) input into the DHPC data fusion workflow was collected by the μCASI-1920 hyperspectral imager (ITRES, Calagary, AB, Canada). The μCASI-1920 is a pushbroom imager that collects spectral information over 288 bands from 401 to 996 nm on a silicon-based focal plane array (Arroyo-Mora et al., 2019). The DSM (0.69 cm spatial resolution) used in the data fusion workflow was generated using a Structure-from-Motion Multiview Stereo (SfM-MVS) workflow from RGB photography collected by a Canon EOS 5D Mark III equipped with a Canon EF 24-70 mm f/2.8 L II USM lens (focal length of 24 mm). In our specific implementation, the radiometric correction (step 1) was completed with proprietary software developed by the sensor manufacturer while the atmospheric correction (step 2) was carried out in ATCOR4 (as described in Soffer et al. (2019)). Steps 3-4 were completed using the presented MATLAB function. The geometric correction (step 5) was completed using proprietary software developed by the sensor manufacturer. The results of the geometric correction are output to a ground coordinate look up table (GLU) that provides the easting, northing and averaged elevation of each pixel from the HSI data in its original sensor geometry. Similar outputs to the GLU are

provided by other geometric correction software such as PARGE (Schläpfer, 2018). To generate the final DHPC, we compiled the GLU and HSI data (radiometrically corrected and atmospherically compensated) into a single text file. In this process, the GLU and HSI data were first imported into MATLAB as three dimensional matrices. The dimensions of the HSI matrix were 2029 by 1833 by 288 (along track pixels by cross track pixels by spectral bands) that contained the spectral information from each pixel of the HSI data. The GLU matrix was imported as a 2029 by 1833 by 3 dimensional matrix that contained the positional information (northing, easting and averaged elevation) of each pixel from the HSI data calculated during the geometric correction. The HSI and GLU matrices were then concatenated into a single 2029 by 1833 by 291 dimensional matrix. The spatial dimensions of this matrix were then flattened, creating a 2029*1833 by 291 matrix. This matrix was exported as a comma delimited text file. Due to memory limitations, this matrix was written out 1833 rows at a time, generating 2029 text files that were then merged using the Microsoft Disk Operating System (MS-DOS) copy command to generate one text file. With the position and spectral information from each pixel of the original HSI data in a single text file, the DHPC was complete.

Table 7.3. Parameters for the hyperspectral imaging data acquired over the Mer Bleue Peatland (MBP) with the μ CASI-1920.

Parameter	MBP μCASI-1920 Data
Number of Cross Track Pixels	1833
Number of Along Track Pixels	2029
Sensor Field of View (°)	34.21
Nominal Flight Line Heading (° True North)	156
Nominal Altitude (m)	45
Nominal Speed (m/s)	2.7
Integration Time (ms)	9
Full width at half maximum of Optical Point Spread Function (pixels)	1.01

The radiometrically and atmospherically corrected μCASI-1920 imagery and the input DSM can be seen in **Figure 7.11A** and **Figure 7.11B**, respectively. The PSF of the μCASI-1920 data (**Figure 7.12**) was derived using the input parameters from **Table 7.3** with the provided MATLAB function. The MATLAB function also convolved the derived PSF with the input DSM, generating the blurred DSM (**Figure 7.11C**) required in the data fusion workflow. The full μCASI-1920 DHPC can be found at http://doi.org/ 10.5281/zenodo.4694950 (HPC_288band_xyz_final.txt). The DHPC is accompanied by a meta data file (HPC_288band_xyz_final_META.txt) that recorded important HSI data parameters such as data acquisition time, data acquisition date, sensor platform, spectral units, wavelength and full width at half maximum of each band, wavelength units, file type and map info. **Figure 7.11D** displays the RGB bands of the DHPC, viewing the point cloud from above. A video displaying the RGB bands of the DHPC can be seen in **Figure 7.11E** (Supplementary Video 1.mp4).

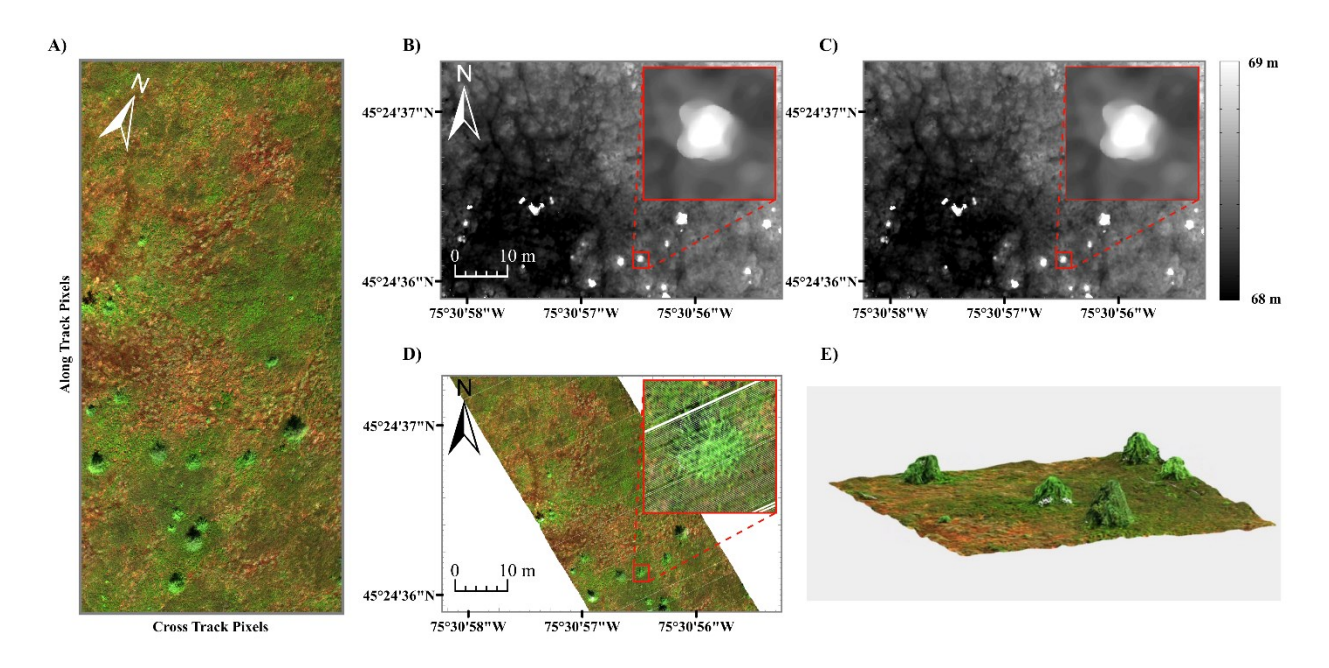


Figure 7.11. The data products used to generate the DHPC over the Mer Bleue Peatland. A) Radiometrically and atmospherically corrected Hyperspectral imaging data in raw sensor geometry from the μ CASI-1920 (R=639.6 nm, G=550.3 nm, B=459.0 nm, linearly stretched from a reflectance value of 0% to 12 % for display purposes). B) Original digital surface elevation model. C) Blurred digital surface model (linearly stretched from a elevation value of 68 m to 69 m). D) The Directly-Georeferenced Hyperspectral Point Cloud (DHPC) viewed from above (R=639.6 nm, G=550.3 nm, B=459.0 nm, linearly stretched from a reflectance value of 0% to 12 % for display purposes). E) A video of the DHPC in a 12 x 12 m region (R=639.6 nm, G=550.3 nm, B=459.0 nm, linearly stretched from a reflectance value of 0% to 12 % for display purposes). The video (Supplementary_Video_1.mp4) can be found in the supplemental material. The full DHPC (HPC 288band xyz final.txt) is also in the supplementary material.

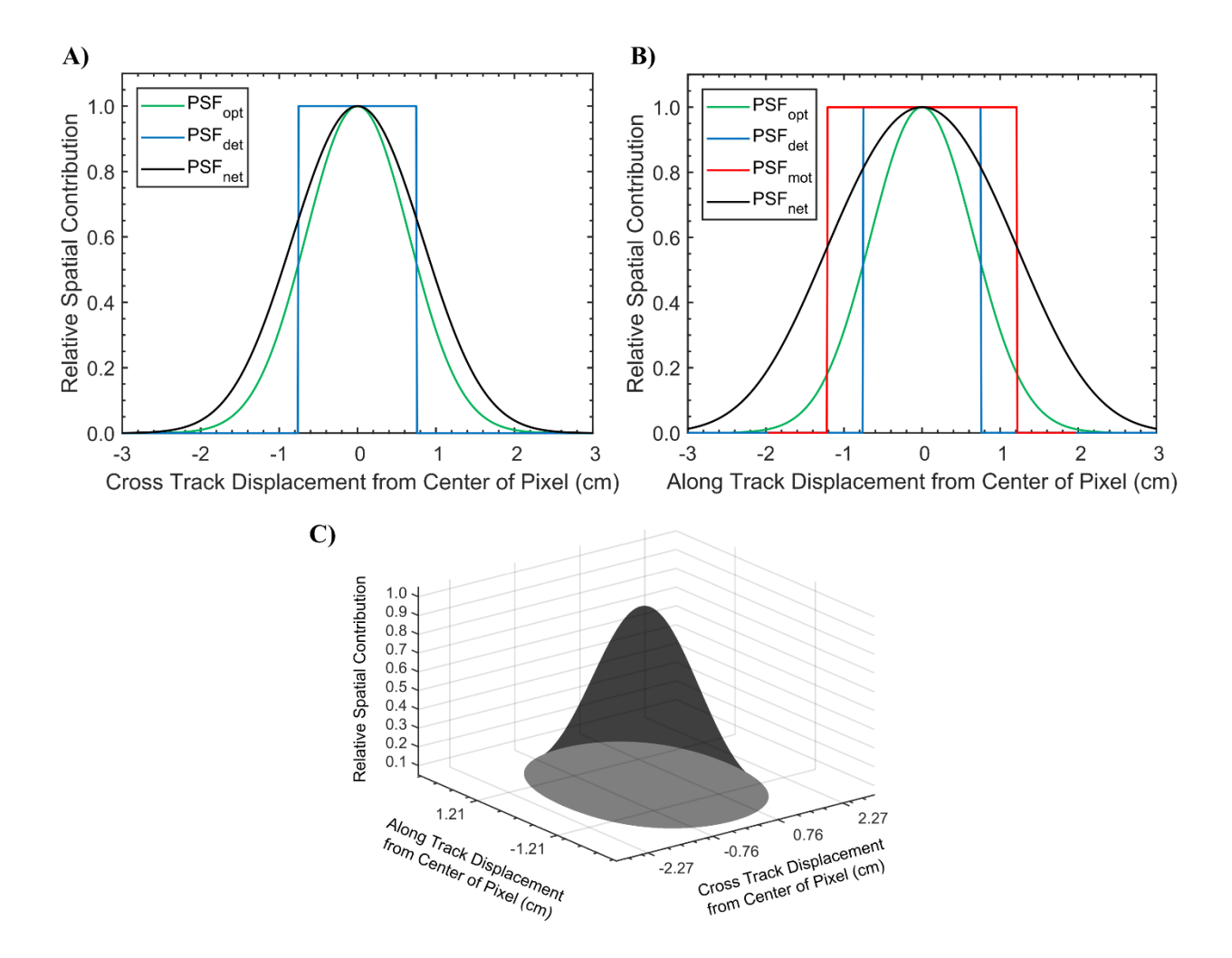


Figure 7.12. The point spread function (PSF) for the μ CASI-1920. Panel A displays the optical PSF (PSF_{opt}), detector PSF (PSF_{det}) and net PSF (PSF_{net}) in the cross track direction. The PSF_{net} is the convolution of the PSF_{opt} and the PSF_{det} in the cross track direction. Panel B displays the PSF_{opt}, PSF_{det}, motion PSF (PSF_{mot}) and PSF_{net} in the along track direction. The PSF_{net} is the convolution of the PSF_{mot}, PSF_{opt} and the PSF_{det} in the along track direction. Panel C displays the net PSF in both dimensions simultaneously.

For the purposes of site exploration, we also provide the DHPC in polygon file format (HPC_3band_xyz_shifted_final.ply in supplementary material). This file can be used to visualize the DHPC in VR and AR. It can be viewed in VR or AR at https://skfb.ly/onA6y. The polygon file format can only support three color channels. Furthermore, the variables encoded in the polygon file format must be representable as 32-bit float values. To generate the polygon file, the GLU and HSI data were first imported into MATLAB as three dimensional matrices as described above. The blue (459.0 nm), green (550.3 nm) and red (639.6 nm) bands of the HSI matrix were spectrally subset into a new 2029 by 1833 by 3 matrix. To ensure that the northing and easting

values could be represented as 32-bit float values, they were centered by subtracting the minimum northing and easting value, respectively. The new HSI and GLU matrices were then concatenated, flattened and exported as a comma delimited text file (as done when generating the full DHPC as a text file). This text file was then imported into CloudCompare Stereo for conversion to polygon file format. The Mer Bleue Peatland is an ideal area for site exploration via VR and AR as the ecosystem is generally fragile and difficult to access. The DHPC allows for widespread accessibility of the site via VR and AR, allowing users to study sections of the peatland in a repeatable and cost-efficient manner (Kalacska et al., 2021).

In Inamdar et al. (2021), the μ CASI-1920 data from Mer Bleue was used to classify the hummock- hollow microtopography across the peatland. The microtopography at Mer Bleue is important to study as it covaries with surface vegetation, hydrology and carbon uptake from the atmosphere (Malhotra et al., 2016). The additional elevational information provided by the DHPC led to an overall classification accuracy that was ~8% greater than the convention raster HSI datasets that contained no elevation data. This example shows the significance of the elevation information encoded in the DHPC.

7.2.6. References

Arroyo-Mora, J.P., Kalacska, M., Inamdar, D., Soffer, R., Lucanus, O., Gorman, J., Naprstek, T., Schaaf, E.S., Ifimov, G., & Elmer, K. (2019). Implementation of a UAV–hyperspectral pushbroom imager for ecological monitoring. *Drones*, *3*, 12

Eismann, M.T. (2012). Hyperspectral Remote Sensing. In: *Hyperspectral Remote Sensing*. Bellingham: SPIE

- Goetz, A.F.H. (2009). Three decades of hyperspectral remote sensing of the Earth: A personal view. *Remote Sensing of Environment*, 113, S5-S16
- Inamdar, D., Kalacska, M., Arroyo-Mora, J.P., & Leblanc, G. (2021). The directly-georeferenced hyperspectral point cloud: Preserving the integrity of hyperspectral imaging data. *Frontiers in Remote Sensing*, 2, 675323
- Inamdar, D., Kalacska, M., Leblanc, G., & Arroyo-Mora, J.P. (2020). Characterizing and mitigating sensor generated spatial correlations in airborne hyperspectral imaging data. *Remote Sensing*, 12, 641
- Kalacska, M., Arroyo-Mora, J.P., & Lucanus, O. (2021). Comparing UAS LiDAR and structure-from-motion photogrammetry for peatland mapping and virtual reality (VT) visualization. *Drones*, *5*, 36
- Le Mouélic, S., Enguehard, P., Schmitt, H.H., Caravaca, G., Seignovert, B., Mangold, N., Combe, J.-P., & Civet, F. (2020). Investigating lunar boulders at the Apollo 17 landing site using photogrammetry and virtual reality. *Remote Sensing*, *12*, 1900

- Liberatore, M.J., & Wagner, W.P. (2021). Virtual, mixed, and augmented reality: a systematic review for immersive systems research. *Virtual Reality*
- Malhotra, A., Roulet, N.T., Wilson, P., Giroux-Bougard, X., & Harris, L.I. (2016). Ecohydrological feedbacks in peatlands: an empirical test of the relationship among vegetation, microtopography and water table. *Ecohydrology*, *9*, 1346-1357
- Müller, R., Lehner, M., Müller, R., Reinartz, P., Schroeder, M., & Vollmer, B. (2002). A program for direct georeferencing of airborne and spaceborne line scanner images. In: *ISPRS Commission I Symposium; Integrating Remote Sensing at the Global, Regional and Local Scale* (pp. 148-153). Graz
- Schläpfer, D. (2018). Parge user manual, version 3.4. In: *Orthorectification for Airborne Scanner Data*: ReSe Applications LLC
- Shlien, S. (1979). Geometric correction, registration, and resampling of landsat imagery. *Canadian Journal of Remote Sensing*, *5*, 74-89
- Smith, A.R. (1995). A pixel is not a little square, a pixel is not a little square, a pixel is not a little square! *Microsoft Computer Graphics, Technical Memo*, 6
- Soffer, R.J., Ifimov, G., Arroyo-Mora, J.P., & Kalacska, M. (2019). Validation of airborne hyperspectral imagery from laboratory panel characterization to image quality assessment: Implications for an arctic peatland surrogate simulation site. *Canadian Journal of Remote Sensing*, 45, 476-508
- Vane, G., Goetz, A.F., & Wellman, J.B. (1984). Airborne imaging spectrometer: A new tool for remote sensing. *IEEE Transactions on Geoscience and Remote Sensing*, *6*, 546-549
- Vreys, K., Iordache, M.-D., Biesemans, J., & Meuleman, K. (2016). Geometric correction of apex hyperspectral data. *Miscellanea Geographica*, 20, 11-15
- Wilkinson, G. (1996). A review of current issues in the integration of GIS and remote sensing data. *International Journal of Geographical Information Science*, 10, 85-101
- Warren, M.A., Taylor, B.H., Grant, M.G., & Shutler, J.D. (2014). Data processing of remotely sensed airborne hyperspectral data using the airborne processing library (apl): Geocorrection algorithm descriptions and spatial accuracy assessment. *Computers & Geosciences*, 64, 24-34

7.2.7. Author Contribution

Conceptualization, D.I., M.K., methodology, D.I., M.K, G.L. and J.P.A.-M.; validation, D.I.; formal analysis, D.I.; investigation, D.I.; resources, M.K., G.L, J.P.A.-M.; data curation, D.I., M.K., G.L. and J.P.A.-M.; writing—original draft preparation, D.I.; writing—review and editing, D.I., M.K., G.L. and J.P.A.-M.; visualization, D.I.

7.2.8. Acknowledgements

This work was funded by the Natural Sciences and Engineering Research Council of Canada (NSERC), the Fonds de Recherche du Québec – Nature et Technologies (FQRNT), the Canadian Airborne Biodiversity Observatory (CABO), the Lorne Trottier Fellowship and the Dr. and Mrs.

Milton Leong Fellowship in Science. The authors would like to thank Dr. Stephen Achal (Pi4Lab) for information regarding the sensor point spread functions and Mr. Raymond Soffer for discussions about the sensor characteristics. The authors further thank the two anonymous reviewers whose comments improved the manuscript.

7.2.9. Supplementary Material

The supplementary material associated with this chapter can be found in the online version of the published manuscript at doi: https://doi.org/10.1016/j.mex.2021.101429

8. Reference List

Aasen, H., Burkart, A., Bolten, A., & Bareth, G. (2015). Generating 3D hyperspectral information with lightweight UAV snapshot cameras for vegetation monitoring: From camera calibration to quality assurance. *ISPRS Journal of Photogrammetry and Remote Sensing*, 108, 245-259

Aasen, H., Honkavaara, E., Lucieer, A., & Zarco-Tejada, P.J. (2018). Quantitative remote sensing at ultra-high resolution with UAV spectroscopy: a review of sensor technology, measurement procedures, and data correction workflows. *Remote Sensing*, 10, 1091

Alcantara, C., Kuemmerle, T., Prishchepov, A.V., & Radeloff, V.C. (2012). Mapping abandoned agriculture with multi-temporal MODIS satellite data. *Remote sensing of environment*, 124, 334-347

Alonso, K., Bachmann, M., Burch, K., Carmona, E., Cerra, D., de los Reyes, R., Dietrich, D., Heiden, U., Hölderlin, A., Ickes, J., Knodt, U., Krutz, D., Lester, H., Müller, R., Pagnutti, M., Reinartz, P., Richter, R., Ryan, R., Sebastian, I., & Tegler, M. (2019). Data products, quality and validation of the DLR Earth Sensing Imaging Spectrometer (DESIS). *Sensors*, 19, 4471

Aneece, I., & Thenkabail, P. (2018). Accuracies achieved in classifying five leading world crop types and their growth stages using optimal Earth Observing-1 Hyperion hyperspectral narrowbands on Google Earth Engine. *Remote Sensing*, 10, 2027

Arif, F., & Akbar, M. (2005). Resampling air borne sensed data using bilinear interpolation algorithm. In: Proceedings of the 2005 IEEE International Conference on Mechatronics (pp. 62-65), Taipei: IEEE

Arroyo-Mora, J., Kalacska, M., Soffer, R., Moore, T., Roulet, N., Juutinen, S., Ifimov, G., Leblanc, G., & Inamdar, D. (2018a). Airborne hyperspectral evaluation of maximum gross photosynthesis, gravimetric water content, and CO₂ uptake efficiency of the Mer Bleue ombrotrophic peatland. *Remote Sensing*, 10, 565-285

Arroyo-Mora, J.P., Kalacska, M., Soffer, R., Ifimov, G., Leblanc, G., Schaaf, E.S., & Lucanus, O. (2018b). Evaluation of phenospectral dynamics with Sentinel-2A using a bottom-up approach in a northern ombrotrophic peatland. *Remote Sensing of Environment*, 216, 544-560

Arroyo-Mora, J.P., Kalacska, M., Inamdar, D., Soffer, R., Lucanus, O., Gorman, J., Naprstek, T., Schaaf, E.S., Ifimov, G., & Elmer, K. (2019). Implementation of a UAV–hyperspectral pushbroom imager for ecological monitoring. *Drones*, *3*, 12

- Arroyo-Mora, J.P., Kalacska, M., Løke, T., Schläpfer, D., Coops, N.C., Lucanus, O., & Leblanc, G. (2021). Assessing the impact of illumination on UAV pushbroom hyperspectral imagery collected under various cloud cover conditions. *Remote Sensing of Environment, 258*, 112396
- Asmat, A., Milton, E.J., & Atkinson, P.M. (2011). Empirical correction of multiple flightline hyperspectral aerial image mosaics. *Remote Sensing of Environment*, 115, 2664-2673
- Asner, G.P., & Martin, R.E. (2016). Spectranomics: Emerging science and conservation opportunities at the interface of biodiversity and remote sensing. *Global Ecology and Conservation*, 8, 212-219
- Asner, G.P., Martin, R.E., Knapp, D.E., Tupayachi, R., Anderson, C.B., Sinca, F., Vaughn, N.R., & Llactayo, W. (2017). Airborne laser-guided imaging spectroscopy to map forest trait diversity and guide conservation. *Science*, 355, 385-389
- Babey, S., & Anger, C. (1989). A Compact Airborne Spectrographic Imager (CASI). In: *Proceedings of the IGARSS '89 Quantitative Remote Sensing: An Economic Tool for the Nineties* (pp. 1028-1031)
- Babey, S., & Anger, C. (1993). Compact Airborne Spectrographic Imager (CASI): A progress review. In: Proceedings of the Society of Photo-Optical Instrumentation Engineers, 1937 (pp. 152-163): SPIE
- Barbieux, K., Constantin, D., & Merminod, B. (2016). Correction of airborne pushbroom images orientation using bundle adjustment of frame images. ISPRS International Archives of the Photogrammetry, Remote Sensing and Spatial Information Sciences, XLI-B3, 813-818
- Barsi, J., & Rocchio, L. (2020). The intervening atmosphere: tracing the provenance of a favorite Landsat infographic: NASA https://landsat.gsfc.nasa.gov/article/the-intervening-atmosphere-tracing-the-provenance-of-a-favorite-landsat-infographic/
- Beekhuizen, J., Heuvelink, G.B.M., Biesemans, J., & Reusen, I. (2011). Effect of dem uncertainty on the positional accuracy of airborne imagery. IEEE Transactions on Geoscience and Remote Sensing, 49, 1567-1577
- Belyea, L.R., & Malmer, N. (2004). Carbon sequestration in peatland: patterns and mechanisms of response to climate change. Global Change Biology, 10, 1043-1052
- Bergen, K.M., Brown, D.G., Rutherford, J.F., & Gustafson, E.J. (2005). Change detection with heterogeneous data using ecoregional stratification, statistical summaries and a land allocation algorithm. Remote Sensing of Environment, 97, 434-446
- Berk, A., Anderson, G.P., Bernstein, L.S., Acharya, P.K., Dothe, H., Matthew, M.W., Adler-Golden, S.M., Chetwynd Jr, J.H., Richtsmeier, S.C., & Pukall, B. (1999). MODTRAN4 radiative transfer modeling for atmospheric correction. In: *Proceedings of the Optical Spectroscopic Techniques and instrumentation for atmospheric and space research III* (pp. 348-353): International Society for Optics and Photonics
- Bernstein, L., Jin, X., Gregor, B., & Adler-Golden, S. (2012). Quick atmospheric correction code: algorithm description and recent upgrades. *Optical Engineering*, *51*, 111719

- Bioucas-Dias, J.M., Plaza, A., Camps-Valls, G., Scheunders, P., Nasrabadi, N., & Chanussot, J. (2013). Hyperspectral remote sensing data analysis and future challenges. *IEEE Geoscience and Remote Sensing Magazine*, 1, 6-36
- Booysen, R., Lorenz, S., Thiele, S.T., Fuchsloch, W.C., Marais, T., Nex, P.A.M., & Gloaguen, R. (2022). Accurate hyperspectral imaging of mineralised outcrops: An example from lithium-bearing pegmatites at Uis, Namibia. *Remote Sensing of Environment*, 269, 112790
- Brell, M., Rogass, C., Segl, K., Bookhagen, B., & Guanter, L. (2016). Improving sensor fusion: A parametric method for the geometric coalignment of airborne hyperspectral and LiDAR data. *IEEE Transactions on Geoscience and Remote Sensing*, *54*, 3460-3474
- Brell, M., Segl, K., Guanter, L., & Bookhagen, B. (2017). Hyperspectral and LiDAR intensity data fusion: A framework for the rigorous correction of illumination, anisotropic effects, and cross calibration. *IEEE Transactions on Geoscience and Remote Sensing*, 55, 2799-2810
- Brell, M., Segl, K., Guanter, L., & Bookhagen, B. (2019). 3D hyperspectral point cloud generation: Fusing airborne laser scanning and hyperspectral imaging sensors for improved object-based information extraction. *ISPRS Journal of Photogrammetry and Remote Sensing*, 149, 200-214
- Brunn, A., Fischer, C., Dittmann, C., & Richter, R. (2003). Quality assessment, atmospheric and geometric correction of airborne hyperspectral Hymap data. In: *Proceedings of the 3rd EARSeL Workshop on Imaging Spectroscopy* (pp. 72-81): *EARSeL*
- Buckley, S.J., Kurz, T.H., Howell, J.A., & Schneider, D. (2013). Terrestrial LiDAR and hyperspectral data fusion products for geological outcrop analysis. *Computers & Geosciences*, 54, 249-258
- Bugya, T., & Farkas, G. (2018). An Alternative Raster Display Model. In: *Proceeding of the 4th International Conference on Geographical Information System Theory, Application and Management (GISTAM)* (pp. 262-268)
- Calders, K., Adams, J., Armston, J., Bartholomeus, H., Bauwens, S., Bentley, L.P., Chave, J., Danson, F.M., Demol, M., Disney, M., Gaulton, R., Krishna Moorthy, S.M., Levick, S.R., Saarinen, N., Schaaf, C., Stovall, A., Terryn, L., Wilkes, P., & Verbeeck, H. (2020). Terrestrial laser scanning in forest ecology: Expanding the horizon. *Remote Sensing of Environment, 251*, 112102
- Cao, J., Liu, K., Liu, L., Zhu, Y., Li, J., & He, Z. (2018). Identifying mangrove species using field close-range snapshot hyperspectral imaging and machine-learning techniques. *Remote Sensing*, 10, 2047
- Carlson, K.M., Asner, G.P., Hughes, R.F., Ostertag, R., & Martin, R.E. (2007). Hyperspectral remote sensing of canopy biodiversity in Hawaiian lowland rainforests. *Ecosystems*, 10, 536-549
- Carver, S.J., & Brunsdon, C.F. (1994). Vector to raster conversion error and feature complexity: an empirical study using simulated data. *International Journal of Geographical Information Systems*, 8, 261-270

- Cavender-Bares, J., Schneider, F.D., Santos, M.J., Armstrong, A., Carnaval, A., Dahlin, K.M., Fatoyinbo, L., Hurtt, G.C., Schimel, D., Townsend, P.A., Ustin, S.L., Wang, Z., & Wilson, A.M. (2022). Integrating remote sensing with ecology and evolution to advance biodiversity conservation. *Nature Ecology & Evolution*, *6*, 506-519
- Chandra, S.N.R., Christopherson, J., Casey, K.A., Lawson, J., & Sampath, A. (2022). 2022 *Joint agency commercial imagery evaluation—remote sensing satellite compendium*. Reston, VA: US Geological Survey
- Chapman, J.W., Thompson, D.R., Helmlinger, M.C., Bue, B.D., Green, R.O., Eastwood, M.L., Geier, S., Olson-Duvall, W., & Lundeen, S.R. (2019). Spectral and radiometric calibration of the Next Generation Airborne Visible Infrared Spectrometer (AVIRIS-NG). *Remote Sensing*, 11, 2129
- Charmisha, K., Sowmya, V., & Soman, K. (2018). Dimensionally reduced features for hyperspectral image classification using deep learning. In, *International Conference on Communications and Cyber Physical Engineering 2018* (pp. 171-179): Springer
- Chaudhuri, S., Velmurugan, R., & Rameshan, R. (2014). Chapter 2 Mathematical background. In: Blind Image Deconvolution: Methods and Convergence: Springer International Publishing
- Chowdhury, A., & Alspector, J. (2003). Data duplication: an imbalance problem? In: ICML'2003 Workshop on Learning from Imbalanced Data Sets (II) (pp. 1-10). Washington, DC: ICML
- Clark, P.E., & Rilee, M.L. (2010). Remote sensing tools for exploration: observing and interpreting the electromagnetic spectrum: Springer Science & Business Media
- Clark, R.N., & King, T.V.V. (1998). Causes of spurious features in spectral reflectance data. In: *Proceedings of the 3rd Airborne Imaging Spectrometer Data Analysis Workshop* (pp. 132-137). Pasadena, California: Jet Propulsion Laboratory
- Cline, J.D., Wilson, J.A., Feher, S.H., & Ward, G.D. (1987). Airborne flight planning and information system.
 - CloudCompare (2022). CloudCompare (version 2.12) [GPL software].
- Cloutis, E.A. (1996). Review article hyperspectral geological remote sensing: evaluation of analytical techniques. *International Journal of Remote Sensing*, 17, 2215-2242
- Cocks, T., Jenssen, R., Stewart, A., Wilson, I., & Shields, T. (1998). The HyMapTM airborne hyperspectral sensor: The system, calibration and performance. In: *Proceedings of the 1st EARSeL workshop on Imaging Spectroscopy* (pp. 37-42): EARSeL
- Conel, J.E., Green, R.O., Vane, G., Bruegge, C.J., Alley, R.E., & Curtiss, B.J. (1987). AIS-2 radiometry and a comparison of methods for the recovery of ground reflectance. In: *Proceedings of the 3rd Airborne Imaging Spectrometer Data Analysis Workshop* (pp. 18-47). Pasadena, California: Jet Propulsion Laboratory
- Congalton, R.G. (1997). Exploring and evaluating the consequences of vector-to-raster and raster-to-vector conversion. *Photogrammetric engineering and remote sensing*, 63, 425-434

- Cooley, T., Anderson, G.P., Felde, G.W., Hoke, M.L., Ratkowski, A.J., Chetwynd, J.H., Gardner, J.A., Adler-Golden, S.M., Matthew, M.W., Berk, A., Bernstein, L.S., Acharya, P.K., Miller, D., & Lewis, P. (2002). FLAASH, a MODTRAN4-based atmospheric correction algorithm, its application and validation. In: 2002 *IEEE International Geoscience and Remote Sensing Symposium* (pp. 1414-1418). Toronto: IEEE Press
- Cornish, N. (2014). Evaluating Signal-to-noise Ratios in Hyperspectral Imagery Summed During versus Post Acquisition. In: McGill University Libraries
- Couclelis, H. (1992). People manipulate objects (but cultivate fields): Beyond the raster-vector debate in GIS. In: A.U. Frank, I. Campari, & U. Formentini (Eds.), *Theories and Methods of Spatio-Temporal Reasoning in Geographic Space* (pp. 65-77). Berlin, Heidelberg: Springer
- Cox, A.B., & Gifford, F. (1997). An overview to geographic information systems. *The Journal of Academic Librarianship*, 23, 449-461
- Curran, P.J. (1989). Remote sensing of foliar chemistry. *Remote Sensing of Environment, 30*, 271-278
- Curran, P.J., & Dungan, J.L. (1989). Estimation of signal-to-noise: a new procedure applied to AVIRIS data. *IEEE Transactions on Geoscience and Remote Sensing*, *27*, 620-628
- Da, R. (1997). Analysis and test results of AIMS GPS/INS system. In: *Proceedings of the 10th International Technical Meeting of the Satellite Division of The Institute of Navigation (ION GPS 1997)* (pp. 771-780)
- Dadon, A., Ben-Dor, E., & Karnieli, A. (2010). Use of derivative calculations and minimum noise fraction transform for detecting and correcting the spectral curvature effect (smile) in Hyperion images. *IEEE Transactions on Geoscience and Remote Sensing*, 48, 2603-2612
- Dale, L.M., Thewis, A., Boudry, C., Rotar, I., Dardenne, P., Baeten, V., & Pierna, J.A.F. (2013). Hyperspectral imaging applications in agriculture and agro-food product quality and safety control: a review. *Applied Spectroscopy Reviews*, 48, 142-159
- Davis, C., Bowles, J., Leathers, R., Korwan, D., Downes, T.V., Snyder, W., Rhea, W., Chen, W., Fisher, J., Bissett, P., & Reisse, R.A. (2002). Ocean PHILLS hyperspectral imager: design, characterization, and calibration. *Optics Express*, 10, 210-221
- de Miguel, E., Fernández-Renau, A., Prado, E., Jiménez, M., de la Cámara, Ó.G., Linés, C., Gómez, J.A., Martín, A.I., & Muñoz, F. (2014). The processing of CASI-1500I data at INTA PAF. In: *34th Annual EARSeL Symposium 2014* (pp. 30-37), Warsaw: EARSeL
- Dennison, W.C., Orth, R.J., Moore, K.A., Stevenson, J.C., Carter, V., Kollar, S., Bergstrom, P.W., & Batiuk, R.A. (1993). Assessing Water Quality with Submersed Aquatic Vegetation. *BioScience*, 43, 86-94
- Dhar, N.K., Dat, R., & Sood, A.K. (2013). Advances in infrared detector array technology. *Optoelectronics-Advanced Materials and Devices*, 7, 149-188
- Disney, M.I., Boni Vicari, M., Burt, A., Calders, K., Lewis, S.L., Raumonen, P., & Wilkes, P. (2018). Weighing trees with lasers: advances, challenges and opportunities. *Interface Focus*, 8, 20170048

- Duveiller, G., Baret, F., & Defourny, P. (2011). Crop specific green area index retrieval from MODIS data at regional scale by controlling pixel-target adequacy. *Remote Sensing of Environment*, 115, 2686-2701
- Eismann, M.T. (2012). Hyperspectral remote sensing. In: *Hyperspectral Remote Sensing*. Bellingham: SPIE
- Elaksher, A.F. (2008). Fusion of hyperspectral images and LiDAR-based DEMs for coastal mapping. *Optics and Lasers in Engineering*, 46, 493-498
 - Emlid (2022). Single-band VS multi-band. In: Emlid Docs
- Eppinga, M.B., Rietkerk, M., Borren, W., Lapshina, E.D., Bleuten, W., & Wassen, M.J. (2008). Regular surface patterning of peatlands: confronting theory with field data. *Ecosystems*, 11, 520-536
- Famiglietti, N.A., Cecere, G., Grasso, C., Memmolo, A., & Vicari, A. (2021). A test on the potential of a low cost unmanned aerial vehicle RTK/PPK solution for precision positioning. *Sensors*, *21*, 3882
- Fang, H., Luo, C., Zhou, G., & Wang, X. (2017). Hyperspectral image deconvolution with a spectral-spatial total variation regularization. *Canadian Journal of Remote Sensing*, 43, 384-395
- Farrell, J.A. (2008). *Aided Navigation*. New York, USA: McGraw-Hill Professional Publishing
- Fisher, P. (1997). The pixel: A snare and a delusion. *International Journal of Remote Sensing*, 18, 679-685
- Folkman, M.A., Pearlman, J., Liao, L.B., & Jarecke, P.J. (2001). EO-1/Hyperion hyperspectral imager design, development, characterization, and calibration. In: *Hyperspectral Remote Sensing of the Land and Atmosphere* (pp. 40-51): International Society for Optics and Photonics
- Fourqurean, J.W., Duarte, C.M., Kennedy, H., Marbà, N., Holmer, M., Mateo, M.A., Apostolaki, E.T., Kendrick, G.A., Krause-Jensen, D., McGlathery, K.J., & Serrano, O. (2012). Seagrass ecosystems as a globally significant carbon stock. *Nature Geoscience*, *5*, 505-509
- Galbraith, A.E., Theiler, J.P., & Bender, S.C. (2003). Resampling methods for the MTI coregistration product. In: *Algorithms and Technologies for Multispectral, Hyperspectral, and Ultraspectral Imagery IX* (pp. 283-293). Orlando: International Society for Optics and Photonics
- Gao, B.-C., Davis, C.O., & Goetz, A. (2006). A Review of Atmospheric Correction Techniques for Hyperspectral Remote Sensing of Land Surfaces and Ocean Color. In: 2006 IEEE International Symposium on Geosciences and remote sensing (pp. 1979-1981): IEEE
- Gao, B.-C., Heidebrecht, K.B., & Goetz, A.F.H. (1993). Derivation of scaled surface reflectances from AVIRIS data. *Remote Sensing of Environment*, 44, 165-178
- Gao, B.-C., Montes, M.J., Davis, C.O., & Goetz, A.F.H. (2009). Atmospheric correction algorithms for hyperspectral remote sensing data of land and ocean. *Remote Sensing of Environment*, 113, S17-S24
- Gao, X., Liu, Y., Li, T., & Wu, D. (2017). High precision DEM generation algorithm based on InSAR multi-look iteration. *Remote Sensing*, *9*, 741

- Gates, D.M., Keegan, H.J., Schleter, J.C., & Weidner, V.R. (1965). Spectral properties of plants. *Applied Optics*, 4, 11-20
- Guanter, L., Kaufmann, H., Segl, K., Foerster, S., Rogass, C., Chabrillat, S., Kuester, T., Hollstein, A., Rossner, G., Chlebek, C., Straif, C., Fischer, S., Schrader, S., Storch, T., Heiden, U., Mueller, A., Bachmann, M., Mühle, H., Müller, R., Habermeyer, M., Ohndorf, A., Hill, J., Buddenbaum, H., Hostert, P., Van der Linden, S., Leitão, P.J., Rabe, A., Doerffer, R., Krasemann, H., Xi, H., Mauser, W., Hank, T., Locherer, M., Rast, M., Staenz, K., & Sang, B. (2015). The ENMAP spaceborne imaging spectroscopy mission for Earth observation. *Remote Sensing*, *7*, 8830-8857
- Gill, S.J., Biging, G.S., & Murphy, E.C. (2000). Modeling conifer tree crown radius and estimating canopy cover. *Forest Ecology and Management*, 126, 405-416
- Goetz, A.F.H. (2009). Three decades of hyperspectral remote sensing of the Earth: A personal view. *Remote Sensing of Environment*, 113, S5-S16
- Goetz, A.F.H., Vane, G., Solomon, J.E., & Rock, B.N. (1985). Imaging spectrometry for Earth remote sensing. *Science*, 228, 1147-1153
- Gomez-Chova, L., Zurita-Milla, R., Alonso, L., Amoros-Lopez, J., Guanter, L., & Camps-Valls, G. (2011). Gridding Artifacts on Medium-Resolution Satellite Image Time Series: MERIS Case Study. *IEEE Transactions on Geoscience and Remote Sensing*, 49, 2601-2611
- Gonsamo, A., & Chen, J.M. (2013). Spectral response function comparability among 21 satellite sensors for vegetation monitoring. *IEEE Transactions on Geoscience and Remote Sensing*, 51, 1319-1335
 - Goodchild, M.F. (2011). Scale in GIS: An overview. Geomorphology, 130, 5-9
- Gorham, E. (1991). Northern Peatlands: Role in the Carbon Cycle and Probable Responses to Climatic Warming. *Ecological Applications*, *1*, 182-195
- Goryl, P. (2018). Workshop objectives. In, LPVE 2018: Land Product Validation and Evolution Workshop. Frascati, Italy: ESA
- Green, R.O., Eastwood, M.L., Sarture, C.M., Chrien, T.G., Aronsson, M., Chippendale, B.J., Faust, J.A., Pavri, B.E., Chovit, C.J., & Solis, M. (1998). Imaging spectroscopy and the airborne visible/infrared imaging spectrometer (AVIRIS). *Remote Sensing of Environment*, 65, 227-248
- Guanter, L., Kaufmann, H., Segl, K., Foerster, S., Rogass, C., Chabrillat, S., Kuester, T., Hollstein, A., Rossner, G., Chlebek, C., Straif, C., Fischer, S., Schrader, S., Storch, T., Heiden, U., Mueller, A., Bachmann, M., Mühle, H., Müller, R., Habermeyer, M., Ohndorf, A., Hill, J., Buddenbaum, H., Hostert, P., Van der Linden, S., Leitão, P.J., Rabe, A., Doerffer, R., Krasemann, H., Xi, H., Mauser, W., Hank, T., Locherer, M., Rast, M., Staenz, K., & Sang, B. (2015). The EnMAP spaceborne imaging spectroscopy mission for Earth observation. *Remote Sensing*, 7, 8830-8857
- Guanter, L., Richter, R., & Moreno, J. (2006). Spectral calibration of hyperspectral imagery using atmospheric absorption features. *Applied Optics*, 45, 2360-2370
- Hagen, N.A., & Kudenov, M.W. (2013). Review of snapshot spectral imaging technologies. *Optical Engineering*, *52*, 1-23, 23

- Hakala, T., Suomalainen, J., Kaasalainen, S., & Chen, Y. (2012). Full waveform hyperspectral LiDAR for terrestrial laser scanning. *Optics Express*, 20, 7119-7127
- Hamlin, L., Green, R.O., Mouroulis, P., Eastwood, M., Wilson, D., Dudik, M., & Paine, C. (2011). Imaging spectrometer science measurements for terrestrial ecology: AVIRIS and new developments. In: *2011 Aerospace Conference* (pp. 1-7)
- Han, T., Goodenough, D., Dyk, A., & Love, J. (2002). Detection and correction of abnormal pixels in Hyperion images. In: *Proceedings of the IEEE International Geoscience and Remote Sensing Symposium (IGARSS'02)*, 3 (pp. 1327-1330): IEEE
- Harris, J.R., Rogge, D., Hitchcock, R., Ijewliw, O., & Wright, D. (2005). Mapping lithology in Canada's Arctic: application of hyperspectral data using the minimum noise fraction transformation and matched filtering. *Canadian Journal of Earth Sciences*, 42, 2173-2193
- Heiskanen, J. (2006). Tree cover and height estimation in the Fennoscandian tundra-taiga transition zone using multiangular MISR data. *Remote Sensing of Environment*, 103, 97-114
- Henrot, S., Soussen, C., & Brie, D. (2013). Fast positive deconvolution of hyperspectral images. *IEEE Transactions on Image Processing*, 22, 828-833
- Holt, J., Durell, C., Russell, B., Conran, D., Arnold, W., & Schiller, S. (2021). *FLARE network performance: automated on-demand calibration for space, airborne and UAV assets*. SPIE
- Hong, D., Gao, L., Yokoya, N., Yao, J., Chanussot, J., Du, Q., & Zhang, B. (2020). More diverse means better: Multimodal deep learning meets remote-sensing imagery classification. *IEEE Transactions on Geoscience and Remote Sensing*, 1-15
- Hörig, B., Kühn, F., Oschütz, F., & Lehmann, F. (2001). HyMap hyperspectral remote sensing to detect hydrocarbons. *International Journal of Remote Sensing*, 22, 1413-1422
- Huang, C., Townshend, J.R.G., Liang, S., Kalluri, S.N.V., & DeFries, R.S. (2002). Impact of sensor's point spread function on land cover characterization: assessment and deconvolution. *Remote Sensing of Environment*, 80, 203-212
- Hug, C., Krzystek, P., & Fuchs, W. (2004). Advanced lidar data processing with LasTools. In, *XXth ISPRS Congress* (pp. 12-23), Istanbul, Turkey
- Ibrahim, A., Franz, B., Ahmad, Z., Healy, R., Knobelspiesse, K., Gao, B.-C., Proctor, C., & Zhai, P.-W. (2018). Atmospheric correction for hyperspectral ocean color retrieval with application to the Hyperspectral Imager for the Coastal Ocean (HICO). *Remote Sensing of Environment*, 204, 60-75
- Immirzi, C., Maltby, E., & Clymo, R.S. (1992). The global status of peatlands and their role in carbon cycling. A report for Friends of the Earth by the Wetland Ecosystem Research Group, Department of Geography, University of Exeter. Oryx, 27(2), 127
- Inamdar, D., Kalacska, M., Arroyo-Mora, J.P., & Leblanc, G. (2021). The Directly-Georeferenced Hyperspectral Point Cloud: Preserving the Integrity of Hyperspectral Imaging Data. *Frontiers in Remote Sensing*, 2675323

- Inamdar, D., Kalacska, M., Leblanc, G., & Arroyo-Mora, J.P. (2020). Characterizing and Mitigating Sensor Generated Spatial Correlations in Airborne Hyperspectral Imaging Data. *Remote Sensing*, 12, 641
- Inamdar, D., Rowan, G.S.L., Kalacska, M., & Arroyo-Mora, J.P. (2022). Water column compensation workflow for hyperspectral imaging data. *MethodsX*, *9*, 101601
- Jackett, C., Turner, P., Lovell, J., & Williams, R. (2011). Deconvolution of MODIS imagery using multiscale maximum entropy. *Remote Sensing Letters*, 2, 179-187
- Jakubowski, M.K., Li, W., Guo, Q., & Kelly, M. (2013). Delineating Individual Trees from Lidar Data: A Comparison of Vector- and Raster-based Segmentation Approaches. *Remote Sensing*, *5*, 4163-4186
- Jemec, J., Pernuš, F., Likar, B., & Bürmen, M. (2017). 2D Sub-pixel Point Spread Function Measurement Using a Virtual Point-Like Source. *International Journal of Computer Vision*, 121, 391-402
- Jia, J., Wang, Y., Chen, J., Guo, R., Shu, R., & Wang, J. (2020). Status and application of advanced airborne hyperspectral imaging technology: A review. *Infrared Physics & Technology*, 104, 103115
- Kalacska, M., Arroyo-Mora, J., Soffer, R., Roulet, N., Moore, T., Humphreys, E., Leblanc, G., Lucanus, O., & Inamdar, D. (2018). Estimating Peatland Water Table Depth and Net Ecosystem Exchange: A Comparison between Satellite and Airborne Imagery. *Remote Sensing*, 10, 687
- Kalacska, M., Arroyo-Mora, J.P., & Lucanus, O. (2021). Comparing UAS LiDAR and Structure-from-Motion Photogrammetry for Peatland Mapping and Virtual Reality (VR) Visualization. *Drones*, 5, 36
- Kalacska, M., Arroyo-Mora, J.P., Soffer, R., & Leblanc, G. (2016). Quality control assessment of the Mission Airborne Carbon 13 (MAC-13) hyperspectral imagery from Costa Rica. *Canadian Journal of Remote Sensing*, 42, 85-105
- Kalacska, M., & Bell, L. (2006). Remote sensing as a tool for the detection of clandestine mass graves. *Canadian Society of Forensic Science Journal*, 39, 1-13
- Kalacska, M.E., Bell, L.S., Sanchez-Azofeifa, G.A., & Caelli, T. (2009). The application of remote sensing for detecting mass graves: An experimental animal case study from Costa Rica. *Journal of Forensic Sciences*, *54*, 159-166
- Kamoske, A.G., Dahlin, K.M., Read, Q.D., Record, S., Stark, S.C., Serbin, S.P., & Zarnetske, P.L. (2022). Towards mapping biodiversity from above: Can fusing LiDAR and hyperspectral remote sensing predict taxonomic, functional, and phylogenetic tree diversity in temperate forests? *Global Ecology and Biogeography*, 31, 1440-1460
- Kennedy, M., & Meyers, C.R. (1977). Spatial information systems: An introduction. (pp. 97): NOS (National Ocean Service)
- Khodor, M., Makki, I., Younes, R., Bianchi, T., Khoder, J., Francis, C., & Zucchetti, M. (2021). Landmine detection in hyperspectral images based on pixel intensity. *Remote Sensing Applications: Society and Environment*, 21, 100468

- Kimerling, A.J. (2002). Predicting Data Loss and Duplication when Resampling from Equal-Angle Grids. *Cartography and Geographic Information Science*, 29, 111-126
- Kirsch, R.A., Cahn, L., Ray, C., & Urban, G.H. (1957). Experiments in processing pictorial information with a digital computer. In, *Papers and discussions presented at the December 9-13*, 1957, Eastern Joint Computer Conference: Computers with deadlines to meet (pp. 221-229)
- Kneizys, F.X. (1988). *Users guide to LOWTRAN* 7. Air Force Geophysics Laboratory, United States Air Force
- Koch, B. (2010). Status and future of laser scanning, synthetic aperture radar and hyperspectral remote sensing data for forest biomass assessment. *ISPRS Journal of Photogrammetry and Remote Sensing*, 65, 581-590
- Kollasch, R.P. (2005). Increasing the detail of land use classification: The Iowa 2002 land cover product In: *Proceedings of the Global priorities in Land and Remote Sensing Conference: PECORA* (pp. 1-9). Sioux Falls: American Society for Photogrammetry and Remote Sensing
- Kolmann, M.A., Kalacska, M., Lucanus, O., Sousa, L., Wainwright, D., Arroyo-Mora, J.P., & Andrade, M.C. (2021). Hyperspectral data as a biodiversity screening tool can differentiate among diverse neotropical fishes. *Scientific Reports*, 11, 16157
- Kopp, G., Smith, P., Belting, C., Castleman, Z., Drake, G., Espejo, J., Heuerman, K., Lanzi, J., & Stuchlik, D. (2017). Radiometric flight results from the hyperspectral imager for climate science (hysics). *Geosci. Instrum. Method. Data Syst.*, 6, 169-191
- Kristóf, D. (2015). An alternative representation of coarse-resolution remote sensing images for time-series processing. In: 8th International Workshop on the Analysis of Multitemporal Remote Sensing Images (Multi-Temp) (pp. 1-4). Annecy: Curran Associates, Inc
- Kristóf, D., & Pataki, R. (2009). Tackling with the limitations of a raster data model: Vector-based preprocessing of MODIS reflective bands. In: 5th International Workshop on the Analysis of Multitemporal Remote Sensing Images (MultiTemp) (pp. 160-167). Groton: Curran Associates, Inc
- Kruse, F.A. (1988). Use of airborne imaging spectrometer data to map minerals associated with hydrothermally altered rocks in the northern grapevine mountains, Nevada, and California. *Remote Sensing of Environment, 24*, 31-51
- Laliberté, E., Schweiger, A.K., & Legendre, P. (2020). Partitioning plant spectral diversity into alpha and beta components. *Ecological Letters*, 23, 370-380
- Lassalle, G., Fabre, S., Credoz, A., Hédacq, R., Dubucq, D., & Elger, A. (2021). Mapping leaf metal content over industrial brownfields using airborne hyperspectral imaging and optimized vegetation indices. *Scientific Reports*, 11, 2
- Lawrence, R.L., Wood, S.D., & Sheley, R.L. (2006). Mapping invasive plants using hyperspectral imagery and Breiman Cutler classifications (randomForest). *Remote Sensing of Environment*, 100, 356-362
- Leblanc, G., Kalacska, M., & Soffer, R. (2014). Detection of single graves by airborne hyperspectral imaging. *Forensic Science International*, 245, 17-23

- Lee, C., & Landgrebe, D.A. (1993). Analyzing high-dimensional multispectral data. *IEEE Transactions on Geoscience and Remote Sensing*, *31*, 792-800
- Lenz, A., Schilling, H., Perpeet, D., Wuttke, S., Gross, W., & Middelmann, W. (2014). Automatic in-flight boresight calibration considering topography for hyperspectral pushbroom sensors. In: *2014 IEEE Geoscience and Remote Sensing Symposium* (pp. 2981-2984). Quebec City: IEEE
- Leslie, R.V. (2018). Microwave Sensors. In: S. Liang (Ed.), *Comprehensive Remote Sensing* (pp. 435-474). Oxford: Elsevier
- Li, W., Guo, Q., Jakubowski, M.K., & Kelly, M. (2012). A new method for segmenting individual trees from the LiDAR point cloud. *Photogrammetric Engineering & Remote Sensing*, 78, 75-84
- Liao, S., Bai, Z., & Bai, Y. (2012). Errors prediction for vector-to-raster conversion based on map load and cell size. *Chinese Geographical Science*, 22, 695-704
- Lim, H. (2008). Raster Data. In: S. Shekhar, & H. Xiong (Eds.), *Encyclopedia of GIS* (pp. 949-955). Boston, MA: Springer US
- Liu, H., Yu, T., Hu, B., Hou, X., Zhang, Z., Liu, X., Liu, J., Wang, X., Zhong, J., Tan, Z., Xia, S., & Qian, B. (2021a). UAV-Borne Hyperspectral Imaging Remote Sensing System Based on Acousto-Optic Tunable Filter for Water Quality Monitoring. *Remote Sensing*, 13, 4069
- Liu, N., Townsend, P.A., Naber, M.R., Bethke, P.C., Hills, W.B., & Wang, Y. (2021b). Hyperspectral imagery to monitor crop nutrient status within and across growing seasons. *Remote Sensing of Environment*, 255, 112303
- Liu, X. (2008). Airborne LiDAR for DEM generation: some critical issues. *Progress in Physical Geography*, 32, 31-49
- Lobell, D.B., & Asner, G.P. (2004). Cropland distributions from temporal unmixing of MODIS data. *Remote Sensing of Environment*, 93, 412-422
- Long, M., Wang, P., Fang, H., & Hu, W. (2019). Progress, Challenges, and opportunities for 2D material based photodetectors. *Advanced Functional Materials*, *29*, 1803807
- Lutes, J. (2005). Resourcesat-1 geometric accuracy assessment. In: *ASPRS 2005 Annual Conference* (pp. 1-12). Baltimore: American Society for Photogrammetric Engineering Remote Sensing
- Maffini, G. (1987). Raster versus vector data encoding and handling: A commentary. *Photogrammetric Engineering and Remote Sensing*, *53*, 1397-1398
- Maguire, D.J. (1992). The raster GIS design model—A profile of ERDAS. *Computers & Geosciences*, 18, 463-470
- Makki, I., Younes, R., Francis, C., Bianchi, T., & Zucchetti, M. (2017). A survey of landmine detection using hyperspectral imaging. *ISPRS Journal of Photogrammetry and Remote Sensing*, 124, 40-53
- Malhotra, A., Roulet, N.T., Wilson, P., Giroux-Bougard, X., & Harris, L.I. (2016). Ecohydrological feedbacks in peatlands: an empirical test of the relationship among vegetation, microtopography and water table. *Ecohydrology*, *9*, 1346-1357

- Manea, D., & Calin, M. (2015). Hyperspectral imaging in different light conditions. *The Imaging Science Journal*, 63, 214-219
- Mariotto, I., Thenkabail, P.S., Huete, A., Slonecker, E.T., & Platonov, A. (2013). Hyperspectral versus multispectral crop-productivity modeling and type discrimination for the HyspIRI mission. *Remote Sensing of Environment*, 139, 291-305
- Markham, B.L., Arvidson, T., Barsi, J.A., Choate, M., Kaita, E., Levy, R., Lubke, M., & Masek, J.G. (2018). Landsat Program. In: S. Liang (Ed.), *Comprehensive Remote Sensing* (pp. 27-90). Oxford: Elsevier
- Marshall, M., & Thenkabail, P. (2015). Advantage of hyperspectral EO-1 Hyperion over multispectral IKONOS, GeoEye-1, WorldView-2, Landsat ETM+, and MODIS vegetation indices in crop biomass estimation. *ISPRS Journal of Photogrammetry and Remote Sensing*, 108, 205-218
- Migdall, S., Klug, P., Denis, A., & Bach, H. (2012). The additional value of hyperspectral data for smart farming. In: Proceedings of IGARSS 2012 (pp. 7329-7332): IEEE
- Moore, P.A., Lukenbach, M.C., Thompson, D.K., Kettridge, N., Granath, G., & Waddington, J.M. (2019). Assessing the peatland hummock–hollow classification framework using high-resolution elevation models: implications for appropriate complexity ecosystem modeling. *Biogeosciences*, 16, 3491-3506
- Moravec, D., Komárek, J., López-Cuervo Medina, S., & Molina, I. (2021). Effect of atmospheric corrections on ndvi: Intercomparability of Landsat 8, Sentinel-2, and UAV sensors. *Remote Sensing*, 13, 3550
- Mouroulis, P., Green, R.O., & Chrien, T.G. (2000). Design of pushbroom imaging spectrometers for optimum recovery of spectroscopic and spatial information. *Applied Optics*, *39*, 2210-2220
- Müller, R., Lehner, M., Muller, R., Reinartz, P., Schroeder, M., & Vollmer, B. (2002). A program for direct georeferencing of airborne and spaceborne line scanner images. *International Archives of Photogrammetry Remote Sensing and Spatial Information Sciences*, 34, 148-153
- Murphy, R.J., Monteiro, S.T., & Schneider, S. (2012). Evaluating classification techniques for mapping vertical geology using field-based hyperspectral sensors. *IEEE Transactions on Geoscience and Remote Sensing*, 50, 3066-3080
- Naprstek, T.; Inamdar, D. (2022). HyPlanT a standalone flight planning application for pushbroom hyperspectral imagers, *Borealis*, v1, https://doi.org/10.5683/SP3/3QKALR
- National Research Council (2010). Seeing photons: Progress and limits of visible and infrared sensor arrays. Washington, DC: National Academies Press
- Noll, A.M. (1971). Scanned-display computer graphics. *Communications of the ACM, 14*, 143-150
- Oliveira, R.A., Tommaselli, A.M.G., & Honkavaara, E. (2019). Generating a hyperspectral digital surface model using a hyperspectral 2D frame camera. *ISPRS Journal of Photogrammetry and Remote Sensing*, 147, 345-360

- Pathakoti, M., Gharai, B., Gaddamidi, S., Venkata Narshimha, R., Kapanaboina, M., Mullapudi, S.V., & Yelisetty, K.M.V. (2018). Estimation of molecular column density of methane (XCH4) using AVIRIS-NG data. *Journal of Applied Remote Sensing*, 12, 046005
- Pau, S., Nippert, J.B., Slapikas, R., Griffith, D., Bachle, S., Helliker, B.R., O'Connor, R.C., Riley, W.J., Still, C.J., & Zaricor, M. (2022). Poor relationships between NEON Airborne Observation Platform data and field-based vegetation traits at a mesic grassland. *Ecology*, 103, e03590
- Pearlman, J.S., Barry, P.S., Segal, C.C., Shepanski, J., Beiso, D., & Carman, S.L. (2003). Hyperion, a space-based imaging spectrometer. *IEEE Transactions on Geoscience and Remote Sensing*, 41, 1160-1173
- Peng, G., Ruiliang, P., Biging, G.S., & Larrieu, M.R. (2003). Estimation of forest leaf area index using vegetation indices derived from hyperion hyperspectral data. *IEEE Transactions on Geoscience and Remote Sensing*, 41, 1355-1362
- Pengra, B.W., Johnston, C.A., & Loveland, T.R. (2007). Mapping an invasive plant, Phragmites australis, in coastal wetlands using the EO-1 Hyperion hyperspectral sensor. *Remote Sensing of Environment*, 108, 74-81
- Pepe, M., Fregonese, L., & Scaioni, M. (2018). Planning airborne photogrammetry and remote-sensing missions with modern platforms and sensors. *European Journal of Remote Sensing*, 51, 412-436
- Popescu, S.C., & Wynne, R.H. (2004). Seeing the trees in the forest. *Photogrammetric Engineering & Remote Sensing*, 70, 589-604
- Pu, R., Kelly, M., Anderson, G.L., & Gong, P. (2008). Using CASI hyperspectral imagery to detect mortality and vegetation stress associated with a new hardwood forest disease. *Photogrammetric Engineering & Remote Sensing*, 74, 65-75
- Qian, S.E. (2021). Hyperspectral satellites, evolution, and development history. *IEEE Journal of Selected Topics in Applied Earth Observations and Remote Sensing*, 14, 7032-7056
- Radoux, J., Chomé, G., Jacques, D.C., Waldner, F., Bellemans, N., Matton, N., Lamarche, C., d'Andrimont, R., & Defourny, P. (2016). Sentinel-2's potential for sub-pixel landscape feature detection. *Remote Sensing*, *8*, 488
- Ramsey, E., Rangoonwala, A., Nelson, G., & Ehrlich, R. (2005). Mapping the invasive species, Chinese tallow, with EO1 satellite Hyperion hyperspectral image data and relating tallow occurrences to a classified Landsat Thematic Mapper land cover map. *International Journal of Remote Sensing*, 26, 1637-1657
- Raney, R.K. (1998). The delay/Doppler radar altimeter. *IEEE Transactions on Geoscience and Remote Sensing*, 36, 1578-1588
- Rasti, B., Hong, D., Hang, R., Ghamisi, P., Kang, X., Chanussot, J., & Benediktsson, J.A. (2020). Feature extraction for hyperspectral imagery: the evolution from shallow to deep: Overview and toolbox. *IEEE Geoscience and Remote Sensing Magazine*, *8*, 60-88
- Rasti, B., Sveinsson, J.R., & Ulfarsson, M.O. (2014). Total variation based hyperspectral feature extraction. In: *2014 IEEE Geoscience and Remote Sensing Symposium* (pp. 4644-4647): IEEE

- Rauchmiller, R.F., & Schowengerdt, R.A. (1988). Measurement of the Landsat Thematic Mapper modulation transfer function using an array of point sources. *Optical Engineering*, 27, 274334
 - Richards, J.A., & Jia, X. (1999). Remote sensing digital image analysis. Springer
- Richter, R., Bachmann, M., Dorigo, W., & Muller, A. (2006). Influence of the Adjacency Effect on Ground Reflectance Measurements. *IEEE Geoscience and Remote Sensing Letters*, 3, 565-569
- Richter, R., & Schläpfer, D. (2020). ATCOR-4 User Guide, Version 7.3.0, March 2020. In: *Atmospheric/Topographic Correction for Airborne Imagery*. Wessling: DLR German Aerospace Center
- Roberts, D.A., Yamaguchi, Y., & Lyon, R.J.P. (1986). Comparison of various techniques for calibration of AIS data. In: *Proceedings of the 2nd Airborne Imaging Spectrometer Data Analysis Workshop* (pp. 21-30)
- Roger, R.E., & Arnold, J.F. (1996). Reliably estimating the noise in AVIRIS hyperspectral images. *International Journal of Remote Sensing*, 17, 1951-1962
- Rowan, G.S.L., Kalacska, M., Inamdar, D., Arroyo-Mora, J.P., & Soffer, R. (2021). Multi-Scale Spectral Separability of Submerged Aquatic Vegetation Species in a Freshwater Ecosystem. *Frontiers in Environmental Science*, *9*, 760372
- Roy, D.P. (2000). The impact of misregistration upon composited wide field of view satellite data and implications for change detection. *IEEE Transactions on Geoscience and Remote Sensing*, 38, 2017-2032
- San, B.T., & Süzen, M.L. (2011). Evaluation of cross-track illumination in EO-1 Hyperion imagery for lithological mapping. *International Journal of Remote Sensing*, 32, 7873-7889
- Schaepman, M.E., de Vos, L., & Itten, K.I. (1998). APEX-Airborne PRISM Experiment: hyperspectral radiometric performance analysis for the simulation of the future ESA land surface processes earth explorer mission. In: *Imaging spectrometry IV* (pp. 253-262): International Society for Optics and Photonics
- Schilling, R.J., & Harris, S.L. (2011). Fundamentals of Digital Signal Processing using MATLAB: an Instructor's Solutions Manual to Accompany. Cengage Learning
- Schläpfer, D., Nieke, J., & Itten, K.I. (2007). Spatial PSF nonuniformity effects in airborne pushbroom imaging spectrometry data. *IEEE Transactions on Geoscience and Remote Sensing*, 45, 458-468
- Schowengerdt, R.A. (2006a). 1.4. Remote-Sensing Systems. *Remote sensing: models and methods for image processing*. Amsterdam, The Netherlands: Elsevier
- Schowengerdt, R.A. (2006b). 3.4. Spatial Response. *Remote sensing: models and methods for image processing*. Amsterdam, The Netherlands: Elsevier
- Schowengerdt, R.A. (2006c). 3.5. Spectral Response. *Remote sensing: models and methods for image processing*. Amsterdam, The Netherlands: Elsevier

- Schowengerdt, R.A., Antos, R.L., & Slater, P.N. (1974). *Measurement Of The Earth Resources Technology Satellite (Erts-1) Multi-Spectral Scanner OTF From Operational Imagery*. SPIE
- Schweiger, A.K. (2020). Spectral field campaigns: planning and data collection. In: *Remote sensing of plant biodiversity* (pp. 385-423): Springer
- Secker, J., Staenz, K., Gauthier, R.P., & Budkewitsch, P. (2001). Vicarious calibration of airborne hyperspectral sensors in operational environments. *Remote Sensing of Environment*, 76, 81-92
- Shlien, S. (1979). Geometric correction, registration, and resampling of Landsat imagery. *Canadian Journal of Remote Sensing*, *5*, 74-89
- Signoroni, A., Savardi, M., Baronio, A., & Benini, S. (2019). Deep Learning Meets Hyperspectral Image Analysis: A Multidisciplinary Review. *Journal of Imaging*, 5, 52
- Silván-Cárdenas, J.L., Caccavari-Garza, A., Quinto-Sánchez, M.E., Madrigal-Gómez, J.M., Coronado-Juárez, E., & Quiroz-Suarez, D. (2021). Assessing optical remote sensing for grave detection. *Forensic Science International*, 329, 111064
- Simms, D.M., Waine, T.W., Taylor, J.C., & Juniper, G.R. (2014). The application of time-series MODIS NDVI profiles for the acquisition of crop information across Afghanistan. *International Journal of Remote Sensing*, *35*, 6234-6254
- Skauli, T. (2012). An upper-bound metric for characterizing spectral and spatial coregistration errors in spectral imaging. *Optics Express*, 20, 918-933
- Skauli, T., Gilchrist, J.R., & Durell, C. (2021). Status of the ieee p4001 working group for standardization in hyperspectral imaging. In, 2021 IEEE Research and Applications of Photonics in Defense Conference (RAPID) (pp. 1-2)
- Smith, A.R. (1995). A pixel is not a little square, a pixel is not a little square, a pixel is not a little square! *Microsoft Computer Graphics, Technical Memo, 6*
- Smith, M.-L., Martin, M.E., Plourde, L., & Ollinger, S.V. (2003). Analysis of hyperspectral data for estimation of temperate forest canopy nitrogen concentration: comparison between an airborne (AVIRIS) and a spaceborne (Hyperion) sensor. *IEEE Transactions on Geoscience and Remote Sensing*, 41, 1332-1337
- Smith, S., Holland, D., & Longley, P. (2004). The importance of understanding error in LiDAR digital elevation models. *International Archives of the Photogrammetry, Remote Sensing and Spatial Information Sciences*, 35, 996-1001
- Soffer, R., Ifimov, G., Pan, Y., & Belanger, S. (2021). Acquisition and Spectroradiometric Assessment of the Novel WaterSat Imaging Spectrometer Experiment (WISE) Sensor for the Mapping of Optically Shallow Coastal Waters. In: *OSA Optical Sensors and Sensing Congress*. Virtual Event: OSA Publishing
- Soffer, R.J., Ifimov, G., Arroyo-Mora, J.P., & Kalacska, M. (2019). Validation of airborne hyperspectral imagery from laboratory panel characterization to image quality assessment: implications for an arctic peatland surrogate simulation site. *Canadian Journal of Remote Sensing*, 45, 476-508

- Sothe, C., Dalponte, M., Almeida, C.M.d., Schimalski, M.B., Lima, C.L., Liesenberg, V., Miyoshi, G.T., & Tommaselli, A.M.G. (2019). Tree species classification in a highly diverse subtropical forest integrating UAV-based photogrammetric point cloud and hyperspectral data. *Remote Sensing*, 11, 1338
- Suárez, J.C., Ontiveros, C., Smith, S., & Snape, S. (2005). Use of airborne LiDAR and aerial photography in the estimation of individual tree heights in forestry. *Computers & Geosciences*, 31, 253-262
- Tan, B., Woodcock, C.E., Hu, J., Zhang, P., Ozdogan, M., Huang, D., Yang, W., Knyazikhin, Y., & Myneni, R.B. (2006). The impact of gridding artifacts on the local spatial properties of MODIS data: Implications for validation, compositing, and band-to-band registration across resolutions. *Remote Sensing of Environment*, 105, 98-114
- Tarrant, P., Amacher, J., & Neuer, S. (2010). Assessing the potential of Medium-Resolution Imaging Spectrometer (MERIS) and Moderate-Resolution Imaging Spectroradiometer (MODIS) data for monitoring total suspended matter in small and intermediate sized lakes and reservoirs. *Water Resources Research*, 46
- Teillet, P.M., Fedosejevs, G., Gauthier, R.P., O'Neill, N.T., Thome, K.J., Biggar, S.F., Ripley, H., & Meygret, A. (2001). A generalized approach to the vicarious calibration of multiple Earth observation sensors using hyperspectral data. *Remote Sensing of Environment*, 77, 304-327
- Thomas, H., Qi, C.R., Deschaud, J.-E., Marcotegui, B., Goulette, F., & Guibas, L.J. (2019). Kpconv: Flexible and deformable convolution for point clouds. In: *Proceedings of the IEEE/CVF international conference on computer vision* (pp. 6411-6420): IEEE
- Thompson, D.R., Roberts, D.A., Gao, B.C., Green, R.O., Guild, L., Hayashi, K., Kudela, R., & Palacios, S. (2016). Atmospheric correction with the bayesian empirical line. *Optics Express*, 24, 2134-2144
- Tiede, D., Hochleitner, G., & Blaschke, T. (2005). A full GIS-based workflow for tree identification and tree crown delineation using laser scanning. In, *ISPRS Workshop CMRT* (p. 2005)
- Tomlin, C.D. (1990). *Geographic information systems and cartographic modelling*. New Jersey, US: Prentice-Hall
- Torres-Rua, A., Ticlavilca, A., Bachour, R., & McKee, M. (2016). Estimation of surface soil moisture in irrigated lands by assimilation of landsat vegetation indices, surface energy balance products, and relevance vector machines. *Water*, 8, 167
- Triggs, B., McLauchlan, P.F., Hartley, R.I., & Fitzgibbon, A.W. (2000). Bundle Adjustment A Modern Synthesis. In B. Triggs, A. Zisserman, & R. Szeliski (Eds.), *Vision Algorithms: Theory and Practice* (pp. 298-372). Berlin, Heidelberg: Springer
- Turner, W., Spector, S., Gardiner, N., Fladeland, M., Sterling, E., & Steininger, M. (2003). Remote sensing for biodiversity science and conservation. *Trends in Ecology & Evolution*, 18, 306-314
- van der Meer, F.D., van der Werff, H.M.A., van Ruitenbeek, F.J.A., Hecker, C.A., Bakker, W.H., Noomen, M.F., van der Meijde, M., Carranza, E.J.M., Smeth, J.B.d., & Woldai, T. (2012).

- Multi- and hyperspectral geologic remote sensing: A review. *International Journal of Applied Earth Observation and Geoinformation*, 14, 112-128
- van der Werf, G.R., Morton, D.C., DeFries, R.S., Olivier, J.G.J., Kasibhatla, P.S., Jackson, R.B., Collatz, G.J., & Randerson, J.T. (2009). Co2 emissions from forest loss. *Nature Geoscience*, *2*, 737-738
- van Ruitenbeek, F.J.A., Cudahy, T.J., van der Meer, F.D., & Hale, M. (2012). Characterization of the hydrothermal systems associated with Archean VMS-mineralization at Panorama, Western Australia, using hyperspectral, geochemical and geothermometric data. *Ore Geology Reviews*, 45, 33-46
- Vane, G., Chrien, T.G., Miller, E.A., & Reimer, J.H. (1987). Spectral and radiometric calibration of the airborne visible/infrared imaging spectrometer. In: *Imaging spectroscopy II* (pp. 91-107): International Society for Optics and Photonics
- Vane, G., Goetz, A.F., & Wellman, J.B. (1984). Airborne imaging spectrometer: A new tool for remote sensing. *IEEE Transactions on Geoscience and Remote Sensing*, 546-549
- Vauhkonen, J., Hakala, T., Suomalainen, J., Kaasalainen, S., Nevalainen, O., Vastaranta, M., Holopainen, M., & Hyyppa, J. (2013). Classification of spruce and pine trees using active hyperspectral LiDAR. *IEEE Geoscience and Remote Sensing Letters*, 10, 1138-1141
- Vermote, E., Tanré, D., Deuzé, J., Herman, M., Morcrette, J., & Kotchenova, S. (2006). Second simulation of a satellite signal in the solar spectrum-vector (6SV). 6S User Guide Version, 3, 1-55
- Vreys, K., Iordache, M.-D., Biesemans, J., & Meuleman, K. (2016a). Geometric correction of APEX hyperspectral data. *Miscellanea Geographica*, 20, 11-15
- Vreys, K., Iordache, M.-D., Bomans, B., & Meuleman, K. (2016b). Data acquisition with the APEX hyperspectral sensor. *Miscellanea Geographica*, 20, 5-10
- Wade, T.G., Wickham, J.D., Nash, M.S., Neale, A.C., Riitters, K.H., & Jones, K.B. (2003). A comparison of vector and raster gis methods for calculating landscape metrics used in environmental assessments. *Photogrammetric Engineering & Remote Sensing*, 69, 1399-1405
- Wallis, C.I.B., Crofts, A.L., Inamdar, D., Arroyo-Mora, J.P., Kalacska, M., Laliberté, É., & Vellend, M. (2023). Remotely sensed carbon content: The role of tree composition and tree diversity. *Remote sensing of environment*, 284, 113333
- Wang, D., Vinson, R., Holmes, M., Seibel, G., Bechar, A., Nof, S., & Tao, Y. (2019). Early Detection of tomato spotted wilt virus by hyperspectral imaging and Outlier Removal Auxiliary Classifier Generative Adversarial Nets (OR-AC-GAN). *Scientific Reports*, *9*, 4377
- Wang, J., Fang, H., Wang, X., Chen, X., Lu, W., & Hu, W. (2017). Recent progress on localized field enhanced two-dimensional material photodetectors from ultraviolet—visible to infrared. *Small*, 13, 1700894
- Wang, Q., Shi, W., & Atkinson, P.M. (2018). Enhancing spectral unmixing by considering the point spread function effect. *Spatial Statistics*, 28, 271-283

- Warren, M.A., Taylor, B.H., Grant, M.G., & Shutler, J.D. (2014). Data processing of remotely sensed airborne hyperspectral data using the Airborne Processing Library (APL): Geocorrection algorithm descriptions and spatial accuracy assessment. *Computers & Geosciences*, 64, 24-34
- Westoby, M.J., Brasington, J., Glasser, N.F., Hambrey, M.J., & Reynolds, J.M. (2012). 'Structure-from-Motion' photogrammetry: A low-cost, effective tool for geoscience applications. *Geomorphology*, 179, 300-314
- Wilkinson, G. (1996). A review of current issues in the integration of GIS and remote sensing data. *International Journal of Geographical Information Science*, 10, 85-101
- Williams, M.D., Kerekes, J.P., & Aardt, J.V. (2017). Application of abundance map reference data for spectral unmixing. *Remote Sensing*, *9*, 793
- Wolter, P.T., Johnston, C.A., & Niemi, G.J. (2005). Mapping submergent aquatic vegetation in the US Great Lakes using Quickbird satellite data. *International Journal of Remote Sensing*, 26, 5255-5274
- Xu, H., & Wang, X.-j. (2007). Applications of multispectral/hyperspectral imaging technologies in military. *Infrared and Laser Engineering*, 36, 13
- Yang, H., Zhang, L., Ong, C., Rodger, A., Liu, J., Sun, X., Zhang, H., Jian, X., & Tong, Q. (2017). Improved aerosol optical thickness, columnar water vapor, and surface reflectance retrieval from combined CASI and SASI airborne hyperspectral sensors. *Remote Sensing*, 9, 217
- Yao, H., Tang, L., Tian, L., Brown, R., Bhatnagar, D., & Cleveland, T. (2011). Using hyperspectral data in precision farming applications. *Hyperspectral Remote Sensing of Vegetation*, 591-607
- Yokoya, N., Miyamura, N., & Iwasaki, A. (2010). Preprocessing of hyperspectral imagery with consideration of smile and keystone properties. In: A. Larar; H. Chung & M. Suzuki, (Eds.) *Multispectral, Hyperspectral, and Ultraspectral Remote Sensing Technology, Techniques, and Applications III*:SPIE
- Yuen, P.W., & Richardson, M. (2010). An introduction to hyperspectral imaging and its application for security, surveillance and target acquisition. *The Imaging Science Journal*, 58, 241-253
- Zhang, B., Zhao, L., & Zhang, X. (2020). Three-dimensional convolutional neural network model for tree species classification using airborne hyperspectral images. *Remote Sensing of Environment*, 247, 111938
- Zhang, C., Zhou, Y., & Qiu, F. (2015). Individual Tree Segmentation from LiDAR Point Clouds for Urban Forest Inventory. *Remote Sensing*, 7, 7892-7913
- Zhang, J., Lin, X., & Ning, X. (2013). SVM-based classification of segmented airborne lidar point clouds in urban areas. *Remote Sensing*, *5*, 3749-3775
- Zhao, H., Cui, B., & Jia, G. (2019). A flight direction design method for airborne spectral imaging considering the anisotropy reflectance of the target in rugged terrain. *Sensors*, 19, 2715

Zheng, Q., Kindel, B.C., & Goetz, A.F.H. (2003). The High Accuracy Atmospheric Correction for Hyperspectral Data (HATCH) model. *IEEE Transactions on Geoscience and Remote Sensing*, 41, 1223-1231

Zhong, Y., Hu, X., Luo, C., Wang, X., Zhao, J., & Zhang, L. (2020). WHU-Hi: UAV-borne hyperspectral with high spatial resolution (H2) benchmark datasets and classifier for precise crop identification based on deep convolutional neural network with CRF. *Remote Sensing of Environment*, 250, 112012